# Proceedings of the IV International Symposium on Applied Geoinformatics – ISAG2024

## Wroclaw University of Science and Technology, 9–10 May 2024

WUST Publishing House
Wrocław 2024

INTERNATIONAL SYMPOSIUM ON

APPLIED GEOINFORMATICS

9-10 May 2024 · Wrocław/Poland

**ISAG2024 – IV International Symposium on Applied Geoinformatics**

ISBN: 978-83-7493-294-3

DOI: 10.37190/ISAG2024

Scientific editors

Prof. Dr. Bulent Bayram

Prof. Dr. Kazimierz Becek

Assist. Prof. Dr. George Arampatzis

We are pleased to bring out this Full Paper Proceedings containing the blind-reviewed abstracts presented at the International Symposium on Applied Geoinformatics (ISAG2024) held in Wroclaw on May 9-10, 2024. The conference's primary goal feature is to bring scientists, engineers, and industry researchers together to exchange and share their experiences and results about most aspects of research, as well as discuss the practical challenges encountered and the solutions adopted in Geoinformatics. The symposium is jointly organized by the Department of Geomatics Engineering, Yıldız Technical University, Istanbul, Turkey, Wroclaw University of Science and Technology, Wroclaw, Poland, and Technical University of Crete, Greece. The ISAG2024 has attracted several invited keynote presentations by eminent researchers in the field, where several oral and poster presentations have contributed to achieving the challenging goal of the conference. The conference has brought together researchers from various countries working in different areas to discuss the current state of knowledge and address challenges in Geoinformatics. The topics covered in this issue include recent advances in artificial intelligence, satellite imagery, advanced remote sensing, photogrammetry, image processing, global navigation satellite systems, height systems, terrestrial laser scanning, GIS/smart cities, and land management. In the Full paper Proceedings of ISAG2024, you will see manuscripts on different aspects of Geoinformatics covering both fundamentals and applications. We thank all the authors for contributing their latest work to ISAG2024. Special thanks to the reviewers for their critical review, which has helped to maintain the high standards of this abstract book. We thank Yıldız Technical University, Wroclaw University of Science and Technology, and the Technical University of Crete for their strong support, all local organizing committee members for their invaluable effort and devoted teamwork, as well as all sponsors for their financial support.

Prof. Dr. Bulent Bayram

Chair of ISAG2024

# COMMITTEES

## INTERNATIONAL ORGANIZATION COMMITTEE

Akpinar Burak, Yıldız Technical University, Türkiye
Arampatzis George, Technical University of Crete, Greece
Bakirman Tolga, Yıldız Technical University, Türkiye
Bayram Bulent, Yıldız Technical University, Türkiye
Becek Kazimierz, Wroclaw University of Science and Technology, Poland
Muszyński Zbigniew, Wroclaw University of Science and Technology, Poland
Ozkaya Bestami, Yıldız Technical University/ Türkiye
Partsinevelovs Panagiotis, Technical University of Crete, Crete, Greece

## SCIENTIFIC COMMITTEE

Abdikan Saygin, hacettepe University, Türkiye
Abujayyab Sohaib, International College for Engineering and Management, Pakistan
Acar Ugur, Yıldız Technical University, Türkiye
Akpinar Burak, Yıldız Technical University, Türkiye
Algancı Ugur, Istanbul Technical University, Türkiye
Alkan Reha Metin, Istanbul Technical University, Türkiye
Arampatzis Georgios, Technical University of Crete, Greece
Arslan Niyazi, Çukurova University, Türkiye
Arslan Ozan, Kocaeli University, Türkiye
Avdan Ugur, Eskişehir Technical University, Türkiye
Ayazli Ercüment, Sivas Cumhuriyet University, Türkiye
Aydin Abdurrahim, Düzce University, Türkiye
Aydin Cuneyt, Yıldız Technical University, Türkiye
Aykut Nedim Onur, Yıldız Technical University, Türkiye
Bacior Stanislaw, University of Agriculture in Cracow, Poland
Bakatsaki Maria, Technical University of Crete, Greece
Bakirman Tolga, Yıldız Technical University, Türkiye
Bayram Bulent, Yıldız Technical University, Türkiye

Becek Kazimierz, Wroclaw University of Science and Technology, Poland
Benndorf Joerg, TU Bergakademie Freiberg, Germany
Blachowski Jan, Wroclaw University of Science and Technology, Poland
Błaszkiewicz Leszek, University of Warmia and Mazury in Olsztyn, Poland
Cakar Tuna, MEF University, Türkiye
Calò Fabiana, Institute for the Electromagnetic Sensing of The Environment, Italy
Cellmer Slawomir, University of Warmia and Mazury in Olsztyn, Poland
Celms Armands, University of Latvia, Latvia
Centeno Jorge, Universidade Federal Do Parana, Brasil
Cetin Zehra, Yıldız Technical University, Türkiye
Czaplicka Marta, University of Warmia and Mazury in Olsztyn, Poland
Dash Jadu, University of Southampton, UK
Dębowski Marcin, University of Warmia and Mazury in Olsztyn, Poland
Demir Nusret, Akdeniz University, Türkiye
Demirel Hande, Istanbul Technical University, Türkiye
Dilo Arta, Netherlands Organization for Applied Scientific Research, Netherlands
Dogan Ugur, Yıldız Technical University, Türkiye
Dogru Ahmet Ozgur, Istanbul Technical University, Türkiye
Duchnowski Robert, University of Warmia and Mazury in Olsztyn, Poland
Duran Zaide, Istanbul Technical University, Türkiye
Duru Anday, Karabük University, Türkiyr
Erenoglu Cuneyt, Çanakkale Onsekiz Mart University, Türkiye
Erenoglu Oya, Çanakkale Onsekiz Mart University, Türkiye
Fialkowska Bitner Agnieszka, University of Agriculture in Krakow, Poland
Gazioglu Cem, Istanbul University, Türkiye
Goksel Cigdem, Istanbul Technical University, Türkiye
Gruen Armin, ETH Zurich, Switzerland
Gul Kilic Fatmagul, Yıldız Technical University, Türkiye
Hajji Rafika, College of Geomatic Sciences and Surveying Engineering, Morocco
Hejmanowska Beata, AGH University of Science and Technology, Poland
Iban, Muzaffer Can, Mersin Üniversitesi, Türkiye

Ilhan, Hamza Osman, Yildiz Technical University, Türkiye

Ince Elmas Sinem, German Research Centre for Geosciences (GFZ-Potsdam), Germany

Isikdag Umit, Mimar Sinan University, Türkiye

Jan Rod, Norwegian University of Science and Technology, Norway

Jansons Aris, SILAVA, Latvia

Jamil Akhtar, National University of Computer and Emerging Sciences, Pakistan

Jóźwiakowski Krzysztof, University of Life Sciences in Lublin, Poland

Jutzi Boris, Karlsruhe Institute of Tecghnology, Germany

Kalaitzidis Chariton, CIHEAM MAICh, Greece

Kaļinka Māris, Riga Technical University, Latvia

Kaminskis Janis, Riga Technical University, Latvia

Karas Ismail Ragip, Karabük University, Türkiye

Krawczyk Artur, AGH University of Science and Technology, Poland

Kavzoglu Taskin, Gebze Technical University, Türkiye

Kaya Sinasi, Istanbul Technical University, Türkiye

Kollo, Karin, Estonian Land Board, Estonia

Krankowski Andrzej, University of Warmia and Mazury in Olsztyn, Poland

Kussul Nataliia, Department Chair, National Technical University of Ukraine, Ukraine

Kutoglu Hakan, Zonguldak Bulent Ecevit University, Türkiye

Lerma Jose Luis, Universitat Politechnicia de Valencia (UPV), Spain

Litwin Urszula, University of Agriculture in Cracow, Poland

Maciuk Kamil, AGH University of Science and Technology, Poland

Milczarek Wojciech, Wroclaw University of Science and Technology, Poland

Mishra Amit Kumar, University of Cape Town, South Africa

Mlakar Izidor, University of Maribor, Slovenia

Musaoglu Nebiye, Istanbul Technical University, Türkiye

Neusch-Landes Tania, INSA Strasbourg, France

Ok Ali Ozgun, Hacettepe University, Türkiye

Ortakci Yasin, Karabük University, Türkiye

Osada Edward, University of Lower Silesia DSW, Poland

Ozener Haluk, Bogazici University, Türkiye

Ozturk Derya, 19 Mayıs University, Türkiye

Ozturk Ozan, Recep Tayyip Erdoğan University, Türkiye

Pal Mahesh, National Institute of Technology Kurukshetra, India

Paršeliūnas Eimuntas Kazimieras, Vilnius Tech, Lithuania

Plewako Marek, University of Agriculture in Cracow, Poland

Popielarczyk Dariusz, University of Warmia and Mazury in Olsztyn, Poland

Poyraz Fatih, Sivas Cumhuriyet University, Türkiye

Puķīte Vivita, Latvia University of Life Sciences and Technologies/ Latvia

Rahman Alias Abdul, Technology University of Malaysia, Malaysia

Rapiński Jacek, University of Warmia and Mazury in Olsztyn, Poland

Reis Catal Hatice, Gümüşhane University, Türkiye

Sanli Balik Fusun, Yıldız Technical University, Türkiye

Sanli Dogan Ugur, Yıldız Technical University, Türkiye

Savvakis Nikolaos, Technical University of Crete, Greece

Seker Dursun Zafer, Istanbul Technical University, Türkiye

Selbesoglu Mahmut Oguz, Istanbul Technical University, Türkiye

Senetra Adam, University of Warmia and Mazury, Poland

Sertel Elif, Istanbul Technical University, Türkiye

Sesli Ahmet Faik, 19 Mayıs University, Türkiye

Sifakis Nikolaos, Technical University of Crete, Greece

Shan Jie, Purdue University, USA

Sivri Nuket, Istanbul University, Türkiye

Sobolewska-Mikulska Katarzyna, Warsaw University of Technology, Poland

Sulzer Wolfgang, University of Graz, Austria

Tanik Aysegul, Istanbul Technical University, Türkiye

Tobias Rudolph, Technische Hochschule Georg Agricola, Germany

Tsinarakis Georgios, Technical University of Crete, Greece

Uzar Melis, Yıldız Technical University, Türkiye

Vardar Nurten, Yıldız Technical University, Türkiye

Varna Inese, University of Latvia, Latvia

Wielgosz Paweł, University of Warmia and Mazury in Olsztyn, Poland

Yakar Murat, Mersin University, Türkiye

Yalcin Mustafa, Afyon kocatepe University, Türkiye

Yalcinkaya Mualla, Karadeniz Technical University, Türkiye

Yastikli Naci, Yıldız Technical University, Türkiye

Yildiz Ferruh, Selçuk University, Türkiye

Yilmaz Alper, The Ohio State University, USA

Zamparelli Virginia, Institute for Electromagnetic Sensing of the Environment (IREA), Italy

## LOCAL ORGANIZATION COMMITTEE

Chair: Kazimierz Becek, Wroclaw University of Science and Technology, Poland
Robert Gradka, Wroclaw University of Science and Technology, Poland
Patrycja Pochwatka, University of Life Sciences in Lublin, Poland
Jarosław Wajs, Wroclaw University of Science and Technology, Poland

# KEYNOTE SPEAKERS

**Prof. Dr. Habil. Beata Hejmanowska**

AGH Technical University of Science and Technology, Poland

Classification accuracy in machine learning, with the example of Land Use Land Cover classification in mining areas.

**Prof. Dr. -Ing. Wolfgang Kresse**

Hochschule Neubrandenburg, University of Applied Sciences, Germany

Origins of important geospatial ISO standards

# THE SPECIAL SESSION OF SATELLITE IMAGERY PROVIDERS

**Benjamin Lieberknecht**

European Space Imaging: Unlocking New Horizons

Harnessing the Power of Worldview Legion and Umbra Radar Data for Comprehensive Earth Observation

**Sybrand van Beijma**

Capella Space

Setting the SAR benchmark with 24/7 global insights

**Rafal Dabrowski,**

Axelspace

Space within your reach – AXELSPACE Corporation services

**Michael Hanley**

Pixxel

High-resolution hyperspectral satellite imagery

**Joe Cotti**

Airbus

Plèiades NEO – a NEO dawn for Earth Observation

## FULL PAPERS

INTERNATIONAL SYMPOSIUM ON
APPLIED
GEOINFORMATICS
9-10 May 2024 · Wrocław/Poland

*International Symposium on Applied Geoinformatics (ISAG2024)*

# Exploring The Influence of LST And NDVI on Real Estate Values in Turkish Cities Through Regression Analysis

Selin Uyar[1], Muzaffer Can Iban[2]*

[1] Mersin University, Institute of Science, Department of Remote Sensing and GIS, Mersin, Türkiye; slnuyarr@gmail.com;
ORCID 0009-0005-4807-0993
[2] Mersin University, Faculty of Engineering, Department of Geomatics Engineering, Mersin, Türkiye;
caniban@mersin.edu.tr; ORCID 0000-0002-3341-1338
* Corresponding Author

## Abstract

This research investigates the correlation between mean housing prices in central districts of Ankara, Istanbul, Izmir, and Mersin and Land Surface Temperature (LST) as well as Normalized Difference Vegetation Index (NDVI) using regression analysis. Its main objective is to explore variations in NDVI and LST values across cities with distinct land use and climate patterns and to discern their impact on real estate values. Housing sales averages for neighborhoods were sourced from the Endeksa.com platform, while NDVI and LST data were extracted from Landsat 8 satellite imagery. Regression analysis, employing $R^2$ scores and p-values, was utilized to assess the significance of the relationship between mean neighborhood sales values and NDVI/LST. Results indicate a notable influence of NDVI and LST on housing prices in specific districts such as Eyüp, Bahçelievler, and Çekmeköy in Istanbul ($R^2 > 0.7$), a lesser effect in Çankaya of Ankara and Güzelbahçe of Izmir, and a more pronounced impact in Yenişehir of Mersin compared to other areas. This study's findings provide insights into urban dynamics by highlighting how the presence of green areas and thermal comfort shape the real estate market at the neighborhood level across cities.

**Keywords:** *Thermal Comfort, NDVI, LST, Remote Sensing, Housing Sale Prices*

## Introduction/Background

In rapidly urbanizing cities, the rise of urban heat islands (UHIs) due to diminishing green spaces adversely affects thermal comfort (Zengin et al., 2019). Research on the impact of green space quantity and Land Surface Temperature (LST) factors on property values in Turkish cities is limited. Thermal comfort, crucial for well-being, is influenced by UHIs, with higher urban temperatures impacting energy use, air quality, and health (Tan et al., 2012). Urban morphology, reducing ventilation and retaining heat, exacerbates UHIs (Taleghani et al., 2013). LST, determined by impermeable surfaces and reduced greenery, correlates negatively with green area density (Tan et al., 2012). Satellite imagery, particularly LST and Normalized Difference Vegetation Index (NDVI), facilitates precise measurement of these factors. A strong negative correlation exists between LST and NDVI, emphasizing the role of poor vegetation in UHI formation (Erdem Okumus and Terzi, 2021; Şekertekin and Zadbagher, 2021). Research in other countries indicates that higher NDVI values correlate with increased property values (Jiao et al., 2017; Holt and Borsuk, 2020; Liebelt et al., 2018; Zambrano – Monserrate et al., 2021). This study aims to explore the relationship between LST, NDVI values during summer, and Average Housing Sales Values (AHSV) in four Turkish cities. It visualizes and discusses the impact of environmental factors on housing markets and regional price variations.

## Materials and Methods

The study areas include Ankara, Istanbul, Izmir, and Mersin, selected for their diverse geographical, climatic, urban, and demographic characteristics. Regression analysis was conducted at the neighborhood level using vector data obtained from local authorities. A total of 39 districts in Istanbul, 8 in Ankara, 11 in Izmir, and 4 in Mersin were included, with densely populated and constructed neighborhoods considered. AHSV data were manually compiled from Endeksa.com for these neighborhoods. Endeksa.com provides real estate data using big data analysis and machine learning methods. Data collection utilized values from November 2022. AHSV data were added as attributes to vector data, ready for Geographic Information System (GIS) software. Remote sensing data from Landsat 8 OLI and TIRS sensors for the summer months of 2022 were used to compile Average NDVI and LST values for neighborhoods. Google Earth Engine (GEE) platform facilitated data management and analysis. LST and NDVI values were overlaid onto vector files, and average values were calculated for each neighborhood. The dataset, comprising 1851 neighborhoods, was prepared for regression analysis in the Python-based Scikit-learn library. Regression analysis examined the relationships between AHSV-NDVI, AHSV-LST, and NDVI-LST in each city's districts. The significance and linearity of the AHSV-LST and AHSV-NDVI relationships were assessed using $R^2$ score and p-value criteria.

## Results and Discussion

The examination of AHSV across the neighborhoods of Ankara, Istanbul, Izmir, and Mersin reveals intriguing patterns, as depicted in Figure 1. In Ankara, for instance, the Oran neighborhood in the Çankaya district boasts the highest AHSV at 33,300 TL/$m^2$, contrasting sharply with the lowest value of 2,914 TL/$m^2$ in the Hacı Bayram neighborhood of Altındağ district. On average, the city's AHSV stands at 10,073 TL/$m^2$, with higher values clustered along the western-northwestern axis. In Istanbul, the Baltalimanı neighborhood in Sarıyer district commands the highest AHSV at 164,100 TL/$m^2$, while Sanayi neighborhood in Pendik district records the lowest at 6,540 TL/$m^2$. Notably, neighborhoods bordering the Bosphorus exhibit higher AHSV values. Izmir showcases the Akdeniz neighborhood in Konak district with the highest AHSV of 75,691 TL/$m^2$, while Ferahlı neighborhood, also in Konak district, reports the lowest at 6,212 TL/$m^2$. Similarly, in Mersin, the Merkez neighborhood in Mezitli district leads with the highest AHSV at 13,087 TL/$m^2$, whereas Civanyaylağı neighborhood in Akdeniz district has the lowest at 2,531 TL/$m^2$. Here, newly developed neighborhoods and those along the western-northern axis typically command higher AHSV values, contrasting with the relatively lower values in eastern and southeastern areas.

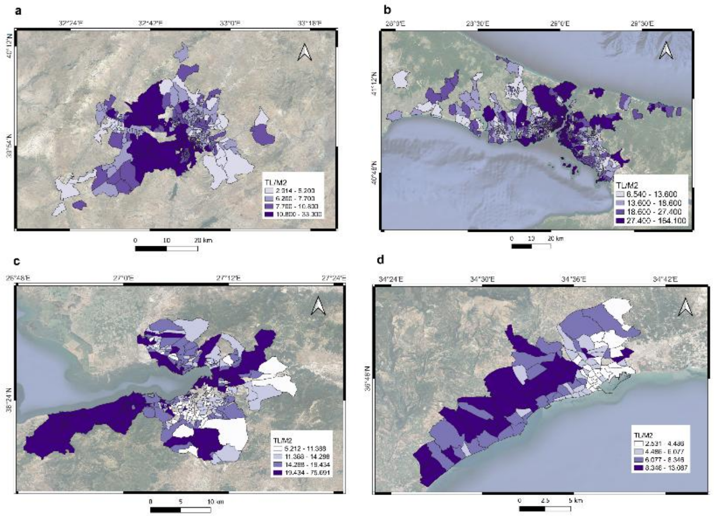

**Figure 1.** AHSV maps of neighborhoods belonging to the cities of Ankara (a), Istanbul (b), Izmir (c), and Mersin (d).

Figure 2 illustrates the average NDVI values across the neighborhoods of the four cities. In Ankara, Mebusevleri neighborhood in Çankaya district records the highest average NDVI value of 0.427, while Alçı OSB neighborhood in Sincan district reports the lowest at 0.113. Similarly, in Istanbul, Bahçeköy Merkez neighborhood in Sarıyer district exhibits the highest average NDVI value of 0.867, contrasting with the lowest value of 0.109 in Vatan neighborhood in Bayrampaşa district. Izmir showcases the 2. İnönü neighborhood in Narlıdere district with the highest average NDVI value of 0.639, while Seyhan neighborhood in Buca district has the lowest at 0.089. In Mersin, Kaleköy neighborhood in Mezitli district records the highest average NDVI value of 0.618, and Mesudiye neighborhood in Akdeniz district exhibits the lowest at 0.097. Notably, neighborhoods situated away from city centers tend to exhibit higher NDVI values.

The Average LST values, as illustrated in Figure 3, offer further insights. In Ankara, Mevlana neighborhood in Sincan district tops the chart with the highest average LST value at 40.80°C, while Güzeltepe neighborhood in Çankaya district records the lowest at 29.93°C. In Istanbul, Turgut Reis neighborhood in Esenler district exhibits the highest average LST value of 36.70°C, while Bahçeköy Merkez neighborhood in Sarıyer district reports the lowest at 24.46°C. Similarly, in Izmir, İzkent neighborhood in Çiğli district showcases the highest average LST value of 40.11°C, contrasting with the lowest value of 29.27°C in 2. İnönü neighborhood in Narlıdere district. In Mersin, Kocavilayet neighborhood in Yenişehir district exhibits the highest average LST value of 33.49°C, while Palmiye neighborhood, also in Yenişehir district, records the lowest at 29.76°C. Notably, neighborhoods along the west-north axis tend to exhibit higher LST values, while those in the south have lower values.

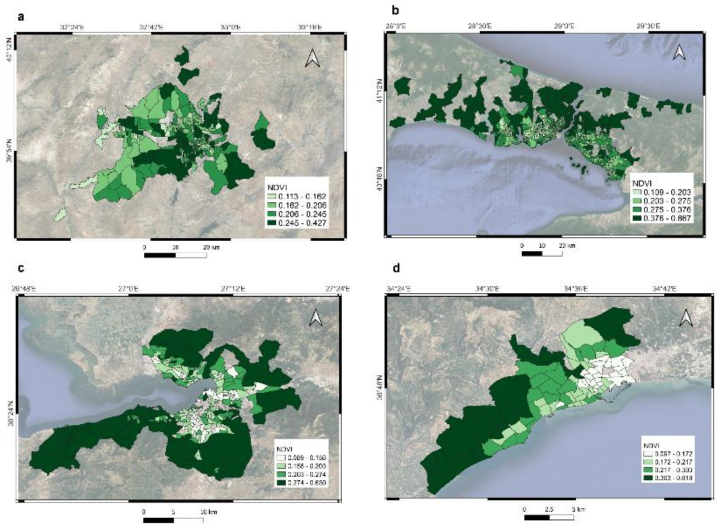

**Figure 2.** NDVI maps of neighborhoods belonging to the cities of Ankara (a), Istanbul (b), Izmir (c), and Mersin (d).

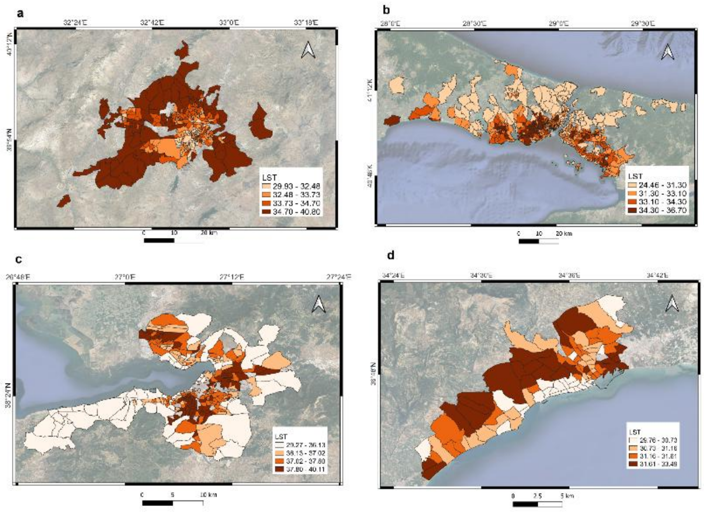

**Figure 3.** LST maps of neighborhoods belonging to the cities of Ankara (a), Istanbul (b), Izmir (c), and Mersin (d).

Regression analysis, as depicted in Table 1, was conducted to assess the relationships between AHSV, NDVI, and LST values. In Ankara's Çankaya district, a significant relationship was observed between NDVI and AHSV, indicating a potential influence of green areas on real estate values. However, further research is warranted to understand regional variations. In Istanbul's Eyüp district, although strong correlations were observed between NDVI, LST, and AHSV, the relationships were not significant, suggesting the influence of other factors. Similarly, in Izmir, while some districts exhibited strong NDVI-LST correlations, no consistent relationship was observed between NDVI-AHSV and LST-AHSV pairs, indicating the need for further investigation. In Mersin, no consistent relationship was found between NDVI-AHSV, LST-AHSV, and NDVI-LST pairs at the district level, highlighting the complexity of factors influencing real estate values.

## Conclusion

This study analyzed the relationships between AHSV, NDVI, and LST in urban districts of Ankara, Istanbul, Izmir, and Mersin. Istanbul exhibited the highest AHSV and NDVI values, particularly in northern districts with more green spaces. In contrast, districts like Arnavutköy, Beykoz, and Şile, characterized by abundant greenery, showed no significant effects of NDVI and LST on AHSV. In Ankara, Çankaya district demonstrated notable associations between NDVI and AHSV, while Pursaklar district showed strong correlations between LST and AHSV. In Izmir, Karsiyaka and Güzelbahçe districts displayed significant relationships between NDVI, LST, and AHSV. However, other districts in Izmir and Mersin lacked consistent associations between these variables. Regression analysis highlighted the multifaceted nature of factors influencing housing values, indicating the need for considering economic, infrastructural, and demographic factors alongside environmental variables. The study underscores the variability of NDVI and LST impacts on AHSV across districts within each city. While some findings align with existing literature, such as the positive relationship between green areas and housing prices, disparities exist, emphasizing the need for context-specific analyses. Limitations included incomplete AHSV data for certain neighborhoods, suggesting the necessity of comprehensive data acquisition strategies. Future research could explore additional factors like building density and incorporate remote sensing data to enhance understanding of urban dynamics and their impact on housing markets.

**Table 1.** $R^2$ score and p-value table of NDVI - AHSV, LST - AHSV, NDVI - LST pairs for districts of for cities

| City | Neighborhood | NDVI- AHSV $R^2$ | LST- AHSV $R^2$ | NDVI-LST $R^2$ | NDVI- AHSV P-value | LST- AHSV P- value |
|---|---|---|---|---|---|---|
| İstanbul | Adalar | 0.00 | 0.34 | 0.30 | 0.3147 | 0.1481 |
| | Arnavutköy | 0.00 | 0.00 | **0.78** | 0.3754 | 0.3779 |
| | Ataşehir | 0.31 | 0.66 | 0.49 | 0.8886 | **0.0008****** |
| | Avcılar | 0.36 | 0.13 | 0.78 | **0.0328***** | 0.1523 |
| | Bağcılar | 0.34 | 0.39 | 0.56 | 0.3136 | **0.0910**** |
| | Bahçelievler | 0.67 | **0.78** | 0.78 | 0.5735 | **0.0381***** |
| | Bakırköy | 0.22 | 0.12 | 0.35 | 0.1753 | 0.7106 |
| | Başakşehir | 0.08 | 0.00 | 0.58 | 0.1373 | 0.2085 |
| | Bayrampaşa | 0.23 | 0.25 | 0.60 | 0.5952 | 0.4487 |
| | Beşiktaş | 0.41 | 0.35 | **0.90** | 0.1368 | 0.7672 |
| | Beykoz | 0.07 | 0.13 | **0.87** | 0.2541 | **0.0866**** |
| | Beylikdüzü | 0.14 | 0.00 | 0.56 | **0.0747**** | 0.1704 |
| | Beyoğlu | 0.33 | 0.00 | 0.18 | 0.1541 | 0.3492 |
| | Büyükçekmece | **0.76** | 0.14 | 0.60 | 0.4790 | 0.5419 |
| | Çatalca | 0.00 | 0.15 | **0.79** | **0.0553**** | **0.0329***** |
| | Çekmeköy | 0.62 | 0.61 | **0.98** | 0.4773 | 0.9321 |
| | Esenler | 0.14 | 0.20 | 0.56 | 0.7774 | 0.2623 |
| | Esenyurt | 0.33 | 0.51 | 0.67 | 0.8203 | **0.0002****** |
| | Eyüp | **0.76** | **0.79** | **0.98** | 0.6974 | 0.1175 |
| | Fatih | 0.17 | 0.00 | 0.32 | **0.0148***** | 0.2127 |
| | Gaziosmanpaşa | 0.13 | 0.14 | **0.76** | 0.7602 | 0.6238 |
| | Güngören | 0.41 | 0.49 | **0.92** | 0.6582 | 0.2050 |
| | Kadıköy | 0.21 | 0.51 | 0.66 | 0.1836 | **0.0009****** |
| | Kağıthane | 0.27 | 0.57 | **0.71** | 0.1526 | **0.0008****** |
| | Kartal | 0.04 | 0.00 | **0.86** | **0.0696**** | 0.1097 |
| | Küçükçekmece | 0.36 | 0.31 | **0.79** | 0.1932 | 0.7963 |
| | Maltepe | 0.28 | 0.54 | 0.61 | 0.6923 | **0.0079****** |
| | Pendik | 0.11 | 0.48 | 0.32 | 0.6082 | **0.0001****** |
| | Sancaktepe | 0.01 | 0.00 | **0.79** | 0.2839 | 0.3398 |
| | Sarıyer | 0.22 | 0.15 | **0.94** | **0.0170***** | **0.0803**** |
| | Şile | 0.06 | 0.15 | **0.81** | 0.4146 | 0.1963 |
| | Silivri | 0.31 | 0.52 | **0.75** | 0.5216 | **0.0404***** |
| | Şişli | 0.44 | 0.47 | 0.64 | 0.1847 | **0.0787**** |
| | Sultanbeyli | 0.17 | 0.01 | 0.44 | **0.0538**** | 0.2769 |
| | Sultangazi | 0.05 | 0.00 | 0.34 | 0.3687 | 0.3687 |
| | Tuzla | 0.16 | 0.13 | 0.30 | 0.3055 | 0.4732 |
| | Ümraniye | 0.01 | 0.34 | 0.67 | **0.0000****** | **0.0000****** |
| | Üsküdar | 0.43 | 0.37 | **0.71** | **0.0473***** | 0.4699 |
| | Zeytinburnu | 0.26 | 0.46 | 0.69 | 0.6077 | **0.0435***** |
| Ankara | Çankaya | 0.25 | 0.10 | 0.10 | **0.0000****** | **0.0035****** |
| | Sincan | 0.18 | 0.10 | 0.47 | **0.0175***** | 0.1790 |
| | Etimesgut | 0.15 | 0.03 | 0.24 | **0.0320***** | 0.8890 |
| | Yenimahalle | 0.06 | 0.01 | 0.06 | **0.0287***** | 0.1520 |
| | Pursaklar | 0.04 | 0.93 | 0.10 | 0.3217 | **0.0023****** |
| | Altındağ | 0.02 | 0.01 | 0.05 | 0.6377 | 0.8296 |
| | Mamak | 0.02 | 0.03 | 0.03 | 0.2291 | 0.1438 |
| | Keçiören | 0.00 | 0.02 | 0.00 | 0.7016 | 0.3629 |
| İzmir | Buca | 0.23 | 0.19 | 0.67 | 0.1060 | 0.5872 |
| | Çiğli | 0.22 | 0.23 | 0.31 | 0.1465 | 0.1312 |
| | Güzelbahçe | 0.19 | 0.46 | 0.75 | 0.1905 | **0.0202***** |
| | Karabağlar | 0.15 | 0.13 | 0.63 | 0.2279 | 0.5101 |
| | Karşıyaka | 0.07 | 0.11 | 0.06 | 0.4397 | **0.0052****** |
| | Balçova | 0.06 | 0.00 | 0.77 | 0.3284 | 0.4223 |
| | Narlıdere | 0.05 | 0.11 | 0.88 | 0.4569 | 0.2837 |
| | Bayraklı | 0.04 | 0.03 | 0.39 | 0.5592 | 0.7228 |
| | Gaziemir | 0.01 | 0.00 | 0.81 | 0.1978 | 0.2096 |
| | Konak | 0.01 | 0.00 | 0.14 | 0.3834 | 0.4400 |
| | Bornova | 0.01 | 0.00 | 0.76 | 0.3633 | 0.4887 |
| Mersin | Yenişehir | 0.15 | 0.20 | 0.26 | 0.3126 | 0.1179 |
| | Akdeniz | 0.12 | 0.19 | 0.17 | 0.1936 | 0.6476 |
| | Toroslar | 0.11 | 0.05 | 0.03 | **0.0195***** | **0.0052****** |
| | Mezitli | 0.02 | 0.01 | 0.04 | 0.5790 | 0.7009 |

**** : p-value ≤ 0.01 (high significance)
*** : 0.01 < p-value ≤ 0.05 (significance)
** : 0.05 < p-value ≤ 0.01 (low significance)
no asterisk: p-value > 0.1 (no significance),
High R2 values (R2 > 0.7) are indicated in bold.

## Acknowledgements

We are indebted to TÜBİTAK for their support to the project with the number 1919B012221063 under the BİDEB 2209-A University Students Research Projects Support Program and the research outlined in this paper.

## References

Erdem Okumus, D., & Terzi, F. (2021). Evaluating the role of urban fabric on surface urban heat island: The case of Istanbul. Sustainable Cities and Society, 73, 103128.

Holt, J. R., & Borsuk, M. E. (2020). Using Zillow data to value green space amenities at the neighborhood scale. Urban Forestry & Urban Greening, 56, 126794.

Jiao, L., Xu, G., Jin, J., Dong, T., Liu, J., Wu, Y., & Zhang, B. (2017). Remotely sensed urban environmental indices and their economic implications. Habitat International, 67, 22-32.

Liebelt, V., Bartke, S., & Schwarz, N. (2018). Hedonic pricing analysis of the influence of urban green spaces onto residential prices: the case of Leipzig, Germany. European Planning Studies, 26(1), 133-157.

Şekertekin, A., & Zadbagher, E. (2021). Simulation of future land surface temperature distribution and evaluating surface urban heat island based on impervious surface area. Ecological Indicators, 122, 107230.

Taleghani, M., Tenpierik, M., Kurvers, S., & Van Den Dobbelsteen, A. (2013). A review into thermal comfort in buildings. Renewable and Sustainable Energy Reviews, 26, 201-215.

Tan, K. C., Lim, H. S., MatJafri, M. Z., & Abdullah, K. (2012). A comparison of radiometric correction techniques in the evaluation of the relationship between LST and NDVI in Landsat imagery. Environmental Monitoring and Assessment, 184(6), 3813-3829.

Zambrano-Monserrate, M. A., Ruano, M. A., Yoong-Parraga, C., & Silva, C. A. (2021). Urban green spaces and housing prices in developing countries: A Two-stage quantile spatial regression analysis. Forest Policy and Economics, 125, 102420.

Zengin, M., Yılmaz, S., & Mutlu, B. E. (2019). Mekansal Termal Konfor Açısından Atatürk Üniversitesi Yerleşkesi Termal Kamera Görüntülerinin Analizi. Atatürk Üniversitesi Ziraat Fakültesi Dergisi, 50(3), 239-247.

INTERNATIONAL SYMPOSIUM ON
APPLIED
GEOINFORMATICS
9-10 May 2024 · Wrocław/Poland

*International Symposium on Applied Geoinformatics (ISAG2024)*

# Variants for Demand-Oriented Citygml-2-IFC ETL Processes with FME

Christoph Frey[1], Alexander Bong[1], Christian Clemen[1]

[1]University of Applied Sciences Dresden, Faculty of Spatial Information, Dresden, Germany;
christoph.frey@htw-dresden.de; ORCID 0009-0004-1900-5183
alexander.bong@htw-dresden.de; ORCID 0009-0006-3919-6065
christian.clemen@htw-dresden.de; ORCID 0000-0002-5807-7698

## Abstract

Building Information Modelling (BIM) facilitates collaboration through the creation and exchange of digital models. Geospatial data plays a key role in the various stages of BIM. Integrating geospatial data such as CityGML into BIM processes, especially openBIM projects, relies on standards like Industry Foundation Classes (IFC). However, the transformation of geospatial data into IFC can be challenging due to the different model intentions and paradigms between BIM and GIS. The Feature Manipulation Engine (FME) from Safe Software Inc. addresses this complexity through automated processes. Our study focuses on an automated FME approach by developing a workflow to convert 3D CityGML data to IFC. This has been tested in a railway BIM project in Germany. The workflow serves as a basic framework for openGIS to openBIM conversion, including steps such as data input management, attribute handling, georeferencing and output management. The results of our research present a customizable workflow for GIS-BIM integration using FME, capable of generating high-quality IFC4 files from CityGML data. The workflow offers flexibility in representing buildings as individual components or unified elements, addressing different BIM scenarios. In conclusion, our study highlights the transformation of 3D building and city models into openBIM using FME, focusing on the information loss-free transformation of geometry, topology, semantics and georeferencing via the Level of Georeferencing (LoGeoRef) concept by (Clemen and Görne 2019) in IFC. The automated workspaces are easy to use and demonstrate the seamless integration of complex 3D models into the IFC4 format while preserving CityGML attributes in PropertySets and QuantitySets. This adaptability, tailored to specific BIM information requirements, is critical for the effective use of geospatial information in BIM projects.

**Keywords:** *BIM-GIS-Integration, FME, IFC, CityGML, 3D City Model*

## Introduction/Background

The process of transforming geospatial data into the IFC format is challenging due to differences in model types in terms of purpose, semantics, geometry representation and georeferencing. That's why many software providers have developed specialized solutions to make this transformation efficient and lossless. A possible solution is the Feature Manipulation Engine from Safe Software Inc. FME is advertised for converting geospatial data into valid IFC files. Our research aims to investigate and implement a suitable workflow for processing 3D building and city models into the IFC4 format. The research is guided by the following questions: How can 3D city models be converted to IFC4 while considering geometry, topology, and semantics? What criteria can be used to evaluate the success of conversion, and how can independent validation be achieved? How can various georeferencing options in IFC be programmatically implemented with FME?

Numerous research initiatives have aimed to develop such efficient and automated transformation programs. An example of such a program is the open-source CityGML2IFC tool developed by Nebras Salheb (2019a). This Python script, available on GitHub (Nebras Salheb, 2019b), converts CityGML to IFC2x3 data. While the tool offers valuable functionality, it requires proficiency in Python programming and faces compatibility issues with newer Python versions, such as v3.12. Hardcoded default values for attributes like IfcSite result in inaccuracies in the IFC files. Additionally, there is inconsistent application of the aggregation hierarchy within the IFC file.

In contrast, our Workspace offers a customizable and user-friendly interface that operates without static values. Users can effortlessly generate building models as single entities or individual components (Wall, Roof, and Slab) in IFC4. The easily adjustable workspace and documentation enable the use of future IFC versions. Table 1 compares the two approaches based on various criteria:

✓ - Criteria is completely fulfilled, (✓) - Criteria is fulfilled but requires changes in the source code, ✕ - Criteria is not fulfilled, (✕) - means that only geographic coordinates if IfcSite are implemented.

**Table 1.** Comparison between our FME workflow and CityGML2IFC.

| Criteria | Our FME workspace | CityGML2IFC (Python) |
|---|---|---|
| Customizable generation of attributes and values from CityGML data | ✓ | (✓) |
| Correct building of the spatial aggregation hierarchy in IFC | ✓ | ✕ |
| Correct processing of input CityGML geometry and mapping to IFC | ✓ | ✓ |
| Preserving of Semantic Information | ✓ | (✓) |
| Generation of Property- and QuantitySets | ✓ | ✕ |
| Georeferencing in IFC | ✓ | (✕) |

A lot of efforts are being made to convert openBIM into openGIS, as demonstrated in the paper 'Integrated modeling of CityGML and IFC for city/neighborhood development for urban microclimates analysis' by Steve Kardinal Jusuf et al. (2017). The authors also use FME to facilitate the transformation of IFC into CityGML, highlighting FME's effectiveness for such tasks. Although the transformation was done in reverse (IFC to CityGML), FME's functionalities are now more advanced and customizable, as proven by our research.

The GeoBIM Benchmark study conducted by Noardo et al. (2021) investigates the performance of software solutions in processing geospatial and BIM data. The GeoBIM project provided a comprehensive frame work to analyze BIM/GIS gap aspects like geometry, semantics, and georeferencing. The study acknowledges FME's commendable ability to seamlessly integrate geospatial and BIM datasets, as well as its proficiency in handling multiple formats and complex spatial relationships. However, Noardo et al. (2021) postulate that there is still room for improvement, particularly when creating high-quality IFC datasets.

The LoGeoRef concept, developed by (Clemen and Görne 2019), explains georeferencing using standard IFC entities. Where LoGeoRef 10 (PostalAdress) and 20 (Geographic Coordinate) are being used as meta-data, where LoGeoRef 30,40 and 50 provide sufficient georeferencing. In this study only the IFC4 standard LoGeoRef 50, using IfcMapConversion and IfcProjectedCRS are implemented.

Furthermore (A. Donaubauer et al. 2023) emphasize that using large coordinate pairs, which results in vast distances from the coordinate origin, can cause issues in some software applications. Large Coordinates can lead to a decrease in precision. Therefore, it is important to transform the geometry to a local project coordinate system, using the IFC means of georeferencing.

## Materials and Methods

Due to inherent differences in the structures of the CityGML schema and IFC, a direct 1:1 mapping is not possible. Therefore, many transformation steps are necessary to map CityGML data (Reader) to the IFC schema (Writer). The high- level steps of the implemented FME workflow are illustrated in Figure 1, where Step 2 is the core of our investigation.

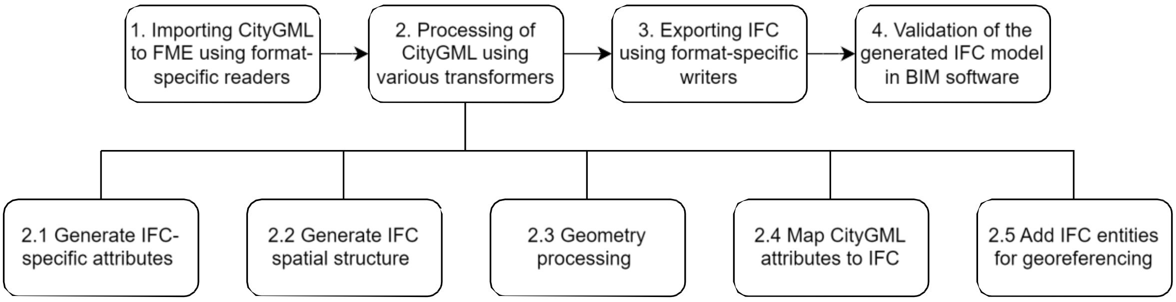

**Figure 1.** The general process for transforming CityGML data to IFC using FME

When converting geospatial data to the IFC format, proper attribute generation and mapping are critical. FME provides transformers for renaming, restricting, creating, managing and editing attributes. Attributes can be created from source data, user parameters or constants, providing flexibility and control over the workflow. User parameters allow FME workflows to be customized for automated processing. They are mainly used to control data flow, handle input and output data, and configure coordinate systems. We also utilized an external JSON file for parameters that are not available in CityGML, such as project name or phase. The FME process can be parameterized using the external configuration file, without requiring any modifications to the FME workspace and therefore allows for the creation of demand-oriented variants.

The spatial structure hierarchy in the IFC data model organizes spatial elements into a hierarchical structure. It starts with the IfcProject class, representing the entire building project, followed by IfcSite, IfcBuilding and IfcBuildingStorey classes. To model this hierarchy in FME, ifc_ids must be linked between classes. Using the AttributeCreator transformer, ifc_ids can be inherited, establishing hierarchical relationships.

Initially, users must choose between generating buildings as complete units or separate components. If the decision is to generate entire buildings, the data flow will be directed toward generating IfcBuildingElementProxy. The building's geometry is extracted from the Building feature in the CityGML file and then converted into Boundary Representation (BREP). BREP is ideal for representing building forms using surfaces defined by their nodes and edges. Alternatively, buildings can be represented as SweptAreaSolids. When considering individual components during conversion, the mapping of CityGML features to IFC entities is as follows: WallSurface to IfcWall, RoofSurface to IfcRoof, and GroundSurface to IfcSlab.

To create a meaningful IFC model, semantic information is integrated through classification and attribution. Classification involves the use of IFC entities, entity types, and IfcClassificationReference. Attribution, on the other hand, utilizes schema attributes, predefined property and quantity sets, and user-defined property and quantity sets. FME allows to create custom IfcPropertySets and IfcQuanitySets. For instance, as in our workflow, the “Pset_Building” contains all unused attributes from the CityGML data. The FeatureWriter is equipped with all necessary IFC classes.

The IFC Geometry is transformed to a local project coordinate system. This requires defining the transformation parameters and let FME transform the coordinates to a local system and store the transformation parameters in IfcMapConversion (LoGeoRef50). For this research, LoGeoRef 10, 20, and 50 were implemented. LoGeoRef 10 uses address data stored in IfcSite, while LoGeoRef 20 stores geographic coordinates in IfcSite attributes. However, implementing LoGeoRef 50 posed a challenge due to the lack of standard FME functions to create the required IFC entities such as IfcMapConversion and IfcProjectedCRS. To address this issue, we used the custom transformer IfcMapConversionWriter, created by Stijn Goedertier (2023). This transformer is a Python script to create the missing IfcMapConversion and IfcProjectedCRS attributes, thereby enhancing FME's georeferencing capabilities.

## Results and Discussion

The research findings have led to a structured, but configurable workflow. The process starts with managing the CityGML input data, where the choice between writing the building components or entire buildings as unified entities is made. The flow of data within the workspace is controlled by the predefined user parameters. The adaptation of the JSON configuration file offers a high level of customization and flexibility. Attribute management and generation are performed to ensure dataset coherence and completeness. Next, georeferencing preparation is carried out to ensure accurate georeferencing in IFC for the different LoGeoRef 10, 20 and 50. The workflow then proceeds with BIM coordinate processing, which involves transforming the CRS to a local BIM project coordinate system. The following step is the classification of the different data streams into their respective IFC classes. The input data is then subjected to geometry processing to refine spatial representations. PropertySets and QuantitySets are created to process the semantics from the CityGML origin. The outcome of this process is an IFC4 file, as illustrated in Figure 2 within the KITModelViewer.

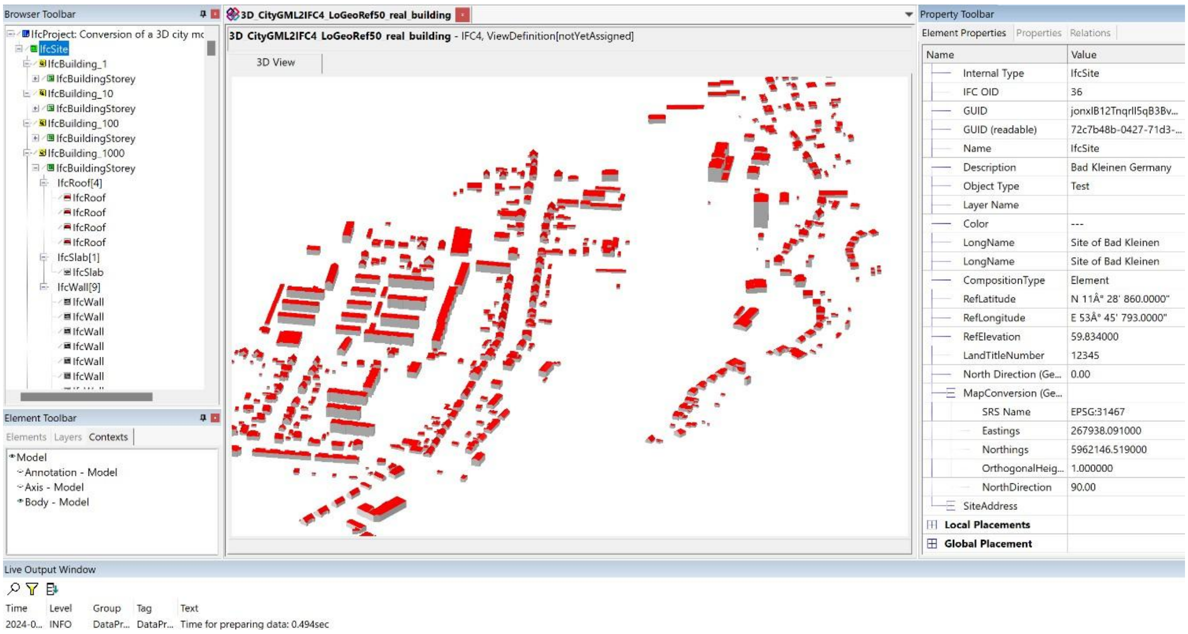

3D_CityGML2IFC4_LoGeoRef50_real_building - IFC4, ViewDefinition[notYetAssigned]

| Name | Value |
|---|---|
| Internal Type | IfcSite |
| IFC OID | 36 |
| GUID | jonxlB12Tnqrll5qB3Bv... |
| GUID (readable) | 72c7b48b-0427-71d3-... |
| Name | IfcSite |
| Description | Bad Kleinen Germany |
| Object Type | Test |
| Layer Name | |
| Color | --- |
| LongName | Site of Bad Kleinen |
| LongName | Site of Bad Kleinen |
| CompositionType | Element |
| RefLatitude | N 11Â° 28' 860.0000" |
| RefLongitude | E 53Â° 45' 793.0000" |
| RefElevation | 59.834000 |
| LandTitleNumber | 12345 |
| North Direction (Ge... | 0.00 |
| MapConversion (Ge... | |
| SRS Name | EPSG:31467 |
| Eastings | 267938.091000 |
| Northings | 5962146.519000 |
| OrthogonalHeig... | 1.000000 |
| NorthDirection | 90.00 |
| SiteAddress | |
| **Local Placements** | |
| **Global Placement** | |

```
Time      Level  Group     Tag       Text
2024-0... INFO   DataPr... DataPr... Time for preparing data: 0.494sec
```

**Figure 2:** Section of the IFC4 results in KITModelViewer

All test data that was transformed to IFC4 was tested in various viewers, validation software and BIM authoring software, such as KITModelViewer, BIMVision, IfcCheckingTool, buildingSMART Validation Service, con terras FME Flow IFC Validator, Revit or even ArcGIS Pro. The only error listed was the empty entity in IfcPerson. However, FME does not currently support this feature and there is no other solution available within the software at this time. In general, the created workflow allows for the transformation of a 3D CityGML file into a valid IFC file.

## Conclusion

In summary, our research shows that it is possible to automate the transformation of 3D CityGML data into high-quality IFC4 files using FME while preserving the semantics and spatial structure necessary for openBIM projects. However, there are limitations. FME's restrictions mean that IfcPropertySets can only be named with the prefix 'Pset_', which violates the implementers' agreement (buildingSMART, 2023) to use this prefix only for standard property sets. Currently, our process relies on an external Python-based transformer for optimal georeferencing results. At present, the transformation from the projected coordinate reference system (CityGML) to the local Cartesian system (IFC) is limited to a simple translation. However, a rotation component will be added in the future. The transformation of CityGML is currently limited to Level of Detail 2, which is sufficient for most GIS to BIM use cases.

Future tasks include making the FME process robust against CityGML dialects, integrating further CityGML ADE, and providing the entire FME process as Software as a Service. The research project also transformed property boundaries and terrain models. However, a holistic approach for transferring heterogeneous geospatial data sources to IFC has yet to be developed.

## Acknowledgements

The project was carried out in collaboration with con terra GmbH (Christian Dahmen and Jens Frolik).

**References**

A. Donaubauer; T. Kutzner; U. Gruber; A. Borrmann; K. Krause (2023): 2.7.2. BIM und GIS-Integration – standardisierte, offene Datenformate. In: Leitfaden Geodäsie und BIM. Version 3.2 (2023), Bd. 3.2. 1. Auflage. Augsburg: Wißner-Verlag, S. 115–131, last checked on 10.04.2024.

buildingSMART (2023): buildingSMART IFC4.3. Online verfügbar unter https://www.buildingsmart.org/the-status-of- ifc-4-3-and-the-benefit-of-further-extensions-as-ifc-4-4/#: :text=ISO has accepted the IFC,of ISO 16739 in 2023., last checked on 11.09.2023.

Clemen, Christian; Görne, Hendrik (2019): Level of Georeferencing (LoGeoRef) using IFC for BIM. In: *Journal of Geodesy, Cartography and Cadastre* (March), S. 15–20.

Nebras Salheb (2019a): Automatic Conversion of CityGML to IFC. Mathesis. TU Delft Architecture and the Built Environment. Online available at http://resolver.tudelft.nl/uuid:455b6060-5152-46eb-8c64-5382f915442b.

Nebras Salheb (2019b): CityGML2IFC. Online available at https://github.com/nsalheb/CityGML2IFC, last checked on 10.04.2024.

Noardo, Francesca; Krijnen, Thomas; Arroyo Ohori, Ken; Biljecki, Filip; Ellul, Claire; Harrie, Lars et al. (2021): Reference study of IFC software support: The GeoBIM benchmark 2019—Part I. In: *Transactions in GIS* 25 (2), S. 805–841. DOI: 10.1111/tgis.12709.

Steve Kardinal Jusuf; Benjamin Mousseau; Gaelle Godfroid; Vincent Soh Jin Hui (2017): Integrated modeling of CityGML and IFC for city/neighborhood development for urban microclimates analysis. In: *Energy Procedia* 122, S. 145–150. DOI: 10.1016/j.egypro.2017.07.329.

Stijn Goedertier (2023): How to georeference a BIM model. Online available at https://github.com/stijngoedertier/georeference-ifc#conclusion, last checked on 29.09.2023.

INTERNATIONAL SYMPOSIUM ON
APPLIED
GEOINFORMATICS
9-10 May 2024 · Wrocław/Poland

*International Symposium on Applied Geoinformatics (ISAG2024)*

# Machine Learning Approaches for Evaluating Forest Fire Impacts on Sentinel-2 Satellite Imagery Across Ukraine

Vik. Hnatushenko[1,3] *, V. Hnatushenko[2], D. Soldatenko[1], C. Heipke[3]

[1]Dept. Information Technologies and Systems, Ukrainian State University of Science and Technologies, Dnipro, Ukraine;vvitagnat,@gmail.com, zeirison@gmail.com;ORCID0000-0001-5304-4144, ORCID 0000-0001-6041-7383
[2]Dept. Information Technologies and Computer Engineering, Dnipro University of Technology, Dnipro, Ukraine; Hnatushenko.V.V@nmu.one; ORCID 0000-0003-3140-3788
[3]Institute of Photogrammetry and GeoInformation, Leibniz Universität Hannover, Germany; heipke@ipi.uni-hannover.de; ORCID 0000-0002-7007-9549
* Corresponding Author

## Abstract

Forest fires have long-term consequences and serious ecological, social, and economic implications. Utilizing multispectral imagery from the Sentinel-2 satellite, we propose an algorithm based on machine learning models for the detection of burnt forest areas. A new dataset on forest fires has been created, suitable for semantic segmentation models. The proposed algorithm uses an approach based on convolutional neural networks (CNN). The results are analyzed and compared in terms of the intersection over union (IoU) score. The proposed algorithm was tested on Sentinel satellite images acquired in October 2022 for the Kinburn Peninsula, Ukraine, to have an accuracy in terms of IoU of 95%.

**Keywords:** *Burnt Forest Area Detection, Machine Learning, Convolutional Neural Networks, Spectral Bands, Ukraine Forests*

## Introduction/Background

Forest fires annually cause significant damage in Ukraine and worldwide, destroying thousands of hectares of forests and deteriorating their water-protective, soil-retaining, CO2-storing and other beneficial properties. Such events disrupt the planned forestry operations and the use of forest resources, leading to substantial economic, social, and ecological losses. Besides the direct impact of fires (Zibtsev et al., 2020), the state of forests depends on a complex of additional factors, which can be altered by fire: abiotic factors (climate and soil-hydrological conditions), biotic factors (diseases and pests of the forest), anthropogenic factors (recreation, environmental pollution, transformation of ecological conditions, etc.).

Burnt forest area detection is a crucial and complex problem that requires the use of accurate, reliable, and efficient methods. The main challenges for this task can be divided into the following categories (Barmpoutiset al., 2020): early detection, detection accuracy, prediction and monitoring, necessary resources, and further constraints (logistics etc.). Traditional methods such as ground patrols or aerial photography are not sufficiently effective in solving these problems:
Ground patrols are limited in their range and may not detect a fire in time, especially in large and inaccessible forest areas.
Aerial photography, although covering larger areas in a short time, is expensive and dependent on weather conditions.

In recent years, there has been an increasing focus on the application of modern technologies such as satellite remote sensing and machine learning across various domains, including monitoring forest fires, mapping flood events, and damage cartography. Satellite remote sensing enables the collection of forest fire data over extensive areas and in real-time, significantly enhancing the speed and accuracy of burnt fire area detection. High-resolution datasets have facilitated the development and application of numerous forest fire mapping methods (Hu et al., 2021). Primarily, these methods focus on detecting changes by creating carefully selected input data characteristics (Hnatushenko et al., 2023). Machine learning, particularly neural networks, assists in rapidly analyzing large volumes of data and in identifying complex patterns indicative of fire presence (Knopp et al., 2020).

The detection and analysis of forest fire outbreaks is a costly and complex process without specialized automated tools. This has led to efforts to create automated systems for detecting and assessing forest fires globally. A key direction in the creation of such systems is the development of methods for processing satellite data and creating extensive fire datasets using multispectral Sentinel-2 imagery, suitable for segmentation models. This significantly simplifies the process of assessing areas covered by fire and enhances the accuracy of the assessments.

## Materials and Methods

Our comprehensive workflow for identifying burnt forest areas using multispectral Sentinel-2 data, from the perspective of machine learning technology application, consists of the following stages:

Manual creation of a dataset on burt forest areas (we use images of the Kinburn Peninsula of Ukraine), based on multispectral Sentinel-2 imagery suitable for machine learning-based semantic segmentation models (Chaurasiaet al., 2021).

Conducting a series of experiments to evaluate the effectiveness of neural network semantic segmentation models for monitoring and detecting burnt forest areas.

Testing a pre-trained neural network capable of detecting burnt forest areas from Sentinel-2 images.

Considering the dynamic nature of natural processes, it was inferred that the satellite data from Sentinel-2A and Sentinel-2B offer a well-balanced combination of spatial, spectral, and temporal indicators. Sentinel data come at two different levels of processing: level-1C and level-2A. The level-1C product includes measurements of top-of-atmosphere (TOA) reflectance and the parameters required to convert them into radiances. Additionally, it provides multispectral registration at a sub-pixel level. On the other hand, the level-2A product provides subpixel multispectral registration and orthorectified bottom-of-atmosphere reflectance. This makes level-2A the more favorable choice.

In the advancement of burnt forest area detection methodologies, a specialized convolutional neural network (CNN) architecture has been developed to capitalize on the spectral properties of Sentinel-2 multispectral imagery (Abdi, 2021). The architecture is grounded in an encoder-decoder framework, meticulously crafted to execute semantic segmentation with high accuracy.

At the core of the CNN architecture lies the encoder, which is designed to methodically extract spectral features from the input data. Through a succession of convolutional layers, the encoder progressively diminishes the spatial dimensions while concurrently expanding the feature map depth. This deliberate reduction and enrichment process is essential for isolating the spectral signatures that are indicative of and land cover class, including wildfire-affected regions.

Transitioning from the encoder, the middle layer of the network serves as an enhancement conduit for the encoded features. Crucially, it retains the spatial dimensions of the feature set, thereby safeguarding the contextual information of the imagery, which is vital for the decoding phase.

The decoder component of the architecture is tasked with the spatial reconstruction of the feature set. It employs a series of decoding blocks that systematically increase the tensor's resolution. This is achieved through transposed convolutions that work in concert with features carried over from the encoder, enabling precise localization of the affected areas.

A defining element of the network's architecture is the integration of Xception blocks. These blocks utilize the concept of depthwiseseparableconvolutions (Chollet, 2017), allowing for the independent processing of spatial and channel features. This approach not only curtails the number of parameters within the model but also significantly enhances computational efficiency. Such efficiency is paramount when dealing with the intricate task of burnt forest area detection, where the model must discern subtle spectral discrepancies indicative of fire damage.

The architectural design of the CNN, with its incorporation of Xception blocks within the encoder-decoder framework, equips the model with the capability to perform real-time burnt forest area detection and monitoring. It is adapted to the dynamic and diverse conditions presented by natural landscapes, ensuring that the segmentation of wildfire-affected areas is both precise and computationally efficient.

## Experiments and Discussion

The test area for carrying out the experiments is the Kinburn Peninsula in Ukraine, which separates the Dnieper-Bug estuary from the Black Sea, see Figure 1. A fire was identified in Sentinel-2 satellite imagery acquired on 04.10.2022. As a result of the outbreak of fires in forested areas and fields, nearby settlements were evacuated. According to the State Emergency Service of Ukraine https://dsns.gov.ua/en, the majority of fires in the territory during the considered period were provoked by missile strikes, leading to chaotic locations of the fires. Consequently, the affected regions are typically non-overlapping and do not coalesce in most instances.

Further Sentinel-2 images were taken during the burning fire with a cloud of smoke, which complicated data processing.

The images were acquired from the official website of the United States Geological Survey (USGS) (USGS. Sentinel-2 Missions: Sentinel-2 Levels of Processing. https://earthexplorer.usgs.gov/). We manually examined the Sentinel-2 level 2-A imagery to identify images captured with less than 1% cloud cover when the affected area was imaged, and then selected the three bands B04, B03 and B02 for further processing.

The neural network, designed for burnt forest area detection from satellite imagery, was trained using the PyTorch library. The dataset for this task included 12 training patches and 3 validation patches representing the result of a burnt areas. Ground truth, which was used for training, validation and testing, was collected manually from the imagery. Commencing with the Adam optimizer, the network's learning rate was set at 0.001. The training was conducted over 50 epochs, with a batch size of 16, carefully chosen to balance computational efficiency and gradient calculation accuracy. To reduce the effects of overfitting, the training incorporated regularization techniques such as Dropout, applied at a rate of 0.5, to enforce the learning of robust features. Early Stopping (Li et al., 2020) was utilized, ceasing training if no improvement in validation loss was noted over a span of 10 epochs.

The model's performance was assessed using the Intersection over Union (IoU) metric, which evaluates the precision of the segmentation predictions. The model with the lowest validation loss was selected for future application in burnt forest area detection tasks.

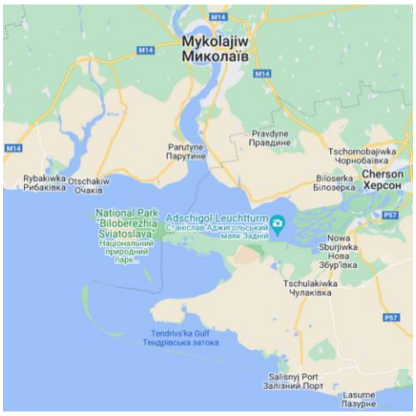

**Figure 1**. Kinburn Peninsula (centre) in the Mykolaiv region, Ukraine.

Area before the fire After the fire Result for detecting of burnt areas

**Figure 2.** The territories covered by fire on theKinburn Peninsula.

Evaluating the precision of identifying wildfire locations in Figure 2 is an essential step. This can be done by comparing the detection results to a reference mask using established measurement indices.In this work we refrained from measuring the overall accuracy (OA) due to its susceptibility to unburned pixels, as the dominance of unburned classes in such imbalanced datasets adversely affects the results. For instance, if the burned area accounts for just 10% of the entire image while the unburned area constitutes 90%, even without detecting any burned area, the model appears to be 90% accurate.

Instead, our assessment involves analyzing both the visual appearance and numerical measures of the results. The intersection over union (IoU), also known as the Jaccard Index (Carass et al., 2020), was employed to assess the accuracy of the segmentation outcomes.

## Results and conclusion

One challenge for image segmentation models utilizing machine learning is the need for accessible sets of publicly available training data to identify features and extract them for making accurate decisions. This is particularly the case for countries and regions that are less studied in the context of forest fire ecology, such as Ukraine. In this study, a dataset on forest fires in Ukraine was created using multispectral Sentinel-2 imagery to develop a remote sensing model for image segmentation, object detection, and classification of burnt forest areas. This dataset supports binary classification for detecting burnt and unburnt areas.

The method presented utilizes result of the burnt areas detection from Sentinel-2A satellite data, offering the best current compromise between spatial, spectral, and temporal resolution among publicly available satellite data, with the aid of convolutional neural networks.Results of the conducted experiments using the created dataset and proposed ML architecture demonstrate an IoUof 95% for the Kinburn Peninsula (Ukraine) for the developed detection model.

Future research will address the challenge of often unbalanced datasets, such as classes with fewer pixels. Multitemporal series of satellite images will be employed to gain more detailed information about the conditions leading to forest fires (e.g., bombardments) and to provide insights into land cover types. Furthermore, efforts will be made to generalize these results to more extensive and larger test sites and to train a neural network to classify the degree of fire impact, which will necessitate field validation.

**References**

Abdi, A. M. (2020). Land cover and land use classification performance of machine learning algorithms in a boreal landscape using Sentinel-2 data. GIScience&RemoteSensing, 57(1), 1-20.

Barmpoutis, P., Papaioannou, P., Dimitropoulos, K., &Grammalidis, N. (2020). A review on early forest fire detection systems using optical remote sensing. Sensors, 20(22), 6442.

Carass, A., Roy, S., Gherman, A., Reinhold, J. C., Jesson, A., Arbel, T., ... &Oguz, I. (2020). Evaluating white matter lesion segmentations with refined Sørensen-Dice analysis. Scientific reports, 10(1), 8242.

Chaurasia, K., Nandy, R., Pawar, O., Singh, R. R., &Ahire, M. (2021). Semantic segmentation of high-resolution satellite images using deep learning. Earth Science Informatics, 14(4), 2161-2170.

Chollet, F. (2017). Xception: Deep learning with depthwise separable convolutions. In Proceedings of the IEEE conference on computer vision and pattern recognition (pp. 1251-1258).

Hnatushenko, V., Hnatushenko, V., Soldatenko, D., and Heipke, C. (2023). Enhancing the quality of CNN-based burned area detection in satellite imagery through data augmentation, Int. Arch. Photogramm. Remote Sens. Spatial Inf. Sci., XLVIII-1/W2-2023(pp.1749–1755).

Hu, X., Ban, Y., & Nascetti, A. (2021). Uni-temporal multispectral imagery for burned area mapping with deep learning. Remote Sensing, 13(8), 1509.

Knopp, L., Wieland, M., Rättich, M., & Martinis, S. (2020). A deep learning approach for burned area segmentation with Sentinel-2 data. Remote Sensing, 12(15), 2422.

Li, M., Soltanolkotabi, M., &Oymak, S. (2020). Gradient descent with early stopping is provably robust to label noise for overparameterized neural networks. In International conference on artificial intelligence and statistics (pp. 4313-4324). PMLR.

Zibtsev, S. V., Soshenskyi, O. M., Myroniuk, V. V., &Gumeniuk, V. V. (2020). Wildfire in Ukraine: an overview of fires and fire management system. Ukrainian Journal of Forest and Wood Science, 11(2), 15-31.

INTERNATIONAL SYMPOSIUM ON
APPLIED
GEOINFORMATICS
9-10 May 2024 · Wrocław/Poland

*International Symposium on Applied Geoinformatics (ISAG2024)*

# The Problem of Overlapping Cadastral Boundaries Cases and Proposed Solutions

BELHOUARI FATIMA ZOHRA[1]*, SEDDIKI AKRAM[2], SIYOUCEF KAMEL[3], LOMBARKIA BILLEL[4], KOUACHI BAKHADA[5]

[1] Agence Spatiale Algérienne, Centre des Techniques Spatiales, Arzew, Alegria, fatimazbelhouari@gmail.com
[2] Agence Spatiale Algérienne, Centre des Techniques Spatiales, Arzew, Alegria, aseddiki@cts.asal.dz
[3] Agence Spatiale Algérienne, Centre des Techniques Spatiales, Arzew, Alegria, ksiyoucef@cts.asal.dz
[4] Agence Spatiale Algérienne, Centre des Techniques Spatiales, Arzew, Alegria, bilouredha@yahoo.fr
[5] Agence Spatiale Algérienne, Centre des Techniques Spatiales, Arzew, Alegria, bakhdakouachi@gmail.com

**Keywords:** *Cadastral Plans, Affine Transformation, Simultaneous Adjustment, Communal Boundaries, GIS.*

### Introduction/Background

Objective of the Algerian cadaster is to unify cadastral plans in a single database and to assemble these plans in a single geographic system. The problems experienced included overlap and duplication; their presence in the thematic information layers of the cadaster affects not just the metric quality of parcels and islands, but also the results of queries, thereby diminishing quality of cadastral information. Goals of study the problems of interconnection of communal boundaries in the Wilaya of Oran and propose Solutions for the Correction of overlapping inter-communal boundaries.

### Materials and Methods (Design/methodology/approach)

Cadastral plans: these are unique plans that represent the municipal territory at the scale of islands and parcels.
Ground control points: The crosses of the planes cadastral or points observed in the field by GNSS.
Tie points: tie-points common details between planes.
Official reports on the boundaries of municipal territory of Oran (PVs).

The first proposal, an affine transformation to adjust cadastral plans individually, and the second, a simultaneous adjustment of all cadastral plans by commune, were programmed in python.

### Results and Discussion (Findings)

After recovering the official records (PVs) of each commune in the Wilaya of Oran, we analyzed each part of the boundaries and classified the points and boundaries.
In order to regulate the inter-communal overlap of the Wilaya of Oran, we collected as many cadastral plans (raw and georeferenced) as possible, and then georeferenced the raw plans using ARC GIS 10.4 software, using 6-parameter affine transformation registration and 4-parameter similarity transformation registration.
Having completed this stage, we moved on to digitizing the communal boundaries from the previous cadastral plans and the PVs, which are considered a basis for managing the work.

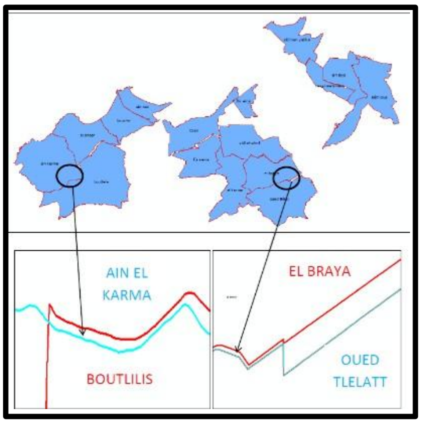

**Figure1.** Vector file of digitized intercommunal boundaries and 02 types of overlap between boundaries.

After digitizing the boundaries of the communes and obtaining the boundary vector file from the land registry, we compared our boundary vector with the boundaries of the land registry and the visual sketches of the PVs and found that there were differences (offset between the boundaries, difference between the 02 boundaries).
Some examples of discrepancies between the digitized boundaries and the visual sketch are illustrated in the following table:

**Table 1**. Examples of anomalies between vectorized and cadastral boundaries.

| Municipal Name | distortion | vector files | official records |
|---|---|---|---|
| **SID SHAMI** | **Difference between digitized boundaries and cadastral vector file and official records** between points 15 and 18. | 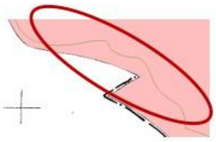 |  |
| **SID SHAMI** | **Difference between digitized boundaries and cadastral vector file and official records** between points **21 and 22.** | 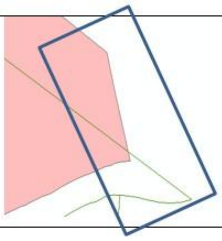 | 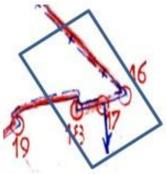 |

We have programmed the affine transformation in the PYTHON programming language,

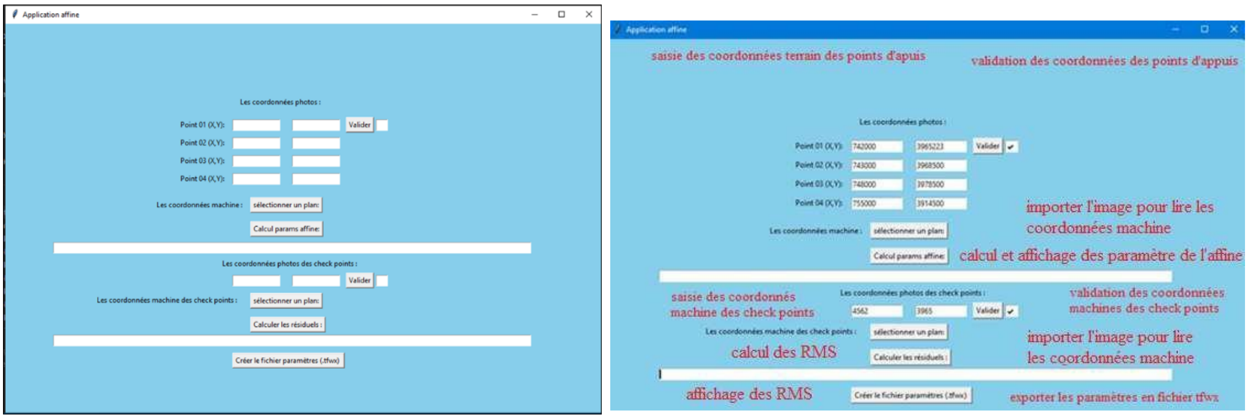

Les coordonnées photos :
Point 01 (X,Y): 742000 3965223
Point 02 (X,Y): 743000 3968500
Point 03 (X,Y): 748000 3978500
Point 04 (X,Y): 755000 3914500
Les coordonnées machine :
Les coordonnées photos des check points : 4562 3965
Les coordonnées machine des check points :

saisie des coordonnées terrain des points d'apuis
validation des coordonnées des points d'appuis
importer l'image pour lire les coordonnées machine
calcul et affichage des paramètre de l'affine
saisie des coordonnés machine des check points
validation des coordonnées machines des check points
importer l'image pour lire les coordonnées machine
calcul des RMS
affichage des RMS
exporter les paramètres en fichier tfwx

**Figure2.** Main window Application of the affine transformation.

After calibrating the section plans by applying the affine transformation, we found that overlaps are still present between section and commune boundaries. Some examples of the results obtained are shown in the figures below.

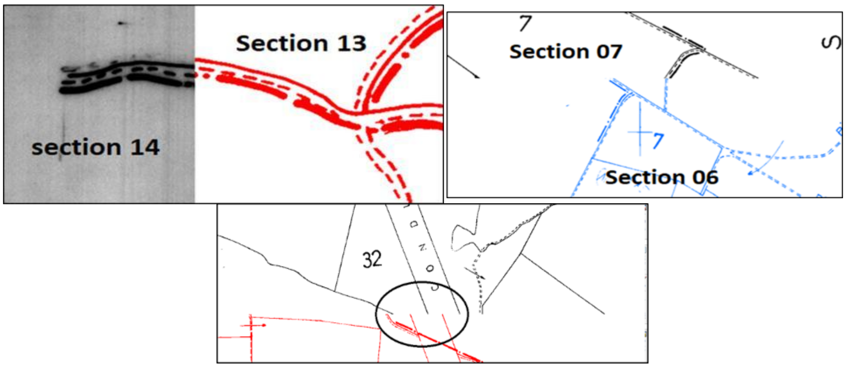

**Figure 3.** examples of the results obtained by applying the affine transformation

Since the alignment of the section planes by applying the affine transformation did not resolve the overlaps between the boundaries, we tried the second solution, a photogrammetric approach called simultaneous block adjustment.
We programmed a Block Adjustment application using the python language, and compared the results with the results of the adjustment code programmed by the matlab language to validate the calculations.

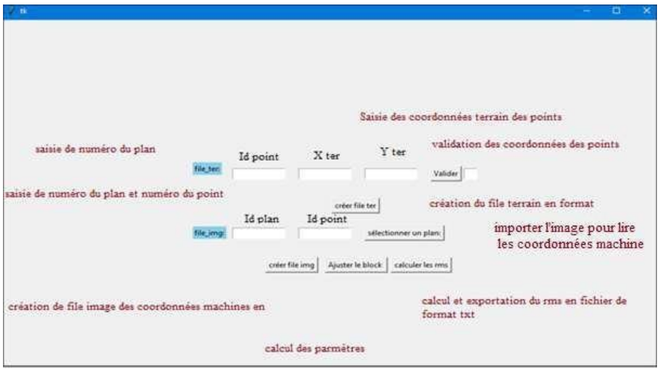

**Figure 4.** Presentation of the application interface.

We chose three neighboring communes to use as a test zone for the block adjustment. We applied two different tests: the first is the commune adjustment, which means we adjust the boundary of each commune independently, in this case the block is one commune.

The second test adjusts all three communes at the same time (global adjustment), then compares the results of the two tests with the ArcGis calibration and calculates the residuals before and after adjustment.
We chose the crosses as ground control points, and always tried to take the ideal case (crosses at the edge of the planes), using as many of these points as possible in the block.

For the tie points, we chose the common details between the planes and tried to use the maximum number of tie points in the block.
The test results are as follows:

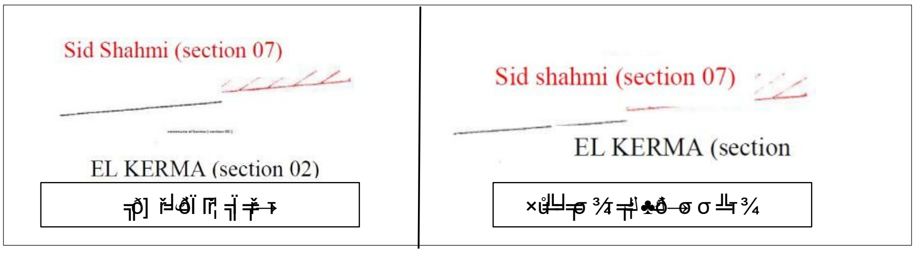

**Figure 5.** Result of first test (adjustment by commune)

**Table 2.** Calculation of residuals in X, Y and the distance in m from the calibration by ArcGis and the adjustment municipality

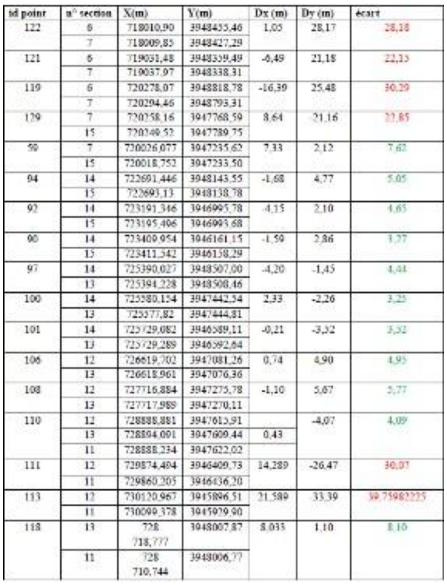

| id point | n° section | X(m) | Y(m) | Dx (m) | Dy (m) | écart |
|---|---|---|---|---|---|---|
| 122 | 6 | 718010,90 | 3948435,46 | 1,05 | 28,17 | 28,18 |
| | 7 | 718009,85 | 3948427,29 | | | |
| 121 | 6 | 719031,48 | 3948339,49 | -6,49 | 21,18 | 22,15 |
| | 7 | 719037,97 | 3948338,31 | | | |
| 119 | 6 | 720278,07 | 3948818,78 | -16,39 | 25,48 | 30,29 |
| | 7 | 720294,46 | 3948793,31 | | | |
| 129 | 7 | 720258,16 | 3947768,59 | 8,64 | 21,16 | 22,85 |
| | 15 | 720249,52 | 3947789,75 | | | |
| 59 | 7 | 720026,077 | 3947235,62 | 7,33 | 2,12 | 7,62 |
| | 15 | 720018,752 | 3947233,50 | | | |
| 94 | 14 | 722691,446 | 3948143,55 | -1,68 | 4,77 | 5,05 |
| | 15 | 722693,13 | 3948138,78 | | | |
| 92 | 14 | 723191,346 | 3946995,78 | -4,15 | 2,10 | 4,65 |
| | 15 | 723195,406 | 3946993,68 | | | |
| 90 | 14 | 723409,954 | 3946161,15 | -1,59 | 2,86 | 3,27 |
| | 15 | 723411,542 | 3946158,29 | | | |
| 97 | 14 | 725390,027 | 3948507,00 | -4,20 | -1,45 | 4,44 |
| | 13 | 725394,228 | 3948508,46 | | | |
| 100 | 14 | 725580,154 | 3947442,54 | 2,33 | -2,26 | 3,25 |
| | 13 | 725577,82 | 3947444,81 | | | |
| 101 | 14 | 725729,082 | 3946589,11 | -0,21 | -3,32 | 3,32 |
| | 13 | 725729,289 | 3946592,64 | | | |
| 106 | 12 | 726619,702 | 3947081,26 | 0,74 | 4,90 | 4,95 |
| | 13 | 726618,961 | 3947076,36 | | | |
| 108 | 12 | 727716,884 | 3947275,78 | -1,10 | 5,67 | 5,77 |
| | 13 | 727717,989 | 3947270,11 | | | |
| 110 | 12 | 728888,881 | 3947615,91 | | -4,07 | 4,09 |
| | 13 | 728894,091 | 3947609,44 | 0,43 | | |
| | 11 | 728888,234 | 3947622,02 | | | |
| 111 | 12 | 729874,494 | 3946409,73 | 14,289 | -26,47 | 30,07 |
| | 11 | 729860,205 | 3946436,20 | | | |
| 113 | 12 | 730120,967 | 3945896,51 | 21,589 | 33,39 | 39,75982225 |
| | 11 | 730099,378 | 3945929,90 | | | |
| 118 | 13 | 728<br>718,777 | 3948007,87 | 8,033 | 1,10 | 8,10 |
| | 11 | 728<br>710,744 | 3948006,77 | | | |

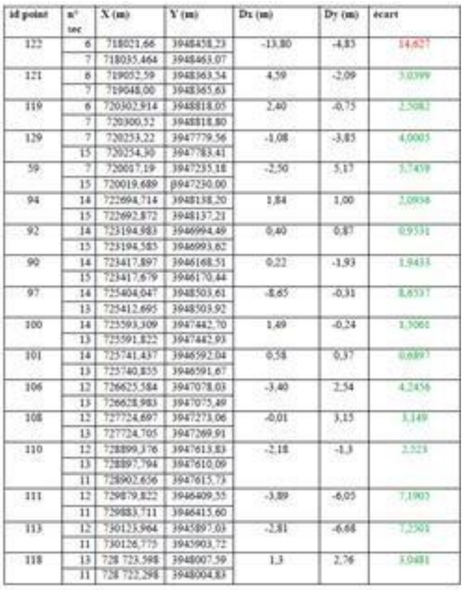

| id point | n° sec | X (m) | Y (m) | Dx (m) | Dy (m) | écart |
|---|---|---|---|---|---|---|
| 122 | 6 | 718021,66 | 3948458,23 | -13,80 | -4,85 | 14,627 |
| | 7 | 718035,464 | 3948463,07 | | | |
| 121 | 6 | 719052,59 | 3948363,54 | 4,59 | -2,09 | 5,0399 |
| | 7 | 719048,00 | 3948365,63 | | | |
| 119 | 6 | 720302,914 | 3948818,05 | 2,40 | -0,75 | 2,5082 |
| | 7 | 720300,52 | 3948818,80 | | | |
| 129 | 7 | 720253,22 | 3947779,56 | -1,08 | -3,85 | 4,0005 |
| | 15 | 720254,30 | 3947783,41 | | | |
| 59 | 7 | 720017,19 | 3947235,18 | -2,50 | 5,17 | 5,7459 |
| | 15 | 720019,689 | 3947230,00 | | | |
| 94 | 14 | 722694,714 | 3948138,20 | 1,84 | 1,00 | 2,0938 |
| | 15 | 722692,872 | 3948137,21 | | | |
| 92 | 14 | 723194,983 | 3946994,49 | 0,40 | 0,87 | 0,9531 |
| | 15 | 723194,583 | 3946993,62 | | | |
| 90 | 14 | 723417,897 | 3946168,51 | 0,22 | -1,93 | 1,9433 |
| | 15 | 723417,679 | 3946170,44 | | | |
| 97 | 14 | 725404,047 | 3948503,61 | -8,65 | -0,31 | 8,6557 |
| | 13 | 725412,695 | 3948503,92 | | | |
| 100 | 14 | 725593,309 | 3947442,70 | 1,49 | -0,24 | 1,5061 |
| | 13 | 725591,822 | 3947442,93 | | | |
| 101 | 14 | 725741,437 | 3946592,04 | 0,58 | 0,37 | 0,6897 |
| | 13 | 725740,855 | 3946591,67 | | | |
| 106 | 12 | 726625,584 | 3947078,03 | -3,40 | 2,54 | 4,2456 |
| | 13 | 726628,983 | 3947075,49 | | | |
| 108 | 12 | 727724,697 | 3947273,06 | -0,01 | 3,15 | 3,149 |
| | 13 | 727724,705 | 3947269,91 | | | |
| 110 | 12 | 728899,376 | 3947613,83 | -2,18 | -1,3 | 2,523 |
| | 13 | 728897,794 | 3947610,09 | | | |
| | 11 | 728902,656 | 3947615,73 | | | |
| 111 | 12 | 729879,822 | 3946409,55 | -3,89 | -6,05 | 7,1903 |
| | 11 | 729883,711 | 3946415,60 | | | |
| 113 | 12 | 730123,964 | 3945897,03 | -2,81 | -6,68 | 7,2501 |
| | 11 | 730126,775 | 3945903,72 | | | |
| 118 | 13 | 728 723,598 | 3948007,59 | 1,3 | 2,76 | 3,0481 |
| | 11 | 728 722,298 | 3948004,83 | | | |

**Table 3.** Distance residual statistics

| | Dist Before Adjustment | Dist After Adjustment |
|---|---|---|
| Min | 3.25235007 | 0.689654986 |
| Max | 39.7598222 | 14.62740613 |
| Mean | 13.4174767 | 4.421618151 |
| RMS | 12 | 3.40 |

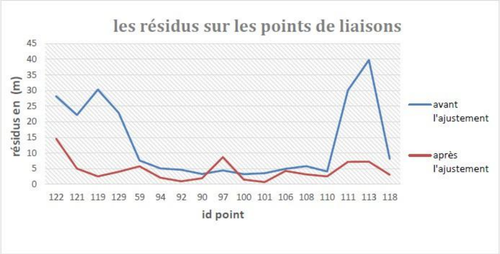

**Figure 5**. Residues on the Tie points.

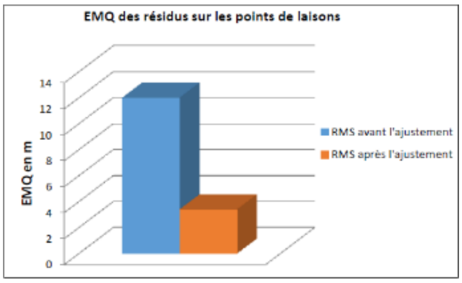

**Figure 6.** The EMQ of residues on the Tie points.

**Results of 2nd test (global adjustment: all neighbouring communes)**

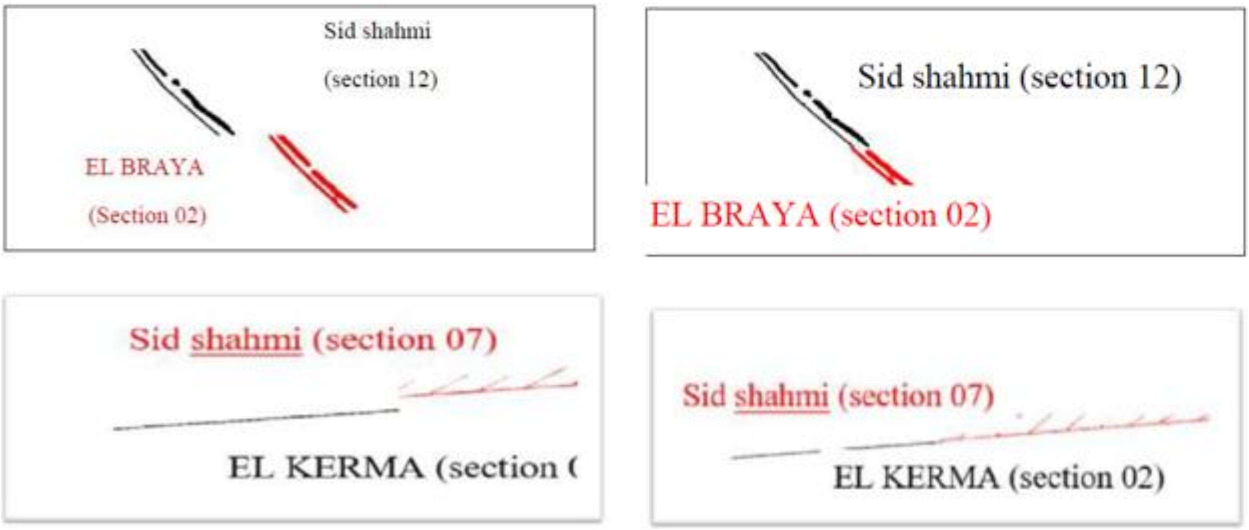

**ArcGis calibration** **Global Adjustment**

**Figure 7.** Results of second test (Global Adjustment).

**Table 4.** Calculation of X and Y residuals and ArcGis calibration distance deviations.

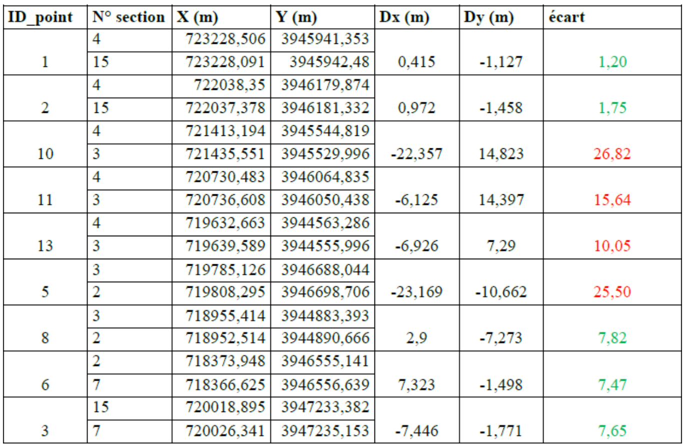

| ID_point | N° section | X (m) | Y (m) | Dx (m) | Dy (m) | écart |
|---|---|---|---|---|---|---|
| 1 | 4 | 723228,506 | 3945941,353 | 0,415 | -1,127 | 1,20 |
| | 15 | 723228,091 | 3945942,48 | | | |
| 2 | 4 | 722038,35 | 3946179,874 | 0,972 | -1,458 | 1,75 |
| | 15 | 722037,378 | 3946181,332 | | | |
| 10 | 4 | 721413,194 | 3945544,819 | -22,357 | 14,823 | 26,82 |
| | 3 | 721435,551 | 3945529,996 | | | |
| 11 | 4 | 720730,483 | 3946064,835 | -6,125 | 14,397 | 15,64 |
| | 3 | 720736,608 | 3946050,438 | | | |
| 13 | 4 | 719632,663 | 3944563,286 | -6,926 | 7,29 | 10,05 |
| | 3 | 719639,589 | 3944555,996 | | | |
| 5 | 3 | 719785,126 | 3946688,044 | -23,169 | -10,662 | 25,50 |
| | 2 | 719808,295 | 3946698,706 | | | |
| 8 | 3 | 718955,414 | 3944883,393 | 2,9 | -7,273 | 7,82 |
| | 2 | 718952,514 | 3944890,666 | | | |
| 6 | 2 | 718373,948 | 3946555,141 | 7,323 | -1,498 | 7,47 |
| | 7 | 718366,625 | 3946556,639 | | | |
| 3 | 15 | 720018,895 | 3947233,382 | -7,446 | -1,771 | 7,65 |
| | 7 | 720026,341 | 3947235,153 | | | |

**Table 5.** Calculation of X and Y residuals and global fit distance deviations.

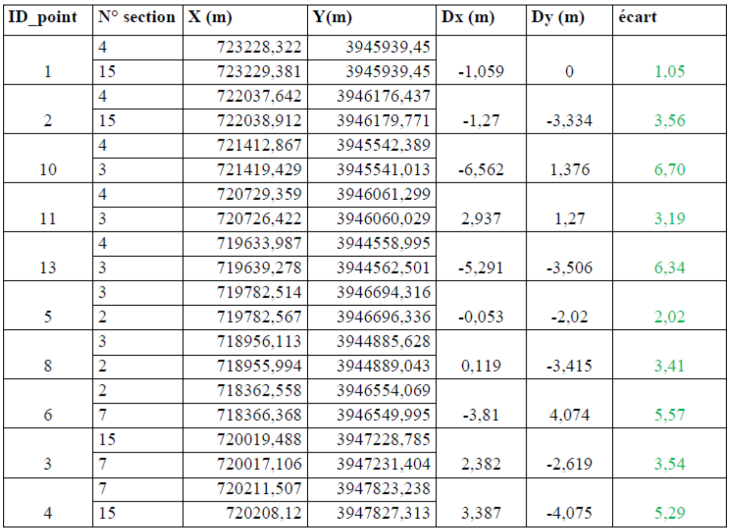

| ID_point | N° section | X (m) | Y(m) | Dx (m) | Dy (m) | écart |
|---|---|---|---|---|---|---|
| 1 | 4 | 723228,322 | 3945939,45 | -1,059 | 0 | 1,05 |
| | 15 | 723229,381 | 3945939,45 | | | |
| 2 | 4 | 722037,642 | 3946176,437 | -1,27 | -3,334 | 3,56 |
| | 15 | 722038,912 | 3946179,771 | | | |
| 10 | 4 | 721412,867 | 3945542,389 | -6,562 | 1,376 | 6,70 |
| | 3 | 721419,429 | 3945541,013 | | | |
| 11 | 4 | 720729,359 | 3946061,299 | 2,937 | 1,27 | 3,19 |
| | 3 | 720726,422 | 3946060,029 | | | |
| 13 | 4 | 719633,987 | 3944558,995 | -5,291 | -3,506 | 6,34 |
| | 3 | 719639,278 | 3944562,501 | | | |
| 5 | 3 | 719782,514 | 3946694,316 | -0,053 | -2,02 | 2,02 |
| | 2 | 719782,567 | 3946696,336 | | | |
| 8 | 3 | 718956,113 | 3944885,628 | 0,119 | -3,415 | 3,41 |
| | 2 | 718955,994 | 3944889,043 | | | |
| 6 | 2 | 718362,558 | 3946554,069 | -3,81 | 4,074 | 5,57 |
| | 7 | 718366,368 | 3946549,995 | | | |
| 3 | 15 | 720019,488 | 3947228,785 | 2,382 | -2,619 | 3,54 |
| | 7 | 720017,106 | 3947231,404 | | | |
| 4 | 7 | 720211,507 | 3947823,238 | 3,387 | -4,075 | 5,29 |
| | 15 | 720208,12 | 3947827,313 | | | |

**Table 6.** Distance residual statistics.

| | Dist Before Adjustment | Dist After Adjustment |
|---|---|---|
| Min | 1.200980433 | 1.059 |
| Max | 26.8245555 | 6.704716251 |
| Mean | 12.22643174 | 4.073316024 |
| RMS | 8.58 | 1.75 |

**Figure 8.** Residues on Tie points.

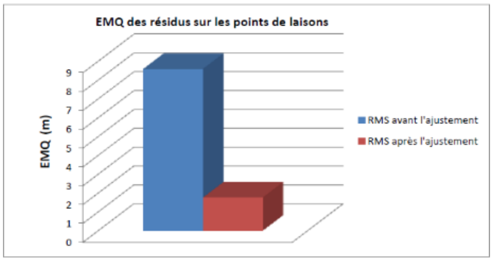

**Figure 9.** The EMQ of residues on Tie points.

## Global Adjustment using GNSS ground control points

Based on simultaneous block adjustment, we tested the Hassi mefsoukh commune section plan assembly.

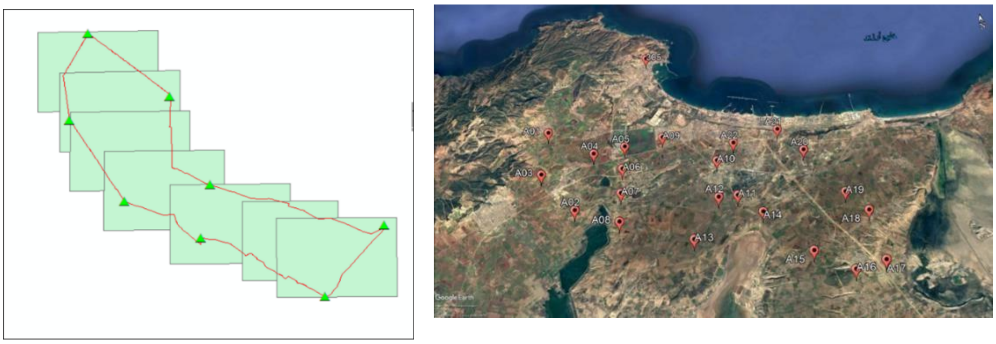

**Figure 10.** Geographical distribution of Ground Control Points. [Google Earth] We interpreted the results of the Hassi mefsoukh adjustment, which gives a good visualization.

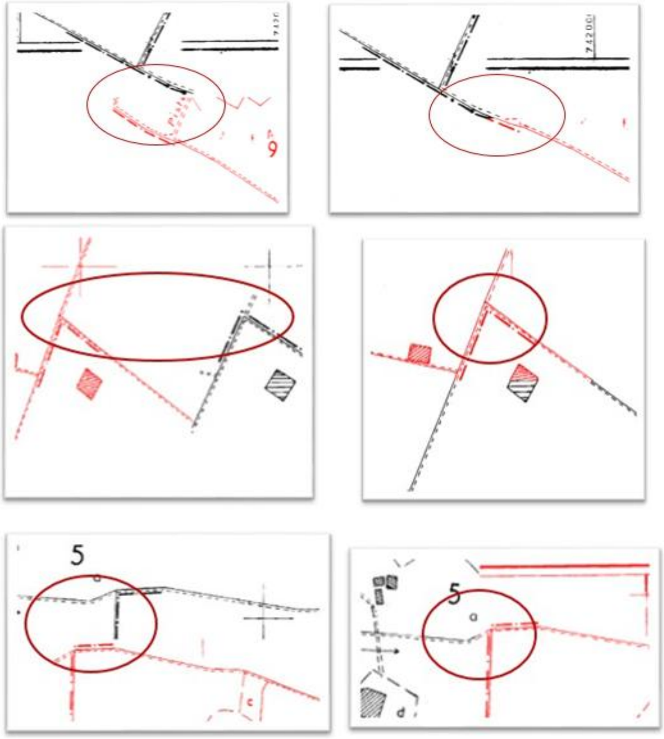

**Figure 11.** Examples of results before and after adjustment.

**Table 7.** Statistics of distance residuals.

| | Dist Before Adjustment | Dist After Adjustment |
|---|---|---|
| Min | 2,78506194 | 0,16263456 |
| Max | 454,649217 | 5,29762664 |
| Mean | 86,2922708 | 1,90639885 |
| RMS | 124,616544 | 1,57456598 |

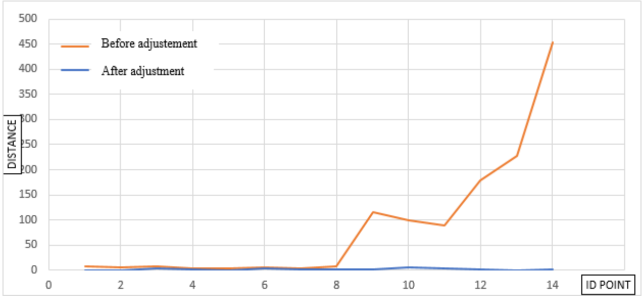

**Figure 12.** Residues on Tie points.

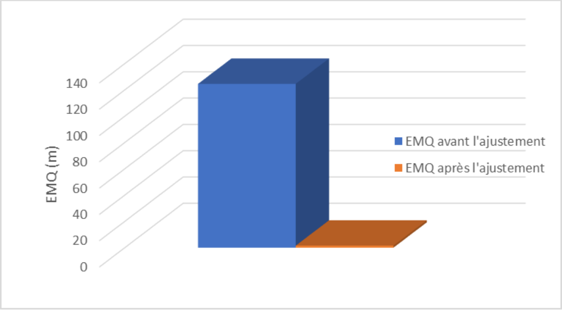

**Figure 13.** The EMQ of residues on Tie points.

## Conclusion

After these tests, it was noted that the fit depended on the quality of the support and connection points used, and their distribution. After this results we decided to test with points observed in the field by GNSS. From the results obtained, we can conclude that global adjustment using GNSS ground control points gives better results.

## References

Ben mouloud**,** Projet DE JUMELAGE ANC (ALGERIE) – DGFIF (France). 2018.
Ben mouloud**,** Projet DE JUMELAGE ANC (ALGERIE) – DGFIF (France). 2018.
Cadastre en Algérie et l'ouverture vers un cadastre multifonctionnel. ANC**.** 2018.
DGFP, France**.** Un extrait dubulletin officiel des finances publiques-impots de la Direction Générale des Finances Publiques publié le 12/09/2012 sous l'intitulé : << CAD – Travaux topographiques du cadastre - Le traitement des raccords entre feuilles de plan cadastral >>. 2012.

Fiche 47 du CNIG. 2001.
Instruction n° 16. Cadastre.
ISO 8402, Fiche du CNIG. 1994.

Mr. Rabah Abdelbasset et Mr.BenMakhlouf Azeddine**.** Traitement des raccords entre sections. Oran : CTS, 2017.

Office fédéral de topographie**.** Guide pour l'application des transformations géométriques en mensuration officielles. s.l. : Direction fédérale des mensurations cadastrales, 2008.

Procès-verbal de délimitation du territoir communal. Oran : DWC, 1986.

St-Pierre Sébastien**,** Etude de l'effet de la qualité métrique de représentation sur la fiabilité du registre foncier. s.l. : l'université LAVAL.

ViglinoJean-Marc, Laurent Guigues et, Bulletin de l'information de l'IGN n° 72 (2003/3) : Géoréférencement automatique de feuilles cadastrales, 2003.

Siyoucef kamel, Mise en place d'une procédure d'une procédure photogrammétrique pour l'assainissement des bases graphiques cadastrales, 2018.

INTERNATIONAL SYMPOSIUM ON
APPLIED
GEOINFORMATICS
9-10 May 2024 · Wrocław/Poland

*International Symposium on Applied Geoinformatics (ISAG2024)*

# From Classical Analysis to Ai: Tracing Methodological Evolution in Spatial Rural-Urban Transformation Studies

Mohamed Rabii Simou[1]*, Safia Loulad[1], Zineb El Faraj[1], Mohamed Benayad[1], Mehdi Maanan[1], Hassan Rhinane[1]

[1] Geosciences Laboratory, Earth Sciences Department, Faculty of Sciences-Ain Chock, University Hassan II, Casablanca, Morocco;

* Corresponding Author

## Abstract

Spatial rural-urban transformation represents a complex and dynamic interplay between rural and urban areas. The challenge is in effectively studying this evolving phenomenon, for which many methods have been and continue to be used. This review paper examines the evolution of methodologies in spatial rural-urban transformation studies and constructs a chronological narrative, highlighting key shifts and technological progressions in research methods over the years. From classical methodologies, such as the Analytic Hierarchy Process (AHP) and other statistical and spatial analysis techniques to focusing on the impact of Artificial Intelligence (AI) and its role in enhancing research methodologies, particularly in the context of Morocco. The results reveals a significant evolution in the methodological approaches to studying rural- urban transformations. Initial findings indicate that while classic methods provided foundational understanding, using AI has greatly improved the accuracy and depth of spatial analysis. Methodologies that used AI, have enabled studies to more effective understanding of urbanization patterns, land-use changes, and socio-economic, and most importantly more automated tasks. The integration of AI offered new perspectives and more detailed analyses to reshape the future trajectory of rural-urban transformation studies. These advancements have a direct implications for urban planning, policy-making, and sustainable development goals strategies.

**Keywords:** *Rural-Urban Transformation, Artificial Intelligence, Geographic Information Systems, Methodological Evolution, Remote Sensing*

## Introduction/Background

The spatial rural-urban transformation encapsulates the evolving dynamics between rural and urban areas, while reflecting both key and fundamental aspects of geographical and socio-economic changes globally. This transformation, is brought by shifts in land use, population migration, economic development, and social structures, marks the transition of regions from primarily rural or agricultural landscapes to urbanized or peri-urban setting (Liu, 2021). Such dynamics could draw out an understanding that would inform devising strategies that would favor sustainable development, guarantee just resource sharing, and minimize environmental impacts brought about by urbanization (Basiago, 1998).

This paper reviews the trajectory of methodological advances in spatial rural-urban transformation studies. It attempts to map some of the key period changes that have characterized urban studies and segment the historical progress very carefully into five distinct periods. Each of these epochs signals a transition from classical theories and statistical analysis to a more sophisticated data-driven approaches, with particular focus on how these methods of AI will drive a transformative impact..

Through the spectrum of application of the methodology of this review, this paper situates itself within a much bigger project directed toward knowledge syntheses from past research for the refinement and enhancement of these multi variables affecting rural-urban transformation in the Moroccan regions. It could hence be considered to be interdisciplinary research of the multiple of factors from socioeconomic to environmental and their complex interrelations, determining the rural-urban transformation. And by so doing, this research adds to the continued discourse by providing a strong, sustainable, flexible methodological framework.

## The evolution of Urban Research Studies

Rural-urban transformation has been defined as the process through which rural areas take up progressively urban characteristics that may lead to changing land use, economic activities, and changes in social structures (Ma et al. , 2018). This can be caused from so many factors, such as industrialization, migration, technological development, and policy reforms. The evolution of research methodologies in the broader field of urban studies has been significant, in this paper it has been divided to 5 periods as shown in Figure 1,

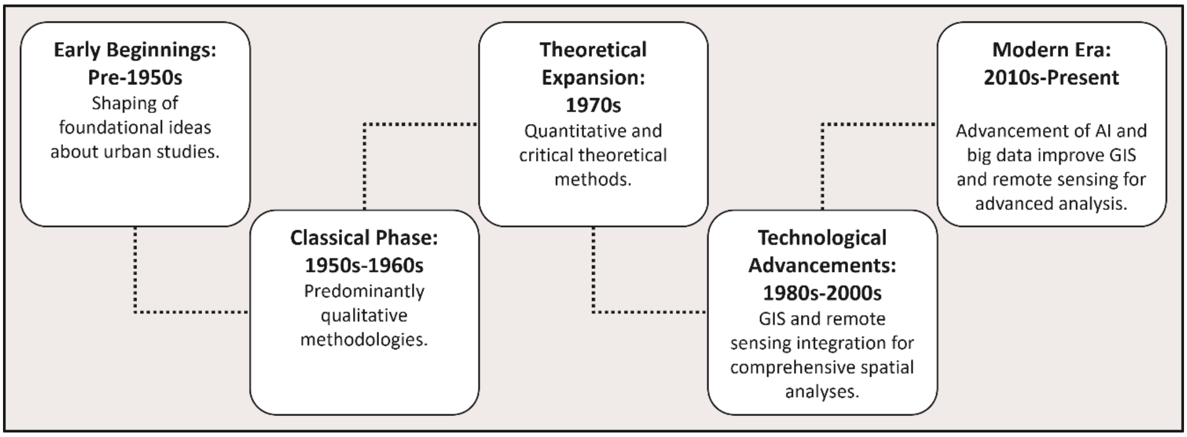

**Figure 1.** Evolution of Urban studies from theory to AI (Artificial Intelligence).

Before the 1950s, urban studies were in mostly theory stages, forming foundational ideas that would be the base of future research, It's generally understood from the literature of many papers that this was a time for shaping the basic concepts, establishing the field of urban geography and sociology and the beginning of a new phase of Urban Sociology (Gottdiener & Feagin, 1988).

The classical period of urban studies, which focused mostly on lower-income regions, implemented qualitative methods in the 1950s and 60s to look into the socioeconomic and cultural composition of urban settings (Topalov, 2003). in the studies of this period, some methods were used, such as ethnography and detailed case studies, had a function: to serve as an explanation of the socio-economic change produced by urban expansion and industrialization, as well as the great multiplicity of experiences of inhabitants in cities. The methods presented here, therefore, gave this as a basic guideline to the complex dynamics within cities and therefore laid a platform for future, much more critical research on the ever- changing urban settings and related complexities of cultural and political variables.

According to (Zukin, 1980). there was a major methodological shift in urban sociology during the 1970s as a result of a theoretical expansion. The field adopted a combination of critical theory and quantitative analysis. This period, which signaled the emergence of a "New Urban Sociology", integrated Marxist and critical theoretical ideas to challenge classical ideas of urban development. Instead of viewing urban areas as purely physical locations, researchers started to study sites as complex battlefields of economic and social dynamics. Many questioned the interests of the government and industrialists while critically assessing the effects of urban planning and policy.

This revolutionary era shifted attention toward more profound socio-economic dynamics that occur in urban areas, laying the foundation for a more complex, diverse understanding of urban phenomena. Many studies examined land use transformation along the border between rural and urban areas using a new approach. Such approaches could not help but draw attention to the difficulty of focusing dynamic processes like urban growth and migration and questioning the impact of capitalism and governmental goals on urban development (Pacione, 2009).

Urban studies made a major shift in the 1980s and 2000s with the widespread adoption and growth of Geographic Information Systems (GIS) and remote sensing technology. Although GIS had been established earlier, this was the period of growing popularity and the creation of advanced software applications that improved the accuracy and availability of spatial analysis (Malczewski, 2004). The methodological progress of this era is most clearly shown by (Liu, 2021), who involve GIS to investigate land-use changes and urban development in China. Additionally, demonstrate how remote sensing information can be combined with GIS to better understand and illustrate the environmental effects of rural-urban transitions. This marked a paradigm change from more manual, classical geographical analysis to large-scale spatial data processing, opening the door to complemented, detailed knowledge and up-to-date policymaking for urban-rural interactions.

Finally, the most recent urban studies of the modern era from the 2010s to the current decade, have integrated big data analytics (Correa, 2015) and Artificial Intelligence technologies (Vozenilek, 2009). AI integrated with GIS and remote sensing indicated the dynamic analysis from urban to rural moving to a superior level of analytics, predictive and prescriptive in nature. This has brought efficiencies and accuracies that had been unachievable before. AI can process highly complex sets of data in land use and, even better, model highly complicated scenarios at the same, enabling the municipality to plan and take policies of the city. For example, in Morocco, AI techniques have been used in forecasting trends of urbanization and assessment of the socio-economic impact in relation to the transformation of rural-urban areas. This suggests advancement in comparing modern methods with classical approaches (Saadani, 2020).

## Methodological Innovations and Challenges

This section includes contemporary methodologies in urban-rural studies, highlighting a significant evolution in approaches as demonstrated by papers showed in Table 1 and which have been advanced from classical statistical models to the current age technologies like Artificial Intelligence (AI) that are boosting precision, depth, and cloud-based automation in spatial and socio-economic analyses.

Initially, researchers like (Huang, 2009) applied logistic regression and land use simulation models based on socio- economic data for use to understand the dynamics of the urban-rural interfaces. Similarly, (Bhatta & Doppler, 2010) applied the Analytic Hierarchy Process (AHP) in dissecting agricultural differentiation at the rural-urban interface, Both papers displaying some of the classical methods that are the basis of spatial analysis evolution.

With advancing methodology, demographic and economic data were applied by (Dorosh & Schmidt, 2010) in combination with spatial analysis to research the expansion of Ethiopian cities. This gives the example of researchers going towards integrating multiple data types which will push boundaries of more complex analyses. For example, (Wang et al., 2016) provided a urban–rural development transformation index (URDTI) based on three indicator systems to provide a nuanced view of the urban-rural development since 1990 in China study, which show more the importance of multi-dimensional data in urban-rural interactions.

The other works of (Yang et al., 2018) further in development to study spatial-temporal patterns of urban growth with the application of the Gravity-Centre Model combined with urban land change analysis. (Diao et al., 2019) go further to show that using Probit models and spatial analysis can help improve understanding of the socio-economic issues specifically in this case to investigate poverty and livelihood patterns in Ghana.

Further delving into the methodological and predictive frontiers, (Niu et al., 2022) apply the Geo-information Tupu method and spatial regression analysis for land-use transitions in urban-rural conditions, while (Ding et al., 2022) applies climate model simulations for the research with remote sensing data.

(Liu et al., 2020) design a semi-automatic framework for urban land mapping using the cloud-based Google Earth Engine (GEE) with different classification algorithms like Classification And Regression Trees (CART), Random Forest (RF), Support Vector Machine (SVM), and Naïve Bayes. This reflects a broader trend of adding AI to automate and enhance the accuracy of analyses. While, (Loulad et al., 2023) employed remote sensing and AI technologies just like the previous paper, using RF using GEE for a classifications, and Generative Adversarial Networks (GANs) for image colorization, and structural similarity index measure (SSIM) for image comparison to analyze rural-urban transformations over extended periods This way, AI enables the depth of land use change and urban dynamics exploration, rather than just becoming a tool for the total automation of tasks.

**Table 1.** This is an example of table formatting.

| Aim of Research | Models/Methods Used | Keywords | Reference |
|---|---|---|---|
| Urban-rural interface analysis | Logistic regression, land use models | Urban modeling, simulation | (Huang et al., 2009) |

| | | | |
|---|---|---|---|
| Farming differentiation factors | AHP | Decision-making, AHP | (Bhatta & Doppler, 2010) |
| Rural-urban transformation in Ethiopia | Quantitative analysis, spatial urbanization analysis | Urbanization, policy analysis | (Dorosh & Schmidt, 2010) |
| Urban-rural development in China | Indicator systems for URDL, URSL, URCL | Spatial integration | (Wang et al., 2016) |
| Urban expansion patterns | Gravity-Center Model, land change analysis | Urban growth, gravity modeling | (Yang et al., 2018) |
| Rural livelihoods in Ghana | Probit models, spatial analysis | Rural livelihoods, poverty | (Diao et al., 2019) |
| Urban land mapping framework | Semi-automatic framework, GEE | Machine learning, remote sensing | (Liu et al., 2020) |
| Land-use transition characteristics | Geo-information Tupu, spatial regression | Spatial-temporal analysis | (Niu et al., 2022) |
| Urban expansion effects | Climate models, remote sensing | Climate modeling, urban effects | (Ding et al., 2022) |
| Rural-urban dynamics in RSK region, Morocco | RF model, GEE, GANs | Machine learning, remote sensing | (Loulad et al., 2023) |

## Suggestions for future studies

As periods went by, the methodologies applied in the study of urban-rural areas have shifted from classical qualitative and quantitative approaches to the most current AI-influenced techniques. AI, cloud computing, and open-source data are starting to shape the reformation of this field by integrating scalable, efficient, and collaborative platforms for future research. This kind of technological progress should help explain the urban-rural dynamics in order to appreciate and deal with the complexities that bear onto sustainable urban planning and policymaking, most especially in a context like Morocco.

Key Points:

Evolution of Methodology: From classical methods of analysis to AI-driven models in urban-rural studies.

Use of Technology: Artificial intelligence is used in combination with cloud computing and GIS to enhance spatial analysis and predictive modeling.

Accessibility and Collaboration: By further tapping into open-source data and adopting a cloud-based model, accessibility to information becomes more democratized in ways that reach out to the global audience.

AI Expansion: Implementation of a variety of AI technologies to be used in handling a wide range of datasets and providing detailed insights.

Impact on Morocco: Changing urban planning and policymaking to tailor-made, data-sourced strategies toward sustainability.

## Conclusion

This review has tracked the main methodological shift in spatial rural-urban transformation studies from classical paradigms to advanced AI-driven methodologies. This development reflects a larger trend within urban studies to use technology for a better comprehension and handling of urbanization issues and their impact on rural areas. There has been a significant shift from the descriptive, qualitative approaches of the 1950s-1960s through the more critical and theoretical frameworks of the 1970s, up to the advanced technological methodologies of the late 20th and early 21st centuries. Each era builds on past methodologies, moving toward more sophisticated, data-informed, technology-enabled ways of understanding and managing urban and rural transformations. This review shows the importance of methodological evolution in enhancing the understanding of rural-urban transformations and guiding effective urban planning and policy- making. The continued advancement and integration of research methodologies will be important in addressing the challenges led by fast urbanization, ensuring sustainable development that benefits both rural and urban areas.

,

## References

Basiago, A. D. (1998). Economic, social, and environmental sustainability in development theory and urban planning practice. Environmentalist, 19(2), 145-161.

Bhatta, G. D., & Doppler, W. (2010). Farming differentiation in the rural-urban interface of the middle mountains, Nepal: Application of analytic hierarchy process (AHP) modeling. Journal of Agricultural Science, 2(4), 37-51.

Correa, F. R. (2015). Is BIM big enough to take advantage of big data analytics?. In ISARC. Proceedings of the International Symposium on Automation and Robotics in Construction (Vol. 32, p. 1). IAARC Publications. Diao, X., Magalhaes, E., & Silver, J. (2019). Cities and rural transformation: A spatial analysis of rural livelihoods in Ghana. World Development, 121, 141-157.

Ding, Q., Shao, Z., Huang, X., Altan, O., & Hu, B. (2022). Time-series land cover mapping and urban expansion analysis using OpenStreetMap data and remote sensing big data: A case study of Guangdong-Hong Kong-Macao Greater Bay Area, China. International Journal of Applied Earth Observation and Geoinformation, 113, 103001.

Dorosh, P., & Schmidt, E. (2010). The rural-urban transformation in Ethiopia (No. 13). Addis, Ethiopia: International Food Policy Research Institute (IFPRI).

Gottdiener, M., & Feagin, J. R. (1988). The paradigm shift in urban sociology. Urban Affairs Quarterly, 24(2), 163-187.

Huang, B., Zhang, L., & Wu, B. (2009). Spatiotemporal analysis of rural–urban land conversion. International Journal of Geographical Information Science, 23(3), 379-398.

Liu, D., Chen, N., Zhang, X., Wang, C., & Du, W. (2020). Annual large-scale urban land mapping based on Landsat time series in Google Earth Engine and OpenStreetMap data: A case study in the middle Yangtze River basin. ISPRS Journal of Photogrammetry and Remote Sensing, 159, 337-351.

Liu, Y. (2021). Urban-rural transformation geography. Singapore: Springer.

Loulad, S., Nguyen, T. T., Simou, M. R., Rhinane, H., & Buerkert, A. (2023). Monitoring rural-urban transformation in the coastal region of Rabat-Sale-Kenitra, Morocco. Plos one, 18(8), e0290829.

Ma, W., Jiang, G., Li, W., & Zhou, T. (2018). How do population decline, urban sprawl and industrial transformation impact land use change in rural residential areas? A comparative regional analysis at the peri- urban interface. Journal of Cleaner Production, 205, 76-85.

Malczewski, J. (2004). GIS-based land-use suitability analysis: a critical overview. Progress in planning, 62(1), 3-65.

Niu, X., Liao, F., Liu, Z., & Wu, G. (2022). Spatial–temporal characteristics and driving mechanisms of land– use transition from the perspective of urban–rural transformation development: A case study of the Yangtze River delta. Land, 11(5), 631.

Pacione, M. (2009). Urban geography: A global perspective. Routledge.

Saadani, S., Laajaj, R., Maanan, M., Rhinane, H., & Aaroud, A. (2020). Simulating spatial–temporal urban growth of a Moroccan metropolitan using CA–Markov model. Spatial Information Research, 28, 609-621.

Topalov, C. (2003). " Traditional working-class neighborhoods": An inquiry into the emergence of a sociological model in the 1950s and 1960s. Osiris, 18, 212-233.

Vozenilek, V. (2009, November). Artificial intelligence and GIS: mutual meeting and passing. In 2009 International conference on intelligent networking and collaborative systems (pp. 279-284). IEEE.

Wang, Y., Liu, Y., Li, Y., & Li, T. (2016). The spatio-temporal patterns of urban–rural development transformation in China since 1990. Habitat International, 53, 178-187.

Yang, Y., Liu, Y., Li, Y., & Du, G. (2018). Quantifying spatio-temporal patterns of urban expansion in Beijing during 1985–2013 with rural-urban development transformation. Land use policy, 74, 220-230.

Zukin, S. (1980). A decade of the new urban sociology. Theory and Society, 9(4), 575-601

INTERNATIONAL SYMPOSIUM ON
APPLIED
GEOINFORMATICS
9-10 May 2024 · Wrocław/Poland

*International Symposium on Applied Geoinformatics (ISAG2024)*

# Assessment of River Basin Water Budget Estimation using Remote Sensing Observations and GIS Techniques

Deliry Sayed Ishaq[1, *], Avdan Uğur[2]

1 Eskisehir Technical University, Department of Remote Sensing and Geographical Information Systems, Eskişehir, Türkiye; deliry.ishaq@gmail.com; ORCID 0000-0002-5467-1403
2 Eskisehir Technical University, Institute of Earth and Space Sciences, Eskişehir, Türkiye; uavdan@eskisehir.edu.tr; ORCID 0000-0001-7873-9874
* Corresponding Author

## Abstract

The utilization of satellite remote sensing products is progressively vital in the management of water resources. A critical element for effective and sustainable management of river basins is the monitoring of water availability and demand. This research estimates the monthly and annual components of the water budget for the Amu Darya and the Kizilirmak River Basins utilizing satellite data and the GLDAS-2.1 Noah and CLSM models for the hydrological years 2014, 2015, 2017, and 2018. Datasets for precipitation (P), evapotranspiration (ET), terrestrial water storage (TWS), and runoff (R) from various model and satellite-based sources, including GPM IMERG, CHIRPS, MODIS SSEBop, GRACE, CLSM, Noah, and streamflow gauges were integrated. The study inferred runoff from the water balance equation as a residual since direct remote sensing observations are not possible. Through processing, analysis, and intercomparison of these datasets, we evaluated the performance of satellite remote sensing in water budget estimation and analyzed the consistency of spatial patterns between satellite and earth system-modeled data. Our findings indicate good agreement in remotely sensed precipitation data; however, discrepancies in ET and TWS change indicate significant uncertainties. There were notable differences between inferred runoff from remote sensing and model outputs compared to observed streamflow measurements. Despite this, the Noah model exhibited better consistency with gauge observations. This investigation highlights the capabilities and limitations of using satellite-based remote sensing alongside GLDAS-2.1 CLSM and Noah models for water budget estimation. It underscores the necessity for caution when employing remote sensing and modeled data in ungauged regions due to the exclusion of human influences in these datasets. Despite inherent uncertainties in GLDAS and remote sensing datasets, they offer valuable insights for evaluating seasonal and interannual variations in water components, crucial for river basin management, especially in regions with sparse data.

***Keywords:*** *Remote Sensing, GLDAS, GRACE, River Basin Water Budget, Terrestrial Water Storage*

## Introduction

River basins management is critical for the equitable distribution and allocation of water within a country or across countries sharing transboundary river basins (Deliry et al., 2022; Gao et al., 2010). Accurate monitoring of water availability and demand, which primarily depends on the hydrology and ecology of the basin, is essential for sustainable and effective management of river basins (Bai et al., 2016; Lakshmi et al., 2018). The significance of water availability within a basin is profoundly influenced by climate change, altering streamflows and impacting both ecological systems and human societies (Moghim, 2018; Mohammed et al., 2018). Accurate delineation of watersheds and their stream channels based on the terrain of the basin is paramount for river basin management, requiring comprehensive information on soil, vegetation, and various water budget components such as precipitation, evapotranspiration, runoff, and surface and groundwater storage (Deliry et al., 2022).

Direct measurements of precipitation can be made using in-situ observations like rain gauges and remote sensing techniques including satellite sensors and weather radars. Despite the spatial variability that can be resolved given sufficient gauge density, the point-based nature of gauge-based observations introduces uncertainties in precipitation values, especially in regions with sparse gauge stations (Kidd et al., 2017; Shen et al., 2020; Tang et al., 2016). Remote sensing techniques offer a solution by providing reliable global precipitation estimates with fine spatial and temporal resolution, which is particularly beneficial for data-scarce regions (Deliry et al., 2022; Funk et al., 2015; Hosseini-Moghari & Tang, 2020). Evapotranspiration (ET) and Terrestrial Water Storage (TWS) changes at large scales are challenging to measure directly through in-situ methods due to their high spatial variability (Deng et al., 2023; Lakshmi et al., 2018; Zheng et al., 2022). Land Surface Models (LSMs), which simulate surface-atmosphere interactions, are crucial tools for studying the terrestrial water budget and predicting land surface dynamics (Fisher & Koven, 2020; Rodell et al., 2004). The Global Land Data Assimilation System (GLDAS) offered by NASA integrates remote sensing and ground-based observations to provide comprehensive information about water and energy components, proving invaluable for global climate change studies (Rui et al., 2020).

Satellite remote sensing products have become increasingly critical for water resources management, providing spatially uniform data compared to ground-based measurements' non-uniformity. These observations offer invaluable data over data-sparse regions and have shown promising results as alternatives in terms of time and space (Deliry et al., 2022; Hosseini-Moghari & Tang, 2020; Hsu et al., 2021; Kidd et al., 2017; Le et al., 2018). Despite the potential, uncertainties in satellite-based water budget estimations exist and vary from basin to basin, necessitating further studies to better understand these variations (Deliry et al., 2022; Deng et al., 2023; Long et al., 2015).

The study focuses on a broad perspective applicable to various large basins. Utilizing remote sensing data and Geographic Information Systems (GIS) techniques, we conducted a thorough analysis of water budget components in the Amu Darya and the Kizilirmak River Basins. This study's findings highlight the importance of integrating satellite remote sensing products with land surface modeling to improve our understanding of hydrological processes and enhance water resources management strategies. The results reveal the strengths and limitations of using satellite-based remote sensing and GLDAS-2.1 CLSM and Noah models in estimating water budget components, highlighting the need for cautious use of these data sources, especially in ungauged regions.

## Materials and Methods

For estimating the water budget components of the Amu Darya and the Kizilirmak River Basins, a comprehensive methodology combining remote sensing data, Earth system modeled datasets, and the processing capabilities of GIS was utilized. The study focused on hydrological years 2014, 2015, 2017, and 2018 covering from October to September.

### Study Area and Data Sources

The study was conducted on the Kizilirmak and the Amu Darya River Basins (Figure 1), representing smaller and larger river systems respectively, to assess water budget estimation using remote sensing data. The Amu Darya River, with a drainage area of approximately 500,000 km² and a length of about 2,500 km, is one of Central Asia's major rivers, flowing through multiple countries from the Pamir Mountains to the Aral Sea. It is crucial for water resources in a region characterized by an arid climate, experiencing hot summers and cold winters. The Kizilirmak River with a drainage area of 82197 km$^2$ and 1,355 km length, is Turkey's longest river, flowing entirely within the country from Central Anatolia to the Black Sea. It is critical for water resources in a region marked by a continental climate, experiencing hot, dry summers and cold, snowy winters.

The study integrated a suite of remote sensing and model outputs to estimate the water budget components, including Precipitation (P), Evapotranspiration (ET), Terrestrial Water Storage (TWS), and Runoff (R). The datasets employed were sourced from several well-recognized global data repositories:

**Precipitation:** Two satellite-based remote sensing products, GPM IMERG V6 and CHIRPS V2.0, along with model outputs from GLDAS-2.1 Noah and GLDAS-2.1 CLSM, provided comprehensive precipitation data.

**Evapotranspiration**: Remote sensing data were obtained from the MOD16A2 product, derived from the Terra MODIS satellite. This was complemented by ET data from the SSEBop model output and the GLDAS-2.1 Noah and CLSM models.

**Terrestrial Water Storage (TWS):** GRACE satellite data, alongside GLDAS-2.1 Noah and CLSM model simulations, were used to assess changes in terrestrial water storage.

**Runoff:** Runoff estimates were directly taken from the GLDAS-2.1 model outputs and compared against streamflow gauge data for validation.

### Methodological Framework

The methodology outlined combines advanced remote sensing data with sophisticated land surface modeling to provide a comprehensive assessment of the water budget in the two River Basins. The study's methodological approach involved several key steps, integrating GIS techniques for data processing and analysis:

**Basin and Stream Network Delineation:** Utilizing the Shuttle Radar Topography Mission (SRTM) Digital Elevation Model (DEM), the river basins and their stream networks were delineated to define the study area precisely.

**Data Processing and Analysis**: The hydrological datasets were processed within the ArcGIS environment. This included converting data units to mm/month using the Raster Calculator function and extracting monthly basin-averaged values with the Zonal Statistics tool.

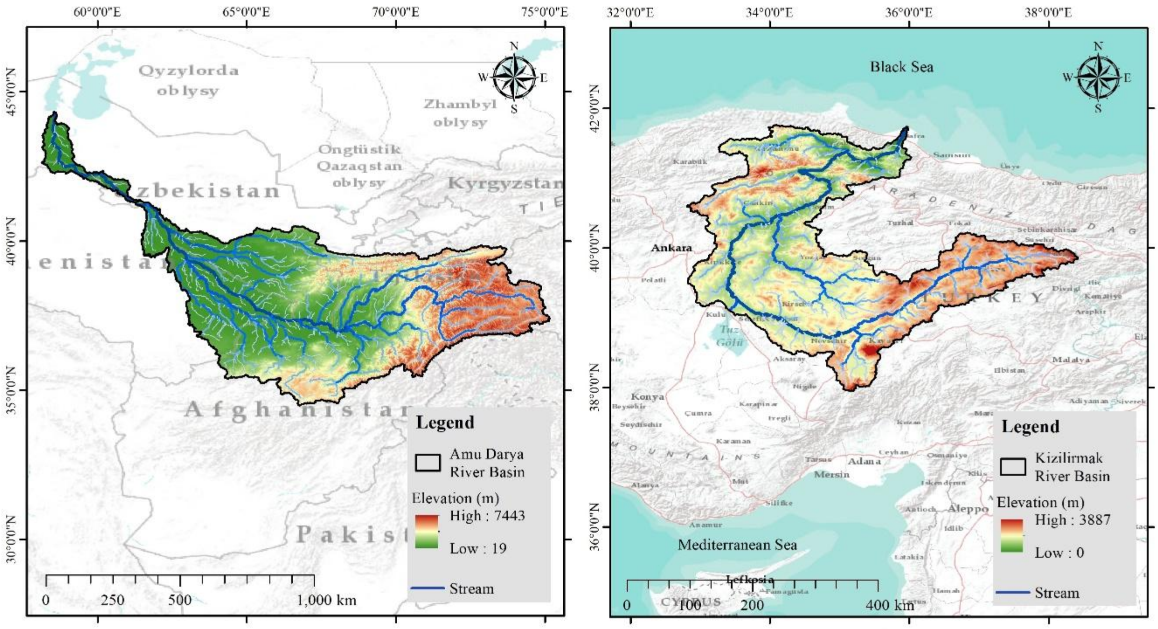

(a) (b)

**Figure 1.** Study area: (a) the Amu Darya River Basin; (b) the Kizilirmak River Basin

**Water Budget Estimation:** The core of the study's methodology was the estimation of the water budget based on the general water balance equation (Eq. 1):

$$\boldsymbol{P} = \boldsymbol{ET} + \mathbf{R} + \boldsymbol{\Delta S} \tag{1}$$

Here, $\boldsymbol{P}$ represents precipitation, $\boldsymbol{ET}$ stands for evapotranspiration, **R** denotes runoff, and $\boldsymbol{\Delta S}$ signifies the change in surface and subsurface water storage. It's important to note that water quantities used for irrigation or other domestic uses were not explicitly included due to the lack of a globally consistent method for their estimation.

**Runoff Estimation:** Since runoff cannot be directly observed from remote sensing data, it was inferred from the water balance equation as a residual. This indirect method was critical for evaluating the feasibility of assessing water budget closure from remote sensing data in ungauged rivers.

**Validation and Comparison:** The remotely sensed and modeled water budget components were compared against each other and available in-situ observations to validate the satellite-based estimates. This involved analyzing the correlation and consistency between different data sources and assessing the strengths and limitations of the methodologies employed.

## Results and Discussion

The study's comprehensive analysis of the Amu Darya and the Kizilirmak River Basins' water budget utilizing remote sensing products and GLDAS-2.1 models for 2014 and 2015 yielded insightful findings across various water budget components. Analysis of precipitation data from satellite observations (GPM IMERG, CHIRPS) and GLDAS-2.1 models (Noah, CLSM) revealed good agreement in estimated precipitation patterns across the basin. Satellite-based estimates generally showed lower precipitation rates compared to model outputs, with notable spatial inconsistencies. The study highlighted the strengths of satellite remote sensing in capturing precipitation dynamics, despite some discrepancies in spatial distribution.

Evapotranspiration estimates derived from remote sensing data (MOD16) and GLDAS-2.1 models demonstrated significant variability. The MOD16 product generally underestimated ET compared to the GLDAS models, which was attributed to differences in methodology and spatial resolution. Despite these disparities, the comparison underscored the potential of integrating satellite-based and modelled ET data for enhancing water budget analysis in large river basins.

Comparisons between terrestrial water storage change (TWSC) estimates from the GRACE satellite mission and GLDAS-2.1 models indicated inconsistencies, particularly due to the coarse resolution of GRACE data and its data gaps. Despite these challenges, the study found that GRACE TWSC data, when available, provides valuable insights into large-scale water storage changes, complementing the model-based estimates and highlighting the importance of continuous satellite observations for hydrological studies.

Runoff estimation proved challenging, primarily due to the lack of direct satellite observations for this component. The study inferred runoff from the water balance equation as a residual, finding significant differences between inferred and observed runoff data. Despite these discrepancies, the GLDAS-2.1 Noah model demonstrated a better correlation with in-situ streamflow measurements, suggesting its potential utility in runoff estimation for ungauged basins.

The study assessed using satellite data only to estimate water budget components. While satellite observations offer valuable spatial and temporal coverage, especially in data-sparse regions, the analysis revealed inherent limitations and uncertainties in satellite-derived estimates, particularly for ET and TWSC. The study emphasized the need for cautious interpretation of satellite-based water budget estimates and highlighted the complementary role of land surface models in addressing these challenges.

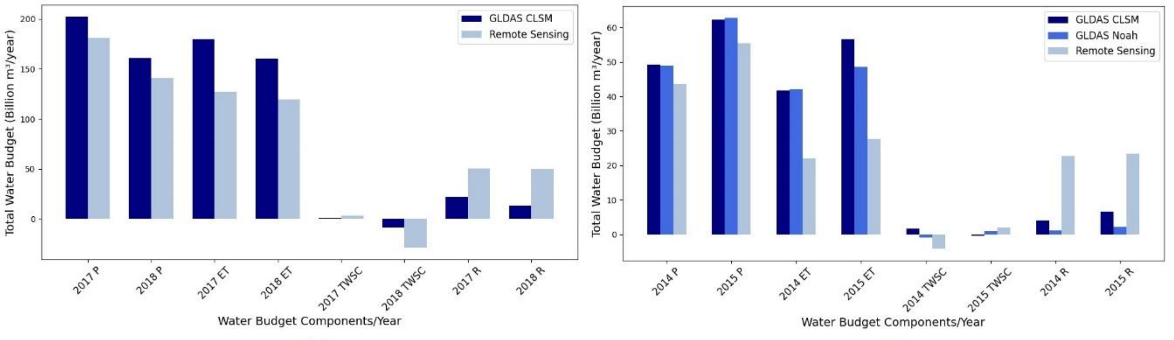

(a) (b)

**Figure 2.** Comparison of water budget components by source. (a) total annual water budget of the Amu Darya River Basin for the water years 2017 and 2018; (b) total annual water budget of the Kizilirmak River Basin for the water years 2014 and 2015

For the Amu Darya and the Kizilirmak River Basins analysis and assessment, the study quantified the annual variations in water balance components—P, ET, R, and TWSC (Figure 2). The analysis shows a 10-12% variation in annual precipitation and a 25-51% difference in evapotranspiration across the data sources for the four years. Additionally, significant uncertainties were identified in ET estimations in the Kizilirmak River Basin, with discrepancies between the SSEBop model, GLDAS CLSM, and MODIS ET ranging from 47-53%. A notable challenge was estimating TWSC due to the coarse resolution of GRACE data as well as data gap and data unavailability for some months. Runoff estimations presented considerable variability; however, the Noah model aligned more closely with in-situ streamflow data, despite a 58-60% difference in runoff estimations for the two study years.

This analysis of water budget components in the two river basins highlights the complexities and challenges in utilizing satellite remote sensing and modeling approaches for hydrological studies. The research highlighted the potential of integrating diverse data sources to enhance the understanding of hydrological processes and support water resources management. However, the study also pointed out significant uncertainties associated with satellite-based estimates, necessitating careful validation and integration with model-based approaches.

Our findings agree with multiple studies that have explored water budget closure through satellite remote sensing, often highlighting discrepancies when compared with in-situ or modeled data. Sheffield et al. (2009) observed significant runoff overestimation in their study due to precipitation bias, a finding echoed by Gao et al. (2010) with noted variations in ET and TWS. Such inconsistencies, particularly in runoff estimation, were further confirmed by subsequent studies (Lv et al., 2017; Oliveira et al., 2014; Penatti et al., 2015; Sahoo et al., 2011), underscoring the challenges in achieving water budget closure due to the overestimation of runoff and underestimation of ET. Despite these barriers, including spatial and temporal discrepancies and instrumental errors, satellite data's utility in hydrological modeling and basin management is undeniable.

## Conclusion

This study investigated the water balance within the Amu Darya and the Kizilirmak River Basins over four years using GIS analysis, satellite data (GPM IMERG, MODIS, GRACE), and GLDAS-2.1 model outputs. The findings stress the importance of advancing remote sensing technologies and methodologies to improve the accuracy and reliability of water budget estimations. Furthermore, the study advocates for continued efforts in developing and validating integrated hydrological models that can effectively incorporate satellite observations, thereby enhancing our ability to manage water resources sustainably in the face of changing climate conditions and increasing human demands. Our findings align with multiple studies that have explored water budget closure through satellite remote sensing, often highlighting discrepancies when compared with in-situ or modeled data. This research reveals the potential and constraints of utilizing satellite remote sensing and GLDAS models for water budget estimation. Despite the limitations such as spatial/temporal gaps and instrument errors, satellite data remains valuable for river basin management, especially in data-sparse regions.

## Acknowledgements

This study, which is part of an ongoing PhD thesis, was supported by Eskişehir Technical University Scientific Research Projects Commission under grant number: 24DRP012.

## References

Bai, P., Liu, X., Yang, T., Liang, K., & Liu, C. (2016). Evaluation of streamflow simulation results of land surface models in GLDAS on the Tibetan plateau. *Journal of Geophysical Research: Atmospheres*, *121*(20), 12,180-12,197. https://doi.org/10.1002/2016JD025501
Deliry, S. I., Pekkan, E., & Avdan, U. (2022). GIS-Based Water Budget Estimation of the Kizilirmak River Basin using GLDAS-2.1 Noah and CLSM Models and Remote Sensing Observations. *Journal of the Indian Society of Remote Sensing*, *50*(7), 1191–1209. https://doi.org/10.1007/s12524-022-01522-x

Deng, S., Liu, Y., & Zhang, W. (2023). A Comprehensive Evaluation of GRACE-Like Terrestrial Water Storage (TWS) Reconstruction Products at an Interannual Scale During 1981-2019. *Water Resources Research*, *59*(3), e2022WR034381. https://doi.org/10.1029/2022WR034381

Fisher, R. A., & Koven, C. D. (2020). Perspectives on the Future of Land Surface Models and the Challenges of Representing Complex Terrestrial Systems. *Journal of Advances in Modeling Earth Systems*, *12*(4), e2018MS001453. https://doi.org/10.1029/2018MS001453

Funk, C., Peterson, P., Landsfeld, M., Pedreros, D., Verdin, J., Shukla, S., Husak, G., Rowland, J., Harrison, L., Hoell, A., & Michaelsen, J. (2015). The climate hazards infrared precipitation with stations—A new environmental record for monitoring extremes. *Scientific Data*, *2*(1), Article 1. https://doi.org/10.1038/sdata.2015.66

Gao, H., Tang, Q., Ferguson, C. R., Wood, E. F., & Lettenmaier, D. P. (2010). Estimating the water budget of major US river basins via remote sensing. *International Journal of Remote Sensing*, *31*(14), 3955–3978.

Hosseini-Moghari, S.-M., & Tang, Q. (2020). Validation of GPM IMERG V05 and V06 Precipitation Products over Iran. *Journal of Hydrometeorology*, *21*(5), 1011–1037. https://doi.org/10.1175/JHM-D-19-0269.1

Hsu, J., Huang, W.-R., Liu, P.-Y., & Li, X. (2021). Validation of CHIRPS Precipitation Estimates over Taiwan at Multiple Timescales. *Remote Sensing*, *13*(2), Article 2. https://doi.org/10.3390/rs13020254

Kidd, C., Becker, A., Huffman, G. J., Muller, C. L., Joe, P., Skofronick-Jackson, G., & Kirschbaum, D. B. (2017). So, How Much of the Earth's Surface Is Covered by Rain Gauges? *Bulletin of the American Meteorological Society*, *98*(1), 69–78. https://doi.org/10.1175/BAMS-D-14-00283.1

Lakshmi, V., Fayne, J., & Bolten, J. (2018). A comparative study of available water in the major river basins of the world. *Journal of Hydrology*, *567*, 510–532.

Le, H. M., Sutton, J. R., Bui, D. D., Bolten, J. D., & Lakshmi, V. (2018). Comparison and Bias Correction of TMPA Precipitation Products over the Lower Part of Red–Thai Binh River Basin of Vietnam. *Remote Sensing*, *10*(10), 1582.

Long, D., Longuevergne, L., & Scanlon, B. R. (2015). Global analysis of approaches for deriving total water storage changes from GRACE satellites. *Water Resources Research*, *51*(4), 2574–2594. https://doi.org/10.1002/2014WR016853

Lv, M., Ma, Z., Yuan, X., Lv, M., Li, M., & Zheng, Z. (2017). Water budget closure based on GRACE measurements and reconstructed evapotranspiration using GLDAS and water use data for two large densely-populated mid-latitude basins. *Journal of Hydrology*, *547*, 585–599. https://doi.org/10.1016/j.jhydrol.2017.02.027

Moghim, S. (2018). Impact of climate variation on hydrometeorology in Iran. *Global and Planetary Change*, *170*, 93–105.

Mohammed, I. N., Bolten, J. D., Srinivasan, R., & Lakshmi, V. (2018). Satellite observations and modeling to understand the Lower Mekong River Basin streamflow variability. *Journal of Hydrology*, *564*, 559–573.

Oliveira, P. T. S., Nearing, M. A., Moran, M. S., Goodrich, D. C., Wendland, E., & Gupta, H. V. (2014). Trends in water balance components across the Brazilian Cerrado. *Water Resources Research*, *50*(9), 7100–7114. https://doi.org/10.1002/2013WR015202

Penatti, N. C., Almeida, T. I. R. de, Ferreira, L. G., Arantes, A. E., & Coe, M. T. (2015). Satellite-based hydrological dynamics of the world's largest continuous wetland. *Remote Sensing of Environment*, *170*, 1–13. https://doi.org/10.1016/j.rse.2015.08.031

Rodell, M., Houser, P. R., Jambor, U. E. A., Gottschalck, J., Mitchell, K., Meng, C.-J., Arsenault, K., Cosgrove, B., Radakovich, J., & Bosilovich, M. (2004). The global land data assimilation system. *Bulletin of the American Meteorological Society*, *85*(3), 381–394.

Rui, H., Beaudoing, H., & Loeser, C. (2020). README document for NASA GLDAS version 2 data products. *Goddart Earth Sciences Data and Information Services Center (GES DISC): Greenbelt, MD, USA*.

Sahoo, A. K., Pan, M., Troy, T. J., Vinukollu, R. K., Sheffield, J., & Wood, E. F. (2011). Reconciling the global terrestrial water budget using satellite remote sensing. *Remote Sensing of Environment*, *115*(8), 1850–1865. https://doi.org/10.1016/j.rse.2011.03.009

Sheffield, J., Ferguson, C. R., Troy, T. J., Wood, E. F., & McCabe, M. F. (2009). Closing the terrestrial water budget from satellite remote sensing. *Geophysical Research Letters*, *36*(7). https://doi.org/10.1029/2009GL037338

Shen, Z., Yong, B., Gourley, J. J., Qi, W., Lu, D., Liu, J., Ren, L., Hong, Y., & Zhang, J. (2020). Recent global performance of the Climate Hazards group Infrared Precipitation (CHIRP) with Stations (CHIRPS). *Journal of Hydrology*, *591*, 125284. https://doi.org/10.1016/j.jhydrol.2020.125284

Tang, G., Zeng, Z., Long, D., Guo, X., Yong, B., Zhang, W., & Hong, Y. (2016). Statistical and Hydrological Comparisons between TRMM and GPM Level-3 Products over a Midlatitude Basin: Is Day-1 IMERG a Good Successor for TMPA 3B42V7? *Journal of Hydrometeorology*, *17*(1), 121–137. https://doi.org/10.1175/JHM-D-15-0059.1

Zheng, Z., Ning, L., Dai, D., Chen, L., Wang, Y., Ma, Z., Yang, Z.-L., & Zhan, C. (2022). Water budget variation, groundwater depletion, and water resource vulnerability in the Haihe River Basin during the new millennium. *Physics and Chemistry of the Earth*, *126*, 103141. https://doi.org/10.1016/j.pce.2022.103141

INTERNATIONAL SYMPOSIUM ON
APPLIED
GEOINFORMATICS
9-10 May 2024 · Wrocław/Poland

*International Symposium on Applied Geoinformatics (ISAG2024)*

# Advances in Engineering Surveying: A Comprehensive Accuracy Assessment of UAS Photogrammetry and Structure from Motion

Deliry Sayed Ishaq[1,*], Avdan Uğur[2]

[1] Eskisehir Technical University, Department of Remote Sensing and Geographical Information Systems, Eskişehir, Türkiye; deliry.ishaq@gmail.com; ORCID 0000-0002-5467-1403
[2] Eskisehir Technical University, Institute of Earth and Space Sciences, Eskişehir, Türkiye; uavdan@eskisehir.edu.tr; ORCID 0000-0001-7873-9874
* Corresponding Author

## Abstract

The increasing interest in accurate and cost-efficient topographic mapping has highlighted the significance of advancements in surveying engineering, especially with the use of Unmanned Aerial Systems (UAS) and the integration of Structure from Motion (SfM) with Multi-View Stereo (MVS) photogrammetry. This research aimed to assess the accuracy of UAS-SfM as a quick and low-cost alternative to traditional surveying methods within the context of engineering surveying. Conducting two flights at altitudes of 100 and 170 meters Above Ground Level (AGL) for nadir imagery, and a third at 16 meters AGL for oblique imagery, using both fixed-wing and rotary-wing UAS equipped with non-metric cameras, this study focused on validating the UAS-SfM products against field measurements taken with Real-Time Kinematic Global Navigation Satellite System (RTK GNSS), terrestrial laser scanner, and total station. Processing of the collected images through three SfM software packages led to the creation of 16 photogrammetric projects, generating point clouds, 3D triangulated models, Digital Surface Models (DSMs), Digital Terrain Models (DTMs), and orthomosaics. These projects were processed with various ground control point configurations, and detailed statistical analysis was conducted on the results. The spatial resolution of orthomosaics and DSMs obtained from 16, 100, and 170 m AGL flights was 0.005, 0.025, and 0.04 m, respectively, with the highest accuracy achieved from the 16 m AGL oblique images. The analysis demonstrated notable correlations between flight height, GCP configurations, and processing software, impacting the geometric accuracy of UAS-SfM-derived products. Confirming UAS-SfM's viability as a cost-effective substitute for traditional engineering surveying tasks, the study highlights its competency in delivering precise 3D models and volumetric calculations. This study reveals the potential of UAS-SfM in providing high-resolution, accurate topographic maps for terrain analysis in civil engineering and other related projects, marking a significant step forward in the domain of engineering surveying.

***Keywords:*** *Engineering Surveying, 3D Modeling, Structure from Motion, Terrestrial Laser Scanning, UAS Photogrammetry*

## Introduction

The quest for accurate and cost-efficient topographic mapping continues to drive advancements in surveying engineering. This highlights the crucial role of evolving technology, especially the integration of Unmanned Aerial Systems (UAS) with Structure from Motion (SfM) and Multi-View Stereo (MVS) photogrammetry techniques. This integration signifies a paradigm shift towards more dynamic, efficient, and cost-effective surveying methodologies, diverging from conventional techniques that, despite their accuracy, often come with high costs and significant time requirements for large-scale applications (Agüera-Vega et al., 2018; Greenwood et al., 2019; Nex & Remondino, 2014).

The advent of UAS for image acquisition, coupled with advancements in automated computer vision algorithms, heralds a new era in photogrammetric surveying. This combination not only facilitates access to high-resolution spatial data but also enhances flexibility in data collection by facilitating image acquisition from diverse orientations and altitudes, hence broadening the scope of engineering applications (Agüera-Vega et al., 2016; Carrivick et al., 2016; Martínez-Carricondo et al., 2018). Structure from motion, a refined photogrammetric approach, blends developments in computer vision with traditional methods. It employs sequences of 2D images from a moving sensor to extract features and create detailed 3D models (Carrivick et al., 2016; Deliry & Avdan, 2021; Snavely et al., 2008). Such capabilities are indispensable in terrain analysis, infrastructure development, environmental monitoring, and a myriad of other engineering tasks that require detailed spatial information.

Recent literature underscores the expanding utility of UAS and SfM in a wide range of engineering and geospatial applications, emphasizing their potential to revolutionize traditional surveying practices. Studies by Colomina and Molina (2014) and Gonçalves and Henriques (2015) elucidate the versatility and efficiency of UAS photogrammetry in capturing high-resolution spatial data across varied terrains and environments. Similarly, studies by Deliry and Avdan (2020; 2021, 2023), Hastaoglu et al. (2023), and Sanz-Ablanedo et al. (2018) demonstrate the enhanced data acquisition capabilities facilitated by SfM, particularly in terms of automation, flexibility, and cost-effectiveness.

This study builds upon the existing body of knowledge by conducting an in-depth examination of UAS-SfM's accuracy, employing experimental flights at varying altitudes—100 and 170 m Above Ground Level (AGL) for nadir imagery and 16 m AGL for oblique imagery—using both fixed-wing and rotary-wing UAS equipped with non-metric cameras. The rigorous accuracy assessment process involved comparing UAS-SfM products against field measurements obtained through Real-Time Kinematic Global Navigation Satellite System (RTK GNSS), terrestrial laser scanning, and total stations, thereby ensuring the reliability of the photogrammetric data generated. The analysis of various ground control point (GCP) configurations across 16 photogrammetric projects serves to underscore the impact of GCP distribution on the geometric accuracy of the derived products, highlighting the importance of strategic GCP planning and implementation. This aspect of the study draws attention to the relationship between flight altitude, GCP configurations, and processing software in determining the geometric accuracy of UAS-SfM-derived products. This paper contributes to the ongoing discourse on the evolution of geospatial data acquisition and analysis, paving the way for future research and applications in the engineering domain.

## Materials and Methods

This section outlines the comprehensive methodology adopted to assess the accuracy and applicability of UAS-SfM in engineering surveying. The study was meticulously designed to evaluate UAS-SfM's capabilities as a viable alternative for traditional surveying methods, emphasizing detailed topographic mapping and volumetric calculations.

### Study Area and Equipment

The primary study area encompassed the Eskisehir Technical University campus in Türkiye, selected for its diverse topography and mix of urban and natural landscapes. This variety provided an ideal setting for assessing UAS-SfM's performance across different terrain types. For aerial surveys, both fixed-wing and multirotor UAS were employed, equipped with non-metric cameras to capture high-resolution imagery. Specifically, the fixed-wing UAS (SenseFly eBee Plus) and the multirotor UAS (DJI Phantom 4 Pro) were chosen for their reliability and widespread use in photogrammetric projects. These UAS surveys were complemented by ground-based equipment, including RTK GNSS for GCP measurement, a terrestrial laser scanner (TLS) for high-accuracy 3D model generation, and a total station for precise distance and angle measurements and accuracy assessments.

### Data Acquisition and Processing

Data acquisition involved conducting flights at altitudes of 100 and 170 m AGL for nadir imagery and 16 m AGL for oblique imagery. These altitudes were selected to investigate the impact of flight height on image resolution and photogrammetric product accuracy. The GCPs were strategically placed and measured across the campus to ensure robust georeferencing and to assess the influence of GCP configurations on the geometric accuracy of the photogrammetric outputs. A total of 200 control points (CPs), located within and outside of GCP polygons were surveyed using Differential GNSS.

The collected images were processed using three leading SfM software packages: Agisoft PhotoScan, Pix4Dmapper, and 3Dsurvey. This approach allowed for a comparative analysis of the software in terms of processing capabilities, ease of use, and the accuracy of the generated photogrammetric products. Each software package was evaluated for its ability to generate point clouds, 3D triangulated models, Digital Surface Models (DSMs), Digital Terrain Models (DTMs), and orthomosaics.

### Accuracy Assessment and Statistical Analysis

Accuracy assessment constituted a critical component of the methodology, involving a comparison of UAS-SfM products against field measurements acquired through RTK GNSS, TLS, and total station data. This comparison enabled a quantitative evaluation of the absolute and relative accuracies of the photogrammetric products. Statistical analyses were performed to identify significant correlations between flight height, GCP configurations, and the choice of processing software on the geometric accuracy of the derived products. The statistical approach adopted in this study aimed to provide a robust framework for understanding the key factors influencing the accuracy and reliability of UAS-SfM in engineering surveying applications. Key to this assessment was the application of the Root Mean Square Error (RMSE) and standards set by the American Society for Photogrammetry and Remote Sensing (ASPRS) to evaluate horizontal and vertical accuracy (2014; Whitehead & Hugenholtz, 2015).

## Results and Discussion

This study rigorously evaluated the accuracy of UAS-SfM across various projects, employing a comprehensive methodology that integrated detailed field measurements, advanced processing techniques, and rigorous statistical analyses. The findings underscore the potential of UAS-SfM as a viable tool for engineering surveying, delivering high-resolution, accurate topographic maps and 3D models.

## Horizontal and Vertical Accuracy

The study meticulously analyzed the horizontal and vertical accuracies ($RMSE_{XY}$ and $RMSE_{Z}$) across varying flight heights—16, 100, and 170 m AGL. The spatial resolutions obtained were 0.005 m for 16 m AGL, 0.025 m for 100 m AGL, and 0.04 m for 170 m AGL flights, respectively. Pairwise elevation correlation matrices for projects at 100 m and 170 m AGL processed with 5 GCPs and 10 GCPs are given in Figure 1. $RMSE_{Z}$ for the 170 m flight height processed with Agisoft, Pix4Dmapper, and 3Dsurvey with 5 GCPs were 0.076 m, 0.103 m, and 0.133 m, respectively. $RMSE_{Z}$ for the same project processed with 10 GCPs were 0.059 m, 0.071 m, and 0.084 m, respectively. Vertical error for the DSMs derived from oblique images obtained at 16 m height processed with Agisoft, Pix4D, and 3Dsurvey were 0.019 m, 0.044 m, and 0.052 m, respectively. $RMSE_{XY}$ for both projects were approximately 0.03 m for Agisoft and Pix4Dmapper and 0.06 m for 3Dsurvey. The accuracy assessment revealed significant findings regarding the horizontal and vertical accuracy of UAS-SfM-derived products. Across the projects, RMSE values varied depending on flight height, GCP configurations, and the SfM processing software used. The lowest $RMSE_{XY}$ and $RMSE_{Z}$ were achieved from the projects utilizing oblique imagery at 16 m AGL, highlighting the benefits of lower flight altitudes for enhanced precision.

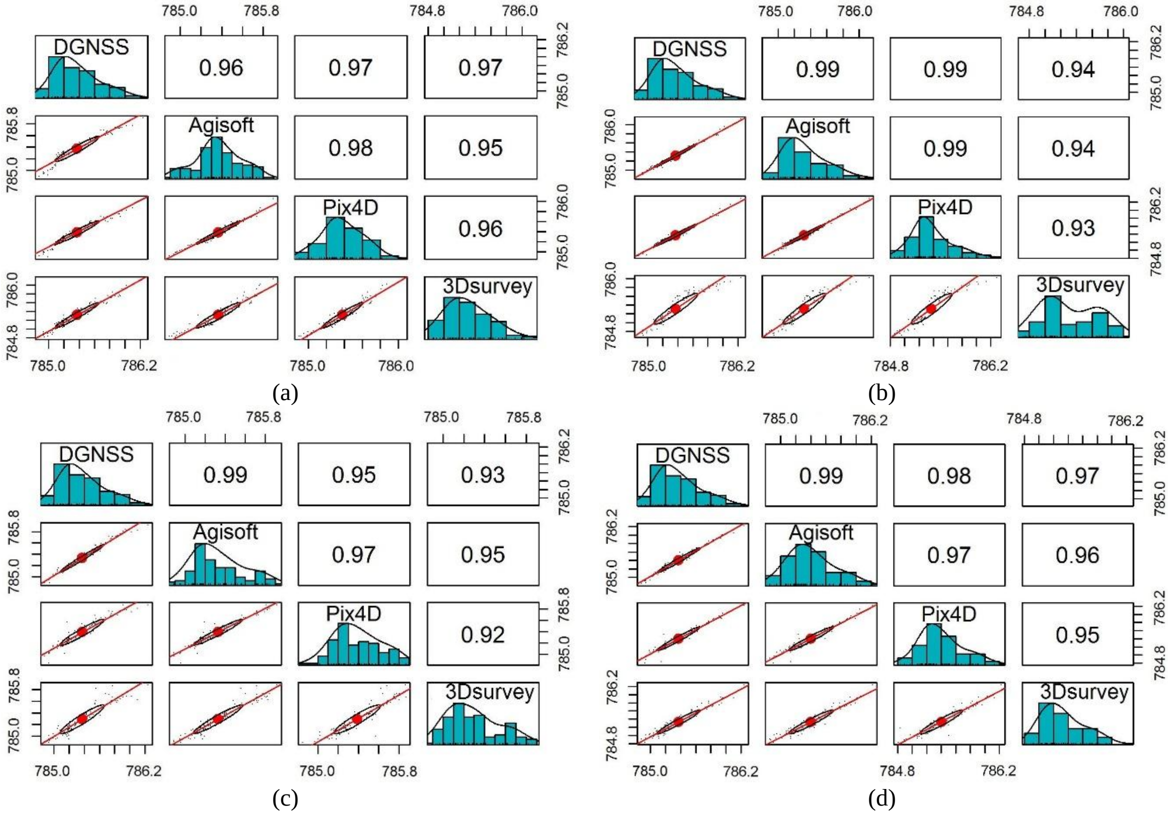

(a) (b)

(c) (d)

**Figure 3.** Correlation scatter plot matrix of DGNSS non-vegetated elevations and UAS-SfM DSM. (a) elevations derived from 100 m AGL nadir images, processed with 5 GCPs. (b) elevations derived from 100 m AGL nadir images, processed with 10 GCPs. (c) elevations derived from 170 m AGL nadir images, processed with 5 GCPs. (d) elevations derived from 170 m AGL nadir images, processed with 10 GCPs.

The impact of various GCP configurations on accuracy was also examined in this study. Projects with optimized GCP layouts demonstrated superior geometric accuracy, highlighting GCPs' critical role in maximizing the potential of UAS-SfM methodologies. Projects incorporating dense GCP layouts particularly benefited in terms of reduced RMSE values, thereby enhancing the overall quality of the photogrammetric outputs. In alignment with the ASPRS positional accuracy standards, the study's results demonstrated that the majority of UAS-SfM products met or exceeded the thresholds for Class 1 or Class 2 accuracy for 1:1,000 mapping scale. This achievement underscores the reliability of UAS-SfM techniques in producing spatial data with sufficient accuracy for a wide range of engineering applications.

In order to check the accuracy of the project combined from different flight heights, a merge process was performed by combining images of both flights. Merged blocks of 100 m and 170 m AGL nadir images were processed using Agisoft PhotoScan with 5 GCPs which resulted in RMSE of 0.051 m and correlation of $R^2$=0.98.

### Volumetric Accuracy

Volumetric accuracy assessment further validated the efficacy of UAS-SfM in engineering surveying, particularly in tasks requiring precise volume calculations such as stockpile assessments, excavation volume estimations, and construction project monitoring. In comparison to TLS models, as result of the survey of a building from 16 m height with a rotary-wing UAS, when processed with Agisoft (using 4 GCPs), the maximum differences in dimensions were at the level of 0.01 m, and 0.66 $m^3$ in volume. Similarly, the results of Pix4Dmapper showed little differences, with maximum dimension and volume differences of about 0.03 m and 1.09 $m^3$, respectively. In contrast, the results from 3Dsurvey exhibited considerable differences, in which the maximum difference in dimensions was approximately 0.06 m and the volumetric difference was 46.32 $m^3$. These volumetric differences ranged from 4-10 m when the building was surveyed by a fixed-wing UAS from 100 and 170 m heights.

### Discussion

The findings from this study affirm the utility of UAS-SfM as a robust tool for engineering surveying, capable of achieving high levels of accuracy in both planimetric and volumetric assessments. The variability in RMSE across different flight heights and GCP configurations emphasizes the importance of meticulous planning and execution of UAS photogrammetric surveys to optimize accuracy. Furthermore, the choice of SfM processing software plays a significant role in determining the quality and precision of the final products, suggesting that practitioners should carefully consider their software options based on the specific requirements of their projects. Moreover, this study's alignment with ASPRS accuracy standards for various applications further validates UAS-SfM as a dependable method within engineering surveying, offering comparable, if not superior, results to traditional surveying techniques. The consistency in high-quality outputs across different projects and conditions reported herein mirrors the positive outcomes documented in broader literature, underscoring UAS-SfM's potential to revolutionize surveying practices. Furthermore, the study revealed that combining nadir images from different flight heights could reduce outlier values and improve vertical accuracy, suggesting a double block image acquisition strategy for complex 3D modeling tasks. The comparison between UAS-based photogrammetry and TLS showed comparable precision in 3D modeling, with the integration of TLS and UAS-SfM presenting a comprehensive approach for capturing detailed object models.The comparison between UAS-SfM-derived volumetric measurements and those obtained from traditional surveying methods (TLS) indicated a high degree of congruence, with discrepancies well within acceptable limits for engineering purposes. This highlights UAS-SfM's capability to provide rapid, cost-effective, and accurate volumetric analyses, essential for efficient project management and decision-making in engineering contexts.

The results from this research contribute to the growing body of evidence supporting the adoption of UAS-SfM technologies. The accuracies attained in this study, when compared with findings from other research in the literature, affirm UAS-SfM's competencies in achieving high precision. The spatial resolutions and RMSE metrics observed at different flight heights and GCP configurations agree with the emerging consensus within the scholarly community about UAS-SfM's reliability and efficacy. Previous studies (Agüera-Vega et al., 2016; Gerke & Przybilla, 2016; Gindraux et al., 2017; Maraş & Nasery, 2023; Martínez-Carricondo et al., 2018) highlight similar trends in accuracy improvements with adjusted flight parameters and GCP configurations, reinforcing the findings of this research. In conclusion, the advancements in UAS photogrammetry and SfM offer promising opportunities for enhancing the efficiency and accuracy of engineering surveying tasks. As technology continues to evolve, further research and methodological refinements are expected to broaden the applicability of these tools, driving innovations in surveying practices and outcomes.

### Conclusion

This study thoroughly assessed the accuracy of UAS photogrammetry and structure from motion, highlighting its potential as a cost-effective alternative to traditional terrestrial surveying methods in engineering surveying. The research underscored the importance of flight height, GCP configurations, and the selection of processing software on the accuracy of UAS-SfM products. Key findings demonstrate that the best horizontal and vertical accuracies were achieved with images taken from 100 m AGL, resulting in a horizontal RMSE of 3 cm for orthomosaics and a vertical RMSE of 4 cm for DSMs. Additionally, the study confirmed the crucial role of GCP configuration in improving both horizontal and vertical accuracies. Notably, a well-planned GCP layout, even with a minimal number of GCPs, significantly enhances model precision, indicating that "more" does not always mean "better" in terms of GCP quantity. The research also highlighted the impact of processing software on the accuracy of SfM-MVS products, with PhotoScan generally outperforming other software in terms of accuracy and quality. Volumetric calculations reinforced UAS-SfM's effectiveness, particularly when precise GCPs and optimized flight parameters are employed. The accuracies obtained from various flight heights met the ASPRS positional accuracy standards, affirming UAS-SfM's viability for terrain analysis and civil engineering projects. Specifically, the accuracy of orthomosaics and DSMs derived from flights with a spatial resolution of 0.005 m to 0.025 m is sufficient for most applications requiring detailed topographic information.

### Acknowledgements

This paper was extracted from an MSc thesis entitled "Accuracy Analysis and Evaluation of UAS Photogrammetry and Structure from Motion in Engineering Surveying."

**Appendix A.** Study area (a) and instruments used in the study (b), including fixed-wing and rotary-wing UASs, DGNSS, TLS, and total station.

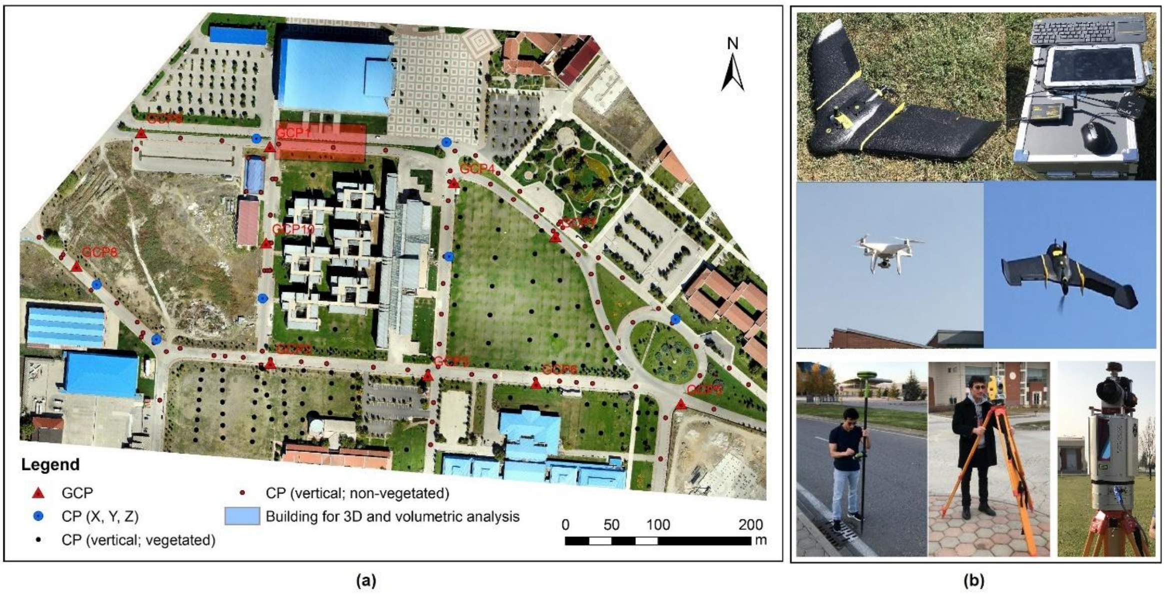

(a) (b)

## References

Agüera-Vega, F., Carvajal-Ramírez, F., & Martínez-Carricondo, P. (2016). Accuracy of digital surface models and orthophotos derived from unmanned aerial vehicle photogrammetry. *Journal of Surveying Engineering*, *143*(2), 04016025. https://doi.org/10.1061/(ASCE)SU.1943-5428.0000206

Agüera-Vega, F., Carvajal-Ramírez, F., Martínez-Carricondo, P., López, J. S.-H., Mesas-Carrascosa, F. J., García-Ferrer, A., & Pérez-Porras, F. J. (2018). Reconstruction of extreme topography from UAV structure from motion photogrammetry. *Measurement*, *121*, 127–138. https://doi.org/10.1016/j.measurement.2018.02.062

American Society for Photogrammetry and Remote Sensing. (2014). *ASPRS Positional Accuracy Standards for Digital Geospatial Data*. https://doi.org/10.14358/PERS.81.3.A1-A26

Carrivick, J. L., Smith, M. W., & Quincey, D. J. (2016). *Structure from Motion in the Geosciences*. John Wiley & Sons. https://doi.org/10.1002/9781118895818

Colomina, I., & Molina, P. (2014). Unmanned aerial systems for photogrammetry and remote sensing: A review. *ISPRS Journal of Photogrammetry and Remote Sensing*, *92*, 79–97. https://doi.org/10.1016/j.isprsjprs.2014.02.013

Deliry, S. I. (2020). *Accuracy Analysis and Evaluation of UAS Photogrammetry and Structure from Motion in Engineering Surveying* [Master's thesis, Anadolu University].

Deliry, S. I., & Avdan, U. (2021). Accuracy of Unmanned Aerial Systems Photogrammetry and Structure from Motion in Surveying and Mapping: A Review. *Journal of the Indian Society of Remote Sensing*, *49*, 1997–2017. https://doi.org/10.1007/s12524-021-01366-x

Deliry, S. I., & Avdan, U. (2023). Accuracy evaluation of UAS photogrammetry and structure from motion in 3D modeling and volumetric calculations. *Journal of Applied Remote Sensing*, *17*(2), 024515. https://doi.org/10.1117/1.JRS.17.024515

Gerke, M., & Przybilla, H.-J. (2016). Accuracy analysis of photogrammetric UAV image blocks: Influence of onboard RTK-GNSS and cross flight patterns. *Photogrammetrie-Fernerkundung-Geoinformation*, *2016*(1), 17–30. https://doi.org/10.1127/pfg/2016/0284

Gindraux, S., Boesch, R., & Farinotti, D. (2017). Accuracy assessment of digital surface models from unmanned aerial vehicles' imagery on glaciers. *Remote Sensing*, *9*(2), 186. https://doi.org/10.3390/rs9020186

Gonçalves, J. A., & Henriques, R. (2015). UAV photogrammetry for topographic monitoring of coastal areas. *ISPRS Journal of Photogrammetry and Remote Sensing*, *104*, 101–111.

Greenwood, W. W., Lynch, J. P., & Zekkos, D. (2019). Applications of UAVs in Civil Infrastructure. *Journal of Infrastructure Systems*, *25*(2), 04019002. https://doi.org/10.1061/(asce)is.1943-555x.0000464

Hastaoglu, K. O., Kapicioglu, H. S., Gül, Y., & Poyraz, F. (2023). Investigation of the effect of height difference and geometry of GCP on position accuracy of point cloud in UAV photogrammetry. *Survey Review*, *55*(391), 325–337. https://doi.org/10.1080/00396265.2022.2097998

Maraş, E. E., & Nasery, N. (2023). Investigating the length, area and volume measurement accuracy of UAV-Based oblique photogrammetry models produced with and without ground control points. *International Journal of Engineering and Geosciences*, *8*(1), Article 1. https://doi.org/10.26833/ijeg.1017176

Martínez-Carricondo, P., Agüera-Vega, F., Carvajal-Ramírez, F., Mesas-Carrascosa, F.-J., García-Ferrer, A., & Pérez-Porras, F.-J. (2018). Assessment of UAV-photogrammetric mapping accuracy based on variation of ground control points. *International Journal of Applied Earth Observation and Geoinformation*, *72*, 1–10. https://doi.org/10.1016/j.jag.2018.05.015

Nex, F., & Remondino, F. (2014). UAV for 3D mapping applications: A review. *Applied Geomatics*, *6*(1), 1–15. https://doi.org/10.1007/s12518-013-0120-x

Sanz-Ablanedo, E., Chandler, J., Rodríguez-Pérez, J., & Ordóñez, C. (2018). Accuracy of unmanned aerial vehicle (UAV) and SfM photogrammetry survey as a function of the number and location of ground control points used. *Remote Sensing*, *10*(10), 1606. https://doi.org/10.3390/rs10101606

Snavely, N., Seitz, S. M., & Szeliski, R. (2008). Modeling the world from internet photo collections. *International Journal of Computer Vision*, *80*(2), 189–210. https://doi.org/10.1007/s11263-007-0107-3

Whitehead, K., & Hugenholtz, C. H. (2015). Applying ASPRS accuracy standards to surveys from small unmanned aircraft systems (UAS). *Photogrammetric Engineering & Remote Sensing*, *81*(10), 787–793.

INTERNATIONAL SYMPOSIUM ON
APPLIED
GEOINFORMATICS
9-10 May 2024 · Wrocław/Poland

*International Symposium on Applied Geoinformatics (ISAG2024)*

# Geometric Analysis of Worldview-2 Geo-Referenced Image Containing Mostly Sea

Gurcan Buyuksalih[1]*, Cem Gazioglu[1], Karsten Jacobsen[2]

[1] Istanbul University, Institute of Marine Science and Management, Istanbul, Türkiye; (gurcanb/cemga)@istanbul.edu.tr; ORCID 0000-0002-7127-4602, ORCID 0000-0002-2083-4008
[2] Leibniz University, Institute of Photogrammetry and Geoinformation, Hannover, Germany; jacobsen@ipi.uni-hannover.de; ORCID 0000-0002-0462-0480

* Corresponding Author

## Abstract

A WorldView-2 (WV2) GeoTIFF image was ordered for the bathymetry work around the Tavsan Island which is the smallest island of Istanbul (previously known as Prince Islands) located in the Sea of Marmara, southeast of Istanbul city. The WV-2 image itself includes just a very small part of the land, but some islands. The geometric definition of the GeoTIFF image was not clear, and therefore needed to be investigated. The image was provided along with Rational Polynomial Coefficients (RPC). For the orientation the RPC-solution, 3D-affine transformation and the direct GeoTIFF with Ground Control Points (GCP) from Google Earth were analyzed. We realized that the correct handling requires orientation through 3D-affine transformation. The image geometry is the base of the following marine application. Bathymetric information can be based on stereo image combination, gray values of the water surface and wave structures.

**Keywords:** Marine Environment, WorldView-2, satellite orientation, GeoTIFF geometry

## Introduction/Background

For marine application, a geolocation accuracy corresponding to topographic maps, of about 2m is required. Based on own experience in other areas, the relative accuracy of Google Earth is in the range between 1.5 m and 2 m in an area with a size covering the entire WV-2 scene, so points which could be clearly identified in Google Earth had been used as ground control points (GCP) . Due to the lack of geometric details of the GeoTIFF images, the 3 orientation methods mentioned above had to be tested.

Bathymetric information from a single WV-2 image is contained in the grey values of the image used and the wave structure, indicating under water objects as well the depth situation of shallow water. A stereo measurement of shallow water requires visibility through the water body as well as a satellite stereo pair.

## Image Geometry

The semantic information of the images must be geo-referenced for use in a GIS-system. This requires knowledge of the image geometry and image orientation. We expect a geo-referenced satellite image to have the geometry of an ortho-image, but the discrepancies at the GCP show that this is not the case (Figure 1, left). The image was captured with an azimuth of 320° and an incidence angle of 38°. The viewing direction is shown in Figure 1, left.

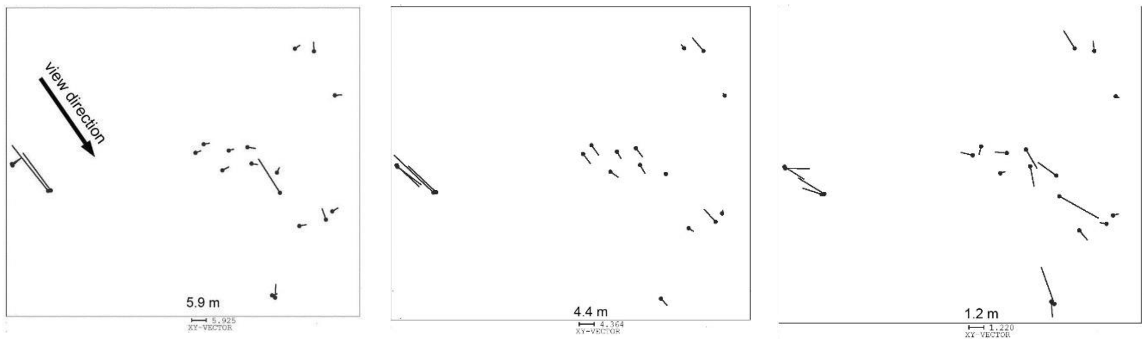

Direct GeoTIFF Bias corrected RPC 3D-affine transformation

**Figure 1.** Differences in GCP depending on method of image orientation (note the different vector scales)

**Table 1.** Results of image orientation

| line | | SX | SY | Number GCP |
|---|---|---|---|---|
| 1 | Direct use of GeoTIFF including elevated points | 5.11 m | 6.64 m | 20 |
| 2 | Direct use of GeoTIFF only 17 GCP with similar ground height | 2.32 m | 2.27 m | 17 |
| 3 | RPC all GCP including elevated points | 4.86 m | 6.64 m | 20 |
| 4 | RPC only 17 GCP with similar ground height | 1.09 m | 1.59 m | 17 |
| 5 | 3D-affine transformation with all GCP | 1.30 m | 1.23 m | 20 |

The GCP have an elevation of 0 m up to 2 m, except for 3 points with a height of 24 m to 31 m and one point with 6 m elevation. In the direct GeoTIFF geometry (Figure 1, left), the 3 more elevated points with large vectors opposite the direction of view can be seen, also the point with 6 m height can be identified (lower right side of the scene). This clearly shows that the image just is projected at sea level height. This geometry also cannot be handled with bias corrected Rational Polynomial Projection (RPC) (Jacobsen et al. 2005), as shown in the center image of Figure 1. The RPC solution is not the correct mathematical model. This is different with 3D-affine transformation, it corrects the influence of the object elevation caused by the tilted viewing direction, regardless of the general geometry of the horizontal coordinates. The standard deviation of X and Y of 1.30 m and 1.23 m confirms the correct geometry (Figure 1 right). Better results cannot be expected by GCP from Google Earth. Table 1 shows the numerical results and line 2 and line 4 demonstrate the influence of GCP height at limited height differences.

An ortho-image is required for subsequent GIS data acquisition. Since we did not have any software for ortho-image generation based on 3D-affine transformation, the program AFF3DORTHO had to be developed. We used the DLR's TanDEMX 30m Edited DEM of the DLR (TDM1-EDEM) as digital elevation model. This Digital Surface Model (DSM) is free available with a point spacing of 1 arcsec (~ 30m). In a flat test area in the USA compared to the LiDAR reference Digital Elevation Model (DEM), TDM1-EDEM has a standard deviation of height of 1.15 m and an NMAD of 0.82 m, and in the open area according to the provided land cover map a standard deviation of 1.05 m and an NMAD of 0.75 m. In other test areas used, TDM1-EDEM is also more accurate than the other height models available worldwide, e.g. GDEM3, SRTM, AW3D30 and TDM90. At an angle of incidence of 38°, the corresponding influence on the horizontal location is affected with 78% of the vertical accuracy. This is completely satisfactory for the marine application.

### Bathymetric Image Information

The Institute for Photogrammetry and Geo-information at the Leibniz University Hannover has conducted an internal study on geo-information in shallow water from aerial and satellite imagery (Jacobsen 2005, 72 pages). In this study, the different methods of water depth information from images were analyzed and described.

The classic photogrammetric method is the stereo measurement of water depth. Like the grey value dependence on the water depth, it depends on the transparency of the water. This is described by the Secchi depth - the depth of water to which a black and white disc can be seen from the surface of the water. The transparency of water can vary greatly depending on the turbidity material in the water. The turbidity material may be sediments from flowing water and/or algae influenced by nutrient content. Sun reflection on the water surface can impair the visibility into the water. Therefore, images should not be directed towards the sun. Reflection is strongly influenced by water waves, which can limit the view into the water.

The transparency of water depends on the wavelength used. Distilled or very clear water can best be penetrated by short-wave light (blue range). The greater the suspended matter content, the more the optimal wavelength shifts towards the green range. The Sea of Marmara is known for its high concentration of algae, so the green channel should be preferred.

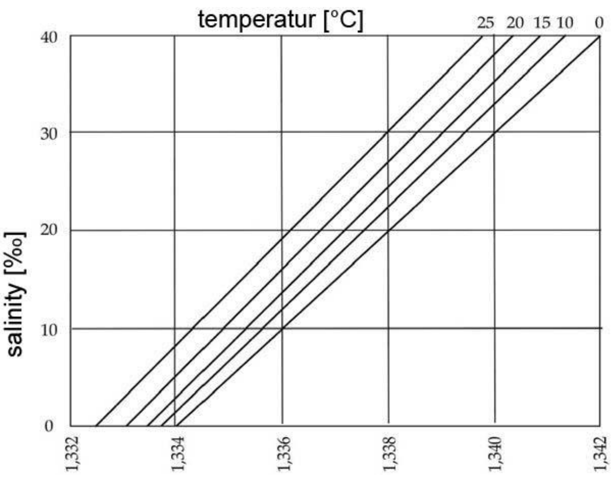

**Figure 2.** refraction index of water

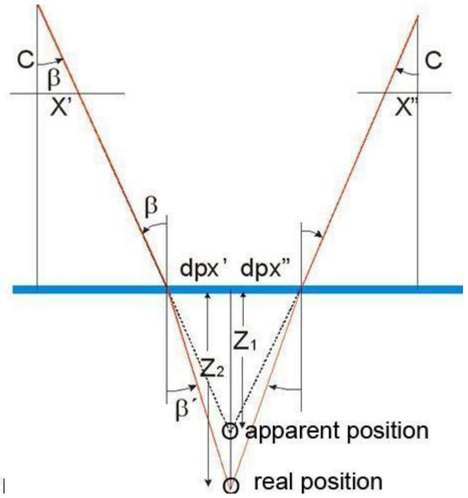

**Figure 3.** Influence of refraction to water depth

In general, the refraction index of water must be taken into account (Figure 2). Simplified, the refraction index is close to a scaling factor for the determined water depth (Figure 3). In a test area of the Baltic Sea near the Kiel harbor, a depth map of up to 5m water depth could be created, while in the Bizerte harbor a depth of only 2.7m was achieved with an IKONOS stereo pair.

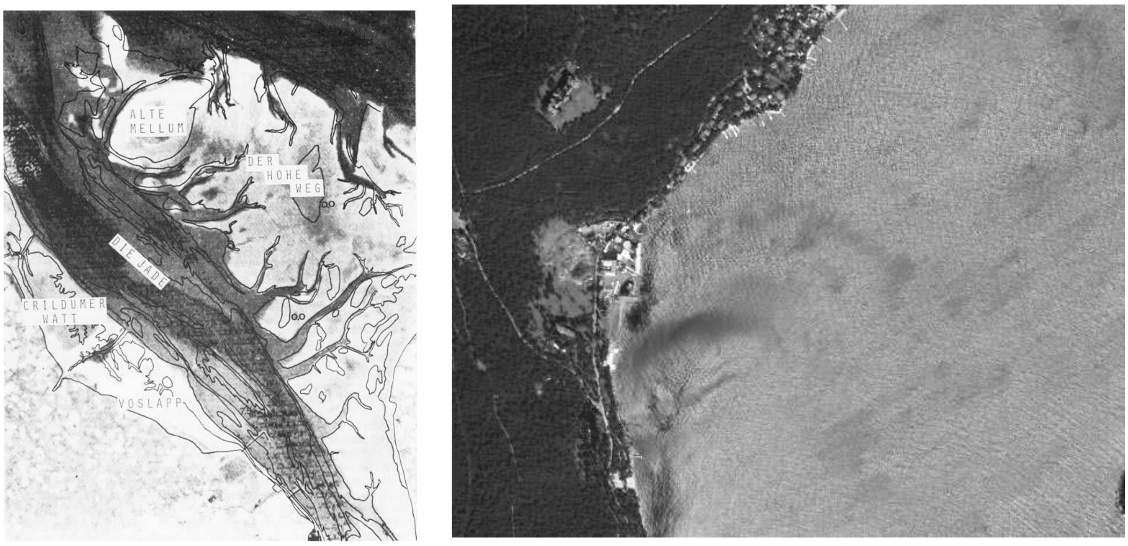

Landsat, Jade on the outside, North Sea WV-4, East of Tavsan Island, not disturbed by waves

**Figure 4.** Gray value information of sea surface from satellite images

If the seabed is homogeneous and the turbidity content is uniform, the water depth can be derived from the gray values of the remote sensing images. Applications in the South Seas are reported in the literature (NASA News, Earth Observatory). (Lohman and v.d. Piepen, 1981) overlaid a Landsat Channel 4 image (500 – 600 nm, yellow green) to a depth map of the Jade on the outside (North Sea) (Figure 4 left). The correlation of the water depth with the grey values is very high. Nevertheless, the grey values indicate the depth, but for numerical depth values local reference measurements or a reference depth map are required. However, the images available for this study from the port of Rostock (Baltic Sea) and Bizerte (Mediterranean Sea) did not allow this method. The darker water surface was supposed to indicate deeper water, but in the harbor areas the fairways had to be dredged down to sand, while the neighboring low water was covered by dark algae. This means that water surfaces are sometimes darker in shallow areas than in deep areas. The gray values of the water surface east of Tavsan Island (Figure 4 right), which is not so much disturbed by waves, may indicate some deeper parts, but the darker areas may also be caused by algae or water pollution – this has to be analyzed with reference data. The bathymetry around Tavsan Island was recently generated in the separate study (see Celik, et al., 2023) using the multispectral bands of same WV-2 image based on machine learning methods. The geometric accuracy of the derived bathymetric map was evaluated against in-situ data obtained by the echo-sounder survey.

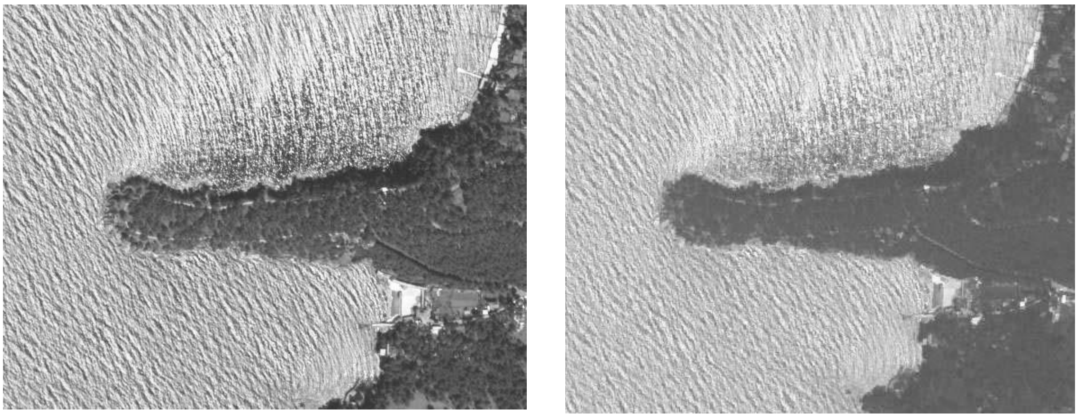

Panchromatic image

Green band

**Figure 5.** Part of the WV-2 scene with wave structures

Figure 5 shows some darker parts north of the peninsula of Tavsan Island. This can be an indication of the water depth. In Figure 5 we also can see the wave structure. The Rijkswaterstaat (national survey administration of the Netherlands) uses such wave structures in the tidal floodplain to support interpolation of depth measurement (Calkoen et al., 2001), but in the Sea of Marmara we have only a limited influence of the tide.

## Conclusion

The RPC-solution is the correct mathematical model for original satellite images, but not for the GeoTIFF geometry. The standard deviation of 1.30m for X and 1.23m for Y achieved by the 3D-affine transformation meets the requirement and confirms that GCP from Google Earth can be used for WV-2 images for marine application. Possibilities of marine application are shortly noted, but this requires additional research.

## References

Celik, O.I., Büyüksalih, G., Gazioglu, C. (2023). Improving the accuracy of satellite-derived bathymetry using multi-layer perceptron and random forest regression methods: A case study of Tavşan Island. Journal of Marine Science and Engineering, 11(11):2090. https://doi.org/10.3390/jmse11112090.

Calkoen, C. J., Hesselmans, G.H.F. M., Wensink, G.J., (2001). The Bathymetry Assessment System: efficient depth mapping in shallow seas using radar images, Int. J. Remote Sensing, 2001, vol.22, no.15, pp. 2973–2998.

Jacobsen, K. Büyüksalih, G., Marangoz, A., Sefercik, U., Büyüksalih, I., (2005). Geometric Conditions of Space Imagery for Mapping, Recent Advances in Space Technologies – RAST 2005, Istanbul 2005

Lohmann, P., van der Piepen, H. 1981: Evaluation of Ocean Bottom Features from Ocean Color Scanner Imagery, Photogrammetria 36 (1981, pp 81 - 89

INTERNATIONAL SYMPOSIUM ON
APPLIED
GEOINFORMATICS
9-10 May 2024 · Wrocław/Poland

*International Symposium on Applied Geoinformatics (ISAG2024)*

# Fuel Type Mapping in Sardegna via Convolutional Neural Network and PRISMA Imagery

Andrea Carbone[1]*, Dario Spiller[2], Giovanni Laneve[2]

[1] Department of Astronautical, Electric and Energy Engineering – Sapienza University, Rome, Italy;
and.carbone@uniroma1.it; ORCID 0000-0002-1119-060X,
[2] School of Aerospace Engineering – Sapienza University, Rome, Italy; dario.spiller@uniroma1.it,
giovanni.laneve@uniroma1.it, ORCID: 0000-0001-6108-9764
* Corresponding Author

## Abstract

Accurate mapping of vegetation fuel types is essential for evaluating wildfire risk and developing effective management strategies. However, achieving precise categorization of combustible materials across vast areas presents a significant challenge. In response, this study presents an innovative approach that integrates remote sensing data and Convolutional Neural Network (CNN) technology to distinguish between various fuel models. Leveraging PRISMA imagery, a CNN-based classification method accurately identifies six primary classes, including broadleaf, conifers, shrubs, grass, urban areas, and water bodies. Subclasses are further derived from these primary classes using Above Ground Biomass (AGB) and Bioclimatic (BC) maps to enhance mapping precision. By aligning with the widely recognized Standard Scott and Burgan fuel classification system, this approach yields promising results. CNN demonstrates exceptional training performance, achieving impressive accuracy, recall, and F1 scores of 0.99%. Notably, in a test case conducted in Sardinia, the network exhibits outstanding accuracy in identifying burnable classes in previously unseen pixels, with broadleaf at 0.93, conifer at 0.72, shrub at 0.75, and grass at 0.85%. This proposed method offers a valuable tool for improving fire management practices, thereby contributing to more effective wildfire prevention and mitigation efforts. As such, it has the potential to support fire management agencies, policymakers, and researchers in refining wildfire risk assessment and management strategies.

**Keywords:** *Land Cover; PRISMA and CNN; Fuel Type Mapping; Scott and Burgan Fuel System.*

## Introduction

Accurate information on fuel types and distribution is crucial for wildfire management (McCaffrey et al., 2004; Bowman et al., 2011; Knorr et al., 2016), ecosystem planning (Pausas et al., 2009), and natural resource management (Eva et al., 2000; Cano et al., 2015). Fuel maps offer detailed insights into vegetation fuel characteristics, traditionally reliant on laborintensive field surveys and visual interpretation of aerial imagery. However, remote sensing technology has advanced, addressing these limitations. Multispectral and hyperspectral imagery can discriminate between fuel types based on spectral signatures (Navalgund et al., 2007; Shaik et al., 2023; Conglaton et al., 2010). Machine learning, particularly deep learning, extracts patterns from remote sensing datasets (Camps-Valls et al., 2009; Maxwell et al., 2018; Lary et al., 2016; Scheunders et al., 2018). It enables timely and cost-effective fuel mapping over large areas, overcoming traditional limitations. Chrysafis et al. (2019) achieved enhanced accuracy in fuel type classification by developing random forest models combining data from satellites with topographic variables. D'Este et al. (2021) estimated fine dead fuel load using field data, remote sensing, and machine learning techniques. Aragoneses and Chuvieco (2023) developed a methodology for fuel mapping using Sentinel-3 images and biomass data, comparing algorithms. Shaik et al. (2022) distinguished wildfire fuel types using PRISMA imagery and SVM. Maniatis et al. (2022) developed a fire risk model using SVM, validated by wildfires in 2020 and 2021. Garcia et al. (2011) classified fuel types using multispectral data and LiDAR information, achieving an overall accuracy of around 88%. Alipour et al. (2023) combined CNN and deep neural network for large-scale fuel estimation. Promising results from remote sensing and machine learning motivate further exploration in fuel mapping. This paper focuses on Sardinia, an Italian region prones to wildfires, averaging 1008 incidents annually (European

Commission, EFFIS, 2021). Several studies generated fuel maps in Sardinia. Bajocco et al. (2015) predicted fire risk using MODIS NDVI data. Oliveira et al. (2018) assessed wildfire vulnerability in Mediterranean Europe. Salis et al. (2021) identified hot-spot areas and enhanced regional wildfire understanding. Aragonese et al. (2023) introduced a European fuel classification system with 88% accuracy.

This study introduces a pioneering approach to differentiate fuel types by integrating PRISMA imagery with CNN technology. Through this method, land cover is categorized into six primary classes (fuel types): broadleaf, conifers, shrubs, grass, urban areas, and water bodies. Furthermore, subclasses are identified using AGB and BC maps, and then, these fuel types are aligned with the Standard Scott and Burgan fuel classification system (Scott and Burgan, 2005). This methodology significantly enhances fire management efforts, contributing to the mitigation of wildfires' detrimental effects on ecosystems and human communities.

## Materials and Methods

This research employed the Level 2D data of PRISMA (PRecursore IperSpettrale della Missione Applicativa) satellite data. The camera has 173 channels of Short-Wave InfraRed (SWIR) and 66 channels of Visible and Near InfraRed (VNIR) in the spectral range of 0.4-2.5 nm. With an accuracy of ±0.1 nm, the average spectral resolution across the entire range is less than 10 nm. The hyperspectral camera's ground sampling distance for PRISMA images is 30 m. (product specifications at https://prisma.asi.it, accessed on 10 April 2024).

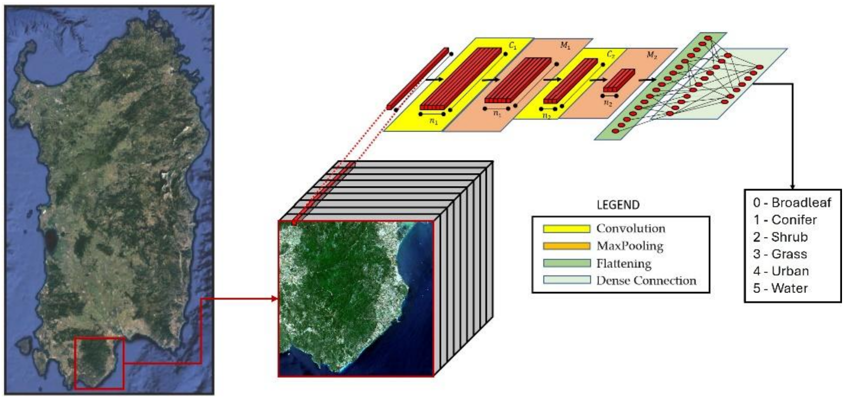

**Figure 1.** Area of Interest and CNN Scheme.

The focus of this study centers around Sardinia, an island situated in the southern region of Italy and renowned as the second-largest landmass in the Mediterranean Sea (shown in Figure 1). In particular, the area of interest is situated east of the city of Cagliari and consists of an expansive forested landscape that traverses undulating terrain, reaching altitudes of approximately 800 m, encompassing a total land area of 32 $km^2$. To assess the fuel map under high-risk fire probability conditions and during periods of significantly increased fuel load, a satellite image captured by the PRISMA on 16 June 2021, during the summer season, was selected for analysis. The CNN training dataset (reported in Table 1) was obtained through a visual inspection of the pseudo-color image derived from the PRISMA image of the region of interest, with the assistance of four land cover maps [see links in References *].

**Table 1.** Number of labeled reference pixels for CNN training dataset

| Broadleaf | Conifer | Shrub | Grass | Urban | Water |
|---|---|---|---|---|---|
| 1910 | 171 | 273 | 124 | 1544 | 9601 |

The CNN architecture, shown in Figure 1, takes as input the PRISMA spectral signatures of each pixel, represented as an array with a length of 230, defined by SWIR and VNIR PRISMA channels. The first hidden layer consists of a one-dimensional convolutional layer with 128 filters, a kernel equal to 3, the same padding, an L2 kernel regularizer equal to $10^{-5}$, and a ReLU activation function. This layer is followed by a max pooling layer with a pool size of 2 and a stride of 2. The sequence comprising convolutional and max pooling layers is replicated immediately thereafter, but with 64 filters in the convolutional layer. Then, the output of the flattening layer is passed through a fully connected layer of 32 units equipped with a ReLU activation function. Lastly, the model includes a dense unit with a softmax activation function for multi-class classification purposes. For optimization, categorical entropy and Adam were employed as the loss function and optimizer, respectively. The training process spanned 1000 epochs, each with a batch size of 1000, and a learning rate set to$10^{-4}$.

The CNN-based classification is cross-referring with the AGB and BC maps to align with the well-known Standard Scott and Burgan fuel classification system. In particular, the AGB represents the total mass of living vegetation per unit area (tons per hectare). The AGB map used in this study was obtained from the European Space Agency's Climate Change Initiative program (Santoro et al., 2023). The map exhibits a continuous range of values, but in this work, biomass values are normalized as percentages relative to the maximum value and divided into three macrogroups based on percentage thresholds: below 40 %, between 40 % and 70 %, and above 70 %. This facilitates analysis and aligns with the Scott and Burgan fuel type classification. This correlation allows for distinguishing between low, medium, and high forest density. Instead, the BC map represents the final stage of processing, achieved through the overlay of multiple layers such as Macrobioclimates, Phytoclimatic Plans, Ombrothermal Index, and Continentality Index (Canu et al., 2015) The overlay produces a BC map with 43 Isobioclimates, reflecting Sardinia's climate diversity. These 43 classes span a range of climate levels, including dry, subhumid, humid, and hyperhumid conditions. Our focus is on a subset of classes among the 43 available, specifically those belonging to one of the four predefined categories. By focusing on these, we generate a simplified map comprising two distinct macrogroups: "Dry," encompassing all dry classes, and "Humid," encompassing the remaining classes (subhumid, humid, and hyperhumid). By considering all possible combinations between the two maps, the resulting ancillary map, known as the Biomass Dryness map (BD), is comprised of six distinct classes as depicted on the left side of Figure 2. Scott and Burgan's Standard Fire Behavior Fuel Models provide a meticulously structured and standardized framework for characterizing vegetation and fuel properties. The system, comprising 45 distinct fuel models, includes five designated as non-burnable types: Urban, Snow/Ice, Agricultural, Open Water, and Bare Soil, as reported in the detailed schematic representation provided in the left side of Figure 2.

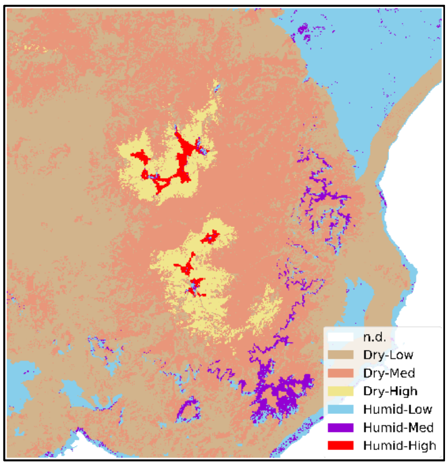

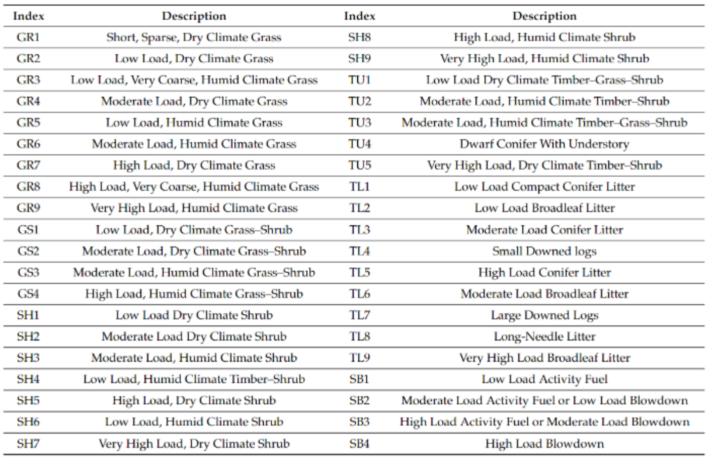

| Index | Description | Index | Description |
|---|---|---|---|
| GR1 | Short, Sparse, Dry Climate Grass | SH8 | High Load, Humid Climate Shrub |
| GR2 | Low Load, Dry Climate Grass | SH9 | Very High Load, Humid Climate Shrub |
| GR3 | Low Load, Very Coarse, Humid Climate Grass | TU1 | Low Load Dry Climate Timber–Grass–Shrub |
| GR4 | Moderate Load, Dry Climate Grass | TU2 | Moderate Load, Humid Climate Timber–Shrub |
| GR5 | Low Load, Humid Climate Grass | TU3 | Moderate Load, Humid Climate Timber–Grass–Shrub |
| GR6 | Moderate Load, Humid Climate Grass | TU4 | Dwarf Conifer With Understory |
| GR7 | High Load, Dry Climate Grass | TU5 | Very High Load, Dry Climate Timber–Shrub |
| GR8 | High Load, Very Coarse, Humid Climate Grass | TL1 | Low Load Compact Conifer Litter |
| GR9 | Very High Load, Humid Climate Grass | TL2 | Low Load Broadleaf Litter |
| GS1 | Low Load, Dry Climate Grass–Shrub | TL3 | Moderate Load Conifer Litter |
| GS2 | Moderate Load, Dry Climate Grass–Shrub | TL4 | Small Downed logs |
| GS3 | Moderate Load, Humid Climate Grass–Shrub | TL5 | High Load Conifer Litter |
| GS4 | High Load, Humid Climate Grass–Shrub | TL6 | Moderate Load Broadleaf Litter |
| SH1 | Low Load Dry Climate Shrub | TL7 | Large Downed Logs |
| SH2 | Moderate Load Dry Climate Shrub | TL8 | Long-Needle Litter |
| SH3 | Moderate Load, Humid Climate Shrub | TL9 | Very High Load Broadleaf Litter |
| SH4 | Low Load, Humid Climate Timber–Shrub | SB1 | Low Load Activity Fuel |
| SH5 | High Load, Dry Climate Shrub | SB2 | Moderate Load Activity Fuel or Low Load Blowdown |
| SH6 | Low Load, Humid Climate Shrub | SB3 | High Load Activity Fuel or Moderate Load Blowdown |
| SH7 | Very High Load, Dry Climate Shrub | SB4 | High Load Blowdown |

**Figure 2.** Biomass Dryness map (on the left side) and Scott/Burgan fuel model scheme (on the right side).

Upon cross-referencing Land Cover and BD, the corresponding classes within Scott and Burgan's Standard Fire Behavior Fuel Models can be identified. This process resulted in a total of 24 classes, i.e., the initial 4 burnable classes (broadleaf, conifer, shrub, and grass) from the classification were combined with the 6 classes from the BD map. Subsequently, these 24 classes were associated with the corresponding fuel models from the Scott and Burgan system, as reported in Table 2.

**Table 2.** Adaptation of the fuel types to the Scott and Burgan system, with the symbols BL, CF, SH, and GR representing Broadleaf, Conifer, Shrub, Grass respectively.

| | **Dry-Low** | **Dry-Med** | **Dry-High** | **Hum-Low** | **Hum-Med** | **Hum-High** |
|---|---|---|---|---|---|---|
| **BL** | TL2 | TL6 | TL9 | TL2 | TL6 | TL9 |
| **CF** | TL1 | TL3 | TL5 | TL1 | TL3 | TL5 |
| **SH** | SH2 | SH5 | SH7 | SH6 | SH3 | SH9 |
| **GR** | GR2 | GR4 | GR7 | GR5 | GR6 | GR9 |

## Results and Discussion

In the practical implementation, the CNN model was implemented in Python using TensorFlow on a personal computer equipped with 12 GB of RAM, an Intel Core i7-12700H 2.70 GHz CPU from the 12th Generation, and an NVIDIA GeForce RTX 3080 Ti GPU with 16 GB of dedicated RAM.

The CNN model's training produced remarkable accuracy (0.996), recall (0.985), and F1 (0.976) scores, underscoring its high performance. These performance metrics are derived solely from the dataset outlined in Table 1, offering insights into the network's effectiveness on this specific dataset. To assess the CNN-based classification's performance on unseen scenarios, the predictions were extended to the entire area of interest (shown on the left side of Figure 3) and compared with the four external maps [see links in References *]. The subsequent cross-validation phase revealed notable accuracy across various classes (as shown in confusion matrix on the right side of Figure 3), showcasing the model's adeptness in accurately generalizing both burnable classes, such as Broadleaf (0.93), Conifer (0.72), Shrub (0.75), and Grass (0.85), and non-burnable ones (Urban 0.88, and Water 0.98). The promising results obtained in evaluating novel scenarios reinforce the robustness of the network and underscore its potential for real-world applications.

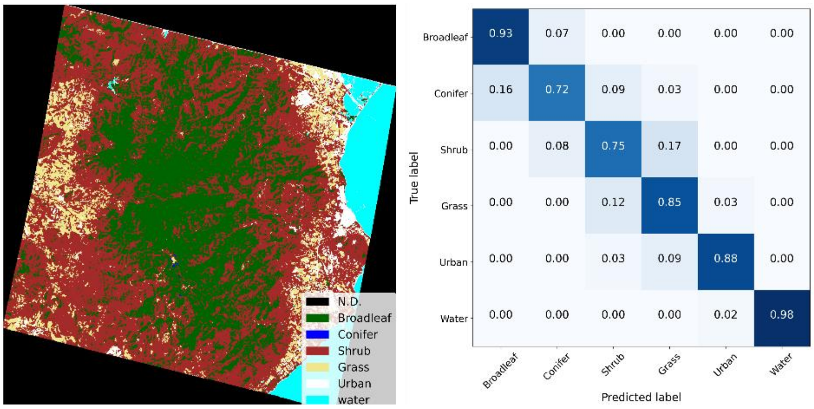

**Figure 3.** Confusion matrix of CNN-based land cover classification.

It is worth mentioning an intriguing observation, although somewhat unrelated to the focus, where the model successfully classifies some vessels located off the East Coast as "urban", even when they were barely visible to the naked eye. This demonstration of the model's overall capability and accuracy is noteworthy and piques further interest in its potential applications.

By cross-referring Land Cover and BD, the Fuel Type Map of the Scott/Burgan type can be derived from Table 2, as shown in Figure 4. The fuel map generation process aligns land cover classification with the Scott and Burgan fuel system, providing a comprehensive representation of fuel characteristics crucial for fire risk assessment and management efforts. The detailed fuel map serves various domains, including land management, fire risk assessment, and emergency response planning, supporting informed decision-making. Compared to previous methods, this study introduces significant advancements, including a high-resolution map generation process and reliance on readily available external maps, reducing the need for extensive data acquisition campaigns.

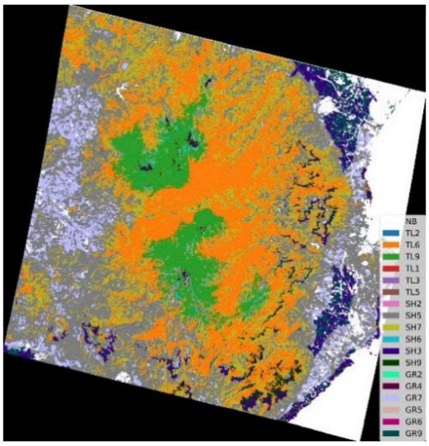

**Figure 4.** Fuel map adaptation to Scott and Burgan.

## Conclusion

Recent years have highlighted the crucial role of machine learning in handling the vast volume of data generated daily by satellite remote sensing. The motivation for this paper originates from research within the FirEUrisk project, aiming to solidify the foundations of these novel techniques and provide an open-source tool for fuel type mapping. This study emphasizes the indispensability of primary machine learning approaches for land cover mapping and monitoring tasks. Aligning fuel type classification with the widely recognized Scott and Burgan standard is a significant step in harmonizing efforts with established wildfire management protocols, ensuring compatibility and simplifying adoption into current fire management practices. This tool enables more efficient and automated analysis of large-scale satellite imagery, benefiting fields such as agriculture, forestry, disaster monitoring, and environmental studies. Future research could expand on this study by incorporating larger datasets sourced from diverse geographical regions to make the model more robust to domain adaptation. Moreover, employing neural network architectures capable of accurately predicting AGB could further enhance the generality of the model.

## References

Aragoneses, E., and Chuvieco, E. (2021). Generation and Mapping of Fuel Types for Fire Risk Assessment. Fire, 4, 59.

Aragoneses, E.; García, M.; Salis, M.; Ribeiro, L.M.; Chuvieco, E. (2023). Classification and mapping of European fuels using a hierarchical, multipurpose fuel classification system. Earth Syst. Sci. Data, 15, 1287–1315.

Bajocco, S.; Dragoz, E.; Gitas, I.; Smiraglia, D.; Salvati, L.; Ricotta, C. (2015). Mapping forest fuels through vegetation phenology: The role of coarse-resolution satellite time-series. PLoS ONE, 10, e0119811.

Canu, S.; Rosati, L.; Fiori, M.; Motroni, A.; Filigheddu, R.; Farris, E. (2015). Bioclimate map of Sardinia (Italy). J. Maps, 11, 711–718.

Chrysafis, I., Damianidis, C., Giannakopoulos, V., Mitsopoulos, I., Dokas, I.M., and Mallinis, G. (2023). Vegetation Fuel Mapping at Regional Scale Using Sentinel-1, Sentinel-2, and DEM Derivatives---The Case of the Region of East Macedonia and Thrace, Greece. Remote Sens., 15, 1015.

Congalton, R.G. (2010). Remote Sensing: An Overview. GISci. Remote Sens., 47, 443–459.

D'Este, M., Elia, M., Giannico, V., Spano, G., Lafortezza, R., and Sanesi, G. (2021). Machine Learning Techniques for Fine Dead Fuel Load Estimation Using Multi-Source Remote Sensing Data. Remote Sens., 13, 1658.

Ensley-Field, M., Shriver, R.K., Law, S., and Adler, P.B. (2023). Combining Field Observations and Remote Sensing to Forecast Fine Fuel Loads. Rangel. Ecol. Manag., 90, 245–255.

European Commission, Joint Research Centre; San-Miguel-Ayanz, J.; Durrant, T.; Boca, R. (2021). Forest Fires in Europe, Middle East and North Africa 2020. Technical Report. European Commission, Joint Research Centre: Luxembourg.

García, M., Riaño, D., Chuvieco, E., Salas, J., and Danson, F.M. (2011). Multispectral and LiDAR data fusion for fuel type mapping using Support Vector Machine and decision rules. Remote Sens. Environ., 115, 1369–1379.

Knorr, W., Arneth, A., and Jiang, L. (2016). Demographic controls of future global fire risk. Nat. Clim. Chang., 6, 781–785.

Lary, D.J., Alavi, A.H., Gandomi, A.H., and Walker, A.L. (2016). Machine learning in geosciences and remote sensing. Geosci. Front., 7, 3–10.

Maniatis, Y., Doganis, A., and Chatzigeorgiadis, M. (2022). Fire Risk Probability Mapping Using Machine Learning Tools and Multi-Criteria Decision Analysis in the GIS Environment: A Case Study in the National Park Forest Dadia-Lefkimi-Soufli, Greece. Appl. Sci., 12, 2938.

Maxwell, A.E., Warner, T.A., and Fang, F. (2018). Implementation of machine-learning classification in remote sensing: An applied review. Int. J. Remote Sens., 39, 2784–2817.

McCaffrey, S. (2004). Thinking of wildfire as a natural hazard. Soc. Nat. Resour., 17, 509–516.

Navalgund, R.R., Jayaraman, V., and Roy, P. (2007). Remote sensing applications: An overview. Curr. Sci., 93, 1747–1766.

Pausas, J.G., and Keeley, J.E. (2009). A burning story: The role of fire in the history of life. BioScience, 59, 593–601.

Santoro, M.; Cartus, O. (2023). ESA Biomass Climate Change Initiative (Biomass_cci): Global Datasets of Forest Above-Ground Biomass for the Years 2010, 2017, 2018, 2019 and 2020, v4. NERC EDS Centre for Environmental Data Analysis: Calgary, AB, Canada.

Santos, F.L., Couto, F.T., Dias, S.S., de Almeida Ribeiro, N., and Salgado, R. (2023). Vegetation fuel characterization using machine learning approach over southern Portugal. Remote Sens. Appl. Soc. Environ., 32, 101017.

Scott, J.; Burgan, R. (2005). Standard Fire Behavior Fuel Models: A Comprehensive Set for Use with Rothermel's Surface Fire Spread Model. USDA Forest Service. U.S. Department of Agriculture: Fort Collins, CO, USA.

Shaik, R.U., Laneve, G., and Fusilli, L. (2022). An automatic procedure for forest fire fuel mapping using hyperspectral (PRISMA) imagery: A semi-supervised classification approach. Remote Sens., 14, 1264.

Shaik, R.U., Periasamy, S., and Zeng, W. (2023). Potential Assessment of PRISMA Hyperspectral Imagery for Remote Sensing Applications. Remote Sens., 15, 1378.

Scheunders, P., Tuia, D., and Moser, G. (2018). Contributions of machine learning to remote sensing data analysis. In Data

Processing and Analysis Methodology, Comprehensive Remote Sensing, pp. 199–243.

** Link External Maps:*

(a) Land Cover (LC) 2021, provided by ISPRA (“Istituto Superiore per la Protezione e la Ricerca Ambientale”), including the Broadleaf, Conifer, Shrub, and Grass classes (https://www.isprambiente.gov.it/it, accessed on 10 April 2024).

(b) ESA World Cover (WC) 2021 identifies seven classes representing different land surface types, including Tree Cover, Shrubland, Grassland, and Cropland (https://worldcover2021.esa.int, accessed on 10 April 2024).

(c) the Forest Type product (FTY) is a part of the European Environment Agency (EEA) Copernicus Land Monitoring Service, and it provides a forest classification with three thematic classes: non-tree areas, broadleaved forest, and coniferous forest (https://land.copernicus.eu/en/products/high-resolution-layer-forest-type, accessed on 10 April 2024).

(d) Grassland (GRA) 2018 is also developed under the EEA Copernicus Land Monitoring Service, and it offers a basic land cover classification with two thematic classes: grass and no grass (https://land.copernicus.eu/en/products/high-resolution-layer-grassland, accessed on 10 April 2024).

INTERNATIONAL SYMPOSIUM ON
APPLIED
GEOINFORMATICS
9-10 May 2024 · Wrocław/Poland

*International Symposium on Applied Geoinformatics (ISAG2024)*

# Graph-Based Modeling of Village Infrastructure Development

Bohdan Potuzhnyi[1,2]*, Vlada Svirsh[1,2] , Natallia Kussul[1,3]

[1] Institute of Physics and Technology, National Technical University of Ukraine "Igor Sikorsky Kyiv Polytechnic Institute", Kyiv, Ukraine;
(bohdan.potuzhnyi/vlada.svirsh25)@gmail.com, nataliia.kussul@lll.kpi.ua; ORCID 0009-0001-2282-7012, ORCID 0009-0004-4006-2705, ORCID 0000-0002-9704-9702
[2] Bern University of Applied Sciences, School of Engineering and Computer Science, Biel, Switzerland
[3] Space Research Institute NASU-SSAU, Kyiv, Ukraine
* Corresponding Author

## Abstract

This study introduces a novel framework for analyzing and enhancing rural infrastructure in Ukraine by employing advanced clustering techniques with OpenStreetMap (OSM) geospatial data. The core methodology integrates spatial data analysis and machine learning, notably through an enhanced KMeans clustering algorithm, to categorize villages based on infrastructure quality. By incorporating postal and mobile data, the study achieves a richer profiling of each village, allowing for more precise developmental strategies.

A significant innovation in this research is the inclusion of a post-clustering reorganization step, which ranks villages within clusters based on their infrastructure needs. This enables targeted interventions for areas that require the most urgent attention. The effectiveness of this methodology was validated across multiple Ukrainian villages, demonstrating its potential to identify and address critical infrastructure disparities. Additionally, the method proposes specific improvements for each village based on its unique infrastructure profile.

The results of the study reveal significant imbalances in rural infrastructure, with the clustering technique successfully highlighting villages with inadequate facilities. These findings not only facilitate informed decision-making but also underscore the importance of integrating socioeconomic data for a holistic development approach. This work contributes to the strategic enhancement of infrastructure in rural areas, emphasizing the necessity of informed policymaking and cost-effective planning in diverse economic conditions. The developed approach offers a scalable model that could be adapted for broader geographic applications, potentially impacting rural development policy both within and beyond Ukraine.

**Keywords:** *Spatial Data Analysis, Machine Learning, Clustering, Graph Convolutional Networks, Geoinformatics, Village Classification*

## Introduction/Background

Recent developments have highlighted the urgent need to enhance rural infrastructure, a challenge that is particularly pressing in Ukraine due to the ongoing effects of conflict and economic difficulties, though this issue also resonates globally. Urban-rural disparities in infrastructure significantly contribute to widening social and economic gaps, impairing national progress. This study introduces an innovative framework designed to tackle these issues by harnessing advanced clustering techniques and leveraging OpenStreetMap (OSM) geospatial data to optimize village infrastructure enhancements. The study is driven by several key objectives:

Formulate a method to classify villages according to their infrastructure quality, utilizing advanced spatial data analysis and machine learning clustering techniques. This methodology aims to establish clear metrics that guide targeted developmental efforts.

Pinpoint developmental deficiencies within rural communities through the analysis of geospatial data from OSM, setting clear standards for necessary infrastructure improvements. This objective ensures that interventions are accurately aligned with the specific needs of each village.

Assess the impact of the newly proposed clustering methods on the strategic planning processes for rural areas, aiming to introduce a more empirical approach to policymaking that can adapt to evolving rural demands.

Develop a decision-support system that recommends specific infrastructural enhancements for each village, incorporating postal and mobile data to identify the most effective strategies for improving infrastructure quality and connectivity.

This research contributes to a larger initiative, "Information Technologies of Geospatial Analysis for the Development of Rural Areas and Communities", sponsored by the Ministry of Education and Science of Ukraine. The initiative highlights the critical national importance of advancing rural infrastructure to promote equitable development throughout the country. The anticipated results of this study will validate a scalable methodology that integrates additional socioeconomic data layers and lays the groundwork for future automation and real-time analytical updates. This project seeks to offer substantial contributions to the strategic improvement of village infrastructure, focusing on cost efficiency and well-informed policymaking, especially given Ukraine’s current economic circumstances.

## Materials and Methods

Our research utilizes a detailed methodology that combines spatial data analysis, advanced machine learning clustering techniques, and extensive geoinformatics data from OpenStreetMap (OSM). We analyze a dataset that includes 28,381 individual entries, each corresponding to a unique geographic location within rural Ukraine. This dataset is rich in details, cataloged across 41 columns that provide a comprehensive view of rural infrastructure through geospatial analytics. For our analysis, we specifically utilize 19 distance-related descriptors, 13 graph-based descriptors, and 6 indicators of mobile connection availability from different operators.

A significant portion of our dataset focuses on proximity measures that quantify the closeness of each village to key infrastructure elements. These measures are essential for our spatial analysis and help in crafting targeted development strategies for these rural communities. All of this data presented in the Table 1.

**Table 1.** Infrastructure distances.

| Type | Objects | Description |
|---|---|---|
| Roads | RD_m1_NEAR, RD_m2_NEAR, RD_m3_NEAR | These objects describe the distance to major, regional, and rural roads. |
| Cities | CITY2_NEAR, Kyiv_NEAR_ | These objects describe the distance to the nearest city and capital of Ukraine |
| Parks | LokPark_NE, NatPark_NE, regPark_NE | These objects describe the distance to the nearest local park, national park, and regional park |
| Elevators | Elevators_ | Distance to the closest elevator |
| Kindergarten | Kinder_NEAR | Distance to the closest kindergarten |
| Bank | Bank_NEAR_ | Distance to the closest bank |
| Church | Cerkva_NEA | Distance to the closest church |
| Education | Education_ | Distance to the education |
| Hotels | Hotels_NEA | Distance to the closest hotel |
| Library | Library_NE | Distance to the closest library |
| Hospital | Likarni_NE | Distance to the closest hospital |
| Shop | Magaz_NEAR | Distance to the closest shop |
| Post | NP_Min_Dist, UP_Min_Dist | Distance to closest Nova Poshta and UkrPoshta |

This study incorporates an additional element: the use of seven mobile network coverage descriptors. These descriptors provide insights into the presence and quality(3G, 4G) of mobile network services from various providers(kyivstar, lifecell, vodafone, trimob) within each village. This enhancement allows for a more comprehensive analysis of connectivity infrastructure, crucial for assessing and planning technological upgrades in rural areas.

Custom Vector Creation involves generating unique vectors for each Point of Interest (POI) by merging graph-based spatial data and distance metrics related to essential infrastructure components. This integration forms a detailed infrastructure snapshot for each village, significantly enhancing our ability to accurately classify villages based on distinct infrastructure characteristics.

In the Enhanced Clustering step, we modify the traditional KMeans clustering method by adding a reorganization step.

This adjustment ranks the clusters based on the quality of their infrastructure from those most in need of improvement to the least, using data from the clustering process. This method simplifies the interpretation of infrastructure status across clusters and provides a structured approach for regional analysis.

Heatmap Visualization is used to depict the results of our clustering. By focusing on normalized data points for each cluster, this technique helps in visualizing complex data sets and emphasizes the infrastructural differences and similarities between clusters. This normalization ensures equitable comparisons across clusters, highlighting critical infrastructural trends and deviations.

Distribution Analysis explores how villages are distributed across the identified clusters to understand the overall state of infrastructure development. This analysis, supported by histograms, identifies variations in infrastructure quality among villages, highlighting trends and outliers and pinpointing areas that require more focused improvements.

Lastly, Strategic Improvement Recommendations are derived by introducing a method to determine actionable steps that can elevate a village's infrastructure to higher cluster standards. This involves comparing the existing infrastructure vectors of a village with those in higher-ranked clusters to find the closest optimal setups. Calculating the differences and distances to these benchmarks allows us to specify the necessary upgrades to improve a village's infrastructural status, guiding the prioritization of development initiatives to ensure efficient resource allocation for the most significant impact.

## Results and Discussion (Findings)

Our comprehensive study led to the creation of a diverse array of visualizations, with a focus on 17 key graphical representations including 3D plots, heatmap plots, and a histogram. These visuals were instrumental in our analysis, providing a multi-dimensional view of the infrastructure landscape in Ukrainian villages. The 3D plot of roads showcased in Figure 1 exemplifies the clusters of road types, each color-coded to represent different levels of access to road infrastructure, ranging from the closest (cluster 0) to the furthest (cluster 9) from essential road types.

The heatmap of normalized cluster centroids, illustrated in Figure 2, further refines our understanding of infrastructure distribution. Each row, representing a different cluster, is juxtaposed with a spectrum of infrastructure features like roads, education centers, medical facilities, and more, giving a clear, color-graded depiction of how each village cluster compares across various infrastructural aspects.

In our discussion, we note the immediate practical applications of these findings. For instance, villages within Cluster 3 highlighted in the 3D plot demonstrate a need for improved connectivity to regional roads, a step that could lead to more evenly distributed development. The heatmap adds a layer of depth by quantifying the specific infrastructural attributes of each cluster, which directly informs our targeted development plans. It reveals, for example, the clusters where postal services are underrepresented, an insight that can guide the enhancement of postal networks in those areas.

Figure 3, the Distribution with Density Plot of Village Infrastructure Quality, presents a histogram overlaid with a kernel density estimation, mapping the frequency of villages against the quality of infrastructure. The distribution appears approximately normal, suggesting a moderate level of infrastructure development across the majority of villages, with some deviations indicative of clusters with particularly high or low infrastructure quality.

Figure 4, the Scatter Plot of Villages with Infrastructure Quality Color Gradient, provides a geographical perspective, placing each village on the map of Ukraine according to its infrastructure quality score. This color-coded gradient reflects the infrastructure quality, revealing regional patterns and the dispersion of infrastructural development, with hues ranging from greens indicating higher quality to reds signaling areas with potential for significant improvement.

Integrating the findings from Figure 3 and 4 with our previous graphical analyses reinforces the narrative that while some villages are well-served, others remain in critical need of infrastructural enhancements. The distribution pattern from the histogram in Figure 3 aligns with the geographical spread depicted in Figure 4, together they suggest a strategic focus for development efforts.

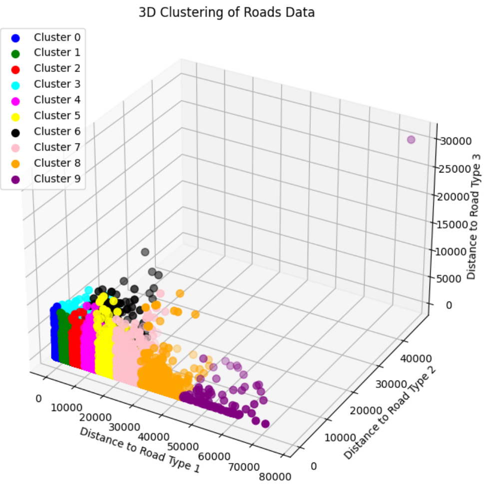

**Figure 1.** Clusters of road types, with each color denoting a distinct cluster. The sequence of clusters is displayed on the upper-left side, where 0 represents the cluster nearest to the objects, and 9 indicates the cluster furthest from all other roads.

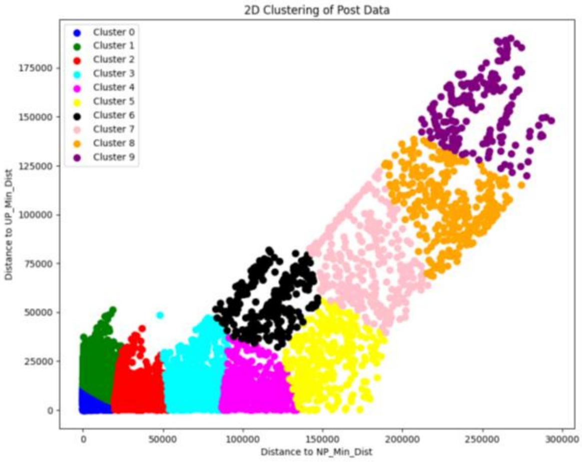

**Figure 2.** A 2D clustering visualization of postal data, with each distinct color corresponding to a different cluster. The arrangement of clusters is indicated, with cluster 0 showing the shortest distance to post services and cluster 9 showing the greatest distance.

Specifically, our clustering technique successfully highlights areas that lack essential facilities, pointing towards potential interventions. These could range from constructing additional regional roads, as indicated by the clustering of road types, to enhancing the availability of local parks and educational amenities, informed by the heatmaps and scatter plots.

Our analysis, grounded in rigorous spatial data and machine learning clustering techniques, offers a systematic and empirical foundation for decision-making. The clustering not only elucidates the current state of rural infrastructure but also prompts targeted developmental strategies. This facilitates informed policymaking, which is particularly crucial given the complex socio-economic landscape within which this study is situated.

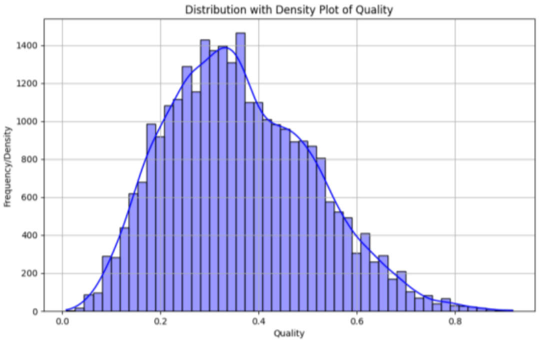

**Figure 3.** Distribution with Density Plot of Village Infrastructure Quality

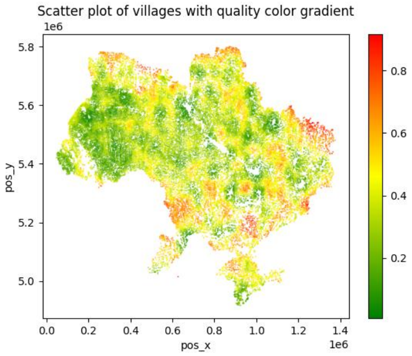

**Figure 4.** Scatter Plot of Villages with Infrastructure Quality Color Gradient, each point is village, and color represents quality green is better and red is worse

## Conclusion

To conclude, our research articulates a robust and innovative framework for the analysis and enhancement of village infrastructure, leveraging clustering techniques and geospatial data. The methodologies and findings presented here not only provide a detailed assessment of the current infrastructural state but also pave the way for actionable strategies towards rural development. Our research offers a scalable and adaptable model for infrastructure enhancement, with the potential to be extended to broader geographical contexts and integrated with additional socio-economic data layers for comprehensive development strategies. Through strategic clustering and insightful visualizations, this study makes a significant contribution to the field of geoinformatics and rural development, with the potential to inform and guide policy decisions in Ukraine and beyond.

## Acknowledgements

This research was conducted with the support of the Ministry of Education and Science of Ukraine under the project titled "Information Technologies of Geospatial Analysis for the Development of Rural Areas and Communities," state registration number 0123U102838. We extend our gratitude to the project for supplying the raw data necessary for this analysis.

**References**

Arintoko, A., Ahmad, A. A., Gunawan, D. S., & Supadi, S. (2020). Community-based tourism village development strategies: A case of Borobudur tourism village area, Indonesia. GeoJournal of Tourism and Geosites, 29(2), 398–413.

Geza, W., Ngidi, M. S. C., Slotow, R., & Mabhaudhi, T. (2022). The dynamics of youth employment and empowerment in agriculture and rural development in South Africa: A scoping review. Sustainability, 14(9), 5041.

Kapoor, N., Ahmad, N., Nayak, S. K., Singh, S. P., Ilavarasan, P. V., & Ramamoorthy, P. (2021). Identifying infrastructural gap areas for smart and sustainable tribal village development: A data science approach from India. Journal of Jimei University International Edition.

Liu, Y., Ke, X., Wu, W., Zhang, M., Fu, X., Li, J., Jiang, J., He, Y., Zhou, C., Li, W., Li, Y., Song, Y., & Zhou, X. (2022). Geospatial characterization of rural settlements and potential targets for revitalization by geoinformation technology. Scientific Reports, 12(8399).

Long, H., Ma, L., Zhang, Y., & Qu, L. (2022). Multifunctional rural development in China: Pattern, process and mechanism. Habitat International, 102530.

Yailymova, H., Yailymov, B., Kussul, N., & Shelestov, A. (2023). Geospatial analysis of life quality in Ukrainian rural areas. Proceedings of the 13th International Conference on Dependable Systems, Services and Technologies (DESSERT), Athens, Greece, pp. 1-5.

INTERNATIONAL SYMPOSIUM ON
APPLIED
GEOINFORMATICS
9-10 May 2024 · Wrocław/Poland

*International Symposium on Applied Geoinformatics (ISAG2024)*

# Design of A Coastal Zone Monitoring System Using an Unmanned Vessel

Marta Wlodarczyk-Sielicka

Marine Technology Sp. z o.o., ul. Roszczynialskiego 4 lok. 6, Gdynia, Poland; m.wlodarczyk@marinetechnology.pl;
ORCID 0000-0002-7489-8437

## Abstract

The article presents an overview of preliminary research for a coastal zone monitoring system utilizing an unmanned vessel. State-of-the-art sensors, including MBES and sonar for underwater data, and a laser scanner and metric camera for ground observations, are mounted on the HydroDron unmanned vessel for data acquisition. The system aims to integrate data from these diverse sensors to create a multidimensional and multi-temporal database of the coastal zone, facilitating visualization through spatial mapping. A significant research challenge addressed is the heterogeneity of systems and the management of large datasets, particularly in the complex coastal environment where data collection is challenging. The methodology developed for utilizing an unmanned vessel for coastal zone measurements encompasses equipment configuration, data transmission, measurement guidelines, and travel routes. A key research objective is the development of methods for sensor geodata processing and fusion, with analysis conducted on data processing methods applicable to the operational system. The proposed system architecture comprises four modules: acquisition, underwater data processing, surface data processing, and operations/visualization, reflecting the integrated data and fusion module. Addressing the challenge of creating a multidimensional and multi-temporal knowledge base for the coastal zone involves developing a detailed specification of the target data model to maintain spatial data integrity from various sources. The system is characterized by its automation, simplifying operation for end-users who need only place measurement data in designated directories. Overall, the article provides insight into the development of a comprehensive coastal zone monitoring system leveraging unmanned vessel technology and advanced sensor capabilities, addressing key challenges in data integration, processing, and knowledge base development.

**Keywords:** monitoring system, data fusion, seafloor mapping, coastal zone, spatial big data

## Introduction

The main purpose of this article is to present preliminary research for a project involving a coastal zone monitoring system utilizing an unmanned vessel. The system, funded by the National Centre for Research and Development of Poland, aims to create a prototype capable of operating in real conditions. Monitoring the coastal zone is a very time-consuming and difficult undertaking. Collection of spatial data in such a zone is often impossible using classical measurement methods such as land and hydrographic surveys. The proposed system will employ an unmanned vessel, enabling data collection from hard-to-reach areas. State-of-the-art sensors mounted on the HydroDron unmanned vessel are utilized for data acquisition: MBES and sonar for underwater data, and a laser scanner and metric camera for ground observations. The unmanned HydroDron catamaran is shown in Figure 1.

**Figure 1.** Unmanned hydrographic vessel: HydroDron.

Nowadays, there is a tumultuous development of modern technologies that make it possible to collect a huge amount of spatial information in a relatively short period of time. The problem of the project revolves around the question of how to visualize spatial data with different characteristics obtained from various sensors so that they are consistent and reasonably accurate. Due to the different peculiarities of individual sensors, direct adaptation is not possible. Instead, it is necessary to develop new methods dedicated to vessels equipped with a variety of modern devices for collecting surface and underwater information. Undertaking this task requires solving several problems in various fields including geoinformatics, hydrography, navigation, data processing, mathematical modeling, and computer science. The proposed system, besides integrating data from different sensors, aims to establish a multidimensional and multi-temporal knowledge base specific to the coastal zone under consideration. It will also facilitate the visualization of this data through spatial mapping. Attention should be given to the challenges posed by the heterogeneity of systems and the management of large datasets, which represent significant research obstacles. The article presents the results of the analyses conducted for spatial data fusion and discusses the encountered research problems.

## Materials and Methods

During the course of this work, a methodology was developed for employing an unmanned vessel to conduct measurements in the coastal zone. This methodology encompasses the configuration of equipment and devices, information transmission protocols, measurement guidelines, and travel routes. The HydroDron vessel is equipped with several sensors, including the PING DSP 3DSS-DX-450 interferometric echosounder, the Velodyne VLP-16 LiDAR, the Blackfly S GigE metric camera, and auxiliary systems such as the Ekinox2 Subsea positioning system (NAVSIGHT-T), the Garmin 18 GPS PPS (for time stamping and synchronization), and the AML SV Xchange and AML SVP Base X2. Additionally, detailed parameters, settings, and configuration requirements for each sensor are specified to ensure proper system operation. The main research objective was to develop methods for processing and fusing sensor geodata. The data fusion model integrates underwater and land information. Underwater data is obtained from a set of measurements acquired from the MBES multibeam echosounder unit and sonar, allowing for the creation of an MBES point cloud of the area beneath the vessel and images of the seabed. Surface data is derived from measurements acquired by a LiDAR unit and a metric camera, enabling the acquisition of a LiDAR point cloud of the area surrounding the vessel and high-resolution video recording.

Sonar acquired data is originally stored in *.xtf format. Multiple unlinked sonar files are acquired as part of a single survey. Their processing involves performing a series of operations to obtain a mosaic map. During the research work, a general method for obtaining a mosaic at optimal parameter values was proposed. The first step in the processing of sonar data is to load the original files in *.xtf format. While reading these files, the values of both channels are determined by concatenating the packets in each *.xtf file. Both channels are required to finally obtain the image intensity table. The channels are subjected to checking and possibly limiting the values to a preset interval from 0 to a factor that has been taken as a $2^{16} - 1$. In addition, the height and width values of the data as well as the slant range are taken. In the next step, data normalization is performed *min-max* (Henderi, 2021). Sonar data has a so-called dead zone, where no measurement has been made (this is the area under the sonar), which should be located and removed. Analysis of the dead zone is based on the use of graphical filters such as Gaussian blur (Kusrini, 2022) and thresholding (Bovik, 2009). It should be noted here that sonar data is stored in the form of a matrix, so the application of graphical filters will mean performing a spline operation between the matrix and the graphical filter (Bonaccorso, 2018). To process the sonar data correctly, a skew correction (due to the projection of the beam onto the seabed position) is performed according to the range function (Burguera, 2016).

In a further stage, a single file georeferencing is also performed, which is based on taking the sonar coordinate values and transforming them to the UTM system. In a further stage of processing, the values of such parameters as position, azimuth $\Theta$ and pitch $\Phi$ are determined using information from the sensor file: direction and sensor roll, which allows the georeferenced coordinate values to be determined by georeferencing transformation. To create a sonar mosaic, arrays are created containing successively flattened data with x, y coordinates and image values. The data prepared in this way are used to generate a 2d histogram (Coltuc, 2006). Note that there is a possibility that the data arrays will not cover the entire area, so there will be some missing points. The reason for this is the way sonar data is acquired - the acquired data is the result of wave propagation between the target and the receiver. When the sonar is in motion, the beam does not cover the full area. To fill in the missing data in the sonar, we perform image thresholding and morphological closure (Haralick, 1987).

In the case of metric camera measurement data, these are video files in *.avi format. Their processing is initially understood as splitting the file into individual video frames. A video frame is represented as a two-dimensional image in a preset RGB (Red-Green-Blue) colour model (Schwarz, 1987). Such an image contains the field of view of the observer; hence the image will contain a view of the waterfront with the shoreline separating it from the water. The first step in processing the camera data is cropping the image relative to the shoreline. Determining the shoreline in the camera image is done by generating a mask using a convolutional neural network (Albawi, 2017 and Falk, 2019). To generate the mask, the neural network will take an image as input, and return the processed image. Hence, the architecture of the neural network is adapted to perform image segmentation to the edge line. Assume that a two-dimensional image will be represented by a set of three matrices. Each of these matrices represents one channel of the selected colour model, or RGB. The output image represents the edge line, so it will be represented by values representing the colour white or black. The architecture of the dedicated U-NET model is composed of the following layers and mechanisms presents in Figure 2. The model has 2167344 parameters, of which 2166352 are learned. The network model is learned using the ADAM algorithm (Kingma, 2015).

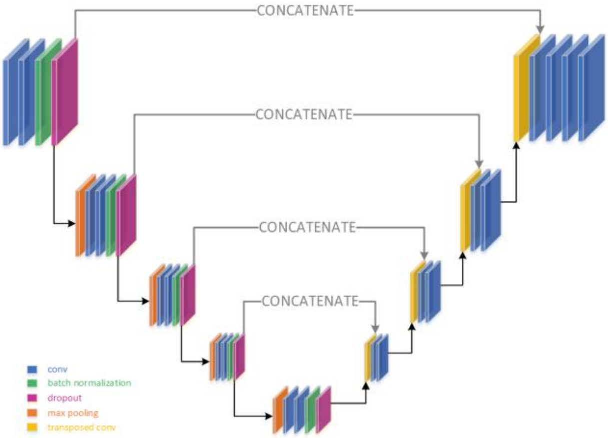

**Figure 2.** Visualization of dedicated U-NET network architecture for shoreline detection.

The set of images (video frames) is processed in the same way, that is, to obtain only the area above the shoreline. Then a selection of frames is made, which will be used in the further analysis process. The selection is based on the choice of frames that can allow the creation of a panorama. The image thus created is subjected to additional graphic processing, which is the removal of the background, for example: the sky. The processed image is used to obtain the average colour values in each row. The result is an array for each colour channel with the average value of that colour in each row of the image. The array of average colour values is used in further determining the assignment of colours to points in the LiDAR cloud. To combine the two, an assignment of colours to point heights is made.

Both the data obtained by mapping the bottom with the multibeam echosounder and the data obtained by LiDAR system are in the form of a point cloud, where each element has the form XYZ. To increase the quality of the obtained solution, the area of analysis and processing of these data is limited by, top-down, polygon with declared vertices. Inside this polygon, a regular grid of points with a fixed, preset, distance between points (the so-called mesh of the grid) is generated. The next step is to divide the points of the generated 2D grid into subsets - MBES, LiDAR and a subset of points that cannot be allocated to the first two at this stage. A point is assigned to the MBES or LiDAR grid subsets, respectively, provided that it is inside the polygon created in the previous step. This approach considers the case of survey sessions where there was an object on the water surface. Thus, if a point belongs to both polygons, it is assigned to both subsets of the grid. Then the projection of LiDAR and MBES data (on the OXY plane) has a common part (points corresponding to the object on the water and those on the bottom of the water body under study). Grid points not assigned to either subset at this stage is stored for later analysis. For each of the subsets so determined, interpolation is performed by the appropriate method (using raw data). There are three methods: linear, natural neighbour and nearest neighbour. The data thus prepared will be used to generate approximate points describing the empty area between the survey data. To enable the most accurate coverage of the area with respect to the OX and OY axes, we use the solution described below, generating points using a heuristic algorithm in each of the possible areas. The fusion between underwater and surface data in each of these subareas (rectangles) is based on the analysis of points on the boundaries of the survey data, that is, within each subarea created, we find the minimum values of the third coordinate of LiDAR points (which determine the upper boundary of the subarea) and the maximum values of the third coordinate of MBES points (which determine the lower boundary of the subarea). In such a sub-area, a heuristic algorithm is applied to generate approximate points describing the area between the survey data. The red fox algorithm (Połap, 2021) was chosen as a representative of these algorithms. The heuristic approach assumes the creation of a certain, often random set of points in a three-dimensional space, bounded in each dimension. Then, using a mathematical function, these points are moved, and the solutions obtained by each point are analysed. The points are evaluated against the adaptation function, which returns information about the quality of the solution obtained. The process is then repeated by successively performing the movement of individuals of the population and re-evaluating against the adaptation function. The algorithm is repeated for a user-specified number of iterations. The greater their number, the more accurate the result. Through the analysis, the use of a heuristic algorithm and the processing of data from the underwater (MBES) and land areas (LiDAR), a coherent set of points in space was generated. Attaching sonar data to the fusion will allow the sonar image to be superimposed on the bottom, or MBES. If an array of colour values extracted from the camera is included, they will be used only for the area covered by LiDAR.

## Results and Discussion

The architecture of the proposed system is structured around four main modules: the acquisition module, underwater data processing module, surface data processing module, and operations/visualization module. These modules encapsulate the functionalities required for data collection, processing, and visualization, forming the core components of the integrated data and fusion module. Each module has undergone thorough study and detailed implementation.

Another significant challenge was to develop a model for a multi-dimensional and multi-temporal knowledge base specific to the coastal zone. This involved designing a database model and establishing guidelines and standards for data storage. The prepared document, intended for end users of the system, outlines the database's purpose, design, and standards for data storage. PostgreSQL was utilized for database preparation, with spatial data obtained from measurements intended to be stored in the relational database. An entity-relationship diagram was developed to illustrate the geodatabase schema. Additionally, a dedicated spatial data model, known as MMTDEF (Multidimensional and Multi-Temporal Data Exchange Format), was created for the project. The MMTDEF spatial data model comprises four primary classes representing templates for bathymetric, sonar, LiDAR, and imagery data representation. Each class inherits attributes from the SensorData abstract class, which includes a uniquely identifiable ID number and a timestamp indicating the time unit in which each measurement data was collected. The data model is visually represented in a diagram format.

This comprehensive approach to system architecture and data modeling ensures the integrity and efficient management of spatial data collected from various sources, facilitating the development of import, export, and processing algorithms for acquired multisensory datasets.

## Conclusion

In building the system, two main technologies were employed: Python 3.1x and Postgres. Their utilization facilitates easy application startup, enables database deployment on a server, and supports communication between the application and database over the network. This approach also ensures scalability of the database, data sharing among multiple applications, and centralization of utilized data. The system is distinguished by its operational automation, requiring end users only to place measurement data in designated directories.

Convolutional U-NET neural networks are utilized for image data processing, precisely identifying the image's edge line to extract data above it. Additionally, computational intelligence was employed to generate data; a heuristic algorithm bridges the gap between underwater and surface data by generating a specified number of points between survey data. These points are then interpolated to create a grid, forming an innovative spatial data fusion model.

All sensors and components of the system will be consolidated on a single survey vessel, allowing data collection in a single pass and subsequent integration into a unified model. Multimodal data from multibeam echo sounder, 3D side-scan sonar, and mobile laser scanner, supported by video images, undergo a sensory fusion process to constitute the content of a spatial spherical map. This approach, unprecedented in the world, offers a futuristic and enhanced means of spatial data analysis and visualization, ensuring improved perception for system users compared to previous solutions.

In addition to placing all sensors and components on a single test unit for streamlined data collection and integration, standards will be developed to ensure the accuracy of the final model. The implemented system can be utilized for various purposes, including coastal zone monitoring such as inventorying coastal infrastructure, updating flood risk maps, expanding geoportals and geo-information systems, and enhancing water tourism. End users gain access to comprehensive and multidimensional data on restricted water bodies, facilitating future forecasting of coastal zone changes.

## Acknowledgements

This work was supported by the National Centre for Research and Development (NCBR) of Poland under grant no. LIDER/4/0026/L-12/20/NCBR/2021.

## References

Albawi, Saad, Tareq Abed Mohammed, and Saad Al-Zawi. (2017), Understanding of a convolutional neural network. 2017 international conference on engineering and technology (ICET), IEEE

Bonaccorso, G. (2018) Algorytmy uczenia maszynowego. Zaawansowane Techniki Implementacji. Helion, Warszawa
Bovik, Alan C., (2009) 1 st ed. The essential guide to image processing. Academic Press

Burguera, Antoni, and Gabriel Oliver. (2016): High-resolution underwater mapping using side-scan sonar. PloS one 11.1: e0146396.

Coltuc, Dinu, Philippe Bolon, and J-M. Chassery (2006), Exact histogram specification. IEEE Transactions on Image processing 15.5, pp 1143-1152.

Falk, Thorsten, et al. (2019), U-Net: deep learning for cell counting, detection, and morphometry. Nature methods 16.1: 67-70.a

Haralick, Robert M., Stanley R. Sternberg, and Xinhua Zhuang. (1987), Image analysis using mathematical morphology.

IEEE transactions on pattern analysis and machine intelligence 4, pp 532-550.

Henderi, Henderi, Tri Wahyuningsih, and Efana Rahwanto. (2021) Comparison of Min-Max normalization and Z-Score Normalization in the K-nearest neighbor (kNN) Algorithm to Test the Accuracy of Types of Breast Cancer. International Journal of Informatics and Information Systems 4.1, 13-20

Kingma, Diederik P., and Jimmy Ba. (2015), Adam: A method for stochastic optimization. 3rd International Conference on Learning Representations, ICLR 2015, San Diego, CA, USA, May 7-9, 2015, Conference Track Proceedings

Kusrini, Kusrini, Muhammad Resa Arif Yudianto, and Hanif Al Fatta. (2022), The effect of Gaussian filter and data preprocessing on the classification of Punakawan puppet images with the convolutional neural network algorithm. International Journal of Electrical and Computer Engineering 12.4, 3752.

Schwarz, Michael W., William B. Cowan, and John C. Beatty. (1987), An experimental comparison of RGB, YIQ, LAB, HSV, and opponent color models. ACM Transactions on Graphics (tog) 6.2, pp 123-158.

Połap, Dawid, and Marcin Woźniak (2021), Red fox optimization algorithm. Expert Systems with Applications 166: 114107.

INTERNATIONAL SYMPOSIUM ON
APPLIED
GEOINFORMATICS
9-10 May 2024 · Wrocław/Poland

*International Symposium on Applied Geoinformatics (ISAG2024)*

# Past, Contemporary and Future Lunar Referent Coordinate System and Digital Elevation Models

Iskren Ivanov[1]*, Lachezar Filchev[1]

**[1] Space Research and Technology Institute, Bulgarian Academy of Sciences, Department Remote Sensing and GIS, Sofia, Bulgaria**
iso.ivanov@space.bas.bg; ORCID 0009-0006-1904-0127, lachezarhf@space.bas.bg; ORCID 0000-0002-6248-0148

## Abstract

Humans have been fascinated with the Moon for centuries, and mapping its surface has been an important part of our exploration. The first recorded sketches of the Moon were made by British astronomer Thomas Harriot in 1609 using a telescope. Since then, many astronomers have contributed to lunar mapping, including Galileo Galilei, who produced detailed drawings of the Moon's surface in the early 17th century.

In the modern era, the Lunar Orbiter program in the 1960s was the first to capture high-resolution images of the Moon's surface. These images were used to create detailed maps of the Moon, which were essential for the Apollo missions that followed. The Lunar Reconnaissance Orbiter (LRO) mission, launched in 2009, has continued to map the Moon's surface and has provided new insights into the Moon's geology and history.

The Lunar Reference Coordinate System (LRCS) is a framework that provides a consistent and standardized way of defining the location of features on the Moon. The LRCS is based on the International Celestial Reference Frame (ICRF) and is used to define the position of the Moon relative to the Earth and other celestial bodies. The Lunar Digital Elevation Model (LDEM) is a dataset that provides information about the topography of the Moon. The LDEM is generated using data from various missions, including the Lunar Reconnaissance Orbiter (LRO) and the Chang'e-1 mission. The LDEM is used to create high-resolution maps of the Moon's surface, which are useful for scientific research and exploration.

Future missions, such as the Artemis program, will continue to improve our understanding of the Moon's surface. These missions will provide new data that can be used to improve the accuracy of the LRCS and LDEM. In addition, new technologies, such as laser altimetry, will allow for even more precise measurements of the Moon's surface. These advancements will help us to better understand the Moon's geology and history, and will pave the way for future exploration and discovery.

**Keywords:** *Lunar Referent Coordinate System, Digital Elevation Model, DEM, LRO*

## Introduction

Humans have long been fascinated by the Moon, with its enigmatic surface serving as a subject of study and exploration for centuries. From early astronomical sketches to modern space missions, our understanding of the Moon's topography has evolved significantly. As we set our sights on a renewed era of lunar exploration, a precise understanding of the lunar surface is paramount for mission planning, scientific discovery, and resource utilization. Over the past decade, significant advancements in lunar mapping techniques have revolutionized our ability to characterize the lunar landscape. This paper delves into these recent developments, focusing on the critical roles played by the Lunar Reference Coordinate System (LRCS) and Digital Elevation Models (DEMs). The Lunar CRS provides a standardized framework for precisely defining the location of features on the lunar surface, enabling seamless integration of data from diverse missions and facilitating comprehensive mapping efforts. Meanwhile, DEMs offer invaluable topographic information, allowing for the creation of detailed elevation maps that enhance our understanding of lunar morphology and terrain. We explore the evolution of the Lunar CRS, highlighting its importance in establishing a standardized framework for lunar data analysis and facilitating cross-mission collaboration. Additionally, we examine the creation and refinement of DEMs, showcasing how these detailed topographic representations are crucial for lunar exploration activities such as safe landing site selection, rover pathfinding, and resource prospecting.

The aim of this paper is through a comprehensive review of peer-reviewed scientific papers and recent advancements in the field, to shed light on the cutting-edge developments in lunar mapping and their implications for lunar exploration. By synthesizing existing knowledge and identifying emerging trends, we aim to provide a comprehensive overview of the current state of lunar cartography and pave the way for future research endeavors in this exciting field.

## Materials and Methods

The foundation of this review paper is built upon an extensive literature review spanning past, contemporary, and emerging research on lunar referent coordinate systems (CRS) and digital elevation models (DEMs). Peer-reviewed scientific papers, conference proceedings, technical reports, and relevant publications from reputable journals were systematically searched and critically evaluated to identify key advancements, methodologies, and findings in the field of lunar cartography. The search encompassed electronic databases including PubMed, IEEE Xplore, Web of Science, Scopus, and Google Scholar. Keywords such as "lunar coordinate system," "lunar DEM," "lunar mapping," and variations thereof were used to identify pertinent articles, reviews, conference papers, and technical reports.

The review focused on selecting papers concerning lunar Coordinate Reference Systems (CRS) and Digital Elevation Models (DEMs), prioritizing recent publications with innovative methodologies or significant findings, alongside seminal works for historical context. Data extraction involved documenting study objectives, methodologies, datasets, and conclusions to identify common themes and trends. Comparative analysis evaluated CRS and DEMs' strengths and limitations in lunar exploration, considering accuracy, resolution, and applications. Synthesizing collected data provided insights into past, present, and future trends, emphasizing advancements, methodologies, and challenges in the field. Limitations such as publication and selection biases were acknowledged, addressed through rigorous search criteria and critical appraisal. Ethical considerations ensured adherence to scientific research standards, including proper citation, respect for intellectual property, and academic integrity.

## Historical development of the unified Lunar Coordinate Systems

This chronology traces the evolution of unified lunar coordinates from early telescopic observations to modern mapping techniques, emphasizing the importance of standardization and collaboration in lunar exploration and research. It begins with early astronomers like Galileo Galilei and Johannes Hevelius mapping the Moon's surface using rudimentary coordinate systems in the 17th century, followed by more detailed mapping efforts with the invention of the telescope by astronomers such as Thomas Harriot and Giovanni Battista Riccioli. The establishment of the first unified lunar coordinate system by the International Astronomical Union (IAU) in the late 20th century addressed the need for standardization amid increasing data volume from lunar missions like NASA's Lunar Orbiter program in the 1960s and the Apollo missions in the late 1960s and early 1970s.

The mid-20th century saw a surge in efforts to establish a precise lunar coordinate system. R.B. Baldwin's work provided the first reliable estimates of the Moon's shape, laying the groundwork for cataloging lunar features and creating detailed control networks by U.S. authorities like the Army Map Service and the Department of Defense in preparation for upcoming spaceflights. Soviet, UK, and international science teams expanded these networks, relying on ground-based telescope photographs. Kiev's Triangulation system attempted to align control points relative to the Moon's mass center. Apollo missions enabled astronauts to measure landmark positions using sextants, while Lunar Orbiters IV provided high-resolution images for the Apollo Zone Triangulation System. Laser Ranging Retroreflectors (LRRR) placed during Apollo missions established precise lunar surface locations, aiding ground-based laser ranging and radio interferometry measurements (Schimerman, 1973). Efforts in the late 20th and early 21st centuries led to the introduction of the Lunar Coordinate System (LCS) and the Unified Lunar Control Network (ULCN) to standardize lunar mapping and promote data sharing. The Unified Lunar Control Network (ULCN) emerged, incorporating Apollo mission, ground-based telescope, and Mariner 10 spacecraft data. Subsequent ULCN iterations, like ULCN 1994 and ULCN 2005, refined and expanded control points, with ULCN 2005 adopting a new approach based on Clementine mission data (Davies et al. 1987; Acrhinal et al 2006). This system was later adopted by the IAU Planetary Gazetteer in October 2010 for reporting lunar feature coordinates. Celestial Reference Frames establish a global system for defining the position and orientation of celestial bodies like the Moon, anchoring lunar coordinates to known celestial points such as stars and quasars. The International Celestial Reference Frame (ICRF) is crucial for celestial navigation, providing precise coordinates for objects including the Moon by integrating data from telescopes and space missions (Fey et al, 2015). Modern mapping techniques such as laser altimetry, photogrammetry, and radar mapping have further refined our understanding of the Moon's surface, enabling the creation of high-resolution digital elevation models (DEMs) and detailed maps of lunar features. A brief timeline of the development of Lunar CRS is presented on Figure 1.

|---------|----------------------------|------------|-------------|----------------|-------------------|-----------------------|
**Early Telescopic Establishment Lunar Apollo Introduction Modern Mapping**
**Observations Mapping of Lunar Orbiter Missions of Unified Techniques**
**(17th c.) (Early 17th c.) Coordinate Program (1960s) Lunar Coordinates (21st c.)**
Systems (Late 20th c.) (1960s)

**Figure 1.** Timeline of the historical developments of the unified Lunar Coordinate Reference Systems (LCRS).

## Historical development of Lunar Digital Elevation Models (LDEMs)

The chronology of lunar Digital Elevation Models (DEMs) tracks the progression of mapping techniques and technologies, from early visual observations to modern remote sensing instruments, each contributing to our understanding of lunar topography, see Figure 2. Early mapping relied on visual observations, lacking precise elevation data. The NASA-led Lunar Orbiter program in the 1960s captured high-resolution images, aiding in the creation of rudimentary elevation models. Apollo missions conducted detailed measurements, refining DEM accuracy. Subsequent missions like Clementine and Lunar Prospector generated global DEMs with enhanced coverage and resolution. Japanese missions, such as Kaguya, contributed high-resolution imagery for detailed DEMs, while NASA's Lunar Reconnaissance Orbiter (LRO) mission significantly advanced mapping efforts with its high-resolution Lunar Orbiter Laser Altimeter (LOLA) instrument. Chinese missions, including Chang'e series, further added to DEM generation. Integration efforts aim to merge lunar DEMs with global datasets for seamless navigation and analysis, supporting future exploration and research on the Moon.

| 1 | Early Mapping | Lunar Orbiter Program | Apollo Missions | Clementine Mission | Lunar Prospector | Japanese Missions | NASA's (LRO) | Chinese Missions & Integration with Global Datasets |
|---|---|---|---|---|---|---|---|---|
|  | (Pre-1960s) | (1960s) | (1960s - 1970s) | (1994) | (1998-1999) | (Kaguya/SELENE, 2007) | (2009 - Present) | Chang'e series) |

**Figure 2.** Timeline of the historical developments of the unified Lunar DEMS

## Methods, Methodologies and Techniques for the evolution of Lunar CRS

Different methodologies like photogrammetry, laser altimetry, and celestial reference frames contribute to lunar Coordinate Reference Systems (CRS) development. Photogrammetry analyzes stereo images to derive three-dimensional lunar feature coordinates, while laser altimetry measures surface elevations accurately using laser pulses.

Photogrammetry analyzes stereo images to derive three-dimensional coordinates of lunar features, enabling the reconstruction of surface topography and the generation of high-resolution digital elevation models (DEMs). The Lunar Reconnaissance Orbiter Camera (LROC), specifically its Narrow Angle Camera (NAC), utilizes photogrammetric techniques to create precise topographic maps of the Moon's surface, achieving resolutions as high as 0.5 meters per pixel (Humm et al. 2016).

Laser Altimetry, using laser pulses emitted from orbiting spacecraft, precisely measures surface elevations on the Moon by calculating the time it takes for the pulses to travel to the surface and back. This method provides accurate elevation profiles and surface roughness data. NASA's Lunar Reconnaissance Orbiter (LRO) equipped with the Lunar Orbiter Laser Altimeter (LOLA) achieves centimeter-level accuracy in measuring lunar surface elevations, producing detailed topographic maps revealing features like craters, mountains, and valleys (Riris et al. 2009).

Mathematical modeling techniques define and transform coordinates within lunar Coordinate Reference Systems (LCRS), considering factors like lunar libration, nutation, and precession affecting the Moon's position relative to Earth and other celestial bodies. The Unified Lunar Control Network (ULCN) employs mathematical models to predict lunar landmark positions, ensuring consistency in lunar mapping. Integrating data from lunar missions and Earth-based observations, ULCN ensures accuracy and reliability in lunar CRS (Mulholland, 1977; Rambaux, & Williams, 2011).

## Contemporary Lunar CRSs

Two LCRS historically define the Moon's body-fixed rotating coordinate system: the Mean Earth/polar axis system (ME) and the Principal Axis system (PA). The ME system, preferred by the International Astronomical Union (IAU) and the International Association of Geodesy (IAG), utilizes the mean Earth direction to establish the prime meridian, with the z-axis denoting the mean rotational pole. Longitude progresses from 0° at the Prime Meridian, while Latitude ranges from 0° at the Equator to 90° at the poles. Conversely, the PA system aligns with the Moon's principal axes, with its prime meridian directed by the longest axis toward Earth. The axes of ME and PA systems deviate by about 1 kilometer at the lunar surface, impacting dynamical calculations like gravity field determination and lunar laser ranging (LLR) (Brent, 2006). The Mean Earth/polar axis (ME) coordinate system serves as the current lunar reference coordinate system, with the JPL DE 421 lunar orientation ephemeris rotated to align with it. ME inherently define north, the equator, and typically includes separate definitions for longitude direction. The International Astronomical Union (IAU) Working Group on Cartographic Coordinates and Rotational Elements (WGCCRE) recognizes both -180° west to +180° east and 0° to 360° east longitude for the Moon, for historical reasons. A spherical reference surface with a radius of 1737.4 km is recommended for measuring elevation and map projection scaling in the ME system. The Lunar Orbiter Laser Altimeter (LOLA) global Digital Elevation Model (DEM) is aligned with the JPL DE421 ME frame, providing a topographic surface for referencing other data. This surface's height is presented in separate products from both the Moon's center and the reference sphere (Final report…, 2021). The Lunar Reference System is the coordinate framework that will power a GPS-like transmission system being built by NASA and others. That's what NGA's World Geodetic System 1984, commonly referred to as WGS 84, and currently provides for GPS here on Earth. GPS is the delivery system (Goodman, 2023).

## Methods, Methodologies and Techniques in the Development of Lunar Digital Elevation Models (DEMs)

Stereophotogrammetry analyzes stereo images from varying perspectives to extract three-dimensional details of the lunar surface. Comparing overlapping images allows researchers to ascertain surface elevation, producing high-resolution Digital Elevation Models (DEMs). NASA's Lunar Reconnaissance Orbiter Camera (LROC) employs stereophotogrammetry techniques to create detailed DEMs of the Moon's surface (Robinson, 2010).

Laser altimetry uses laser pulses emitted from orbiting spacecraft to measure lunar surface elevation by precisely timing their return. This method enables researchers to create detailed Digital Elevation Models (DEMs) with high accuracy. NASA's Lunar Orbiter Laser Altimeter (LOLA) on the LRO mission employs laser altimetry to measure lunar surface elevations and generate high-resolution DEMs (Smith et al. 2010).

Radar altimetry sends radar signals to the lunar surface, measuring their return time to provide elevation data for generating DEMs, particularly useful in areas with challenging lighting or surface features. NASA's Lunar Reconnaissance Orbiter (LRO) employs the Miniature Radio Frequency (Mini-RF) instrument for radar altimetry, mapping surface elevations and creating DEMs of the Moon's polar regions (Cahill et al, 2014).

Gravimetry measures lunar gravitational field variations influenced by surface topography and subsurface density. This data helps infer surface elevations and create DEMs of the lunar surface. The Gravity Recovery and Interior Laboratory (GRAIL) mission, with twin spacecraft orbiting the Moon, employed gravimetry to map gravitational field variations, aiding in inferring lunar surface topography and generating DEMs (Zuber et al. 2013).

Photogrammetric techniques analyze spacecraft images to derive elevation data via stereo imaging and feature matching algorithms, creating DEMs with varying resolutions and coverage. China National Space Administration's (CNSA) Chang'e missions employ photogrammetry to generate lunar surface DEMs using onboard camera imagery (Hu et al. 2013).

## Contemporary Lunar DEMs

In 2013, the Moon LRO LOLA DEM 118m v1 digital elevation model (DEM) was created from data collected by NASA's Lunar Reconnaissance Orbiter (LRO) spacecraft's Lunar Orbiter Laser Altimeter (LOLA) between July 2009 and July 2013. This DEM comprises over 6.5 billion measurements, with elevations determined by subtracting the lunar reference radius from surface measurements, resulting in an average horizontal accuracy of better than 20 meters and a vertical accuracy of approximately 1 meter. Generated using Generic Mapping Tools software, it has a resolution of 256 pixels per degree, equivalent to 118 meters at the equator. In 2015, the Moon LRO LOLA - SELENE Kaguya TC DEM Merge 60N60S 59m v1 was produced through collaboration between LOLA and SELENE Kaguya Teams. Covering latitudes within ±60°, this DEM has a horizontal resolution of 512 pixels per degree (about 59 meters per pixel at the equator) and a typical vertical accuracy of 3 to 4 meters. It was created by incorporating approximately 4.5 billion geodetically-accurate topographic heights from LOLA and co-registering 43,200 stereo-derived DEMs (each 1°×1°) from the Terrain Camera (TC). The resulting merged DEM, referred to as "SLDEM2015," is referenced to a radius of 1,737,400 meters (Barker, et al. 2015).

## Conclusion

Recent advancements in lunar mapping, including the establishment of Lunar Coordinate Reference Systems (CRS) and high-resolution Digital Elevation Models (DEMs), have significantly improved our understanding of the Moon's surface geology and morphology. Despite progress, challenges persist in lunar CRS, such as resolution and accuracy variations across datasets, discrepancies in coordinate systems used by different missions, and the need for continuous updates to accommodate new data. Future research may focus on developing advanced CRS using technologies like machine learning and artificial intelligence, as well as integrating lunar CRS with other planetary coordinate systems for interplanetary exploration and navigation. Upcoming missions like NASA's Artemis program and China's Chang'e missions are expected to enhance lunar coordinate accuracy and resolution, while technological advancements, including AI and machine learning, will refine lunar mapping techniques. Integrating lunar coordinate systems with planetary systems, like the International Celestial Reference Frame (ICRF), will facilitate seamless navigation across celestial bodies, supporting interplanetary missions and broadening our understanding of the solar system. Collaboration among space agencies, research institutions, and international organizations is essential for standardizing lunar coordinate systems, ensuring accuracy, accessibility, and comprehensiveness in lunar mapping efforts. In conclusion, lunar referent coordinate systems are vital for lunar exploration and research, providing a standardized framework for geolocation and spatial analysis. This review contributes to advancing lunar exploration by examining the evolution, methodologies, applications, challenges, and future directions of lunar CRS. Continued efforts in mapping refinement and data integration will further enhance our understanding of the Moon and support future lunar exploration endeavors.

## Acknowledgements

Iskren Ivanov is a full-time PhD student in Space Research and Technology Institute – Bulgarian Academy of Sciences. Mr. Ivanov expresses his gratitude to his tutor, Professor PhD Lachezar Filchev and gratefully acknowledges HUAWEI Seeds for the Future 2023 scholarship program for providing financial support during the course of this research.

## References

Archinal, B., Rosiek, M.R., Redding, B.. (2006). Unified Lunar Control Network 2005 and Topographic Model.

Barker, M. K., Mazarico, E., Neumann, G. A., Zuber, M. T., Haruyama, J., Smith, D. E. (2015). "A new lunar digital elevation model from the Lunar Orbiter Laser Altimeter and SELENE Terrain Camera," Icarus, Volume 273, p. 346-355. http://dx.doi.org/10.1016/j.icarus.2015.07.039

Cahill, J. T. S., Thomson, B. J., Patterson, G. W., Bussey, D. B. J., Neish, C. D., Lopez, N. R., Turner, F. S., Aldridge, T., McAdam, M., Meyer, H. M., Raney, R. K., Carter, L. M., Spudis, P. D., Hiesinger, H., & Pasckert, J. H. (2014). The Miniature Radio Frequency instrument's (Mini-RF) global observations of Earth's Moon. Icarus, 243, 173-190. https://doi.org/10.1016/j.icarus.2014.07.018

Davies, Merton E., Tim R. Colvin, and David Meyer, A Unified Lunar Control Network — The Near Side, RAND Corporation, N-2664-NASA, 1987. As of March 22, 2024: https://www.rand.org/pubs/notes/N2664.html

Fey, A. L., Gordon, D., Jacobs, C. S., Ma, C., Gaume, R. A., Arias, E. F., … & Boboltz, D. (2015). The Second Realization of the International Celestial Reference Frame by Very Long Baseline Interferometry. The Astronomical Journal, 150(2), 58

Goodman, A. (2023). NGA Leads Development of Navigational Reference System for the Moon. NGA. https://www.nga.mil/news/NGA_Leads_Development_of_Navigational_Reference_Sy.html (Accessed on 4/14/2024)

Hu, Wenmin & Di, Kaichang & Liu, Zhaoqin & Ping, Jinsong. (2013). A new lunar global DEM derived from Chang'E-1 Laser Altimeter data based on crossover adjustment with local topographic constraint. Planetary and Space Science. 87. 173–182. 10.1016/j.pss.2013.08.004.

Humm, D. C., Tschimmel, M., Brylow, S. M., Mahanti, P., Tran, T. N., Braden, S. E., Wiseman, S., Danton, J., Eliason, E. M., & Robinson, M. S. (2016). Flight Calibration of the LROC Narrow Angle Camera. Space Science Reviews, 200, 431–473

Brent, A. (2006) Lunar Coordinates and Cartography: Coordinate System Establishment, Improvement, and Control (Registration) of Lunar Datasets, from Past, Present and Future U. S. and Foreign Missions Response to "Request for Information (RFI): Developing a Strategy for Future Exploration of the Moon and Beyond" 2006 May 12 Archinal Astrogeology Team U. S. Geological Survey.

Mulholland, J. D. (1977). Mathematical Modelling of Lunar Laser Measures and Their Application to Improvement of Physical Parameters. In Scientific Applications of Lunar Laser Ranging (pp. 9-18). D. Reidel Publishing Company.

Rambaux, N., & Williams, J. G. (2011). The Moon's physical librations and determination of their free modesCelestial Mechanics and Dynamical Astronomy, 109, 85–1001.

Riris, H., Cavanaugh, J. F., Sun, X., Ramos-Izquierdo, L., Liiva, P., Rodriguez, M., Schmidt, S., McGarry, J., Peters, C., Jackson, G. B., & Smith, D. E. (2009). The Lunar Orbiter Laser Altimeter (LOLA) on NASA's Lunar Reconnaissance Orbiter (LRO) MissionCLEO: 2009 - Laser Science to Photonic Applications

Robinson, M. S., et al. (2010). Lunar Reconnaissance Orbiter Camera (LROC) Instrument Overview. Space Science Reviews, 150(1-4), 81-124.

Schimerman, Lawrence A., (1973). editor. Lunar Cartographic Dossier. St. Louis, MO: Defense Mapping Agency for NASA.

Smith, D. E., et al. (2010). Initial observations from the Lunar Orbiter Laser Altimeter (LOLA). Geophysical research letters, Vol. 37, L18204, doi:10.1029/2010GL043751

Zuber, M. T., et al. (2013). Gravity Field of the Moon from the Gravity Recovery and Interior Laboratory (GRAIL) Mission. Science, 339 (6119), 668-671.

Final Report of the Lunar Critical Data Products Specific Action Team (September 2021)

Chinese National Space Administration (CNSA). (n.d.). Chang'e Program. Retrieved from http://www.cnsa.gov.cn/n6758823/n6758838/index.html

NASA. (n.d.). Lunar Reconnaissance Orbiter (LRO). Retrieved from
https://www.nasa.gov/mission_pages/LRO/main/index.html

*International Symposium on Applied Geoinformatics (ISAG2024)*

# GEOMORPHOLOGICAL STRUCTURAL MAPPING OF DRYDEN CRATER ON THE MOON USING MAPPY TOOL PLUGIN IN QGIS SOFTWARE

Iskren Ivanov[1]*, Lachezar Filchev[1]

**[1] Space Research and Technology Institute, Bulgarian Academy of Sciences, Department Remote Sensing and GIS, Sofia, Bulgaria**
iso.ivanov@space.bas.bg; ORCID 0009-0006-1904-0127, lachezarhf@space.bas.bg; ORCID 0000-0002-6248-0148

## Abstract

The Moon, Earth's natural satellite, has been a subject of increasing interest for scientific exploration and understanding of planetary evolution. This paper presents a detailed geological structural map of Dryden Crater on the Moon, utilizing advanced mapping techniques within the Quantum Geographic Information System (QGIS) software. The study leverages the capabilities of the Mappy Tool Plugin, a specialized tool designed for planetary geological cartography.

The methodology involves the integration of high-resolution lunar data, including imagery acquired from lunar missions and digital elevation model, created by the instrument's team. These datasets are processed and manipulated within the QGIS environment, allowing for the creation of a comprehensive geological structural map. The Mappy Tool Plugin, specifically tailored for planetary geology applications, enhances the mapping process by providing advanced functionalities.

The resulting geological map of Dryden Crater showcases detailed structural features and delineates their boundaries. The identification and characterization of the different feature units contribute to a better understanding of the crater's geological history and evolution. The map serves as a valuable resource for future lunar exploration missions. It helps researchers identify potential safe landing sites, exploration routes for robotic or human missions, study impact craters, volcanic structures, and geological processes that have shaped the lunar surface over time.

This paper highlights the significance of employing open-source GIS software, such as QGIS, in conjunction with specialized plugins like Mappy Tool, for lunar geological studies. It contributes to the ongoing efforts to unravel the geological mysteries of the Moon, paving the way for deeper insights into planetary processes and evolution.

**Keywords:** *Geologic mapping, Cartography, Impact crater, Dryden, Moon*

## Introduction

The Moon, our closest celestial neighbor, holds secrets about our solar system's formation and is closely linked to Earths evolution (Bottke, 2016). Studying impact craters contributes to a deeper understanding of the Moon's formation and geological history. Craters excavate material from deep below the surface, present in the crater's ejecta material and central peaks. These peaks result from the rebound of the compressed material underlying the crater bottom. Analyzing craters sheds light on the evolution and composition of the lunar crust, offering valuable geological insights. Investigating the crater's features and composition helps us reconstruct the Moon's and early solar system's geological history. Studies of crater density within impact craters and their ejecta provide insights about the absolute age of the studied lunar surface. By understanding the crater's characteristics, we can inform observation strategies for orbiting probes and select high-interest locations for future missions. These locations can include safe landing sites and traverses for rovers, as well as pinpointing scientifically valuable exploration sites within the craters or revealing potential resources crucial for future human presence on the Moon, guiding resource-focused missions. Craters are a compelling target for exploration due to their unique characteristics (National Research Council, 2007).

Nestled on the far side of the Moon within the Apollo basin, Dryden crater boasts a complex morphology despite its ~52 km diameter. Located at -33.1°S, 156.1°W, this crater displays a distinctive lack of rays but possesses discernible ejecta.

Dryden's irregular shape is further accentuated by its sharp-crested rim. Rising from the hummocky crater floor is a preserved central peak, reaching a height of ~0.7 km. This peak, formed by the impact's rebounding crust, stands out noticeably against the surrounding terrain. Its slightly off-center position suggests an oblique impact origin in the NE-SW direction of about 35-20 degrees, further supported by the distribution of the crater's ejecta (Kenkmann, 2014). Unlike surrounding areas, the crater surface exhibits no signs of volcanic activity. Instead, numerous slumped terraces grace the hummocky floor, remnants of material sliding down the crater walls. Classified as an Imbrian-aged crater in both the 2013 Lunar 1:5M Geologic Map Renovation (Wilhelms, 2013) and the 2020 Unified Geologic Map of the Moon (1:5M) (Ivanov, 2018), (Fortezzo, 2020), Dryden stands out as one of the Apollo basin's largest and most preserved impact craters. Dating to the Upper Imbrian period, Dryden displays a more subdued morphology compared to younger Eratosthenian and Copernican craters. Notably, it formed later than the Orientale basin and the flat, smooth, and low-albedo surfaces, likely basaltic lava flows, found within 100 km within the Apollo basin (Ivanov, 2018). Recent crater counts estimate Dryden's absolute model age at 3.68 ± 0.03/-0.04 billion years (Ga) (Ivanov, 2018). This study utilizes morpho-stratigraphic mapping techniques to conduct a comprehensive geological analysis of Dryden crater. By analyzing data from the Lunar Reconnaissance Orbiter's Wide Angle Camera, the research reveals that a sequence of tectonic events and gravitational collapses have shaped the crater over its existence. These events are evidenced by the formation of slump terraces originating from the crater wall, rim, and surrounding area.

## Materials and Methods

Our study involved creating a morpho-stratigraphic map of Dryden crater using photo-geological interpretation. The foundation for this map was the Lunar Reconnaissance Orbiter Wide Angle Camera (LROC-WAC) monochrome global mosaic basemap with a resolution of ~100 meters per pixel "Moon LRO LROC WAC Global Morphology Mosaic 100m v3" (Speyerer, 2018). We also incorporated topographic data obtained by the merging of Lunar Orbiter Laser Altimeter (LOLA) and the Kaguya TC Digital Elevation Model (DEM) "Moon LRO LOLA - SELENE Kaguya TC DEM Merge 60N60S 59m v1", "SLDEM2015" (Barker, 2016). This combined data has a resolution of ~59 meters per pixel and allowed us to generate a surface slope map, differentiating areas based on their steepness (ranging from high angles above 35 degrees to low angles below 10 degrees). To produce the map, we plotted it over the Moon LRO LOLA - SELENE Kaguya TC Shaded Relief Merge 60N60S 59m v1 (Figure 1). USGS Astrogeology Science Center website is the source we have retrieved the LROC-WAC and DEM basemaps. We used QGIS 3.34.1 software with the Mappy plugin (Penasa, 2022) to create the morpho-stratigraphic map. This plugin simplifies geological map creation and utilizes a polar stereographic projection (Hargitai, 2017) with the D_MOON datum. The chosen mapping scale of 1:200,000 is determined by the formula:

$$Sm = Rr \times 2000$$

where Sm is the mapping scale and Rr is the raster resolution of the used basemap data (Tobler, 1987). To distinguish various features on the map, we created a dedicated geodatabase. Linear features like contacts, morphologies, and structures were represented by lines, while distinct geological units were depicted using polygonal areas. The mapping process involved defining these features, delineating boundaries between units, and finally generating the final geological units based on the established contacts.

## Results

In order to create the morpho-stratigraphic map of Dryden few additional by-product maps have been created using the DEM, such as map of surface slopes, see Figure 1.

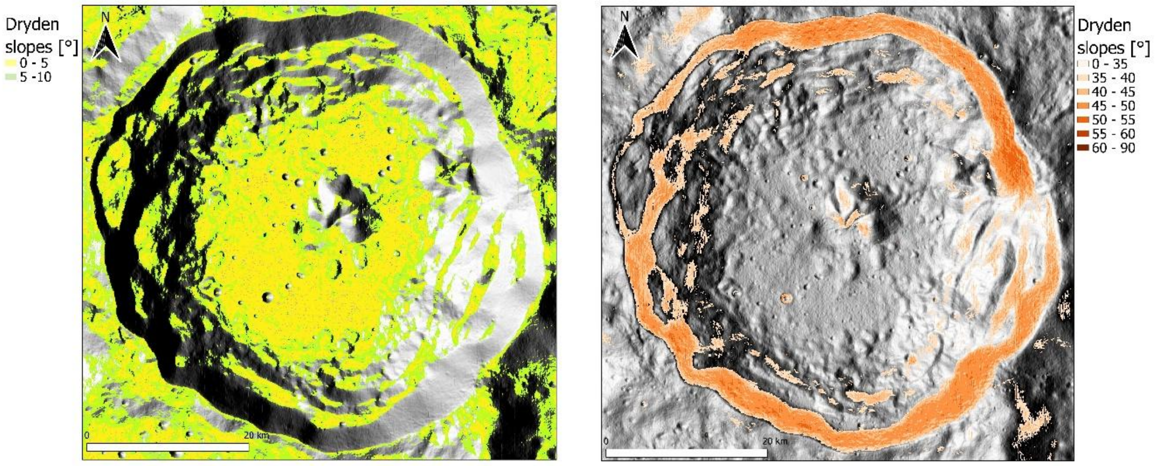

**A)** **B)**

**Figure 1.** A) Surface slope map for slopes < 10°; B) Surface slope map for slopes >35° on top of the Moon LRO LOLA - SELENE Kaguya TC Shaded Relief Merge 60N60S 59m v1. The lunar far side Dryden crater in polar stereographic projection.

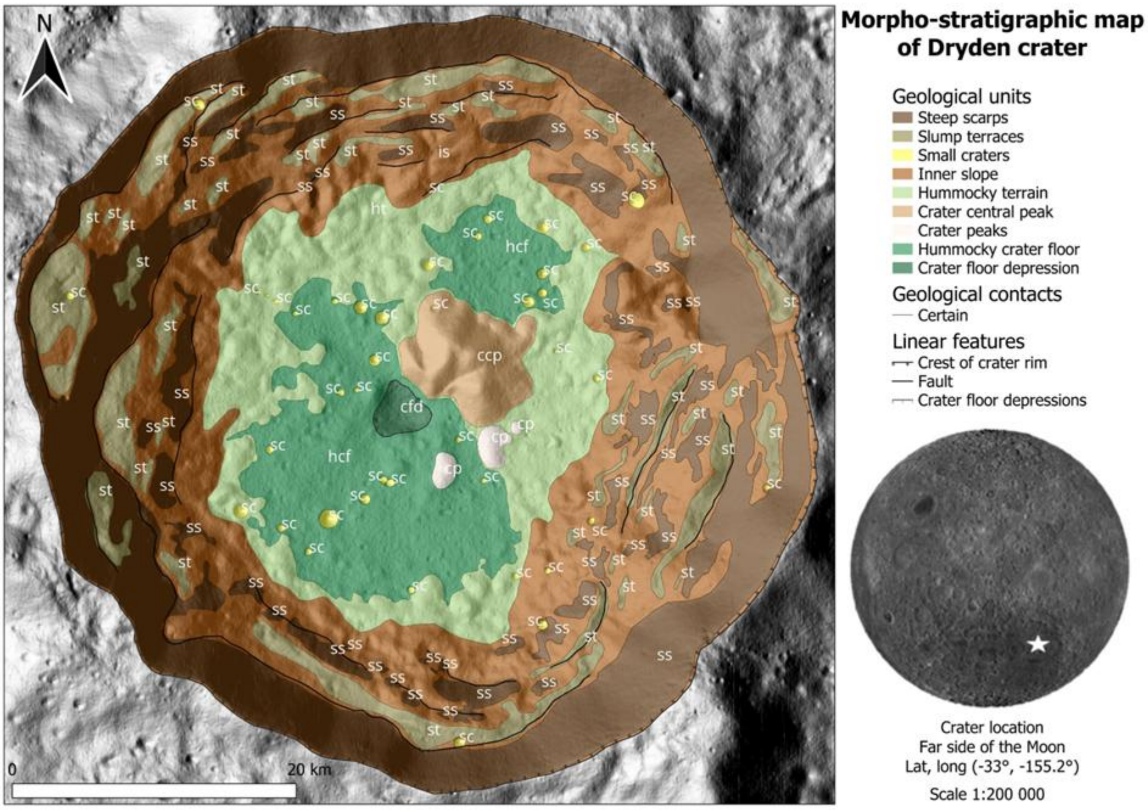

**Figure 2.** Morpho-stratigraphic map of Dryden crater on top of the Moon LRO LOLA - SELENE Kaguya TC Shaded Relief Merge 60N60S 59m v1.

The morpho-stratigraphic map is shown in Figure 2 on top of the Shaded Relief Merge DEM basemap. Hereinafter, follows a brief description of the geologic units associated with unit labels enlisted in stratigraphic order:

ss – steep scarps: exposed steep scarps with slopes ≥ 35°.

st – slump terraces: sections of the rim and walls of a crater's initial excavation cavity that slumped into the cavity during the modification stages (Kenkmann, 2012) of crater formation with slopes ≤10°.

sc – small craters: small impact craters rarely reaching diameter over 1 km.

is – inner slope: scarps ≥10° and ≤ 35° generated by the inward collapse of the crater inner slope during the modification stage.

ht – hummocky terrain: terrain distinguished with its rolling hummocky areas and characterized by smooth space weathered relatively bright material reworked during the impact that slumped from the crater walls and rough rocky brighter (high albedo) material that were pushed inwards of the subsequent slump terraces.

ccp – crater central peak: central peak morphology rising about 0.7 km above the hummocky crater floor.

cp – central peaks: central peaks morphology rising about 0.2 km above the hummocky crater floor.

hcf – hummocky crater floor: particularly horizontal (mostly ≤ 5°) terrain characterized by smooth space weathered relatively bright material reworked during the impact with sparsely scattered rough rocky brighter (high albedo) material, punctured by minor impacts rarely reaching diameter of > 700 m.

cfd – crater floor depression: terrain ~200 m under the altitude of the hummocky crater floor characterized by smooth space weathered relatively bright material reworked during the impact and sparsely scattered rough brighter rocky material, punctured by minor impacts.

The crater rim delimits mapping area, see Figure 2. The morphology of this complex crater allowed distinguishing 5 main units on the crater floor, three more units on the crater walls and in addition the small craters into the crater. The stratigraphic correlations between the different geologic units were inferred determining the genesis of an impact crater formation and by observing morphological evidences.

Dryden crater exhibits complex terraced walls, hummocks, central peaks and hummocky floor. It is characterized by a polygonal rim outline and terraced crater walls, results of the modification phenomena of rim slumping (Settle, 1979). Terrace ledges ascend to greater elevations as the radial range increases. Slump terraces are interpreted to be sections of the rim and walls of crater's initial excavation cavity that slumped into the cavity during the modification stage (Kenkmann, 2012) of crater formation due to tectonic and gravitational forces towards the crater floor. The terraced blocks within the structure of wall terraces retained significant cohesion during the rim slumping event. Crater central peak and surrounding peaks result of the floor rebound due to the high compression of the underlying material (French, 1998).

## Conclusion

Dryden crater is a complex impact crater with a complex geological history, located on the far side of the Moon within the Apollo basin. At ~52 km in diameter, it exhibits a subdued morphology compared to younger lunar craters. Recent crater counts estimate its absolute model age at 3.68 ± 0.03/-0.04 billion years (Ga), classifying it as an Imbrian crater. Analysis of the crater's off-center central peak and ejecta distribution points towards an oblique impact origin in the NE-SW direction of about 35-20 degrees. Despite lacking rays, Dryden crater exhibits a distinct character with discernible ejecta, an irregular shape, and a sharp-crested rim. A prominent feature is its central peak, reaching nearly 0.7 kilometers high and rising from a hummocky crater floor. Intriguingly, the absence of volcanic activity contrasts with the presence of numerous slumped terraces, formed by a sequence of tectonic events and gravitational collapses that shaped the crater over its existence. Dryden is a valuable example of an impact crater significantly modified by subsequent geological processes.

## Acknowledgements

Iskren Ivanov is a full-time PhD student in Space Research and Technology Institute – Bulgarian Academy of Sciences. Mr. Ivanov expresses his gratitude to his tutor, Professor PhD Lachezar Filchev and gratefully acknowledges HUAWEI Seeds for the Future 2023 scholarship program for providing financial support during the course of this research.

## References

Barker, M.K. Mazarico, E. Neumann, G.A. Zuber, M.T. Haruyama, J. Smith, D.E. (2016). A new lunar digital elevation model from the Lunar Orbiter Laser Altimeter and SELENE Terrain Camera, Icarus, Volume 273, Pages 346-355, ISSN 0019-1035, DOI:https://doi.org/10.1016/j.icarus.2015.07.039.

Bottke, W.F. Allen, C. Anand, et. al. (2016). Exploring the Bombardment History of the Moon, Bulletin of the AAS, 53, 2011-2020, DOI:https://doi.org/10.3847/25c2cfeb.20cfd0a3.

Fortezzo, C.M., Spudis, P. D. and Harrel, S. L. (2020). Release of the Digital Unified Global Geologic Map of the Moon At 1:5,000,000- Scale. Paper presented at the 51st Lunar and Planetary Science Conference, Lunar and Planetary Institute, Houston, TX.

French, B.M. (1998). Traces of Catastrophe: A Handbook of Shock-Metamorphic Effects in Terrestrial Meteorite Impact Structures, LPI Contribution No. 954, 120 pp, Lunar and Planetary Institute, Houston.

Hargitai, H. Wang, J. Stooke, P. Karachevtseva, I. Kereszturi, A. Gede, M. (2017). Map Projections in Planetary Cartography, DOI:https://doi.org/10.1007/978-3-319-51835-0_7.

Ivanov, M. Hiesinger, H. van der Bogert, C. Orgel, C. Pasckert, J. Head, J. (2018). Geologic History of the Northern Portion of the South Pole-Aitken Basin on the Moon, Journal of Geophysical Research: Planets, 123, DOI:https://doi.org/10.1029/2018JE005590.

Kenkmann, T. Collins, G. Wünnemann, K. (2012). The Modification Stage of Crater Formation, DOI:https://doi.org/10.1002/9781118447307.ch5.

Kenkmann, T. Poelchau, M. Wulf, G. (2014). Structural geology of impact craters, Journal of Structural Geology, 62, DOI:https://doi.org/10.1016/j.jsg.2014.01.015.

National Research Council. (2007). The Scientific Context for Exploration of the Moon, The National Academies Press, ISBN 978-0-309-10919-2, Washington, DC, USA.

Penasa, L. Pozzobon, R. Galluzzi, V. Brandt, C. H. Frigeri, A. Lucchetti, A.Toffoli, B. D. Naß, A. Rossi, A. P. Massironi, M. (2022). Mappy: A Python Plugin to Ease Geological Mapping with QGIS; SGI Trieste, DOI:https://doi.org/10.5281/zenodo.5233646.

Robinson, M.S. Brylow, S.M. Tschimmel, M. Humm, D. Lawrence, S.J. Thomas, P.C. Denevi, B.W. Bowman-Cisneros, E. Zerr, J. Ravine, M.A. et al. (2010). Lunar reconnaissance orbiter camera (LROC) instrument overview, Space Sci. Rev., 150, 81–124. DOI:https://doi.org/10.1007/s11214-010-9634-2

Settle, M. and Head, J. (1979). The role of slumping in the modification of lunar impact craters, J. Geophys. Res., 84, DOI:https://doi.org/10.1029/JB084iB06p03081.

Speyerer, E.J. Robinson, M.S. Denevi, B.W. & LROC Science Team. (2011). Lunar Reconnaissance Orbiter Camera global morphological map of the Moon, Paper presented at the 42nd Lunar Planetary Science Conference, Lunar and Planetary Science Institute, Houston, TX, https://www.lpi.usra.edu/meetings/lpsc2011/pdf/2387.pdf.

Tobler, Waldo. (1987). Measuring spatial resolution, Proceedings, Land Resources Information Systems Conference, 12-16.

Wilhelms, D. E. MacCauley, J. F. Lucchitta, B. K. El-Baz, F. Stuart-Alexander, D. E. Scott, D. H. West, M. N. (2013). Lunar 1:5M Geologic Map Renovation, 44th Lunar and Planetary Science Conference, 2114, USGS Astrogeology Science Center.

INTERNATIONAL SYMPOSIUM ON
APPLIED
GEOINFORMATICS
9-10 May 2024 · Wrocław/Poland

*International Symposium on Applied Geoinformatics (ISAG2024)*

# INTEGRATED GEOSPATIAL ANALYSIS FOR RURAL DEVELOPMENT METRICS

Vlada Svirsh[1,2]*, Bohdan Potuzhnyi[1,2] , Natallia Kussul[1,3]

**[1]** Institute of Physics and Technology, National Technical University of Ukraine “Igor Sikorsky Kyiv Polytechnic Institute”, Kyiv, Ukraine;
(vlada.svirsh25/ bohdan.potuzhnyi)@gmail.com, nataliia.kussul@lll.kpi.ua; ORCID 0009-0004-4006-2705, ORCID 0009-0001-2282-7012, ORCID 0000-0002-9704-9702
**[2]** Bern University of Applied Sciences, School of Engineering and Computer Science, Biel, Switzerland
**[3]** Space Research Institute NASU-SSAU, Kyiv, Ukraine
* Corresponding Author

## Abstract

In an era where data drives development, this study introduces an innovative geospatial framework to advance the rural infrastructure policy-making landscape in Ukraine. Focusing on enhancing the granularity of village infrastructure analysis, we explore statistical precision and unbiased representation of data derived from OpenStreetMap (OSM) and integrate it with additional datasets from postal services and mobile network providers. The research pivots on constructing detailed descriptions that capture the unique development needs of all Ukrainian villages. Our methodology distills multiple layers of open-access geospatial data, assessing the proximity and characteristics of essential infrastructure—urban centers, healthcare, education, transportation, and commercial services. By harnessing advanced statistical tools, we unravel the complex fabric of rural accessibility, unveiling not just the physical but also the communicative ties that bind these communities. Our results offer a multi-dimensional perspective of village infrastructure, transcending beyond mere spatial analysis to encompass the quality of network connectivity and service availability. The expanded dataset serves as a rich repository for empirical research, providing pivotal insights into the developmental dynamics of rural areas. It underpins strategies for infrastructure enhancement tailored to the diverse tapestry of village life in Ukraine. Our conclusions advocate for data-driven decision-making in rural development, emphasizing the transformative impact of integrating geospatial analysis with real-time service data. This integrated approach stands as a beacon for similar developmental endeavors globally, offering a scalable model for uplifting rural communities through targeted and informed infrastructure investments.

**Keywords:** *Geospatial Analysis, Rural Infrastructure Enhancement, Data Integration, Open Data Application, Village Development Metrics*

## Introduction

Crucial to the advancement of rural areas is the resolution of issues pertaining to the lacunae in infrastructure and the hurdles to accessibility faced by village communities. This research is committed to facilitating decision-making grounded in evidence within the Ukrainian context, pioneered by a state-of-the-art geospatial analytical framework that is concentrated on the intricate dynamics of rural settlements.

The central inquiries of this research are threefold:

What methodologies can be adopted to develop refined descriptors that capture the accessibility of villages to essential infrastructure, such as healthcare, transportation, and public services, in relation to actual proximity associations?

Is it possible to preserve the statistical essence of original accessibility data while gaining deeper insight through graph-based representations of rural infrastructure connectivity?

How can we create precise infrastructure linkage maps for individual villages that can pinpoint developmental shortcomings and delineate areas for prioritized intervention?

In pursuit of answers, this study synergizes a variety of geospatial data strata, primarily utilizing the collective data repository of OpenStreetMap. The adopted methodologies extend beyond standard practices and engage specialized computational algorithms along with stringent statistical analyses to enhance the data transformation process for rural locales. These methodologies refine the outputs beyond the conventional large-scale general overviews or the isolated spot-checks of accessibility.

Our extensive infrastructure graphs weave a comprehensive network, connecting an array of Ukrainian rural settlements to proximate pivotal facilities, including healthcare institutions, educational establishments, and commercial entities. This networking yields an elaborate and actionable overview of how village accessibilities correlate with their developmental requisites. It carves out a roadmap to pinpoint and tackle local developmental lacunae and optimizes opportunities for growth.

Benefiting from the patronage of the Ministry of Education and Science of Ukraine, this analytical initiative aims to substantially contribute to the rural revitalization process. It presents strategic insight into the amalgamation of technological infrastructures and lays bare the disparities in access. The innovative descriptive power vested in this approach harbors the potential for adaptation and application across diverse global rural developmental scenarios.

## Materials and Methods

### Materials

The research was underpinned by a comprehensive set of geospatial data, significantly enriched by the inclusion of datasets that characterize the communication infrastructure essential for rural development. This integrative approach utilized the following data sources:

Geospatial Data: Extracted from OpenStreetMap (OSM), encompassing roads, education, healthcare, commerce, accommodation, and religious facilities.

Humanitarian Data: Village and city locations sourced from the Humanitarian Data Exchange (HDX), providing a basis for spatial distribution analysis.

Communication Infrastructure Data: Detailed coverage maps for postal services and mobile network providers were integrated into the geospatial framework to assess the communication landscape.

A reference table summarizing these data layers is provided in the Table 1.

**Table 1.** Geospatial data.

| Data | Layers | Source |
|---|---|---|
| Villages | Villages | The Humanitarian Data Exchange (as of 17.07.2021) |
| Cities | City | The Humanitarian Data Exchange (as of 17.07.2021) |
| Elevators | Elevators | Elevators in Ukraine (as of 23.02.2022) |
| Roads | Major, Secondary and Rural roads | OSM |
| Education | School, College, University | OSM |
| Hotels | Hotel, guesthouse, shelter | OSM |
| Medicine | Hospital, clinic, pharmacy | OSM |
| Shops | Supermarket, mall, clothes, marketplace | OSM |
| Bank | Bank | OSM |
| Church | Church | OSM |
| Library | Library | OSM |
| Kindergarten | Kindergarten | OSM |
| Parks | Local, National and Regional Parks | OSM |
| Post | “Nova poshta” and Ukrainian Post departments | Postal providers (Nova Poshta and Ukrainian Post) |
| Mobile network | Kyivstar, Lifecell, Vodafone, Trimob | Mobua.net data |

### Methods

The methodological framework consisted of a systematic process for transforming raw data into actionable insights:

Data Extraction and Preprocessing: Geospatial data was initially extracted into GeoDataFrames (GDFs), enabling spatial operations and analyses. Data cleansing and preprocessing were performed to ensure consistency and accuracy.

Buffer Zone Analysis: For each POI category, spatial buffer zones were created to delineate the effective catchment area for each village. This method identified the closest amenities based on pre-established distance thresholds.

Integration of Communication Data: Datasets detailing the coverage of postal services and mobile network providers were superimposed onto the geospatial map. This allowed for an assessment of the communication infrastructure's adequacy and accessibility in rural areas.

Statistical Validation: Statistical methods, including histograms, boxplots, and correlation matrices, were employed to analyze the distribution of infrastructure features and validate the integrity of the new descriptors.

Graph-Based Representation: A graph database model was constructed to represent the connectivity between rural settlements and infrastructure amenities. This model facilitated the identification of infrastructure gaps and potential development opportunities.

The approach balanced the quantitative rigor with practical applicability, ensuring that the insights derived from the analysis were grounded in empirical evidence and statistically valid representations. The methodologies detailed here were pivotal in generating a multifaceted view of rural infrastructure, laying the foundation for data-driven policy-making and strategic rural development initiatives.

## Results and Discussion

### Graph-based Accessibility Descriptors

The experiment transitioned initial distance measures into elaborate graph-based structures, illustrating the connections between rural villages and nearby Points of Interest (POIs), such as healthcare, educational, transit, and other essential services. Figures 1 and 2 present histograms and boxplot distributions of the distance descriptors, elucidating the frequency and spread of villages in relation to various POIs. These visuals underscore the heterogeneity in accessibility, with certain amenities like major roads showing a right-skewed distribution, hinting at disparities that require strategic infrastructure development.

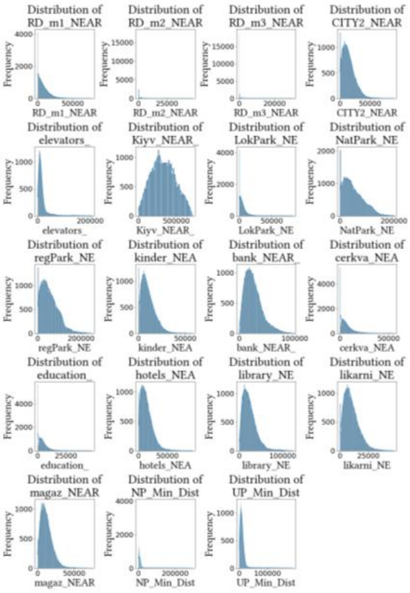

**Figure 1.** Histogram distribution of the distance descriptors

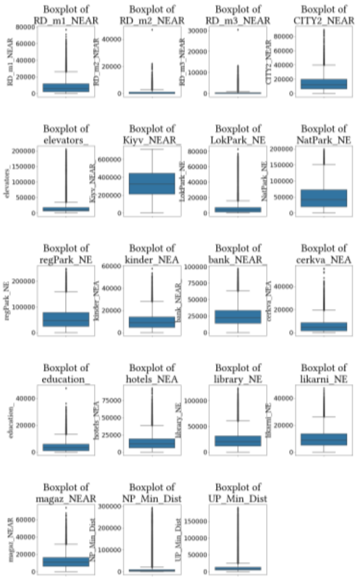

**Figure 2.** Boxplot distributions of the distance descriptors

### Correlation of Infrastructure and Accessibility

Figure 3 illustrates a correlation matrix of the distance descriptors, providing insight into how various infrastructural elements are interrelated in terms of village proximity. This analysis is critical, as it highlights areas where synergistic development can significantly enhance accessibility and, by extension, quality of life. For example, the proximity of educational facilities and healthcare services to the nearest city underscores the urban-centric bias in infrastructural development.

### Visual Representation of Rural Infrastructure

Figure 4's scatter plot depicts the total count of POIs for each village within the newly constructed graph structure. The visualization transitions from green to red, with green suggesting higher POI availability and, presumably, better accessibility. This visual mapping is pivotal, as it not only identifies under-serviced regions but also underscores the utility of the graph-based descriptors in informing targeted and evidence-based policy-making. The integration of postal and mobile network coverage data has expanded the understanding of village accessibility, extending beyond physical infrastructure to include the pivotal communicative dimensions that facilitate modern rural life.

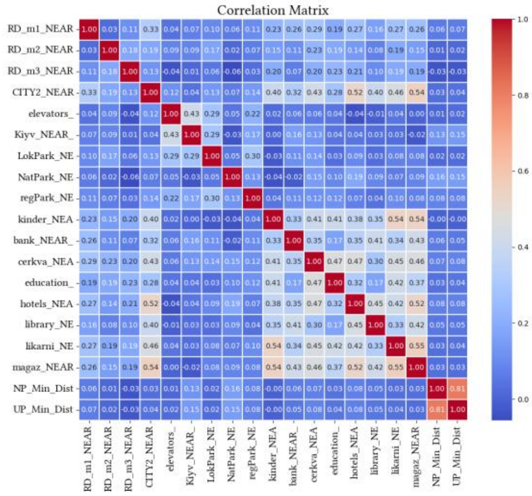

| | RD_m1_NEAR | RD_m2_NEAR | RD_m3_NEAR | CITY2_NEAR | elevators_ | Kiyv_NEAR_ | LokPark_NE | NatPark_NE | regPark_NE | kinder_NEA | bank_NEAR_ | cerkva_NEA | education_ | hotels_NEA | library_NE | likarni_NE | magaz_NEAR | NP_Min_Dist | UP_Min_Dist |
|---|---|---|---|---|---|---|---|---|---|---|---|---|---|---|---|---|---|---|---|
| RD_m1_NEAR | 1.00 | 0.03 | 0.11 | 0.33 | 0.04 | 0.07 | 0.10 | 0.06 | 0.11 | 0.23 | 0.26 | 0.29 | 0.19 | 0.27 | 0.16 | 0.27 | 0.26 | 0.06 | 0.07 |
| RD_m2_NEAR | 0.03 | 1.00 | 0.18 | 0.19 | 0.09 | 0.09 | 0.17 | 0.02 | 0.07 | 0.15 | 0.11 | 0.23 | 0.19 | 0.14 | 0.08 | 0.19 | 0.15 | 0.01 | 0.02 |
| RD_m3_NEAR | 0.11 | 0.18 | 1.00 | 0.13 | -0.04 | 0.01 | 0.06 | -0.06 | 0.03 | 0.20 | 0.07 | 0.20 | 0.23 | 0.21 | 0.10 | 0.19 | 0.19 | -0.03 | -0.03 |
| CITY2_NEAR | 0.33 | 0.19 | 0.13 | 1.00 | 0.12 | 0.04 | 0.13 | 0.07 | 0.14 | 0.40 | 0.32 | 0.43 | 0.28 | 0.52 | 0.40 | 0.46 | 0.54 | 0.03 | 0.04 |
| elevators_ | 0.04 | 0.09 | -0.04 | 0.12 | 1.00 | 0.43 | 0.29 | 0.05 | 0.22 | 0.02 | 0.06 | 0.06 | 0.04 | -0.04 | -0.01 | 0.04 | 0.00 | 0.01 | 0.02 |
| Kiyv_NEAR_ | 0.07 | 0.09 | 0.01 | 0.04 | 0.43 | 1.00 | 0.29 | -0.03 | 0.17 | 0.00 | 0.16 | 0.13 | 0.04 | 0.04 | 0.03 | 0.03 | -0.02 | 0.13 | 0.15 |
| LokPark_NE | 0.10 | 0.17 | 0.06 | 0.13 | 0.29 | 0.29 | 1.00 | 0.05 | 0.30 | -0.03 | 0.11 | 0.14 | 0.03 | 0.09 | 0.03 | 0.08 | 0.08 | 0.02 | 0.02 |
| NatPark_NE | 0.06 | 0.02 | -0.06 | 0.07 | 0.05 | -0.03 | 0.05 | 1.00 | 0.13 | -0.04 | -0.02 | 0.15 | 0.10 | 0.19 | 0.09 | 0.07 | 0.09 | 0.16 | 0.15 |
| regPark_NE | 0.11 | 0.07 | 0.03 | 0.14 | 0.22 | 0.17 | 0.30 | 0.13 | 1.00 | 0.04 | 0.11 | 0.12 | 0.12 | 0.07 | 0.04 | 0.10 | 0.08 | 0.08 | 0.08 |
| kinder_NEA | 0.23 | 0.15 | 0.20 | 0.40 | 0.02 | 0.00 | -0.03 | -0.04 | 0.04 | 1.00 | 0.33 | 0.41 | 0.41 | 0.38 | 0.35 | 0.54 | 0.54 | -0.00 | -0.00 |
| bank_NEAR_ | 0.26 | 0.11 | 0.07 | 0.32 | 0.06 | 0.16 | 0.11 | -0.02 | 0.11 | 0.33 | 1.00 | 0.35 | 0.17 | 0.35 | 0.41 | 0.34 | 0.43 | 0.06 | 0.05 |
| cerkva_NEA | 0.29 | 0.23 | 0.20 | 0.43 | 0.06 | 0.13 | 0.14 | 0.15 | 0.12 | 0.41 | 0.35 | 1.00 | 0.47 | 0.47 | 0.30 | 0.45 | 0.46 | 0.07 | 0.08 |
| education_ | 0.19 | 0.19 | 0.23 | 0.28 | 0.04 | 0.04 | 0.03 | 0.10 | 0.12 | 0.41 | 0.17 | 0.47 | 1.00 | 0.32 | 0.17 | 0.42 | 0.37 | 0.03 | 0.04 |
| hotels_NEA | 0.27 | 0.14 | 0.21 | 0.52 | -0.04 | 0.04 | 0.09 | 0.19 | 0.07 | 0.38 | 0.35 | 0.47 | 0.32 | 1.00 | 0.45 | 0.42 | 0.52 | 0.08 | 0.08 |
| library_NE | 0.16 | 0.08 | 0.10 | 0.40 | -0.01 | 0.03 | 0.03 | 0.09 | 0.04 | 0.35 | 0.41 | 0.30 | 0.17 | 0.45 | 1.00 | 0.33 | 0.42 | 0.05 | 0.05 |
| likarni_NE | 0.27 | 0.19 | 0.19 | 0.46 | 0.04 | 0.03 | 0.08 | 0.07 | 0.10 | 0.54 | 0.34 | 0.45 | 0.42 | 0.42 | 0.33 | 1.00 | 0.55 | 0.03 | 0.04 |
| magaz_NEAR | 0.26 | 0.15 | 0.19 | 0.54 | 0.00 | -0.02 | 0.08 | 0.09 | 0.08 | 0.54 | 0.43 | 0.46 | 0.37 | 0.52 | 0.42 | 0.55 | 1.00 | 0.03 | 0.03 |
| NP_Min_Dist | 0.06 | 0.01 | -0.03 | 0.03 | 0.01 | 0.13 | 0.02 | 0.16 | 0.08 | -0.00 | 0.06 | 0.07 | 0.03 | 0.08 | 0.05 | 0.03 | 0.03 | 1.00 | 0.81 |
| UP_Min_Dist | 0.07 | 0.02 | -0.03 | 0.04 | 0.02 | 0.15 | 0.02 | 0.15 | 0.08 | -0.00 | 0.05 | 0.08 | 0.04 | 0.08 | 0.05 | 0.04 | 0.03 | 0.81 | 1.00 |

**Figure 3.** Correlations of descriptors of closest distances to the objects

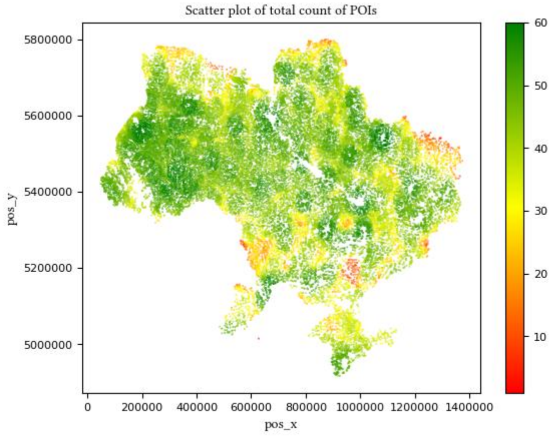

**Figure 4.** Total count of all types of Points of Interest (POIs) present for each village within the graph structure

## Conclusion

Our research represents a pivotal step in understanding and enhancing rural infrastructure in Ukraine. Through a meticulous geospatial analysis that integrated novel data sources, we mapped out a detailed landscape of village accessibility, connectivity, and service availability. Our work highlights the stark disparities in infrastructure distribution and points towards a need for targeted interventions.

We discovered that the proximity of critical services to village centers is not uniform, indicating potential focal points for development. Moreover, incorporating data on postal and mobile networks proved crucial, revealing the digital divide that rural communities face.

The implications of this study are twofold. It presents a clear case for policymakers to consider a holistic approach to rural development that includes digital connectivity as a cornerstone. Furthermore, it lays the groundwork for future research to build upon these findings, potentially influencing rural development strategies on a global scale.

This study is a testament to the power of integrated data analysis in crafting informed, strategic, and impactful rural development policies. It underscores the importance of evidence-based planning in bridging the urban-rural divide and fostering sustainable community growth.

## Acknowledgements

This research was conducted with the support of the Ministry of Education and Science of Ukraine under the project titled “Information Technologies of Geospatial Analysis for the Development of Rural Areas and Communities,” state registration number 0123U102838. We extend our gratitude to the project for supplying the raw data necessary for this analysis.

## References

Liu, Y., Ke, X., Wu, W., Zhang, M., Fu, X., Li, J., Jiang, J., He, Y., Zhou, C., Li, W., Li, Y., Song, Y., & Zhou, X. (2022). Geospatial characterization of rural settlements and potential targets for revitalization by geoinformation technology. Scientific Reports, 12, 8399.

Herfort, B., Lautenbach, S., Porto de Albuquerque, J., Anderson, J., & Zipf, A. (2023). A spatio-temporal analysis investigating completeness and inequalities of global urban building data in OpenStreetMap. Nature Communications, 14, 3985.
Yailymova, H., Yailymov, B., Kussul, N., & Shelestov, A. (2023). Geospatial Analysis of Life Quality in Ukrainian Rural Areas. Proceedings of the 13th International Conference on Dependable Systems, Services and Technologies (DESSERT), Athens, Greece, pp. 1-5.

Maryada, A., & Thatiparthi, V. L. (2020). Geospatial technology for mapping and analysis of social and infrastructural facilities at village level: a case study of Chinnapendyala village. Modeling Earth Systems and Environment, 6, pp. 1763–1781.

OpenStreetMap. (n.d.). Ukraine. Retrieved from https://download.geofabrik.de/europe/ukraine.html

The Humanitarian Data Exchange. (n.d.). Retrieved from https://data.humdata.org/

Elevators in Ukraine. (n.d.). Retrieved from https://elevatorist.com/karta-elevatorovukrainy

INTERNATIONAL SYMPOSIUM ON
APPLIED
GEOINFORMATICS
9-10 May 2024 · Wrocław/Poland

*International Symposium on Applied Geoinformatics (ISAG2024)*

# Automatization of 3D Point Cloud Semantic Segmentation Using PointNet++ Algorithm

Salih Bozkurt[1]*, Zaide Duran[2], Dursun Zafer Seker[2]

[1] Istanbul Technical University, Graduate School, Geomatics Engineering Program, Maslak, 34469 Istanbul, Türkiye; bozkurts18@itu.edu.tr; ORCID 0009-0009-5954-8453
[2] Istanbul Technical University, Faculty of Civil Engineering, Geomatics Engineering Department, Maslak, 34469 Istanbul, Türkiye, duranza@itu.edu.tr; seker@itu.edu.tr; ORCID 0000-0002-1608-0119, ORCID 0000-0001-7498-1540

* Corresponding Author

## Abstract

With advancements in hardware and software, research on large-scale data processing has increased, expanding application areas. 3D point clouds are widely used in the healthcare, automotive, defense, and film sectors. Manual interpretation of dense and complex point clouds introduces errors and costs. This study focuses on the automatic segmentation and analysis of 3D dense and complex point clouds using artificial intelligence. The primary dataset selected for this research comprises open-source DublinCity LIDAR 3D point cloud data. The DublinCity dataset was created in 2015 in the city of Dublin, the capital of Ireland, using the Aerial Light Detection and Ranging (A/LiDAR) method. The dataset was generated through the collection and labeling of LiDAR data on a city-wide scale. It consists of 13 classes hierarchically organized. These classes are further divided into four main categories: building, vegetation, ground, and undefined. Within these main categories, there are subcategories such as window, door, tree, and others. One of the most popular contemporary approaches employed is the PointNet++ algorithm to automatically analyze point cloud data. PointNet++ is an advanced 3D deep learning algorithm designed for point cloud data processing. It introduces a hierarchical neural network architecture for capturing hierarchical features from local to global scales, enabling the effective handling of complex structures. PointNet++ uses a set abstraction and feature propagation module for efficient sampling and aggregating local features into global representations, making it robust for segmentation and object recognition. Within the scope of this study, segmentation results were generated using the PointNet++ algorithm on DublinCity LIDAR data for different class numbers, and class-specific analyses were conducted. The analyses revealed accuracy values reaching ~90%.

**Keywords:** *Point Cloud Segmentation, Artificial Intelligence, 3D Data Processing, PointNet++*

## Introduction/Background

With the developments in today's technology, research in the field of artificial intelligence has gained intensity and diversity. Particularly, the use of artificial intelligence in the analysis of large and complex data has significantly increased. Large and complex data is used in various fields such as healthcare, defense, automotive, cinema, archaeology, virtual reality, and many others. Among these large datasets, 3D point clouds are prominent. One of the costliest processes in processing and analyzing point clouds is the segmentation process. This is because the segmentation process is still largely operator-dependent. Processes that depend on operators often lead to operator errors and costs. Therefore, this study aims to automate segmentation processes using 3D deep learning algorithms. The DublinCity 3D point cloud was used as the main dataset in this study. For the segmentation process, the PointNet++ algorithm, which is one of the popular approaches today, was used. Point clouds can be generated in many different ways, such as RADAR, LiDAR, 3D cameras, and photogrammetric methods, and can be used for many different purposes. Based on all these, it is believed that the study will guide future studies and shed light on them. Point clouds and artificial intelligence are currently areas of interest and need, with many different studies in these fields. For example, in the study by (Shen & Li, 2022), comprehensive research was conducted on deep learning algorithms used for 3D point cloud segmentation.

Different deep learning models and how they can be used for 3D point cloud segmentation are discussed. Additionally, recent research studies in this field and future research directions are also addressed. (Zang & Cui, 2021) examine various algorithms used for 3D point cloud segmentation. The algorithms are divided into two categories: traditional methods and AI algorithms. Algorithms in both categories are discussed and compared in detail. (Wang & Liu, 2020) evaluate existing deep learning approaches on 3D point cloud segmentations, providing guidance on how they can be used in different areas. (Qi et al., 2017) describe the PointNet algorithm, which forms the basis of the PointNet++ algorithm used in this study. The PointNet algorithm is one of the first algorithms to directly process point clouds. The proposed PointNet algorithm is compared with current approaches, showing that the proposed algorithm produces highly effective results in complex segmentation processes. (Qi et al., 2017) also present the PointNet++ algorithm, built on the PointNet algorithm architecture, and conduct comparative analyses with current algorithms. It is noted that, unlike the PointNet algorithm, the PointNet++ algorithm manages learning and prediction processes in a hierarchical order. The results obtained indicate that the proposed algorithm achieves significant results, similar to those of the PointNet algorithm. (Wu et al., 2019) propose a new deep learning approach called ShapeNets for representing 3D shapes. Results of the proposed algorithm are shared regarding segmentation processes obtained from popular algorithms. (Li et al., 2020) propose a graph neural network structure for performing road segmentations. According to the proposed approach, graph neural networks are used to encode geometric and topological relationships in point clouds. Examination of the results reveals that segmentation results with high accuracy are achieved. (Landrieu et al., 2018) present a method using superpoint graphs for large-scale point cloud classification. They note that superpoint graphs are used to encode local and global information in 3D point clouds. (Garcia et al., 2017) present a point cloud segmentation algorithm using semantic priors. They argue that the specified semantic priors can be obtained from an image or a map and strengthen the segmentation process. (Zhao et al., 2019) present a deep learning-based framework called PointSeg for 3D point cloud segmentation. PointSeg uses various deep learning models to encode geometric and visual information in point clouds. (Liu et al., 2022) examine recent developments and applications in deep learning algorithms used for 3D point cloud segmentation. Different deep learning models and how they can be used for 3D point cloud segmentation are discussed. Additionally, recent research studies in this field and future research directions are also addressed. (Tchapmi et al., 2021) examine various methods used for 3D point cloud segmentation. The methods are divided into two categories: traditional methods and deep learning-based methods. Methods in both categories are discussed and compared in detail. Finally, (Guo et al., 2020) examine point cloud segmentation methods used for 3D object detection. Different methods and how they can be used for 3D object detection are discussed.

## Materials and Methods (Design/methodology/approach)

### DublinCity LiDAR 3D Point Cloud Data

The DublinCity dataset, established in 2015 within the urban landscape of Dublin, the capital city of Ireland, was created using the Aerial Light Detection and Ranging (A/LiDAR) technique. This dataset was meticulously compiled through the systematic acquisition and annotation of LiDAR data across the entire city. It comprises 13 classes, organized in a hierarchical manner. These classes are further classified into four primary categories: buildings, vegetation, ground, and undefined areas. Under these overarching categories, there are subcategories such as windows, doors, trees, and others. The sample view of the DublinCity dataset is presented in the Figure 4.

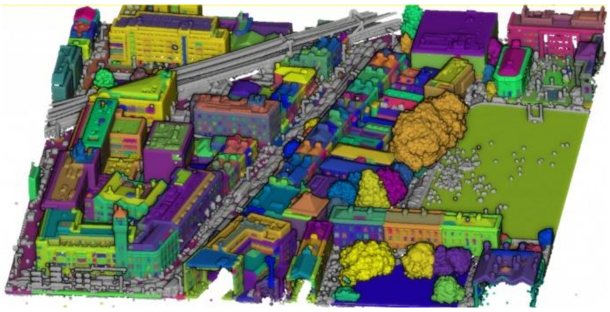

**Figure 4**. DublinCity LiDAR data sample (Zolanvari et al., 2019)

### PointNet++ Algorithm

PointNet++ builds upon the foundational PointNet by addressing its limitations in capturing complex details and structures. It introduces a hierarchical methodology that utilizes PointNet iteratively on input point clouds, progressively enhancing its ability to learn local features by incorporating broader contextual scales through metric space distances. A key advancement is its segmentation of points into overlapping local regions, similar to Convolutional Neural Networks (CNNs), which facilitates multi-scale feature extraction. PointNet++ comprises three fundamental sub-layers: sampling, grouping, and PointNet layer, which collectively establish a hierarchical framework for abstracting local features. This innovative approach enhances the network's capability to grasp contextual information effectively. The architectural concept of PointNet++ is visually depicted in Figure 5, illustrating how the algorithm's hierarchy processes and abstracts local features from the input point cloud.

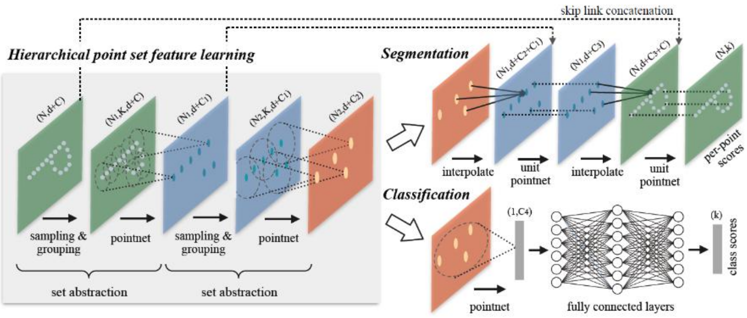

**Figure 5.** Illustration of PointNet++ (Qi et al., 2017).

## Results and Discussion (Findings)

The PointNet++ algorithm used in the study has been used in Matlab R2022a. The license required for Matlab has been provided by Istanbul Technical University. The main dataset, DublinCity, could not be directly used in the algorithm due to its hierarchical subclass structure. Therefore, improvements were made to separate classes in the .Net environment according to their own labels. This enabled the dataset to be divided into appropriate class labels, and preprocessing operations were completed. Subsequently, training and testing processes were carried out for different classes. The numbers of classes were determined as 6, 4, and 3, respectively, and the performance of the PointNet++ algorithm at different levels of detail was analyzed. The dataset with 6 classes includes objects of buildings, doors, ground, roofs, vegetation, and windows. The 4-class dataset contains 3D point cloud data for buildings, doors, roofs, and windows. Lastly, the 3-class datasets consist solely of point cloud data related to buildings, roofs, and ground. The hardware specifications for the training and testing processes are presented in Table 1, and the network parameters are shown in Table 2.

**Table 1.** Used hardware specifications.

| Definition | Value |
|---|---|
| GPU | Nvidia Quadro RTX 4000 |
| CPU | Intel Xeon E-2276G @ 3.80GHz |
| Cores | 6 cores with 6 virtual cores |
| Memory | 32 GB |

**Table 2.** Network parameters.

| Definition | Value |
|---|---|
| Learning Rate | 0.01 |
| L2 Regularization | 0.01 |
| Learning Rate Drop Factor | 0.1 |
| Gradient Decay | 0.9 |
| Optimizer | Adam |
| Used Processor | GPU |

The results of the training and testing processes conducted with the parameters specified in Table 2 are presented in Table 3.

**Table 3.** Results of the work**.**

| Definition | Accuracy | Recall | Mean IoU | F1 Score | Kappa | Precision | Weight IoU |
|---|---|---|---|---|---|---|---|
| 6 Classes | 0.8074 | 0.4623 | 0.3828 | 0.4723 | 0.6875 | 0.5009 | 0.6959 |
| 4 Classes | 0.8789 | 0.4138 | 0.3634 | 0.4165 | 0.6655 | 0.4212 | 0.7863 |
| 3 Classes | 0.9016 | 0.8315 | 0.7611 | 0.8537 | 0.8352 | 0.8960 | 0.8223 |

When examining Table 3, it was observed that there is an inverse relationship between the number of classes and the level of detail with the accuracy value. Analyzing the results specifically for the 6-class dataset, it was noted that the results, particularly the mean and weighted IoU values, were deemed inadequate for detailed features such as doors and windows. Therefore, analyses were conducted using the 4-class dataset, which has lower detail levels. Results for the 4-class dataset showed higher accuracy values compared to the 6-class dataset. However, despite the increase in accuracy values, it was observed that objects were mixed, as indicated by the mean IoU values. To address this, the detailed window data was removed from the 4-class dataset, creating a 3-class dataset. Repeating the training and testing processes with the 3-class dataset showed a significant increase in all values.

## Conclusion

When examining the study's results, it was observed that the PointNet++ algorithm yielded low results for objects with remaining details using the current dataset and parameters. To improve accuracy for objects like doors and windows, which are considered at the detail level, it is anticipated that increasing data density and diversity will be necessary. Additionally, it is believed that enhancing the hardware specifications, particularly the GPU memory, followed by increasing the minimum batch size in the network parameters, will positively impact the results. Since DublinCity is a LiDAR-based dataset with relatively low-resolution and only includes geometric features, the low accuracy values at the detail level are attributed to these factors. Therefore, it is expected that results obtained from point clouds generated photogrammetrically, which are denser and include color information, will achieve more successful outcomes at the detail level. Future studies are planned to further investigate these aspects. In conclusion, based on the current data, the PointNet++ algorithm is deemed to produce successful results in large point clouds with complex geometries. It can be applied in tasks such as object identification and tracking, which involve large geometric objects.

## References

Garcia-Garcia, A., Orts-Escolano, S., Oprea, S., Villena-Martinez, V., & Garcia-Rodriguez, J. (2017). Point cloud segmentation using semantic priors. In Proceedings of the IEEE International Conference on Computer Vision (pp. 4474-4483).

Guo, Y., Wang, H., Hu, Q., Liu, H., & Liu, L. (2020). Point cloud segmentation for 3D object detection: A survey and benchmark. arXiv preprint arXiv:2007.00428.

Landrieu, L., & Simonovsky, M. (2018). Large-scale point cloud classification with superpoint graphs. In Proceedings of the IEEE Conference on Computer Vision and Pattern Recognition (pp. 9359-9367).

Li, Y., Bu, R., Sun, M., Wu, W., Di, X., & Chen, B. (2020). Point cloud segmentation for road extraction with graph neural networks. In Proceedings of the IEEE International Conference on Robotics and Automation (pp. 6476-6481).

Liu, W., Angioni, A., & Rosinol, A. (2022). Point cloud segmentation using deep learning: Recent advances and applications. arXiv preprint arXiv:2201.08385.

Qi, C. R., Su, H., Mo, K., & Guibas, L. J. (2017). PointNet: Deep learning on point sets for 3D classification and segmentation. In Proceedings of the IEEE Conference on Computer Vision and Pattern Recognition (pp. 652-660).

Qi, C. R., Yi, L., Su, H., & Guibas, L. J. (2017). Pointnet++: Deep hierarchical feature learning on point sets in a metric space. Advances in neural information processing systems, 30.

Shen, C., & Li, H. (2022). Point cloud segmentation using deep learning: A survey and benchmark. arXiv preprint arXiv:2208.01485.

Tchapmi, L., Choy, C., & Gwak, J. (2021). A survey of 3D point cloud segmentation methods. arXiv preprint arXiv:2105.08325.

Wang, Y., & Liu, S. (2020). Point cloud segmentation with deep learning: A survey. arXiv preprint arXiv:2001.09529.

Wu, Z., Song, S., Khosla, A., Yu, F., Zhang, L., & Xiao, J. (2019). 3D ShapeNets: A deep representation for volumetric shapes. In Proceedings of the IEEE Conference on Computer Vision and Pattern Recognition (pp. 5618-5627).

Zhang, Z., & Cui, S. (2021). Point cloud segmentation: A review and benchmark. IEEE Transactions on Pattern Analysis and Machine Intelligence, 44(1), 115-132.

Zhao, H., Shi, J., Qi, X., Wang, X., & Jia, J. (2019). PointSeg: A deep learning framework for point cloud segmentation. In Proceedings of the IEEE Conference on Computer Vision and Pattern Recognition (pp. 6520-6529).

Zolanvari, S. M., Ruano, S., Rana, A., Cummins, A., da Silva, R. E., Rahbar, M., & Smolic, A. (2019). DublinCity: Annotated LiDAR point cloud and its applications. arXiv preprint arXiv:1909.03613.

INTERNATIONAL SYMPOSIUM ON
APPLIED
GEOINFORMATICS
9-10 May 2024 · Wrocław/Poland

*International Symposium on Applied Geoinformatics (ISAG2024)*

# Semantic Segmentation Using Segformer for Precise Building Damage Identification: Case study Marrakech Earthquake, Morocco.

Hakima Zair [1]*, Samir Zouhri [1], Safia Laoulad [1], Mohamed Rabii Simou [1], Houssine Boutarouine [1], Mehdi Maanan [1], Hassan Rhinane [1]

[1]Hassan II University, Faculty of Sciences aïn chock, Departement of Geology, Casablanca, Morocco; zairhakima1@gmail.com

**Abstract**

The majority of the damage caused by natural disasters is to buildings, and assessing the damage is crucial to providing emergency relief after the event. In this study, we addresse the urgent need for an accurate assessment of building damage in the recent aftermath of the earthquake in the Al Haouz region in Marrakech, Morocco. This study aims to improve the efficiency and rapidity of house damage investigations by utilising UAV images and advanced deep- learning algorithms for image recognition. We applied the SegFormer model to classify post-earthquake UAV imagery into four classes: destroyed, damaged, undamaged, and minor damaged buildings. Our methodology included preparing an annotated dataset of 134 images, dividing it into training (70%), validation (20%), and test sets (10%), and using the cross-entropy loss function with class balancing techniques. The model was initialised with pre-trained weights, fine-tuned using Adam optimizer, and augmented for dataset diversity. This approach effectively classified building damage, with evaluation metrics showing an accuracy rate of 0.9493, precision of 0.848, F1 score of 0.6700, mean intersection over union (mIoU) of 0.5636, and a recall rate of 0.726. The experimental findings have demonstrated the effectiveness of our approach in identifying building damage. These results have significant implications for disaster response strategies and urban development planning, establishing our method as a benchmark for similar disaster assessments and aid initiatives.

**Keywords:** *Marrakech, Earthquake, UAV, SegFormer, Building damage.*

## Introduction

In order to ascertain the impact on property and life following a natural catastrophe, it is critical to promptly and precisely estimate damage in the affected region. Natural disasters represent a serious danger to both safety and the economy. Since buildings are the primary locations for habitation and a concentration of people and property, it is crucial to identify the hardest-hit regions for post-disaster emergency relief efforts and to carry out quick damage detection of structures directly connected to human life (Koshimura et al., 2020).

As one of the countries marked by a history of significant seismic dynamics, Morocco, due to its pivotal position at the convergence of the African and Eurasian plates, has experienced numerous seismic events, predominantly concentrated in the country's northern region, (Nayak et al., 2023). Specifically, the Atlas zone has emerged as one of the most active seismogenic areas among all Moroccan regions. According to the analysis of the Hamdache study from 2015 Seismic events with a magnitude exceeding 5.0 occur at intervals of approximately 3.5, 1.5, 11.5, 18.5, and 41 years in the Atlas, Tell, Rif, High Plateau, and Meseta zones, respectively (Mohamed et al., 2015).

Rural regions, where roughly 40% of the population resides, are high risk due to their high population density, failing infrastructure, and fragile structures (Boutayeb, 2012). This problem increases during seismic events, as demonstrated by the most recent earthquake that significantly affected both rural and urban areas of the High-Atlas of Al Haouz region. This study is located in a challenging rural area with a cluster of primarily clay-built houses. Such settings provide significant challenges for accurately detecting and differentiating between buildings and the adjacent clay fields. Due to the buildings' inherent similarity to the clay-rich surroundings, tasks like semantic segmentation and conventional object detection are more challenging.

Although they usually have strong, robust performance and effective detection, traditional algorithms like Faster R- CNN (Ren et al., 2017), Mask R-CNN (He et al., 2017), and Cascade R-CNN (Cai & Vasconcelos, 2018) have a slower detection speed and make it challenging to meet the real-time detection requirement (Yu et al., 2022). Although YOLO series models (YOLOv3 (Redmon & Farhadi, 2018), YOLOv4 (Bochkovskiy et al., 2020), YOLOv6 (Li et al., 2022), YOLOv7 (C. Wang et al., 2023), YOLOF (Chen et al., 2021), YOLOX (Ge et al., 2021), etc.) encounter several difficulties when trying to enhance the identification of small, dense objects in remote sensing photos. This is because these models anticipate big, medium, and tiny targets, respectively, using three downsamplings to 1/32, 1/16, and 1/8 of the original image resolution, this downsampling results in the loss of the target location data (Yu et al., 2022). However, with the rapid improvement of deep learning in image processing, and the new technologies of remote sensing instruments for monitoring post-disaster extraction of information about damaged buildings, has led to a new phase of development in image semantic segmentation (Bai et al., 2020). In this context, our research proposes the use of SegFormer model for a better and efficient damage detection. The main objective of this project is to investigate how well Segformer works in solving the particular problems that come with rural landscapes. The results will be insightful for applications in environmental monitoring, disaster response, and rural development.

## Materials and Methods

### Study Area

Our research focuses on the area around the 6.8 magnitude (Mw) Al Haouz earthquake that struck on September 8, 2023, at a depth of 19 km, in Marrakech, Morocco (https://earthquake.usgs.gov). The epicenter of this seismic event was located at 31.055◦ N 8.389◦ W, resulting in significant impacts on the surrounding areas. Due to its proximity to the convergence of the African plate and the Eurasian plate, Morocco is prone to high seismic activity (Nayak et al., 2023). A faulting system located 75 kilometers southwest of Marrakech in the High Atlas Mountains is what caused the earthquake that occurred (Akilan et al., 2014). However, this project specifically focuses on one of the severely affected villages, Douar Ighill (30◦59'00.6"N 8◦17'19.7" W)(Figure**1**) , 20 km away from the epicenter, a small town and rural commune located in the south-western of the Al Haouz Province of the Marrakesh-Safi region of Morocco with approximately 850 households, The majority of the residences are constructed out of clay, with a smaller percentage using reinforced concrete.

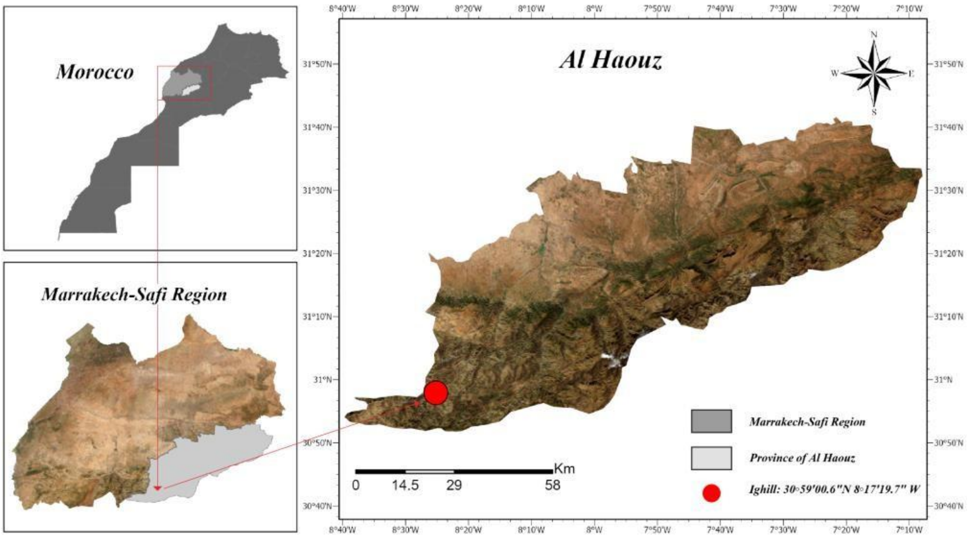

Figure1: Geographic Context of the Study Area.

### Data

The framework employed comprised three primary processes, comes first data labeling, followed by model training, and evaluation; and lastly predictions. Before data labeling, we carried out a series of preparatory steps, such as the collection of high-resolution image data, captured by WingtraOne GEN II drone, the flight mission covered approximately 103 ha, 134 image were acquired just after the earthquake and then processed to carefully generate detailed elevation models and orthophotos, ensuring precise georeferencing. Figure**2** shows an example of pre- and post- event images of the earthquake.

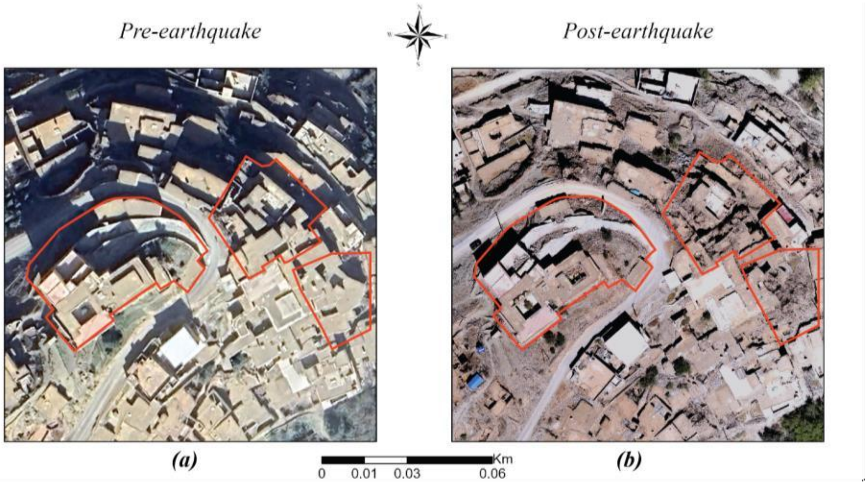

**Figure2.** Example from the Ighill dataset showing images before and after the earthqake. (a) shows satellite imagery of buildings before the earthquake and (b) shows UAV imagery of buildings destroyed after the earthquake.

In this study, we categorized the impact of the disaster on buildings into various distinct levels of damage severity. We defined the impact by visually examining intact, partially damaged, severely damaged, and irreparably damaged buildings. Using this definition and the Ighill images, we suggested the use of four-level damage categories for this study:

**Undamaged:**
Smooth and uniform surfaces.
No visible cracks, fractures, or structural deformations.
No debris or rubble is present around the building exterior.
**Minor Damaged:**
Minor cracks or fissures are visible on building roofs, walls, and facades.
Slight structural distortions, such as leaning walls or tilting roofs.
Limited debris or rubble accumulation around the building perimeter.
**Damaged:**
Significant structural damage is evident, extensive cracks, fractures, or partial collapses.
Significant structural damage is evident, extensive cracks, fractures, or partial collapses.
Walls may exhibit severe leaning or bulging, indicating structural instability.
Debris and rubble are scattered around the
**Destroyed:**
Complete structural collapse, irreparable damage, leaving only remnants of the building's former structure.
Extensive debris and rubble cover the building site, making it difficult to discern the original footprint.
No functional utilities remain intact, with doors, windows, and roofs destroyed.

## Method:

### Data labeling

Deep learning-based segmentation methods require a large number of labeled image samples, so we started our process by using original images captured by UAVs. In the data labeling phase, we used Roboflow to annotate 134 UAVs' original images with dimensions of 7956x5304 pixels. Subsequently, corresponding masks were generated to outline building damage and severity-level classes. To enrich the dataset, we applied various data augmentation techniques, including horizontal and vertical flips, 90° rotations (both clockwise and counter-clockwise), and blurring (up to 2.5 pixels). This augmented dataset was subsequently employed for model training. The images and masks were resized to a target width and height of 2048 and 1536 pixels due to hardware limitations. In order to comply with the Segformer model's input size requirements, we divided the large images into smaller patches that measured 512x512 pixels. The segmentation process produced 3096 training tiles, which were used as input data for the next step in model training iterations.

### Model Training and Evaluation

The SegFormer model was utilized to investigate the potential and effectiveness of semantic segmentation models in disaster assessment for identifying damages. A testing and validation dataset were used to evaluate the performance of the segmentation model. Two main objectives were the focus of our use of the SegFormer model. The first step is to accurately identifying high-risk areas, which facilitates large-scale automated interpretation. The second objective is to accurately classify different impact categories. SegFormer uses mainly consisted of the encoder to extract features from the input image and fuses high-level semantic information and low-level feature information on the multi-stage output of the encoder, and uses the encoder to achieve pixel-by-pixel classification (Long et al., 2014). Its structure is straightforward and has low computational complexity. The two main components of the SegFormer semantic segmentation model are (1) a transformer-based hierarchical encoder (Dosovitskiy et al., 2020) (Liu et al., 2021), and (2) a decoder based on the MLP c. The model's performance in both aspects was then evaluated using three evaluation metrics, which included IoU, Precision, and Recall.

To enhance the generalization performance of the model and speed up the training process, we utilized a pre-trained segmentation model, specifically, the SegformerForSemanticSegmentation model initialized with weights from the "MIT-b5" checkpoint accessible in the NVIDIA Model Zoo. Our semantic segmentation framework is based on this model, which allows us to process images with varying dimensions efficiently while ensuring compatibility with our dataset's output classes. During the training stage, we utilized the AdamW optimizer with a learning rate (lr) set to 0.001 to optimize the parameters of our model. The training process was specifically conducted using the available CUDA- enabled GPU.

## Results and Discussion

In our case study, the Segformer model demonstrated such a pretty good performance in semantic segmentation tasks, reaching a mean Precision about 0.8482, mean Intersection over Union (mIoU) of 0.5636, and mean Recall of 0.7260. The predictions did successfully classify and recognized classes, specifically the damaged and destroyed classes, due to the large amount of data representing these two classes.

The obtained evaluation metrics reflect the effectiveness of the SegFormer model in semantic segmentation tasks, specifically in classifying damaged and destroyed buildings due to the large amount of data representing these two classes. However, the model still faced challenges primarily derived from the similar appearance between the undamaged and minor damage classes, and, this is relies on the class imbalance between undamaged/minor damage and damage/destroyed classes, which leads to difficulties in classification for the model, for example in some predictions, the model misclassified buildings as damage due to a small part or the roof of the building that was destroyed showing no visible cracks from a panoramic view (Figure**3**(**C**)). This highlights the need for addressing class imbalance and enhancing the model's ability to distinguish subtle differences between classes.

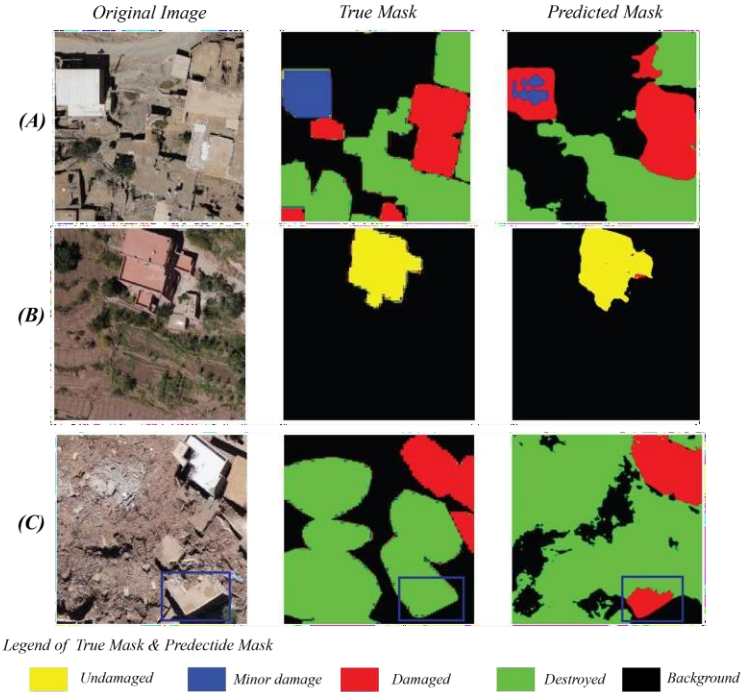

**Figure3.** Examples of segmentation results.

## Conclusion

In order to identify automatically the impacted areas in the Al Haouz region, this paper presents a segmentation framework using high-resolution UAV images and the SegFormer model. The experimental results demonstrated the strong feature extraction and discrimination capacities of SegFormer, in predicting various degrees of impact. In future works, we believe that the constructed Ighill segmentation dataset can be the database to identify disaster-affected areas in other regions. we may also involve augmenting the dataset to better represent underrepresented classes to improve performance in challenging scenarios.

**References:**

Akilan, A., Azeez, K. K. A., Schuh, H., & Yuvraaj, N. (2014). Large-Scale Present-Day Plate Boundary Deformations in the Eastern Hemisphere Determined from VLBI Data: Implications for Plate Tectonics and Indian Ocean Growth. Pure and Applied Geophysics, 172(10), 2643–2655.

Bai, Y., Hu, J., Su, J., Liu, X., Liu, H., He, X., Meng, S., Mas, E., & Koshimura, S. (2020). Pyramid Pooling Module-Based Semi-Siamese Network: A Benchmark Model for Assessing Building Damage from xBD Satellite Imagery Datasets. Remote Sensing, 12(24), 4055.

Birouk, A., Ibenbrahim, A., Mouraouah, A. E., & Kasmi, M. (2020). New integrated networks for monitoring seismic and tsunami activity in Morocco. *Annals of Geophysics (Print)*, *63*(2).

Bochkovskiy, A., Wang, C., & Liao, H. M. (2020, April 23). YOLOV4: Optimal speed and accuracy of object detection. arXiv.org.

Boutayeb, A. (2012). Evolution of rural–urban health gaps in Morocco: 1992–2011. BMC Research Notes, 5(1).

Cai, Z., & Vasconcelos, N. (2018). Cascade R-CNN: Delving Into High Quality Object Detection. 2018 IEEE/CVF Conference on Computer Vision and Pattern Recognition.

Chen, Q., Wang, Y., Yang, T., Zhang, X., Cheng, J., & Sun, J. (2021). You Only Look One-level Feature. 2021 IEEE/CVF Conference on Computer Vision and Pattern Recognition (CVPR).

Ding, J., Zhang, J., Zhi-Ming, Z., Tang, X., & Wang, X. (2022). A precision efficient method for collapsed building detection in Post-Earthquake UAV images based on the improved NMS algorithm and faster R-CNN. Remote Sensing, 14(3), 663.

Dosovitskiy, A.; Beyer, L.; Kolesnikov, A.; Weissenborn, D.; Zhai, X.; Unterthiner, T.; Dehghani, M.; Minderer, M.; Heigold, G.; Gelly, S. An image is worth 16 × 16 words: Transformers for image recognition at scale. arXiv 2020, arXiv:2010.11929.

Ge, Z., Liu, S., Wang, F., Li, Z., & Sun, J. (2021, July 18). YOLOX: Exceeding YOLO Series in 2021. arXiv.org.

He, K., Gkioxari, G., Dollár, P., & Girshick, R. (2017). Mask R-CNN. 2017 IEEE International Conference on Computer Vision (ICCV).

Koshimura, S., Moya, L., Mas, E., & Bai, Y. (2020). Tsunami Damage Detection with Remote Sensing: A Review. Geosciences, 10(5), 177.

Li, C., Li, L., Jiang, H., Weng, K., Geng, Y., Li, L., Ke, Z., Li, Q., Cheng, M., Nie, W., Li, Y., Zhang, B., Liang, Y., Zhou, L., Xu, X., Chu, X., Wei, X., & Wei, X. (2022, September 7). YOLOV6: A Single-Stage Object Detection Framework for Industrial Applications. arXiv.org.

Liu, Z.; Lin, Y.; Cao, Y.; Hu, H.; Wei, Y.; Zhang, Z.; Lin, S.; Guo, B. Swin transformer: Hierarchical vision transformer using shifted windows. In Proceedings of the IEEE/CVF International Conference on Computer Vision, Montreal, QC, Canada, 10–15 October 2021; pp. 10012–10022.

Long, J.; Shelhamer, E.; Darrell, T. Fully convolutional networks for semantic segmentation. In Proceedings of the IEEE Conference on Computer Vision and Pattern Recognition, Boston, MA, USA, 7–12 June 2015; pp. 3431–3440.

Mohamed, H., Peláez, J. A., Kijko, A., & Sawires, R. (2015). Characteristic Parameters of a seismogenic Source Zone Model in the Algeria-Morocco Region.

Nayak, K., López-Urías, C., Romero-Andrade, R., Sharma, G., Guzman-Acevedo, G. M., & Trejo-Soto, M. E. (2023). Ionospheric Total Electron Content (TEC) Anomalies as earthquake precursors: Unveiling the geophysical connection leading to the 2023 Moroccan 6.8 MW earthquake. Geosciences (Basel), 13(11), 319.

Redmon, J., & Farhadi, A. (2018, April 8). YOLOV3: an incremental improvement. arXiv.org.

Ren, S., He, K., Girshick, R., & Sun, J. (2017). Faster R-CNN: Towards Real-Time Object Detection with Region Proposal Networks. IEEE Transactions on Pattern Analysis and Machine Intelligence, 39(6), 1137– 1149.

Wang, C., Bochkovskiy, A., & Liao, H. M. (2023). YOLOv7: Trainable Bag-of-Freebies Sets New State-of- the-Art for Real-Time Object Detectors. 2023 IEEE/CVF Conference on Computer Vision and Pattern Recognition (CVPR).

Yu, Z., Chen, Z., Sun, Z., Guo, H., Leng, B., He, Z., Yang, J., & Xing, S. (2022). SeGDetector: a deep learning model for detecting small and overlapping damaged buildings in satellite images. Remote Sensing, 14(23), 6136.

INTERNATIONAL SYMPOSIUM ON
APPLIED
GEOINFORMATICS
9-10 May 2024 · Wrocław/Poland

*International Symposium on Applied Geoinformatics (ISAG2024)*

# A Novel Vector Cellular Automata Model for Modelling Urban Growth: Preliminary Findings

Ahmet Emir Yakup[1], Ismail Ercument Ayazli[2*]

**[1]** Hitit University, Department of Architecture and Urban Planning, Corum, Türkiye;
emiryakup@hitit.edu.tr; ORCID 0000-0002-1789-4448
**[2]** Sivas Cumhuriyet University, Faculty of Engineering, Department of Geomatics Engineering, Sivas, Türkiye;
eayazli@cumhuriyet.edu.tr; ORCID 0000-0003-0782-5366

## Abstract

The raster data structure, which reduces geospatial entities into regular units, has been frequently used in cellular automata (CA) based urban growth simulation models (UGSM). However, lands are geometrically irregular and cannot be accurately represented by a raster data structure. Representing lands in a vector data structure can provide more accurate and precise models. This study aims to develop a UGSM based on vector cellular automata (VCA) by modifying CA components with regular structure. In order to increase cellular operability, cells and neighborhoods representing lands are reduced to a structure called growth vectors. Thus, by creating dynamic neighborhoods specific to the local area, a VCA-based UGSM with flexible transformation rules was created. The model was tested in the Istanbul metropolitan area, one of the most populated cities in Europe. Data for the study area were obtained from CORINE, Open Street Map (OSM), and The United States Geological Survey (USGS) open-source services. Possible urban growth trends in Istanbul were investigated with the simulation model created. According to the results of the simulation model for the year 2050, it was determined that approximately 10% of agricultural land and 6% of forest areas could be transformed into residential areas. The best performance of the model was obtained with an F1 score of 83.31%. The results show that more accurate and precise UGSMs can be created with a vector data structure that increases the representation capacity of lands.

**Keywords:** *Urban Growth, Vector Cellular Automata, Simulation, Land Use/Cover Change*

## Introduction/Background

One of the main reasons why urban growth models have become widespread is the rapid increase in the urban population and the environmental problems caused by this increase (X. Li & Gong, 2016). According to a report published by the United Nations (UN), the world population, which is currently approaching 8 billion, is projected to increase by 1.2% annually to 8.5 billion in 2030 and 9.7 billion in 2050, and population growth in urban areas is projected to account for almost all of the future growth rate of the world population (UN, 2019). Uncontrolled urban growth poses challenges to effectively using limited (scarce) environmental resources and implementing sustainable development policies (UN, 2015). Regarding the sustainable urban management perspective, urban growth should be controlled.

Modeling is one of the most important methods of monitoring urban growth (Alien et al., 2017; Jantz et al., 2010; van Vliet et al., 2013; White, 1998). The developments in informatics, remote sensing, and geographical information systems technologies have enabled many parameters to be analyzed quickly (Batty, 2007; Benenson & Torrens, 2004; White, 1998). Many methods can be used in studies where urban growth is modeled by simulation. However, the main reason for choosing CA is its simplicity, intuitiveness, flexibility, and transparency. Thanks to its time, neighborhood, transformation rules, state set, and regular grid network components, CA is particularly suitable for modeling complex processes that exhibit nonlinear behavior and are self-organizing (J. Li et al., 2013).

In the 1990s, Benenson, Clarke, and Batty successfully used HO models to understand the process and pattern of urban growth and conducted pioneering studies (Batty, 2007; Benenson & Torrens, 2004; Clarke & Gaydos, 1998). These studies resulted in the Dynamic Urban Evolution Model (DUEM) by Batty and Xie and Clarke's SLEUTH urban growth simulation models (Clarke, 1998; Xie & Batty, 2004). These studies have led to many raster HO-based researches as a field open for development.

Initially, raster data facilitated the creation of simulation models by performing calculations on a regular grid network. However, the generated raster HO models fail to describe complex land use transitions of highly irregular, fragmented, and inconsistent geometric objects in urban areas (Yao et al., 2021). Another important problem for raster HO is selecting the appropriate cell size. A large cell size reduces the data volume and may decrease spatial accuracy (Yeh & Li, 2006). Land cover can be represented more realistically using vector data instead of raster (Barreira-González et al., 2015). In the Vector HO (VHO) model, each object has a geometric representation (a polygon) that evolves according to a transition function that depends on the influence of neighboring polygons. In this model, the neighborhood is defined as the region of influence on each geospatial object, and neighbors are all geospatial objects located within the region of influence (Moreno et al., 2008).

In the VCA model, cells can be presented according to the geospatial entities' geometry and attributes. The transition rules of the VCA model can be improved by considering the urbanization dynamics of the study area (Lu et al., 2015). Cells are the basic functional unit in urban development, urban planning, and land policy. Urban growth is the change of land cover type depending on the cell (Yao et al., 2021). Thus, since each cell differs, neighborhood factors and their effects can be defined more flexibly when creating transition rules. Within the scope of VCA, several recent studies have shown that using VCA instead of raster CA significantly improves urban growth simulation accuracy (Lu et al., 2015; Yao et al., 2021; Zhuang et al., 2022).

The Istanbul metropolitan area, which is dynamic regarding urbanization, was determined as the study area. Between 2000 and 2018, the population in Istanbul increased by more than 50%, from 10,018,735 to 15,067,724 (TÜİK, 2023). Accordingly, land cover changes triggered by urban growth have also increased. In the study, the historical land cover dataset for the region was created from CORINE data, accessibility data from OSM open source service data, and suitability data from Shuttle Radar Topography Mission (SRTM) data.

## Materials and Methods (Design/methodology/approach)

For 1990, 2000, 2006, 2012, and 2018, CORINE land cover/use data in vector form produced in line with the standards set by the European Environment Agency (EEA) were used. The 1990 CORINE land cover data represents the seed year of the model. Accessibility data was obtained from the Open Street Map (OSM) web service. The accessibility data considers the centerline of provincial roads, state roads, and international roads as primary importance. The zoning parameter was created to include the restriction of only those areas classified as water bodies. In other areas, a scenario suitable for urbanization was created. As the digital elevation model (DEM) needed for topographic suitability, SRTM data freely available from the Earth Explorer web service of the United States Geological Survey (USGS) was used.

**Table 1.** Data used in the research.

| Data Groups | Periods | Data Source |
|---|---|---|
| Land Cover | 1990<br>2000<br>2006<br>2012<br>2018 | CORINE |
| Transportation | 1990<br>2024 | OSM and Satellite Images |
| Zoning | - | CORINE |
| Suability | - | SRTM |

The developed model is based on cellular automata. The concept of Cellular Automata consists of five basic components. These are grid network, state, neighborhood, transformation rules, and time (Benenson & Torrens, 2004). Cells are the smallest units that are adjacent to each other. Cells come side by side to form the grid network. Each cell has a state. An infinite number of state types can be specified in the state set. Depending on time, the transformation function changes the cell states according to the state of neighboring cells. The regular structure of the principal components is flexed in this study to be compatible with the vector structure.

The developed VCA-based model has three main phases: preprocessing, calibration, and prediction. In the preprocessing stage, parameter extraction and matching operations are performed for each cell. In the calibration stage, the historical urban growth trends of the study area are determined. This stage can be iterated for a specified number of iterations. With the model parameters obtained in the calibration stage, UGSMs are generated in the prediction stage.

CA-based UGSM studies often use a parametric equation to define each cell's transformation potential. The value obtained from this equation indicates a cell's urban growth probability according to its neighborhood (N), accessibility (A), suitability (S), and zoning (Z). The parametric equation applied for each node is presented below. In this equation, the $P_i^t$ represents a node's potential urbanization probability.

$$P_i^t = Z_i^t \times S_i^t \times N_{\mathrm{i}}^t \times A_i^t \times cons \qquad (1)$$

Polygons and their attributes are abstracted into a node-edge structure to obtain growth vectors, with each node also storing its attributes. Once the nodes are created, edges are defined between nodes belonging to neighboring polygons. The table of growth vectors is created independently of the cells. They are associated one-to-many through the primary key of the cells that form the edge. On the other hand, the directions of the growth vectors are determined according to the land cover classes. The final score of the growth vector is obtained using the land cover classes and probability scores of the nodes forming the edge.

$$P_{i,j}^t = P_i^t \times P_j^t \times E_{i,j}^t \qquad (2)$$

It represents the urban growth potential of the growth vector $P_{i,j}^t$, the probability scores of the nodes that make up the growth vector $P_i^t$ and $P_j^t$, and the number of probability coefficients obtained depending on the Euclidean distance of the base formed by the growth vector $E_{i,j}^t$. Thus, nodes closer to each other will be able to interact more efficiently, while nodes farther apart will be able to interact with each other relatively less.

A decision threshold is determined by evaluating the relationship between the distributions of the resulting probability scores obtained in the model and the actual values. The growth vectors' transformation scores are considered potential decision thresholds. All growth vector scores within a generation correlate with known classes of target cells identified through change analysis. The True Positive Rate (TPR) and False Positive Rate (FPR) are calculated individually if the scores are chosen as possible cut-points. The difference between TPR and FPR is expected to be the highest.

$$TPR = Recall = TP \div (TP + FN) \qquad FPR = FP \div (FP + TN) \qquad (3)$$

TP (true positive) indicates how many of the areas predicted as urban are urban. TN (true negative) indicates how many of the areas predicted as non-urban are non-urban. FP (false positive) indicates how many urban areas are predicted to be non-urban. FN (false negative) measures how many non-urban areas are predicted to be urban. The F1 score is considered for evaluating the model. The F1 Score is the harmonic mean of the precision and sensitivity values.

$$precision = TP \div (TP + FP) \qquad F1 = 2 \times \left( {}^{precision \times recall}\!/_{precision + recall} \right) \qquad (4)$$

**Results and Discussion (Findings)**

The model was tested in the study area, and preliminary results were obtained. UGSMs of the area for the year 2050 were produced. The calibration phase was repeated ten times, resulting in F1 score values of 0.8331, 0.805, and 0.791, respectively. Change analysis was performed for the study area between 2018 and 2050. The results of the change analysis are presented in Table 2. According to the change analysis results, it is estimated that 5.7% of forest areas, 9.6% of agricultural areas, and 0.11% of wetlands in Istanbul are threatened by urbanization.

**Table 2.** Change detection analysis.

| Land Cover Class | 2018 – 2050 (ha) | % |
|---|---|---|
| Agriculture | 39,367.24 | 9.6 |
| Forest | 34,169.93 | 5.7 |
| Wetland | 1,033 | 0.11 |
| Waterbody | - | - |

The UGSM has identified potential urban growth areas for 2050. The orange areas in Figure 1 show the possible urbanization areas between 2018 and 2050.

**Figure 1.** UGSM for 2050

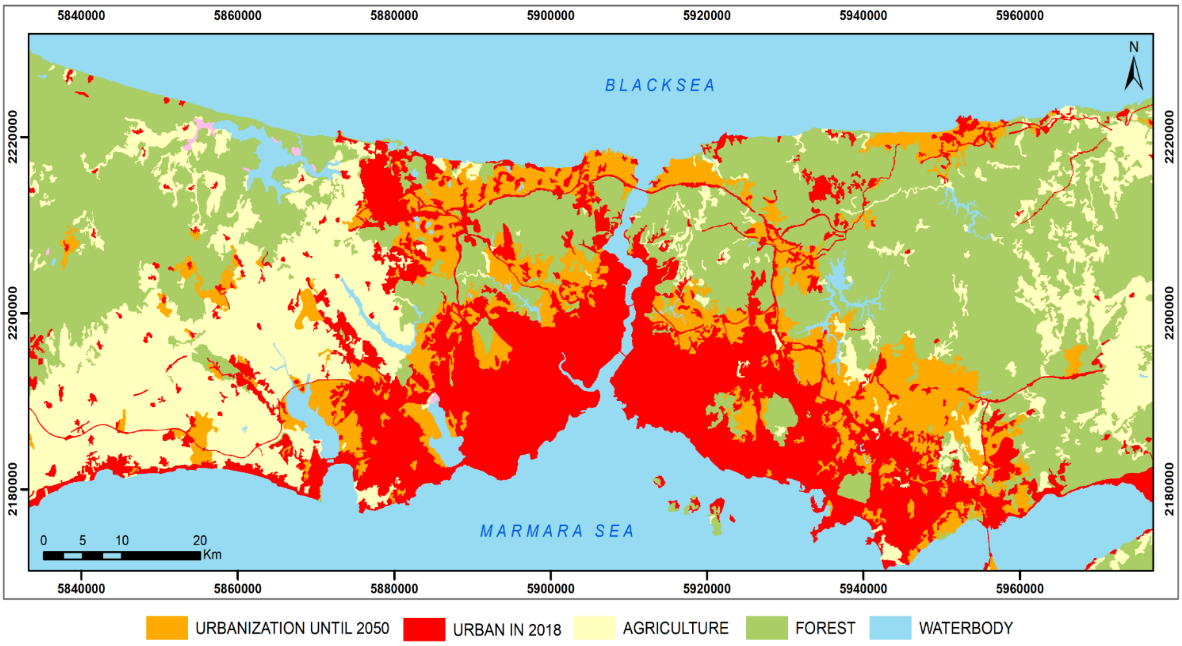

## Conclusion

In this study, the CA components are modified and reimagined into a vector data structure that can more accurately represent the LULC change. The capacity to generate dynamic neighborhoods using growth vectors was tested and the model was found to work within a reasonable computation time.

Our findings demonstrate the potential of VCA-based UGSMs to provide useful information for sustainable urban planning by accurately predicting future LULC changes.

## Acknowledgements (Optional)

This study is supported by TUBITAK in the scope of project number 114Y025.

## References

Aien, A., Rajabifard, A., Kalantari, M., & Williamson, I. (2017). Review and Assessment of Current Cadastral Data Models for 3D Cadastral Applications. In A. AbdulRahman (Ed.), *Advances in 3d Geoinformation* (pp. 423–442). Springer International Publishing Ag. https://doi.org/10.1007/978-3-319-25691-7_24

Barreira-González, P., Gómez-Delgado, M., & Aguilera-Benavente, F. (2015). From raster to vector cellular automata models: A new approach to simulate urban growth with the help of graph theory. *Computers, Environment and Urban Systems*, *54*, 119–131. https://doi.org/10.1016/j.compenvurbsys.2015.07.004

Batty, M. (2007). *Cities and complexity: Understanding cities with cellular automata, agent-based models, and fractals* (world). The MIT press. https://doi.org/10.5555/1543541

Benenson, I., & Torrens, P. (2004). *Geosimulation: Automata-based Modeling of Urban Phenomena*. John Wiley & Sons.

Clarke, K. C. (1998). *Project Gigalopolis, University of California-Santa Barbara*.

Clarke, K. C., & Gaydos, L. J. (1998). Loose-coupling a cellular automaton model and GIS: Long-term urban growth prediction for San Francisco and Washington/Baltimore. *International Journal of Geographical Information Science*, *12*(7), 699–714. https://doi.org/10.1080/136588198241617

Jantz, C. A., Goetz, S. J., Donato, D., & Claggett, P. (2010). Designing and implementing a regional urban modeling system using the SLEUTH cellular urban model. *Computers, Environment and Urban Systems*, *34*(1), 1–16. https://doi.org/10.1016/j.compenvurbsys.2009.08.003

Li, J., Wan, J., Lu, Y., Chen, J., & Fu, Y. (2013). A new object-oriented approach towards GIS seamless spatio-temporal data model construction. *Pervasive Computing and the Networked World: Joint International Conference, ICPCA/SWS 2012, Istanbul, Turkey, November 28-30, 2012, Revised Selected Papers*, 318–331.

Li, X., & Gong, P. (2016). Urban growth models: Progress and perspective. *Science Bulletin*, *61*(21), 1637–1650. https://doi.org/10.1007/s11434-016-1111-1

Lu, Y., Cao, M., & Zhang, L. (2015). A vector-based Cellular Automata model for simulating urban land use change. *Chinese Geographical Science*, *25*(1), 74–84. https://doi.org/10.1007/s11769-014-0719-9

Lu, Y., Laffan, S., Pettit, C., & Cao, M. (2020). Land use change simulation and analysis using a vector cellular automata (CA) model: A case study of Ipswich City, Queensland, Australia. *Environment and Planning B: Urban Analytics and City Science*, *47*(9), 1605–1621. https://doi.org/10.1177/2399808319830971

Moreno, N., Ménard, A., & Marceau, D. J. (2008). VecGCA: A Vector-Based Geographic Cellular Automata Model Allowing Geometric Transformations of Objects. *Environment and Planning B: Planning and Design*, *35*(4), 647–665. https://doi.org/10.1068/b33093

TÜİK. (2023). *Adrese Dayalı Nüfus Kayıt Sistemi Sonuçları*. Adrese Dayalı Nüfus Kayıt Sistemi Sonuçları. https://data.tuik.gov.tr/Bulten/Index?p=Adrese-Dayali-Nufus-Kayit-Sistemi-Sonuclari-2022-49685

UN. (2015). Take Action for the Sustainable Development Goals. *United Nations Sustainable Development*. https://www.un.org/sustainabledevelopment/sustainable-development-goals/

UN. (2019). *World population prospects*. United Nations Department of International. https://population.un.org/wpp/Download/Standard/MostUsed/

van Vliet, J., Naus, N., van Lammeren, R. J. A., Bregt, A. K., Hurkens, J., & van Delden, H. (2013). Measuring the neighbourhood effect to calibrate land use models. *Computers, Environment and Urban Systems*, *41*, 55–64. https://doi.org/10.1016/j.compenvurbsys.2013.03.006

White, R. (1998). Cities and cellular automata. *Discrete Dynamics in Nature and Society*, *2*, 111–125. https://doi.org/10.1155/S1026022698000090

Xie, Y., & Batty, M. (2004). Integrated Urban Evolutionary Modeling∗. In *GeoDynamics* (pp. 297–318). CRC Press. https://www.taylorfrancis.com/chapters/edit/10.1201/9781420038101-24/integrated-urban-evolutionary-modeling-8727-yichun-xie-michael-batty

Yao, Y., Li, L., Liang, Z., Cheng, T., Sun, Z., Luo, P., Guan, Q., Zhai, Y., Kou, S., Cai, Y., Li, L., & Ye, X. (2021). *UrbanVCA: A vector-based cellular automata framework to simulate the urban land-use change at the land-parcel level*. https://doi.org/10.48550/arXiv.2103.08538

Yeh, A. G.-O., & Li, X. (2006). Errors and uncertainties in urban cellular automata. *Computers, Environment and Urban Systems*, *30*(1), 10–28.

Zhuang, H., Liu, X., Yan, Y., Zhang, D., He, J., He, J., Zhang, X., Zhang, H., & Li, M. (2022). Integrating a deep forest algorithm with vector-based cellular automata for urban land change simulation. *Transactions in GIS*, *26*(4), 2056–2080. https://doi.org/10.1111/tgis.12935

INTERNATIONAL SYMPOSIUM ON
APPLIED
GEOINFORMATICS
9-10 May 2024 · Wrocław/Poland

*International Symposium on Applied Geoinformatics (ISAG2024)*

# Determınatıon of Forest Fıre Damage Through Coherence Values from InSAR Data

Goktug Yasar Cukurlu[1], Nusret Demir[2*], Pol Kolokoussis[3]

[1] Akdeniz University, Faculty of Science, Department of Space Science and Technologies, Antalya, Türkiye;
202351045003@ogr.akdeniz.edu.tr; ORCID 0009-0008-9233-7626
[2]Akdeniz University, Faculty of Science, Department of Space Science and Technologies, Antalya, Türkiye;
nusretdemir@akdeniz.edu.tr; ORCID 0000-0002-8756-7127
[3] National Technical University of Athens, Remote Sensing Laboratory, Athens, Greece;
pol@survey.ntua.gr; ORCID 0000-0002-5420-0900
* Corresponding Author

## Abstract

Detection of forest fires using optical sensors is a commonly employed technique. However, during a fire, the presence of a dense smoke cloud in the region makes it difficult to identify the fire area using optical sensors. Leveraging the Sentinel-1 SAR (C band), an active system, is highly advantageous for the detection of forested fires as it can penetrate through clouds or smoke, enabling imaging of the area beneath them. So in this study, to estimate the amount of vegetation lost, we used coherence variation analysis both before and after forest fires. This research compares single-look complex (SLC) format images that were processed at various periods over the same place using C-band Sentinel-1 SAR data. In our technique, we use three stages to monitor changes in coherence: before, during, and after the fire. The findings indicate a direct correlation between coherence dips and vegetation loss resulting from forest fires and similar patterns of change observed in regions with similar fire intensity. Significantly, InSAR's ability to penetrate clouds and smoke—limitations often faced by optical sensors—underlines its usefulness in evaluating fire-affected areas hidden by atmospheric conditions after a fire. In this study, it was found that there is a strong correlation between the amount of plant damage caused by fire and the coherence histograms that are obtained from Sentinel-1 SAR data, making them invaluable instruments for assessing the effects of forest fires. Moreover, given the potential for refinement inherent in the acquired results, it is envigading that forthcoming research endeavors will incorporate enhanced capabilities for autonomus computation. The test sites are Antalya Manavgat and Mugla Mazikoy.
**Keywords:** *Sentınel-1, Insar, Coherence, Forestfire*

## Introduction

In 2021, large forest fires in Turkey resulted in the loss of forest areas and forest wildlife. In the Antalya/Manavgat and Mugla/Marmaris regions, approximately 50 thousand hectares of land burned on a large scale (KOLUKIRIK et al., 2022). Due to the dense smoke cloud that formed during the fire, it was very difficult to take data with Sentinel-2 and Landsat-8 satellites, so the fire damage assessment could only be analyzed after the fire was completely stopped. Clouds and smoke do not affect Sentinel-1 SAR (Synthetic Aperture Radar) (Tsai et al., 2020), allowing it to image the fire area during the fire or in areas with continuous clouds. This study investigated the usability of InSAR data and coherence values, primarily used for displacement analysis, in determining the severity of fires. InSAR coherence $\gamma$ is the complex correlation between two complex SAR images that consists of a phase and a magnitude component. The magnitude varies between 0 and 1, at which 0 refers to no correlation and 1 to perfect correlation (Abdel-Hamid et al., 2021). SAR microwaves scatter in the leaves, resulting in a continuous phase difference in vegetation areas. Therefore, coherence values are low in the InSAR coherence dataset (Closson & Milisavljevic, 2017). Based on this basic knowledge, the feasibility of fire and change detection using InSAR coherence was examined, since vegetation loss and leaf loss will occur as a result of the burning of forested areas. We have also explored the possibility of estimating the fire area through the interpretation of coherence changes. The test areas were determined to be Antalya/Manavgat and Mugla/Mazikoy forest fires.

## Materıals and Methods

### Study Area

Within the scope of investigating the detectability of forest fires with InSAR coherence data, forest fires that occurred in 2021 (August 2, 2021, Mugla/Mazikoy forest fire, July 27, 2021, Antalya/Manavgat forest fire) in the provinces of Antalya in the Mediterranean region and Muğla in the Aegean region of Turkey were determined as the test area.

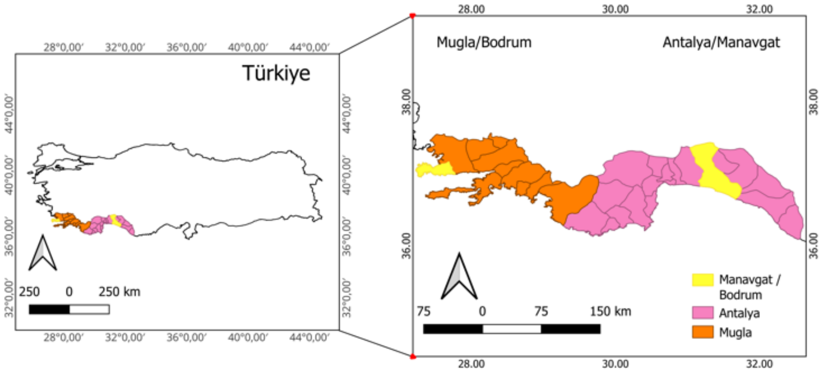

**Figure 1**. Locations of test areas (Antalya/Manavgat, Mugla/Mazikoy)

### Data and Processing

To generate InSAR images of the forest fires in the Antalya/Manavgat and Muğla/Mazıköy regions, data was collected from two different dates prior to the fire. The same process was then repeated during the fire, using one data point from before the fire and one from within the fire date range. Finally, data was collected approximately two weeks after the fire for post-fire analysis. The alaska.asf platform provided Sentinel-1 SAR (C-band) SLC (Single Look Complex) data in DESCENDING mode. The esaSNAP program, developed by the European Space Agency, was used for the extraction of InSAR coherence. The data procedures are outlined in Figure 2. Various other methods for coherence extraction were attempted, with comparable results. Following the processing, histograms were generated for the coherence-based map. Additionally, histograms were recorded for the periods before, during, and after the fire. The IW1 route was used for the Antalya/Manavgat region, whereas the IW2 route was employed for Muğla/Mazıköy. We implemented the procedures outlined in Figure 2 to extract coherence from two distinct Sentinel-1 SAR (C band) pictures. All parameters were maintained at a consistent level throughout the applications. Information was collected from alaska.asf. We implemented the prescribed protocols using the esaSNAP program. In the TOPS-SPLIT stage, we used Interferometric Wide Swath (IW) data that covers the specific area of interest. We used VV polarization to derive coherence from Sentinel-1 SLC data.

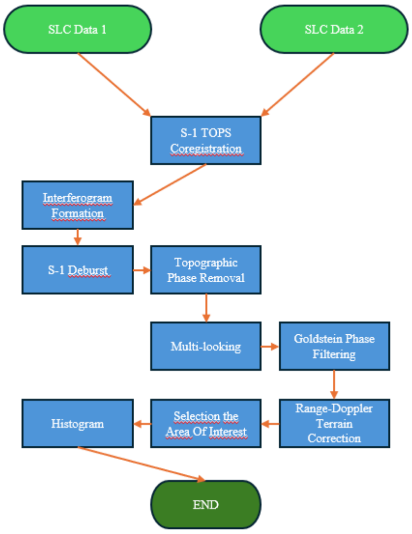

**Figure 2**. Workflow diagram for coherence extraction

## Results and Dıscussıon

The results obtained from the implemented techniques are shown in Figures 3 and 4. Given the similarity of the findings, it is feasible to detect forest fires using coherence.

The histograms derived from InSAR Coherence extraction reveal that the coherence values before to the fire were low, indicating little consistency. However, throughout the fire, the coherence values represented significant changes. Subsequently, following the fire, the coherence values were seen to be high, indicating a greater level of consistency. As previously stated (Closson & Milisavljevic, 2017), the observed outputs were consistent with expectations, likely owing to the disparity in phases between wooded and vegetated regions.

An investigation was conducted on the forest fire that originated on July 28, 2021 in the Antalya/Manavgat region, which was designated as the first test site. The pre-fire data corresponds to June 5, 17, 2021. The data collected during the occurrence of the fire corresponds to the dates of July 23 and August 16, 2021, whereas the data collected after the fire corresponds to the dates of August 16 and 28, 2021.

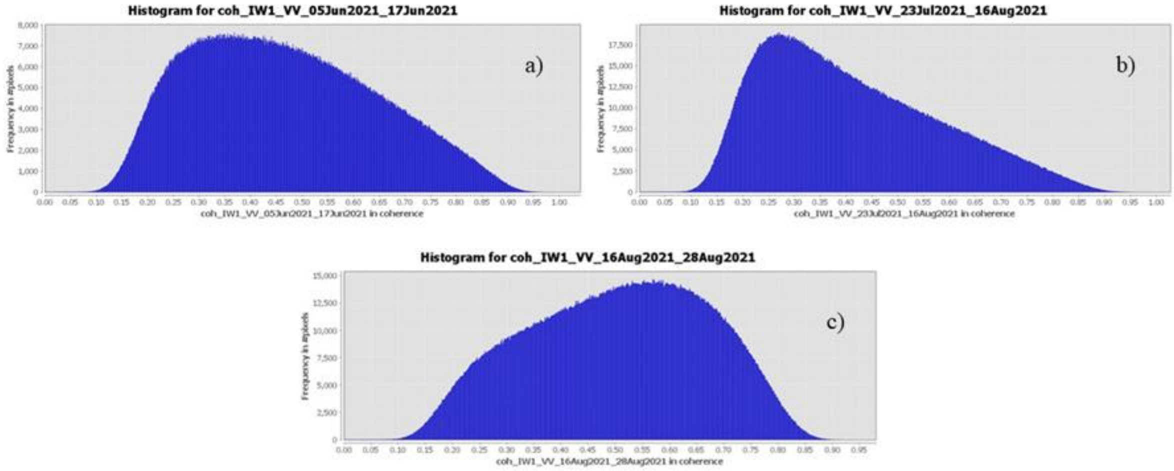

**Figure 3.** Coherence histograms of ANTALYA/MANAVGAT, a) pre-fire, b) during-fire, c) post-fire coherence values

When analyzing the coherence values for the Antalya/Manavgat area, we can see that there is a noticeable decrease in coherence before to the occurrence of the fire. Additionally, there is a significant drop in coherence values at the period of the fire, indicating a clear change. Following the fire, the majority of pixels exhibit high coherence values. The second test location had a forest fire in Mugla/Mazikoy on August 2, 2021. Sentinel-1 SAR (C Band) data were used for the Mazikoy wildfire, both before to, during, and after the occurrence of the fire. The pre-fire data corresponds to the dates of July 21 and 27, 2021. The data collected during the occurrence of the fire corresponds to the period between July 27 and August 14, 2021, whereas the data collected after the fire corresponds to December 07 and 19, 2021.

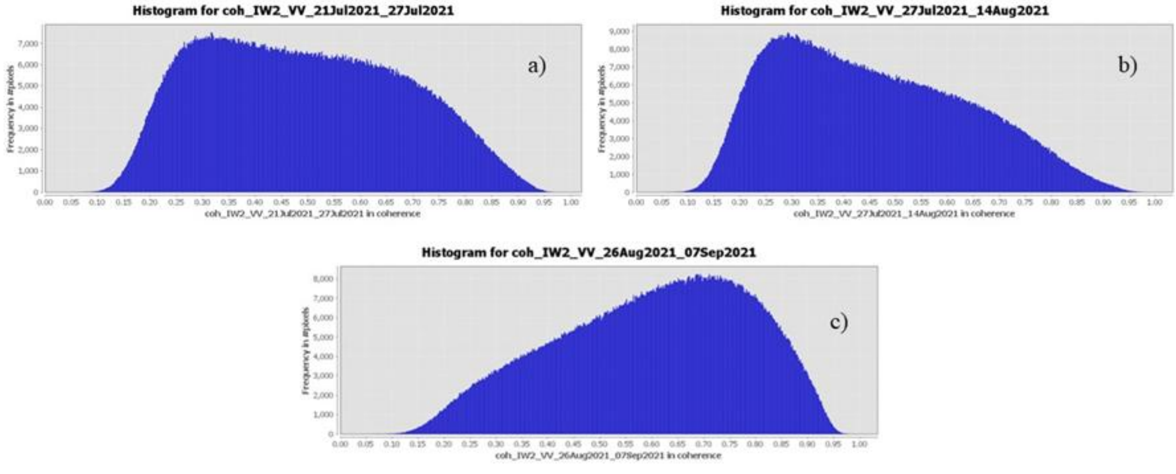

**Figure 4.** Coherence histograms of MUGLA/MAZIKOY, a) pre-fire, b) during-fire, c) post-fire coherence values

The Mugla/Mazkoy region's coherence histograms are similar to the Antalya/Manavgat region's coherence values. In the Mugla/Mazıkoy test area, the histogram of the fire moment shows a graph with a lower standard deviation and mostly low values. The studies conducted in two different test areas revealed a high correlation between the coherence values and the large-scale changes occurring in the forested areas. Washaya et al. (2018) extracted previous studies on forest fire inference with InSAR coherence from coherence-based SAR maps. In these studies, methods such as change detection, the Copernicus Emergency Management Service, etc. were used. Although monitoring forest fires by creating a histogram with InSAR coherence extraction is faster and simpler than other methods, a new method can be created by associating changes in coherence values with fire areas. Since the forest areas destroyed in the Antalya/Manavgat forest fire and the Mugla/Mazıkoy fire were relatively close to each other (approximately 50,000 ha. for each region), it was observed that the changes in coherence values were relatively close to each other. The coherence histograms, which had a pick value of approximately 0.30 before the fire, changed close to each other after the fire (approximately 0.60 in Antalya/Manavgat and approximately 0.70 in Mugla/Mazkoy). By using more test areas, it may be possible to estimate fire areas only based on the changes in the InSAR coherence histogram. In addition, the extraction of coherent histograms can be turned into an algorithm to make the use of InSAR data in fire detection more widespread and reduce the workload considerably.

## Conclusıon

Based on investigations done in two distinct test locations, it was revealed that there is a link between InSAR coherence histograms and forest fires. Forest fires might potentially be detected using Synthetic Aperture Radar (SAR) data in regions with cloud cover or in locations where optical sensors are unable to capture photos owing to dense smoke resulting from the fire. One may analyze the variation in coherence values in places with relatively mild fire damage to see whether the size of the forest fire impacts these changes. Simultaneously, the correlation between the change in coherence value and the extent of forest fire may be quantified by identifying additional test locations.

## Acknowledgement

This study has been supported and financed by Scientific and Technological Research Council of Turkey (TUBITAK) with the Project Nr. 123Y274 with coordination and support from the COST Action CA20118.

## References

Abdel-Hamid, A., Dubovyk, O., & Greve, K. (2021). The potential of sentinel-1 InSAR coherence for grasslands monitoring in Eastern Cape, South Africa. *International Journal of Applied Earth Observation and Geoinformation*, *98*. https://doi.org/10.1016/j.jag.2021.102306
Closson, D., & Milisavljevic, N. (2017). InSAR Coherence and Intensity Changes Detection. In *Mine Action - The Research Experience of the Royal Military Academy of Belgium*. InTech. https://doi.org/10.5772/65779

Kolukırık, S., Arslan, D. A., & Gökalp Yımaz, G. (2022). Orman Yangınlarının Toplumsal Etkileri ve Görünümü: Medya Paylaşımlarında 2021 Büyük Antalya-Manavgat Yangını. *Afet ve Risk Dergisi*, *5*(2), 560–580. https://doi.org/10.35341/afet.1086418

Tsai, Y. L. S., Klein, I., Dietz, A., & Oppelt, N. (2020). Monitoring large-scale inland water dynamics by fusing sentinel-1 sar and sentinel-3 altimetry data and by analyzing causal effects of snowmelt. *Remote Sensing*, *12*(23), 1–30. https://doi.org/10.3390/rs12233896

Washaya, P., Balz, T., & Mohamadi, B. (2018). Coherence change-detection with Sentinel-1 for natural and anthropogenic disaster monitoring in urban areas. *Remote Sensing*, *10*(7). https://doi.org/10.3390/rs10071026

INTERNATIONAL SYMPOSIUM ON
APPLIED
GEOINFORMATICS
9-10 May 2024 · Wrocław/Poland

*International Symposium on Applied Geoinformatics (ISAG2024)*

# GIS Based Decision Support Tool for Assisting Parcel Locker Field Operation

Ortak Ece[1], Doğru Ahmet Özgür [2,*]

[1] Department of Informatics Applications, Geographic Information Technologies Programme, Istanbul Technical University, ortak20@itu.edu.tr
[2] Faculty of Geoengineering, Geomatics Engineering, Istanbul Technical University, ozgur.dogru@itu.edu.tr
* Corresponding Author

## Abstract

The increasing prevalence of e-commerce has escalated the demand for deliveries, making last-mile delivery the most expensive, inefficient, and environmentally harmful segment of the entire logistics chain. Alternative methods, such as centralized multi-deliveries and 24/7 service-enabled smart lockers, known as parcel lockers, have been developed. The accurate placement of parcel lockers plays a crucial role in their successful utilization. Geographic Information Systems (GIS) provide effective tools for solving multi-criteria spatial decision-making problems.

This study aims to identify local requirements for parcel locker location selection and develop a GIS-based location selection model for decision-makers. Potential site selection criteria were determined through a comprehensive literature review and consideration of local demands. Data required for the analysis were collected for five districts of Istanbul and processed using ArcMap software. A decision support model focused on hexagonal grids with a side length of 500 meters was developed using the Model Builder tool. This automated system evaluates the suitability of the hexagonal grids for parcel locker operations, offering a user-friendly solution for decision-makers. The results of the application conducted in five districts of Istanbul revealed that the most suitable hexagonal grids were concentrated in the districts of Kadıköy, Üsküdar, and Ümraniye, classified as most suitable, suitable, and moderately suitable. The developed location selection criteria and model provide valuable guidance for future studies. This study demonstrates general applicability, whether in Istanbul or other regions of Turkey. To promote the widespread use of parcel lockers, similar studies should be conducted across the e-commerce sector, academia, and public domain planning processes.

**Keywords:** *Parcel Lockers, Multi-Criteria Spatial Decision-Making, GIS, Site Selection*

## Introduction

Over the past decade, technological developments have made online shopping increasingly popular, gradually replacing traditional in-store shopping. More and more people prefer purchasing products online rather than visiting physical stores. The global growth of online shopping has influenced people's activity and travel patterns and the last-mile delivery of goods. The e-commerce sector is struggling to organize last-mile deliveries to meet both economic and environmental sustainability requirements. Currently, last-mile delivery is considered the most expensive, inefficient, and environmentally polluting part of the entire logistics chain for the sector (Gevaers et al., 2014; Dablanc, 2011). Home deliveries are often the preferred method for deliveries. However, unsuccessful home deliveries result from many recipients not being at home during delivery hours. Failed deliveries contribute to an increase in vehicle kilometers traveled by courier companies and recipients to collect or return packages. Therefore, this situation contributes to urban transportation problems and worsens urban environmental quality (Ortak, 2024).

In recent years, many studies have focused on alternative measures, such as service points and secure delivery lockers offering the possibility of multiple deliveries to a single location, to mitigate the negative aspects and impacts of last-mile deliveries. Secure delivery lockers are smart locked cabinets that provide 24/7 service, assisting consumers in receiving and returning products purchased from e-commerce marketplaces. These lockers have rapidly spread worldwide and have become the focus of recent research in both the world and Turkey. In today's Turkey, the main companies operating in the field of locker delivery services include Trendyol Gel Al 7/24, Hepsimat, Easy Point, PTT Kargomat, Pudo Box, Yurtiçi Kargo Plus 7/24, and Kargopark (Ortak, 2024). However, there is currently no widespread network of locker delivery systems across the country, and the existing locker delivery systems are not being utilized efficiently. The locations of

secure delivery lockers play a crucial role in their successful use. When positioning these lockers, various factors such as demographic structure, shopping and travel habits of consumers, urban land use, and proximity to homes and workplaces should be taken into consideration (Wygonik & Goodchild, 2012; Ortak, 2024). Additionally, the criteria used to determine the locations of delivery points may vary from country to country due to local conditions.
Site selection is indeed one of the oldest challenges humanity has faced, captivating many researchers due to its complex nature. The decision for site selection is a strategic and long-term investment. Changing this decision is difficult and costly and should be analytically modeled. A Geographic Information System (GIS) integrates hardware, software, and data to capture, manage, analyze, and visualize all types of geographically referenced information. GIS provides a digital representation of the real world and is used to answer questions and support decisions in operational management and decision-making processes (Longley et al., 2015; Ortak, 2024). Geographic Information Systems help expedite site selection studies and present results through a more synthetic approach. Location analysis is conducted more efficiently and at a lower cost. Therefore, GIS-based location analysis should be integrated into the decision-making process.

This study aims to identify criteria that could play important roles in the location selection of delivery points in Turkey, based on the criteria discussed in the literature related to the location selection of secure delivery lockers. The study also aims to create a GIS-based location selection model (Ortak, 2024).

## Materials and Methods

This study employs Geographic Information Systems (GIS) combined with multi-criteria decision analysis techniques to determine the optimal locations for parcel lockers. The study was conducted in five districts of Istanbul: Üsküdar, Kadıköy, Ataşehir, Ümraniye, and Maltepe, which were selected due to their demographic diversity, commercial density, and transportation infrastructure. ArcMap 10.8.2 software was used for spatial data preparation, analysis, and visualization. The TUREF/TM 30 projection system was adopted to ensure uniformity in coordinate systems. Data were transformed and integrated through tools available within ArcMap to facilitate further analysis.

The selection criteria for the study were determined through a comprehensive literature review and consultation with industry professionals. Twelve criteria were established, focusing on accessibility to critical infrastructure such as fuel stations, public transportation stops, residential areas, shopping centers, business hubs, educational institutions, and proximity to main roads and parking facilities. Weights were assigned to these criteria based on their recurrence in the literature and feedback from experts.

A hexagonal grid system with a side length of 500 meters was created using the Generate Tesselation tool in ArcMap. This grid structure was selected due to its uniform spatial coverage and ability to minimize spatial bias in the analysis. Each grid cell was assigned a unique ID (GRID_ID) for data management. Data integration was performed by overlaying multiple spatial datasets on the hexagonal grid system. The following steps were applied:

- Population Data: Population density and socio-economic group distributions were calculated at the neighborhood level and integrated into the grid system using the Intersect tool.
- Accessibility Data: Proximity to critical infrastructure, such as transportation stops, fuel stations, shopping centers, and schools, was analyzed using Buffer and Overlay tools.
- Transportation Data: Main road accessibility and parking areas were incorporated to assess transportation-related suitability.

Suitability scores for each grid cell were calculated by applying weighted overlay analysis, where each criterion's importance was factored into the scoring process. The resulting scores were mapped, creating a spatial representation of grid suitability for parcel locker placement. The developed GIS-based model offers a streamlined and automated process for evaluating site suitability, ensuring consistency and replicability for future implementations in urban logistics planning.

## Results and Discussion

This study aims to develop a model for the location selection of smart parcel lockers in Turkey. The research addresses the challenges of last-mile delivery in e-commerce by identifying the criteria for selecting optimal locations for these lockers. Using GIS, the study combines various criteria to create a location selection model, with a specific focus on several districts in Istanbul as a case study. The study provides a scientific foundation for determining how to place smart parcel lockers effectively, considering local conditions and infrastructure. The main outcome of the study is the site selection model built as a spatial decision support tool. Figure 1 presents overall model structure.

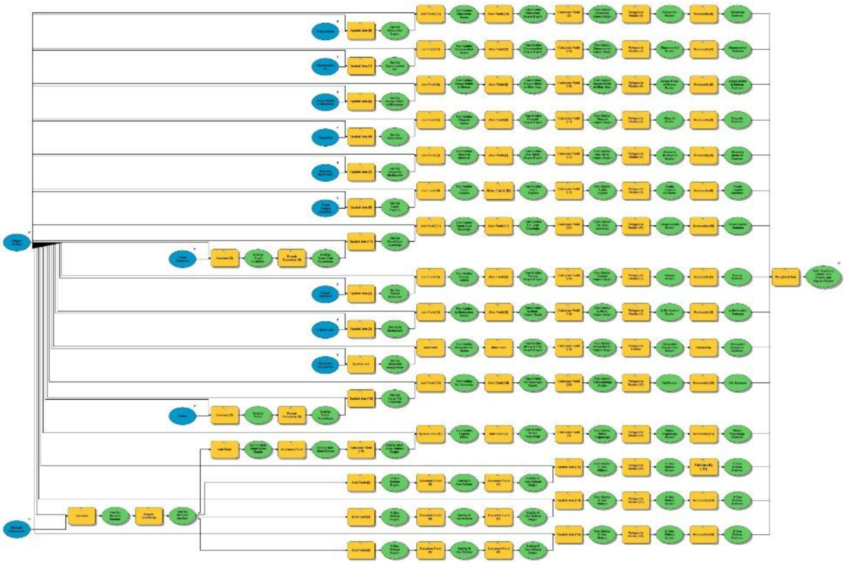

Figure 1. Produced site selection model.

The main output of the site selection model is the availability map. Figure 2 presents the availability map, which is produced by running the model using data of the study area as the implementation. Additionally Figure 3 highlights the existing parcel locker locations on the availability map.

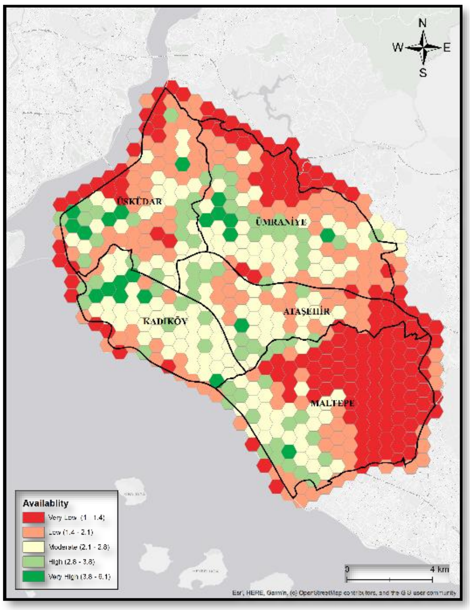

Figure 2. The availability map.

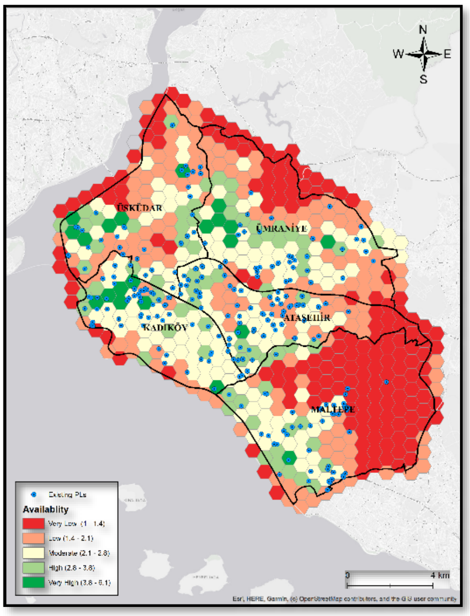

Figure 3. Existing lockers locations based on availability.

One of the key findings of the study is that the location selection model applied to the districts of Kadıköy, Üsküdar, Ümraniye, Ataşehir, and Maltepe in Istanbul largely aligns with the existing locations of parcel lockers. Of the 579 hexagonal grids used in the model, 3% were classified as "Very Suitable", 12% as "Suitable", and 28% as "Moderately Suitable" (see Figure 3 and Figure 4). These results indicate that the current parcel locker locations are mostly situated in areas that the model identifies as suitable or moderately suitable. Furthermore, the suitability levels in the districts of Kadıköy, Üsküdar, and Ümraniye were found to be higher, with the most optimal locations for locker placement being concentrated in these areas. On the other hand, Maltepe and Ataşehir districts exhibited a more balanced distribution of suitability classes, with Maltepe showing a higher percentage of areas classified as "Not Suitable" due to the presence of large green spaces and less urbanization.

The suitability classification across districts provides a detailed understanding of how urban dynamics influence the optimal location for parcel lockers. Kadıköy, Üsküdar, and Ümraniye stand out as the most suitable districts for locker placement, primarily due to their high population density, commercial areas, and proximity to transportation hubs. Maltepe, while having several "Suitable" locations, also has more "Not Suitable" areas, primarily because of its large green spaces and less dense urban areas. This finding highlights the importance of considering local conditions and urbanization patterns in the location selection process.

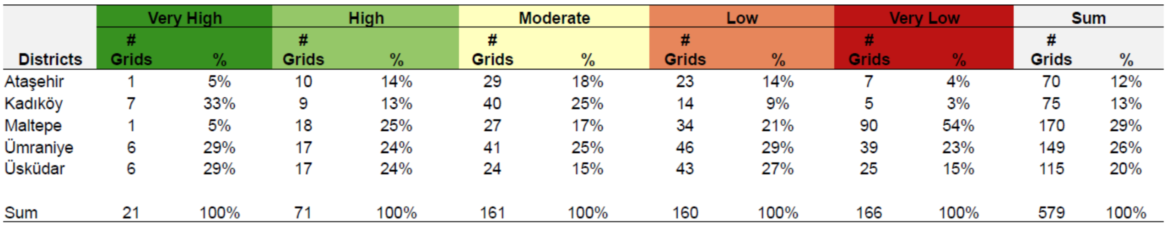

| Districts | Very High |  | High |  | Moderate |  | Low |  | Very Low |  | Sum |  |
|---|---|---|---|---|---|---|---|---|---|---|---|---|
|  | # Grids | % | # Grids | % | # Grids | % | # Grids | % | # Grids | % | # Grids | % |
| Ataşehir | 1 | 5% | 10 | 14% | 29 | 18% | 23 | 14% | 7 | 4% | 70 | 12% |
| Kadıköy | 7 | 33% | 9 | 13% | 40 | 25% | 14 | 9% | 5 | 3% | 75 | 13% |
| Maltepe | 1 | 5% | 18 | 25% | 27 | 17% | 34 | 21% | 90 | 54% | 170 | 29% |
| Ümraniye | 6 | 29% | 17 | 24% | 41 | 25% | 46 | 29% | 39 | 23% | 149 | 26% |
| Üsküdar | 6 | 29% | 17 | 24% | 24 | 15% | 43 | 27% | 25 | 15% | 115 | 20% |
| Sum | 21 | 100% | 71 | 100% | 161 | 100% | 160 | 100% | 166 | 100% | 579 | 100% |

**Figure 4.** Evaluation of the availability results.

In addition to the general findings, the district-based evaluation further reinforces the significance of considering local urban dynamics in optimizing the placement of parcel lockers. In districts such as Kadıköy, Üsküdar, and Ümraniye, which are characterized by high commercial activity and robust infrastructure, the results indicated a concentration of "Very Suitable" areas for locker placement. These districts show the potential to benefit greatly from the implementation of smart parcel lockers due to their high population density and excellent access to transportation networks. Conversely, Maltepe and Ataşehir presented more challenges, with Maltepe in particular showing a higher proportion of "Not Suitable" regions due to its expansive green spaces and lower urbanization. This suggests that while these districts may still be appropriate for some parcel locker installations, additional planning and consideration of local urban characteristics would be needed to optimize placement in these areas.

While the model has demonstrated its validity within the context of Istanbul, its potential for application in other cities and regions must be explored. Future studies could investigate how the model performs in cities with different urban layouts, economic conditions, and transportation infrastructure. Additionally, refining the criteria based on local preferences and behaviors could increase the model's accuracy. The inclusion of more granular data, such as neighborhood-specific transportation patterns or preferences for delivery times, could also improve the robustness of the model.

## Conclusion

In conclusion, the study demonstrates that the location selection model based on GIS tools is effective in identifying suitable areas for the installation of smart parcel lockers in urban environments. The model's ability to align with existing locations suggests its practical applicability for improving logistics efficiency in last-mile delivery while also reducing operational costs and environmental impact. The district-based analysis provides a valuable tool for understanding the spatial distribution of parcel locker suitability, offering a framework for future research and implementation in other regions. The study also highlights the need for continuous updates to the model using current data and the potential for further refinement based on user experience and specific business requirements.

This work makes a significant contribution to the field of e-commerce logistics and urban planning by offering a comprehensive, GIS-based decision support system for selecting optimal locations for smart parcel lockers. Future research should continue to refine this model, incorporating real-time data and user feedback to ensure that the system remains adaptive and scalable in the face of rapidly changing urban landscapes and market demands.

## References

Dablanc, L. (2011). Freight transport, a key for the new urban economy. European Transport, 47(1), 55-76.

Gevaers, R., Van de Voorde, E., & Vanelslander, T. (2014). Cost modelling and simulation of last-mile characteristics in an innovative B2C supply chain environment with implications on urban areas and cities. Procedia Social and Behavioral Sciences, 125, 398-411.

Longley, P. A., Goodchild, M. F., Maguire, D. J., & Rhind, D. W. (2015). Geographic Information Systems and Science. John Wiley & Sons.

Ortak, E. (2024). GIS Based Decision Support Tool For Assisting Parcel Locker Field Operations, MSc Thesis, İTÜ Graduate School, Geographical Information Technology Programme, İstanbul Türkiye. (In Turkish).

Wygonik, E., & Goodchild, A. (2012). Evaluating the efficacy of shared-use vehicles for reducing greenhouse gas emissions: A US case study of grocery delivery. Journal of the Transportation Research Forum, 51(2), 111-126

INTERNATIONAL SYMPOSIUM ON
APPLIED
GEOINFORMATICS
9-10 May 2024 · Wrocław/Poland

*International Symposium on Applied Geoinformatics (ISAG2024)*

# Analysis of Surface Displacements and VS30 Models of Kartal-Istanbul and Antalya

Nusret Demir*[1], Dilara Solmaz[1], Ufuk Yazgan[2]

[1] Akdeniz University, Faculty of Science, Department of Space Science and Technologies, Antalya, Türkiye;
nusretdemir@akdeniz.edu.tr; dilarasolmaz02@gmail.com, ORCID 0000-0002-8756-712
[2] Istanbul Technical University, Institute of Disaster Management and Earthquake Eng., Istanbul-Türkiye;
ufukyazgan@itu.edu.tr; ORCID 0000-0003-0092-8848
* Corresponding Author

## Abstract

The rapid urbanization and infrastructure development in İstanbul have heightened concerns regarding ground stability and seismic risk management. The Kartal region of İstanbul, situated within a seismically active zone, provides a unique environment for examining surface deformation processes in urban areas. The selected region is Antalya city center which has various type of the ground surface. Various remote sensing methods can be employed to identify the ground surface displacements. InSAR methodologies are useful to monitor the time series of the respective regions accordingly. Beside this, VS30 is a measure representing the seismic velocity parameter of the ground and plays a significant role in seismic risk analyses. This parameter defines the first-level seismic velocity of the soil layer up to 30 meters from the surface. The Vs30 value is a crucial indicator determining the elastic properties of the soil and the propagation speed of seismic waves. In this study, Short Baseline Subsets (SBAS) method has been used with applying LICSBAS Tool. The method relies on already processed interferograms which are distributed in COMET-LiCS Sentinel-1 InSAR portal. This portal has Sentinel 1 SAR Data based interfergrams fort he risky areas around the globe We analyze the Kartal region of Istanbul for the years between 2014-2022 to calculate the displacements. The displacements have been calculated both for ascending and descending modes. Then we have analyzed the results with the USGS based VS30 data. The first tests show that a slight negative correlation between these VS30 and displacement values, suggesting that as VS30 increases, the absolute values of the displacement values tend to decrease slightly especially for Antalya site. Kartal site has no significant difference between the absolute displacement among different vs30 values. This is assumed because the vs30 values are large below 400 and not have standard deviation like Antalya dataset. This study has been supported and financed by Scientific and Technological Research Council of Turkey (TUBITAK) with the Project Nr. 121M706.

**Keywords:** *InSAR, Displacement, VS30, Earthquake Risk*

## Introduction

Antalya, in recent times, has been mostly impacted by earthquakes that occur in its surrounding geographical area. According to Dipova and Cangir (2011), significant earthquakes in the Antalya region are often reported along the Fethiye-Burdur Fault Zone and the Hellenic-Cyprus Arc. The research conducted by Dipova and Cangir provides an analysis of the active and prospective fault zones in Antalya [1]. In addition, the metropolitan region of Istanbul is at a significant risk of earthquakes owing to the uncertain structural integrity of structures and a high likelihood of experiencing earthquakes with a magnitude of 7 or higher on a yearly basis (Durukal et al., 2008). According to a study, there is a 62% likelihood of experiencing intense shaking in Istanbul during the next 30 years. This is caused by the transfer of stress from past earthquakes to faults that are closer to Istanbul. The statement highlights the urgent need for earthquake preparation and measures to reduce its impact (Parsons et al., 2000). Detailed displacement analysis of Istanbul city which is created with LICSAR can be found at (Demir and Yazgan, 2023)

The Kartal region of İstanbul is located at Asian part of the city, where the active faults are placed in the south of its center. The faults around Antalya and Kartal are shown in Figure 1.

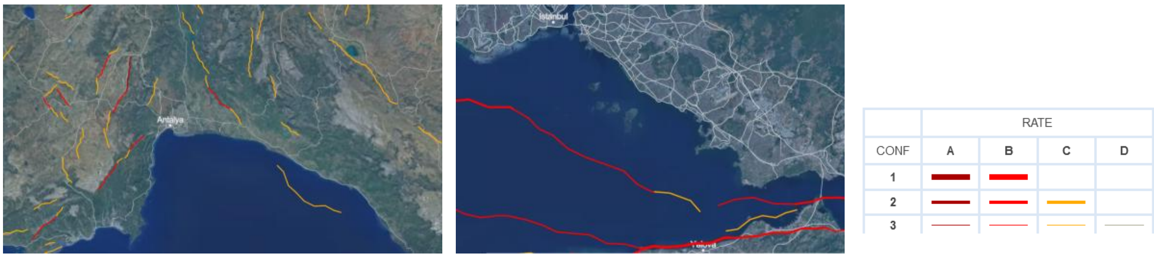

**Figure 1.** shows the faults around Antalya and Kartal

Figure 1. shows the faults around Antalya and Kartal. CONF (Confidence  refesr to the confidence level in the data or predictions about fault lines. It's common to assess the reliability of the information based on evidence quality, data accuracy, or modeling precision. RATE (Rate of Movement) indicates the rate at which a fault line is moving or has moved historically.

VS30 is a metric employed in the field of earthquake engineering to assess the seismic characteristics of a place. The value shows the mean velocity of shear waves, which are seismic waves that propagate through the Earth, in the upper 30 meters of the Earth's surface. This number is essential for evaluating the potential intensity of earthquake shaking, as it aids in the modeling of how ground motion might be amplified by the top layers of the Earth. VS30 values classify sites based on their geological characteristics, ranging from solid bedrock to soft soil. These characteristics have a significant impact on the design and construction of structures and infrastructure to ensure their resilience against seismic events. It can be accessible through the U.S. Geological Survey (USGS) website, which offers comprehensive resources for VS30 models and data. They provide a global VS30 mosaic based on topographic slope with custom embedded maps, as well as a compilation of VS30 measurements obtained by studies funded by the USGS and other governmental agencies.

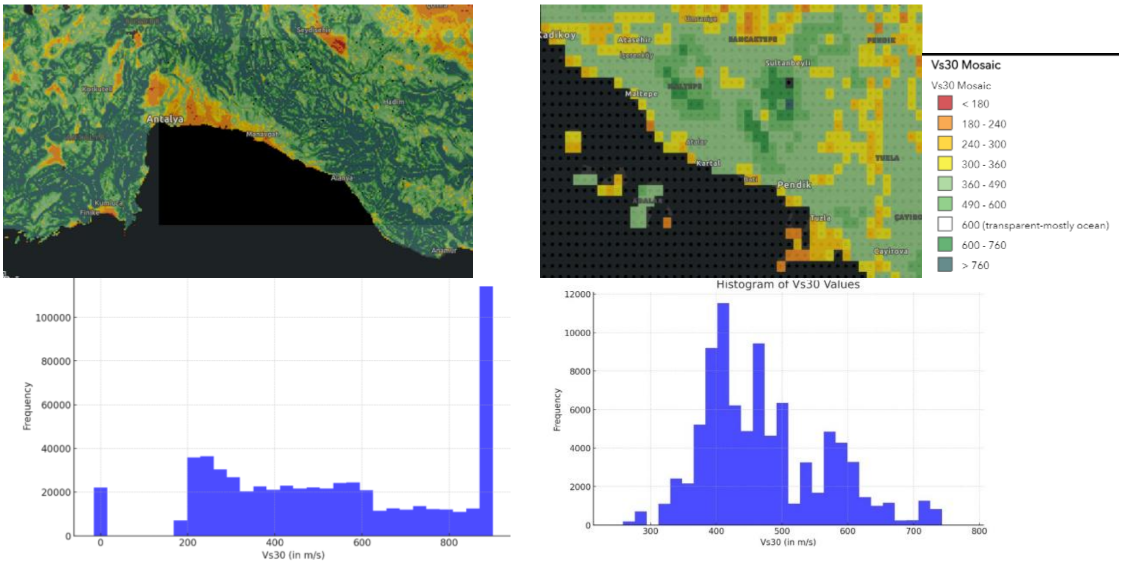

**Figure 1.** shows the faults around Antalya (Left) with standard deviation of 259.49 and Kartal (Right) with standard deviation of 92.40.

## Materials and Methods

The identification of the surface displacement has been facilitated via the utilization of satellite data, such as synthetic aperture radar pictures and optical satellite data. Sentinel 1 is a constellation of two radar satellites, namely Sentinel 1A and 1B. It plays a vital role in monitoring Earth's surface characteristics and is a key component of the Copernicus program, an effort by the European Union that offers free and unrestricted access to Earth observation data. Sentinel 1 is equipped with a C-band wavelength capability and offers the choice of HH and VV polarization choices. It operates in a sun-synchronous orbit at an altitude of 693 km. The sensors provide many acquisition modes, such as Strip Map Mode, Interferometric Wide Swath Mode, Extra-Wide Swath Mode, and Wave Mode. These modes have different swath widths and spatial resolutions. The Strip Map Mode has a swath width of 80 km and a spatial resolution of 5 m. The Interferometric Wide Swath Mode has a swath width of 250 km and a spatial resolution of 5 m x 20 m. The Extra-Wide Swath Mode has a swath width of 20 km and a spatial resolution of 20 m x 40 m. Lastly, the Wave Mode has a swath width of 20 km and a spatial resolution of 5 m x 20 m.
The LICSAR tool was employed with precalculated interferograms obtained from the Comet Portal (Lazeckỳ et al., 2020) The LICSAR package, which is part of the Looking into the Continents from Space effort, utilizes an online platform to

produce automated and synthetic aperture radar (SAR) interferograms using data collected by the Sentinel-1 satellites. This technique is crucial for generating comprehensive, precise, and dependable InSAR data, which is highly significant for monitoring global long-term deformation.

## Results and Discussion

A total of 435 interferograms between May 17th, 2020 and March 21st, 2023 are used in the data analysis. Figure 3 displays the computed displacement map.

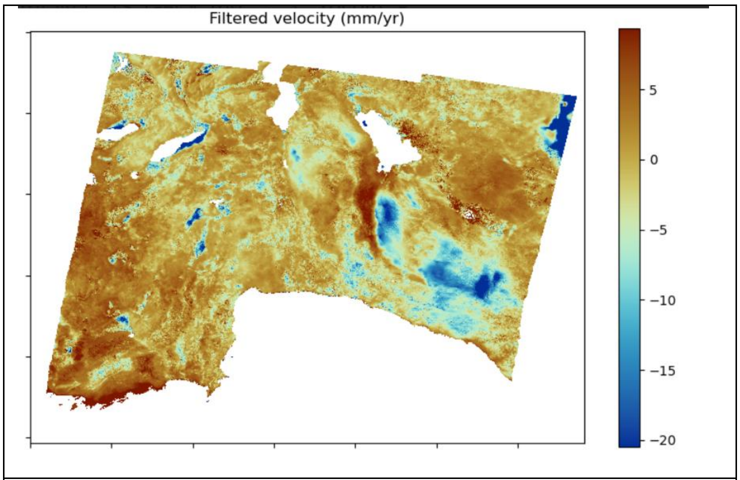

**Figure 3.** The displacement velocity map (LOS-Descending) of Antalya

Regarding Kartal, a more extensive dataset has been used, and the corresponding information may be found in Table 1.

Table 1. Use data- Kartal site

| YEAR | ASC | DESC |
|---|---|---|
| 2015 | 30 | 26 |
| 2016 | 32 | 37 |
| 2017 | 59 | 57 |
| 2018 | 57 | 56 |
| 2019 | 56 | 59 |
| 2020 | 31 | 33 |
| 2021 | 43 | 54 |

The displacement maps are created for each year individually both for ascending and descending. The following figure shows an example from the year 2014 and 2017.

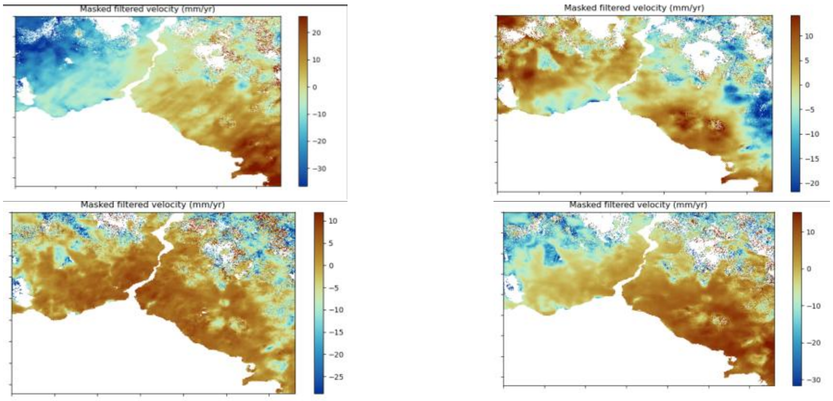

**Figure 4.** The displacement velocity maps for Kartal, Ascending and Descending 2015 and 2016.

When analyzing the displacements for Antalya, the western part has been subjected to a small amount of subsidence movement. The agricultural fields, the burned forest areas have significant subsidence. Besides this, the Kartal region has an uplift movement in general. Regarding VS30 values, Antalya city center has low values since Kartal has better conditions with higher values compared to Antalya city Figure 2. Below Table 2 shows the mean, standard deviation, maximum values of the absolute value of calculated displacements over the listed vs30 values.

**Table 2.** Statistics of the displacement values, Antalya

| VS30 Range | Mean | Std. Dev. | Max |
|---|---|---|---|
| 0-200 | 4.97 | 3.050 | 42.17 |
| 200-400 | 5.40 | 2.79 | 59.36 |
| 400-600 | 4.79 | 2.53 | 42.72 |
| 600-800 | 5.24 | 2.67 | 23.11 |
| 800-1000 | 5.68 | 2.95 | 20.25 |

The table above shows that the maximum displacement values are apparent in the lower VS30 values since the standard deviation values are also showing higher values. The correlation coefficient between VS30 range and the maximum values is calculated at 0.79. Regarding Kartal, the Table 3 is shown below, there is no values in the range of 0-200 and 600-800.

**Table 3.** Statistics of the displacement values, Kartal

| VS30 Range | Mean | Std. Dev. | Max |
|---|---|---|---|
| 200-400 | 11.75 | .2.72 | 19.32 |
| 400-600 | 12.29 | 2.95 | 23.07 |

The first tests show that a slight negative correlation between these VS30 and displacement values, suggesting that as VS30 increases, the absolute values of the displacement values tend to decrease slightly especially for Antalya site. Kartal site has no significant difference between the absolute displacement among different vs30 values. This is assumed because the vs30 values are largle below 400 and not have standard deviation like Antalya dataset.

## Conclusion

This study presents a thorough method for evaluating the danger of earthquakes in Istanbul's Kartal District. It does this by combining modern remote sensing techniques with data analysis. Our approach leverages the distinctive features of Synthetic Aperture Radar (SAR) technology, including the Sentinel 1 SBAS technique These methods have been extremely effective in evaluating surface displacement providing crucial insights into seismic vulnerability. This work represents a time-series data of Kartal and Antalya displacement. The tests of this work show that lower VS30 values cause higher absolute displacements in case a large standard deviation of vs30 values is present, but further investigations are highly recommended.

## Acknowledgements

This study has been supported and financed by Scientific and Technological Research Council of Turkey (TUBITAK) with the Project Nr. 121M706.

## References

Demir, N., Yazgan, U., 2023. INSAR-BASED INVESTIGATION OF SURFACE DISPLACEMENT OVER THE AREA OF THE COLLAPSED BUILDINGS IN ISTANBUL. Int. Arch. Photogramm. Remote Sens. Spat. Inf. Sci. XLVIII-M-1–2023, 81–85. https://doi.org/10.5194/ISPRS-ARCHIVES-XLVIII-M-1-2023-81-2023

Durukal, E., Erdik, M., Uçkan, E., 2008. Earthquake risk to industry in Istanbul and its management. Nat. Hazards 44, 199–212. https://doi.org/10.1007/S11069-007-9119-0/TABLES/3

Lazecký, M., Spaans, K., González, P.J., Maghsoudi, Y., Morishita, Y., Albino, F., Elliott, J., Greenall, N., Hatton, E., Hooper, A., Juncu, D., McDougall, A., Walters, R.J., Watson, C.S., Weiss, J.R., Wright, T.J., 2020. LiCSAR: An Automatic InSAR Tool for Measuring and Monitoring Tectonic and Volcanic Activity. Remote Sens. 2020, Vol. 12, Page 2430 12, 2430. https://doi.org/10.3390/RS12152430

Parsons, T., Toda, S., Stein, R.S., Barka, A., Dieterich, J.H., 2000. Heightened odds of large earthquakes near Istanbul: An interaction-based probability calculation. Science (80-.). 288, 661–665. https://doi.org/10.1126/SCIENCE.288.5466.661/SUPPL_FILE/1049447.XHTML

INTERNATIONAL SYMPOSIUM ON
APPLIED
GEOINFORMATICS
9-10 May 2024 · Wrocław/Poland

*International Symposium on Applied Geoinformatics (ISAG2024)*

# Machine Learning for Urban Traffic Prediction: Towards Intelligent Urban Planning Case Study: Casablanca

Laaziza Hammoumi[1*], Chaymae Khaloua[1], Mohamed Benayad[1], Mehdi Maanan[1], Hassan Rhinane[1]

[1] University Hassan II, Faculty of Science Aïn Chock, Department of Geology, Geoscience Laboratory, Casablanca, Morocco; Laaziza.hammoumi@gmail.com

* Corresponding Author

## Abstract

Urban planning faces unprecedented challenges in optimizing traffic flow and enhancing mobility within metropolitan cities. Lack of efficient traffic management and holistic urban planning strategies lead to congestion compromising city mobility and citizen well-being. This study addresses the diverse factors associated with traffic patterns, contributing to the identification of problematic zones within metropolitan areas. Our case study focuses on the city of Casablanca in Morocco, serving as an example of metropolitan areas in emerging economies. By employing different Machine Learning (ML) algorithms, such as: Random Forest RF, Artificial Neural Network ANN, Support Vector Machine (SVM), and K-nearest neighbors (KNN), we developed a predictive model that leverages multi-source urban data. The dataset used includes Waze data metrics (traffic incidents, traffic flow rate, real-time traffic conditions…), GIS data (road network, land use patterns, population density…), and other urban indicators. These algorithms have been compared in order to select the best one, aiming to anticipate traffic patterns, optimize urban planning strategies, and propose intelligent solutions for better mobility, reduced congestion, and enhanced accessibility. Random Forest (RF) and Artificial Neural Network (ANN) emerged as the best-trained models, exhibiting the highest level of accuracy in this pursuit, with respectively an AUC of 0,884 and 0,808. This study not only contributes to the development of a predictive model for urban planning but also provides actionable insights that can be utilized by road authorities and urban planners for effective decision-making, in the city of Casablanca.

**Keywords:** Mobility, Traffic accidents, Machine Learning, Intelligent Urban Planning.

## Introduction

Urban planning is increasingly interlinked with smart cities initiatives that aim to enhance the efficiency, operational effectiveness, and sustainability of urban environments (Batty, 2013). Metropolitan areas, in particular, benefit from this integration as it focuses on leveraging advanced technologies to optimize traffic flow and enhance mobility, significant aspects of urban quality of life (Caragliu et al., 2011). Intelligent urban planning uses data-driven approaches to address congestion and enhance city mobility, thereby improving citizen well-being and reducing environmental impacts (Neirotti et al., 2014).

Transitioning from the broader context to our specific study area, Casablanca, Morocco's largest city, exemplifies the challenges faced by emerging economies in managing urban traffic and ensuring road safety. The city suffers from high rates of traffic congestion and road accidents, which profoundly impact public health and urban mobility (HCP, 2014). These issues are compounded by rapid urban growth and insufficient infrastructure, making traffic management an urgent area of concern for urban planners and public authorities (Rodrigue et al., 2013). The frequent traffic jams and accidents not only lead to economic losses but also restrict access to emergency services, exacerbating the challenges in urban management (UN-Habitat, 2013).

In response to these challenges, this study aims to employ machine learning as a tool to analyze and predict traffic patterns and identify accident-prone zones in Casablanca. The objective is to develop a predictive framework that can inform and enhance urban planning processes, thereby improving road safety and urban mobility. By analyzing comprehensive urban data, including traffic metrics and geographical information systems (GIS) data, this research seeks to provide actionable insights that can aid in the decision-making processes for urban development and traffic management (Shaw et al., 2013).

## Materials and Methods

### The Study Area

Casablanca, the economic heart of Morocco and its largest urban center, is strategically located along the Atlantic coast, approximately 80 km south of Rabat. The city encompasses an area of 1,140.54 km² and is administratively divided into 16 prefectures. As the largest city in the Maghreb and a crucial transportation hub, Casablanca experiences significant urban density and traffic challenges, making it a pertinent case study for traffic management and urban planning (HCP, 2014).

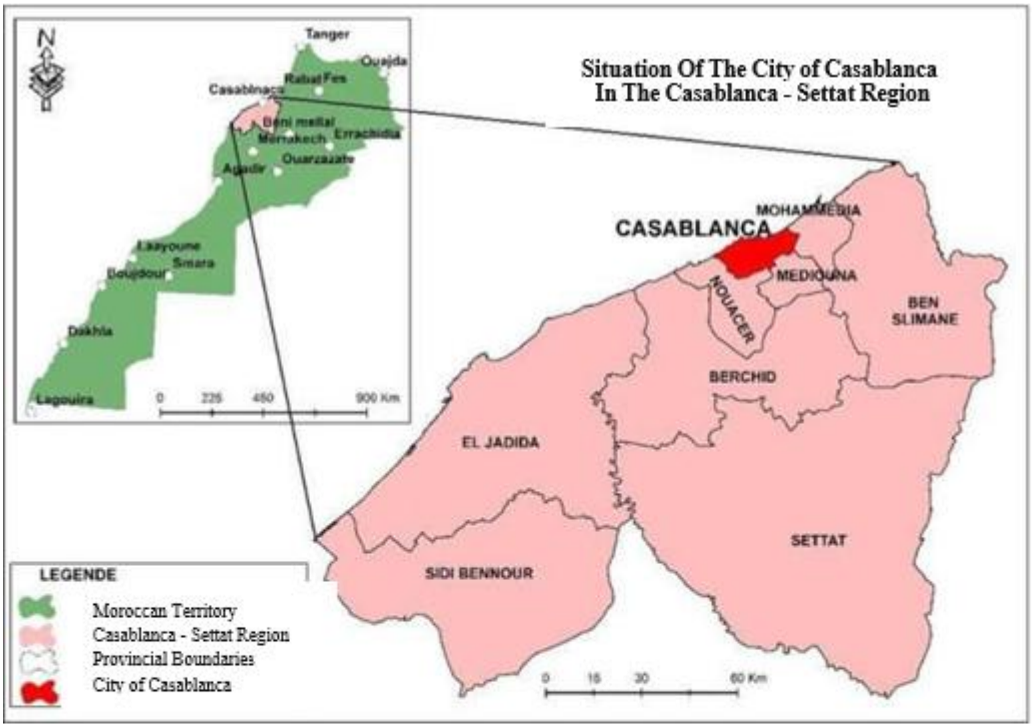

**Figure 1.** Study Area Map Covering Casablanca and Neighboring Provinces.

### The Collected Data

This study integrates two primary sources of data: traffic metrics from Waze and geographic information from GIS (Figure2). The Waze data provides a real-time snapshot of traffic conditions, including incident reports, flow rates, and congestion levels, which are pivotal for analyzing day-to-day traffic variability and immediate urban mobility challenges. The GIS data enriches this analysis by adding a spatial dimension, incorporating detailed mappings of road networks, land usage patterns, and population distribution. This layered approach allows for a comprehensive examination of how geographical and infrastructural factors influence traffic behavior, aiding in the identification of persistent congestion zones and accident hotspots (Goodchild, 2011; Shaw et al., 2013). Integrating these datasets facilitates a multifaceted study of the interdependencies within urban systems, which is essential for effective planning and management.

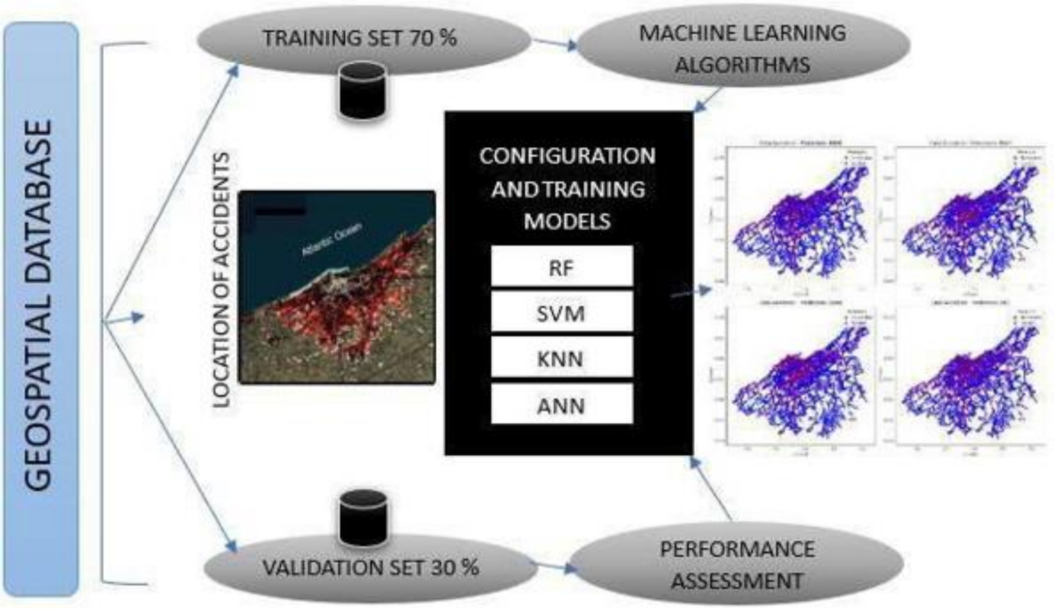

**Figure 2.** Workflow of the methodology used in this study.

### Machine Learning Algorithms

The complexity and volume of urban data require robust analytical methods, which is why this study employs a suite of advanced machine learning algorithms, each chosen for their specific strengths in handling such data. Random Forest (RF) is utilized for its proficiency in classification and regression tasks, managing both bias and variance effectively to avoid overfitting while dealing with large datasets (Breiman, 2001). Support Vector Machines (SVM) are applied due to their ability to find optimal hyperplanes in high-dimensional space, making them excellent for distinguishing between congested and non-congested areas. Artificial Neural Networks (ANN) offer the capability to learn and model non-linear and complex relationships, which are common in urban traffic patterns. Lastly, K-Nearest Neighbors (KNN) is selected for its simplicity and effectiveness in classification based on proximity, which is particularly useful in spatial data analysis. Together, these algorithms provide a comprehensive toolkit for analyzing, predicting, and providing insights into traffic management and urban planning challenges in Casablanca.

### Results and Discussion

The primary objective of this study was to predict road accidents in Casablanca using machine learning models. The analysis began with constructing a comprehensive accident inventory map that integrated historical accident data to serve as the target variable. A total of 4289 accident incidents recorded between July and September 2022 were considered. This data was derived from Waze under the Connected Citizens Program, which facilitates data-driven decisions and optimizes incident response efficiency.

The collected data were divided into training (70%) and validation (30%) sets to establish robust predictive models. This split ensured that the models were trained on a representative sample of the data while validation was performed on an independent set to assess the model's generalization capabilities. The models implemented included Random Forest (RF), Support Vector Machine (SVM), Artificial Neural Network (ANN), and K-Nearest Neighbors (KNN), each chosen for their ability to handle complex datasets like those involving urban traffic and road accidents.

### Detailed Algorithm Performance

Random Forest (RF): Demonstrated exceptional performance with an Accuracy of 88.43%, Precision of 89.38%, and Sensitivity of 83.26%. These metrics underscore RF's capability in managing the complexity and variability inherent in urban road accident data, making it highly suitable for processing diverse and non-linear data structures.

K-Nearest Neighbors (KNN): Showed a solid performance with an Accuracy of 79.29%, Precision of 77.18%, and Sensitivity of 74.30%. While KNN did not reach the performance heights of RF, its results highlight its utility in scenarios where a less complex model might be preferable.

Support Vector Machine (SVM): Yielded an Accuracy of 76.65%, with Precision of 72.10%, and Sensitivity of 75.47%. SVM’s performance, while slightly lower compared to RF and KNN, still indicates its potential effectiveness in predicting road accidents under certain conditions.

Multilayer Perceptron (MLP): This algorithm provided competitive results with an Accuracy of 80.85%, Precision of 78.67%, and Sensitivity of 76.71%. Positioned between RF and KNN in terms of predictive accuracy, MLP offers a balanced approach, capturing subtleties in the data which might be overlooked by other models.

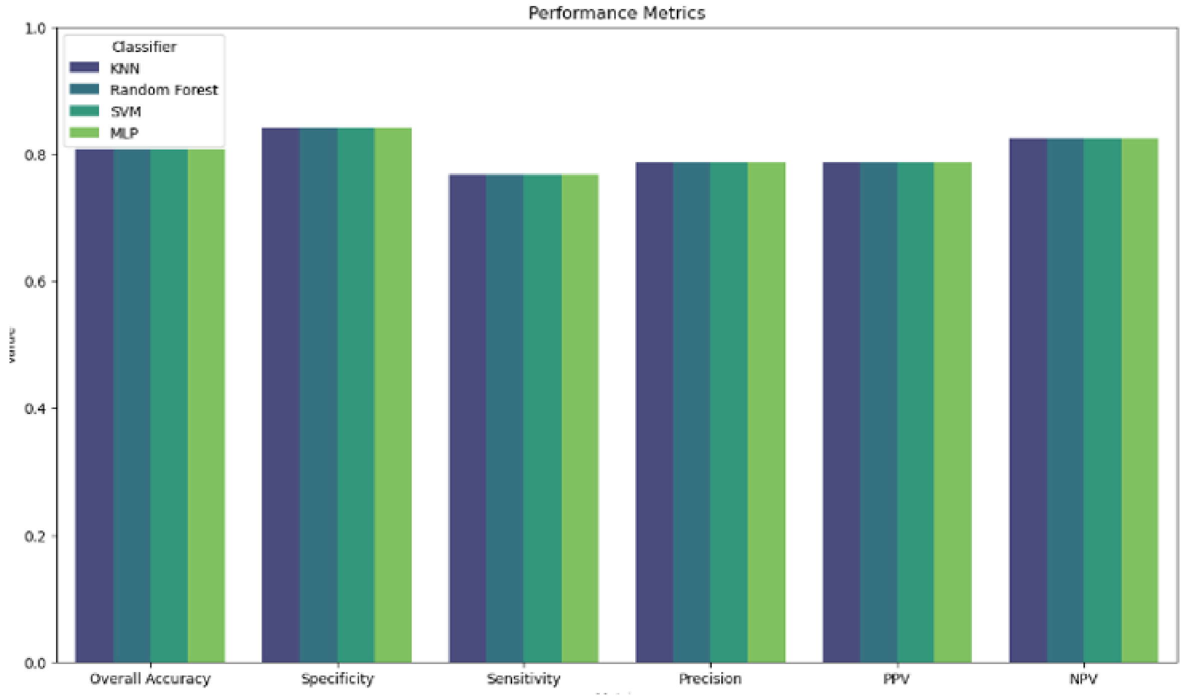

**Figure 3.** Performance Diagram of Machine Learning Models for Road Accident Prediction.

Figure 3 presents a performance diagram of these machine learning models, illustrating their effectiveness in predicting road accidents. This diagram is crucial in understanding the comparative performance of the models based on established metrics like accuracy, precision, sensitivity, and specificity.

The integration of machine learning into road accident analysis in Casablanca offers transformative potential for urban planning and traffic management. By leveraging the predictive capabilities of these models, urban planners and public authorities can proactively address high-risk areas and implement targeted interventions.

Given the effectiveness of our current models in predicting road accidents, it would be beneficial to continue developing road accident sensitivity maps, utilizing advanced geospatial visualization techniques. This approach would enhance the depiction of accident hotspots, further improving traffic safety and management strategies in Casablanca.

## Conclusion

This study demonstrates the power of machine learning in enhancing the accuracy of road accident predictions and the utility of such models in supporting data-driven urban planning. The results not only highlight the technical feasibility of applying complex algorithms to urban safety challenges but also underscore the practical implications for improving road safety and optimizing city-wide traffic management strategies.

These findings and methodological approaches ensure a comprehensive analysis of road accident sensitivity in Casablanca, providing valuable insights into areas prone to road accidents. This analytical framework, underpinned by rigorous data preprocessing, model training, and sensitivity mapping, sets a precedent for future research and applications in urban traffic safety analysis.

## References

Batty, M. (2013). Big Data, Smart Cities and City Planning. Dialogues in Human Geography. Breiman, L. (2001). Random Forests. Machine Learning, 45(1), 5-32.

Caragliu, A., Del Bo, C., & Nijkamp, P. (2011). Smart cities in Europe. Journal of Urban Technology. Goodchild, M. F. (2011). Geographical information systems and science. Wiley.

Haut-Commissariat au Plan (HCP), (2014). Casablanca in Figures.

Neirotti, P., De Marco, A., Cagliano, A. C., Mangano, G., & Scorrano, F. (2014). Current trends in Smart City initiatives: Some stylised facts. Cities.

Rodrigue, J.P., Comtois, C., & Slack, B. (2013). The Geography of Transport Systems. Routledge.

Shaw, S. L., Tsou, M. H., & Ye, X. (2013). Human Extensibility and Individual Hybrid-Accessibility in Space-Time: A Multi-Scale Representation Using GIS. International Journal of Geographical Information Science.

United Nations Human Settlements Programme (UN-Habitat) (2013). State of the World's Cities 2012/2013: Prosperity of Cities.

INTERNATIONAL SYMPOSIUM ON
APPLIED
GEOINFORMATICS
9-10 May 2024 · Wrocław/Poland

*International Symposium on Applied Geoinformatics (ISAG2024)*

# Monitoring Artificial Light Pollution Using a Multispectral Camera

Katarzyna Bobkowska [1*], Paweł Tysiąc [2], Paweł Burdziakowski [3], Jakub Szulwic [4]

[1] Faculty of Civil and Environmental Engineering, Gdansk University of Technology, katarzyna.bobkowska@pg.edu.pl
[2] Faculty of Civil and Environmental Engineering, Gdansk University of Technology, pawel.tysiac@pg.edu.pl
[3] Faculty of Civil and Environmental Engineering, Gdansk University of Technology, pawel.burdziakowski@pg.edu.pl
[4] Faculty of Civil and Environmental Engineering, Gdansk University of Technology, szulwic@pg.edu.pl
[*] Corresponding Author

## Abstract

Studying the adverse phenomenon of artificial light pollution requires systematic monitoring based on various methods. One commonly used technique involves assessing the intensity of light reflected from surfaces using different types of digital cameras at various measurement levels. However, such an approach doesn't always fully allow for understanding the characteristics of the light source. In our study, we focused on the potential application of the multispectral camera, designed for mounting on a drone (UAV), to evaluate the spectrum of the light source. We conducted laboratory measurements using the Micasense Dual RedEdge-MX multispectral camera. Recording scenes representing both the light source and reflected light, we also took reference measurements using a spectrometer. Employing classical methods of image analysis and mathematical analysis, we verified the potential for assessing the spectral characteristics of light sources. Based on the results, we developed a concept and conducted tests for monitoring light pollution using multispectral cameras mounted on drones. Our research emphasizes challenges related to photogrammetry and remote sensing under night conditions. The short exposure time of the camera shutter significantly limits the registration of data necessary for creating orthomosaics using multispectral cameras. An alternative solution was found through correlating data with a classic nocturnal orthomosaic and point analysis of registered clusters of bright pixels in images used to assess the characteristics of light sources. Our studies indicate a significant potential for using multispectral cameras to monitor artificial light pollution. Expanding the range of data recorded in small spectral ranges allows for a more accurate assessment of this phenomenon, which is crucial in identifying sources that may have a negative impact on the environment, such as flora, fauna, or even humans.

**Keywords:** Light Pollution, Night Photogrammetry And Remote Sensing, UAV, Night Orthomosaic, Environmental Protection

## Introduction

The utilization of a drone equipped with a multispectral camera appears to be a promising solution that could contribute to gathering a greater amount of data regarding the usage of artificial lighting in highly and sparsely urbanized areas (Mander, 2023). Information regarding the spectral characteristics of light sources is crucial for the assessment and monitoring of existing lighting or its classification. Various species of fauna, flora, and humans (Owens, 2020, Sung, 2022, Wang, 2023) exhibit different reactions to different light spectra. Focusing on the negative impact of artificial lighting necessitates a more detailed specification of the visible light wavelength range emitted by lighting fixtures. Multispectral cameras, as opposed to conventional RGB cameras (Massetti, 2022), possess precise bands characteristics in which they record electromagnetic radiation, such as wavelength and bandwidth. Unfortunately, they are not inherently designed for measurements in challenging lighting conditions, (Burdziakowski, 2021) leading to low exposure obtained in nocturnal images. Such an effect typically precludes the use of classical methods for developing orthomosaics (OM), which could serve as valuable products containing information on recorded visible light within ranges pertinent to the camera's specifications. Therefore, the authors attempt an alternative method of employing a multispectral camera mounted on a drone to acquire the spectrum of artificial light reflected from or emitted by surfaces.

## Materials and Methods

Our research was based on two aspects. The first, which served to evaluate the unprocessed data collected by the popular commercial multispectral camera Micasense Dual RedEdge-MX, RedEdge-MX BLUE (Amarasingam, 2022) regarding the registration of artificial light sources. For this evaluation, data collected through measurements using the UPRtek MK350D spectrometer were utilized. In this case, a measurement setup was prepared, consisting of an artificial light source – an LED bulb generating light in various colors (16 colors). The acquired data was analyzed using a proprietary automatic algorithm allowing for the verification of the registration of a given range of spectral light by the multispectral camera.

The next aspect of our research was the preliminary development of a method enabling the automatic recognition of lighting sources in images recorded by the multispectral camera. The purpose of this was to obtain responses regarding the spectral ranges in which the given source emits artificial light. To recognize the light source in images from Micasense (MS), a own image matching algorithm with Micasense images was utilized for nighttime orthomosaic development based on photos from a classical RGB camera. This article briefly outlines the operation of this algorithm.

In the initial step, it was necessary to indicate the region of interest (ROI). Ultimately, the aim is to automate this procedure based on GPS location data during the execution of photos from the multispectral camera. The selected image area undergoes processing – conversion to grayscale, histogram operation, Gaussian filtering for image smoothing and noise removal, and binarization. Parameters depend on the quality and resolution of the orthomosaic. Then, the binary image is subjected to analysis to select bright clusters of pixels and perform their labeling and determination of the centroids of these areas. A similar procedure is performed on the Micasense image resulting from adding all images (from 9 camera bands). Based on the drone's flight altitude and the orthomosaic resolution, a coordinate transformation scale factor is calculated for the centroids of the extracted bright point group. Using the ICP algorithm (Besl, 1992), point registration is performed for two groups of points corresponding to centroids from both images. After successful point registration, corresponding pairs are indicated, and the extracted pixel brightness values are obtained for the 9 bands recorded by the multispectral camera.

## Result and Discussion

Based on the analyses conducted using a light bulb emitting light in various colors, data regarding pixel brightness values for the brightest clusters of points automatically identified (noise removed from the image) were obtained for each individual image (there were 144 images – 9 (bands) x 16 (light source colors)). Additionally, 144 values were acquired from measurements performed with a spectrometer. These values represented the reflectance coefficient for a given wavelength – corresponding to a particular band of the multispectral camera and corresponding to a specific light source color. An example of the representation of registered images for white light and one of the green colors is presented in Figure 1.

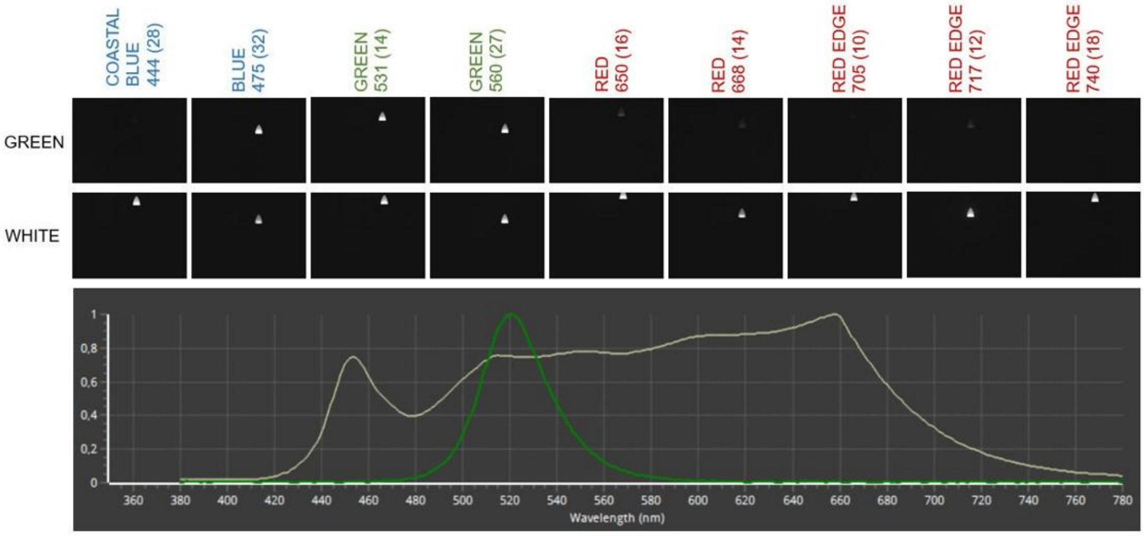

**Figure 1.** Images from the multispectral camera for 9 bands acquired during the registration of a light bulb emitting white and green light, along with spectral curves recorded by the spectrometer for these sources.

Analyzing datasets corresponding to different colors of light sources confirms that at the moment electromagnetic waves of a given wavelength are registered by the spectrometer, the multispectral camera also registers this electromagnetic radiation. To consider the utilized multispectral camera as a device that could allow for the interpolation of a spectral curve, camera calibration would be necessary. However, using unprocessed data for this purpose is not advisable.

An essential part is verifying how such data can be utilized when recorded from a low-altitude aerial perspective. Therefore, for areas with varying and unevenly distributed artificial lighting, a method of matching images from the multispectral camera and a nighttime orthomosaic for the analyzed area was proposed. Images from the multispectral camera can supplement photometric data about artificial light sources. The effect in the form of a graphical representation of image matching and displaying data regarding pixel brightness registration was presented in Figure 2. The ultimate outcome in the form of characteristic points is significant information. It is noted that the light reflected from the surface/emitted by the source in the case of points 1, 2, 3 (points assigned labels extracted from areas on the image created by adding images from Micasense) has a different characteristic compared to points 5 and 6 (these two characteristics are also different), indicating completely different forms of artificial lighting.

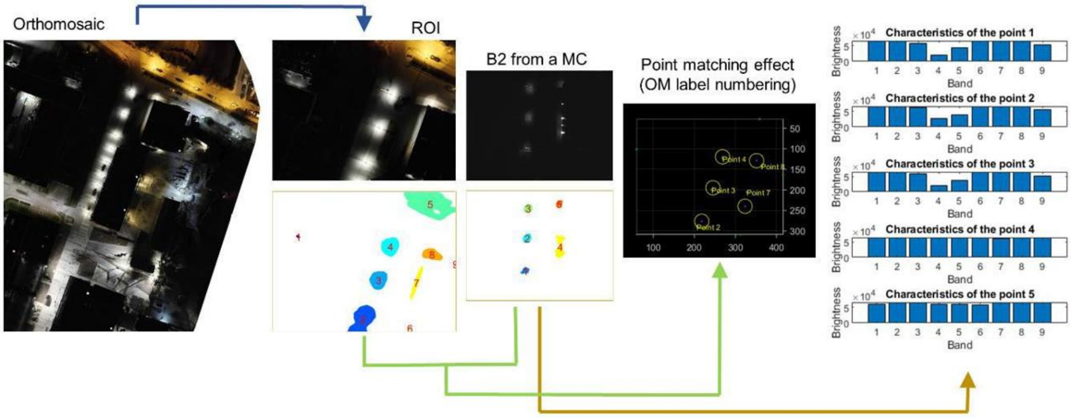

**Figure 2.** Matching Micasense images to orthomosaics aims to gather information about the pixel brightness values of reflected/emitted electromagnetic radiation in the visible spectrum.

## Conclusion

The conducted analyses indicate the validity of using multispectral cameras in monitoring artificial lighting, and consequently, light pollution. However, it is important to remember that the unprocessed data collected using multispectral cameras do not directly provide information about the photometric values of light sources. The developed algorithms for image correlation matching and obtaining information about pixel brightness values for each band for the registered light are initial elements that will be further developed and improved to fully automate and precisely correlate data from multispectral cameras with classical orthomosaics.

## Acknowledgements

Financial support of these studies from Gdańsk University of Technology by the DEC-42/2020/IDUB/I.3.3 grant under the ARGENTUM— ‘Excellence Initiative-Research University’ program is gratefully acknowledged.The article benefited from translation services provided by an AI assistant.

## References

Amarasingam, N., Salgadoe, A. S. A., Powell, K., Gonzalez, L. F., & Natarajan, S. (2022). A review of UAV platforms, sensors, and applications for monitoring of sugarcane crops. Remote Sensing Applications: Society and Environment, 26, 100712.

Besl, P. J., & McKay, N. D. (1992, April). Method for registration of 3-D shapes. In Sensor fusion IV: control paradigms and data structures (Vol. 1611, pp. 586-606). Spie.

Burdziakowski, P., & Bobkowska, K. (2021). UAV photogrammetry under poor lighting conditions—Accuracy considerations. Sensors, 21(10), 3531.

Mander, S., Alam, F., Lovreglio, R., & Ooi, M. (2023). How to measure light pollution—A systematic review of methods and applications. Sustainable Cities and Society, 92, 104465.
Massetti, L., Paterni, M., & Merlino, S. (2022). Monitoring light pollution with an unmanned aerial vehicle: A case study Comparing RGB images and night ground brightness. Remote Sensing, 14(9), 2052.

Owens, A. C., Cochard, P., Durrant, J., Farnworth, B., Perkin, E. K., & Seymoure, B. (2020). Light pollution is a driver of insect declines. Biological Conservation, 241, 108259.

Sung, C. Y. (2022). Light pollution as an ecological edge effect: Landscape ecological analysis of light pollution in protected areas in Korea. Journal for Nature Conservation, 66, 126148.

Wang, T., Kaida, N., & Kaida, K. (2023). Effects of outdoor artificial light at night on human health and behavior: a literature review. Environmental Pollution, 323, 121321

INTERNATIONAL SYMPOSIUM ON
APPLIED
GEOINFORMATICS
9-10 May 2024 · Wrocław/Poland

*International Symposium on Applied Geoinformatics (ISAG2024)*

# Measuring Integration and Accessibility Levels of M7 Yildiz-Mahmutbey Metro Line

Esra Gizem Ugur[1]*, Zaide Duran[2], Dursun Zafer Seker[3]
[1] Istanbul Technical University, Informatics Institute, Geographic Information Technologies, Istanbul, Türkiye;
ugure15@itu.edu.tr
[2] Istanbul Technical University, Faculty of Civil Engineering, Geomatics Engineering, Istanbul, Türkiye;
duranza@itu.edu.tr; ORCID 0000-0002-1608-0119
[3] Istanbul Technical University, Faculty of Civil Engineering, Geomatics Engineering, Istanbul, Türkiye;
seker@itu.edu.tr; ORCID 0000-0001-7498-1540
* Corresponding Author

## Abstract

As the population in cities grows, urban spaces are expanding, resulting in an increased need for urban transportation and spatial accessibility. Therefore, it is necessary to integrate and enhance the accessibility of public transportation modes within cities. An integrated and accessible public transportation system reduces the number of private vehicles in traffic and decreases air pollution resulting from fossil fuel usage. In consequence, urban sustainability and quality of life improve, social exclusion decreases due to enhanced spatial accessibility, and spatial justice is enhanced. This study aims to measure the integration and accessibility levels between the M7 Yıldız-Mahmutbey metro line stations and other public transportation stops. To achieve this, a method was developed by utilizing PTAL index criteria, which measure spatial accessibility. Secondly, four stations along the M7 Yıldız-Mahmutbey metro line were chosen, and a service area analysis was conducted using a GIS software for walking distances of 5, 10, and 15 minutes. The $S_{PTAL}$ value from the method developed for all public transportation stops within a 15-minute walking distance was calculated, and based on this value, the $M_{PTAL}$ value for the M7 metro stations was determined. Thereby integration and accessibility levels of four stations are established. Open-source data such as the locations of rail systems, metrobus, and bus stops, roads, the number of public transport vehicles passing through stops, and their operating hours were used in the study. Upon examination of the $M_{PTAL}$ values calculated for the identified four stops, it was observed that stops with a higher number of different transportation modes (DMT) in their vicinity also had higher scores, indicating that this parameter is a determining factor. Additionally, the spatial distribution of roads and stops, the reliability of the transportation mode (RM), and the average waiting time at stops (AWT) directly impact integration and accessibility.

**Keywords:** *Integrated Public Transportation Systems, PTAL Index, Public Transportation Accessibility, GIS*

## Introduction/Background

Public transportation accessibility is a crucial criterion in urban planning as it affects urban sustainability, spatial justice, air pollution, and quality of life. Therefore, several indices have been developed to measure accessibility to public transportation. Some of these indices include PTAI, PTAL, and SI (Saghapour, Moridpour, Thompson, 2016). PTAL is the most widely used index (Yang et al., 2019). The PTAL index is utilized by the governments of London, Delhi, and New South Wales to measure accessibility to public transportation and develop projects accordingly. While the components of the PTAL index may vary depending on the application, they generally include different types of modes, mode reliability, walking distance to points of interest (POI), and average waiting time at stops (Mayor of London, 2015; NIUA, 2021).

In the study, a method was developed by adapting the PTAL index to measure the integration and accessibility between the identified stops along the M7 Yıldız-Mahmutbey metro line and other public transportation vehicles within a 15-minute walking distance.

## Materials and Methods (Design/methodology/approach)

In the study, the parameters of the PTAL index, used to calculate the level of accessibility to points of interest (POIs) via public transportation, were adapted and applied to the M7 metro stations and surrounding public transportation stops. This allowed for the measurement of the accessibility and integration levels of the M7 metro stops with public transportation. The PTAL index is calculated based on four key parameters: walking distance from the stop to the POI, the number of transportation modes around the POI, transportation mode reliability, and waiting time at the stop (Mayor of London, 2015; NIUA, 2021). When adapting this index for the research, the POIs were considered as the M7 metro stations, and the surrounding stops were regarded as the public transportation stops around the M7 metro station.

Road data for the study was obtained from Istanbul Earthquake Science Board Studies of Istanbul Metropolitan Municipality (İBB), transportation stop data from OpenStreetMap (OSM), and the number of buses passing a stop in half an hour and the average waiting time for vehicles were acquired from the timetable panel on Google Maps.

The topological validation of road data was conducted using ArcGIS Pro software. Topological check rules were "must not overlap," "must not self-overlap," and "must not self-intersect" defined for the road data. As a result of the topological check, overlapping road segments were identified as tunnels or bridges, and these errors were disregarded. The stop data retrieved from OpenStreetMap (OSM) was classified into bus, metro, and metrobus stops. If the classified metro stops did not intersect with road data, they were aligned with the nearest road segment. Subsequently, service area analysis was performed using ArcGIS Pro to calculate 5, 10, and 15-minute walking distances towards the M7 metro stations defined as destination points. Slope was not considered during the service analysis. In "Assessing Transport Connectivity in London", the average walking speed was determined as 4.8 km/h (Mayor of London, 2015). The 5, 10, and 15-minute distances were calculated as 400, 800, and 1200 meters, respectively, based on an average walking speed of 4.8 km/h.

The stops were divided into two classes: those with a dedicated lane for themselves, including metrobus and rail systems, and bus stops. The $S_{PTAL}$ values for the stops were measured individually. To calculate the $S_{PTAL}$ value, three basic parameters that are average waiting time at the stop (AWT), mode reliability (RM), and distance to the M7 station (DFS) were scored and then summed with each other shown in Eq. (1).

$$S_{PTAL} = AWT + RM + DFS \tag{1}$$

When calculating the average waiting time at the stop (AWT), the total number of vehicles passing the respective stop during any 30-minute period between 09:00 and 17:00 is determined. The total time (TT) of 30 minutes is divided by the total number of vehicles (TNV), resulting in the average waiting time at the stop (AWT) calculated as in Eq. (2).

$$AWT = \frac{TT}{TNV} \tag{2}$$

Bus, metrobus, and railway system stops other than M7 were assigned scores based on the average waiting times (AWT) within the ranges of 0-5 minutes receiving 4 points, 6-10 minutes receiving 3 points, 11-15 minutes receiving 2 points, and 16 minutes and above receiving 1 point.

Regarding the distance from the M7 metro station (DFS), stops within 0-400 meters get 3 points, those between 401-800 meters get 2 points, and those between 801-1200 meters get 1 point.

In terms of mode reliability (RM) component, stops outside the M7 metro station were given 2 points if the transportation mode had its own lane or road, and 1 point if it did not. Therefore, metrobus and other rail system stops received 2 points, while bus stops received 1 point. Although the metrobus line in the study area has its own lane, thus having the same mode reliability score as rail system stops, different values can be assigned for different metrobus stops in future studies.

**Table 1.** Values that $M_{PTAL}$ parameters can get.

| Values | AWT | RM | DFS | DMT |
|---|---|---|---|---|
| 4 | 0-5 min. | - | - | - |
| 3 | >5-10 min. | - | 0-400 mt | RS, MB, BS |
| 2 | >10-15 min. | RS, MB | >400-800 mt | MB, BS / RS, BS |
| 1 | >15 min. | BS | >800-1200 mt | BS |

The $M_{PTAL}$ value, which determines the level of accessibility and integration of the M7 metro stations with other public transportation modes is calculated as shown in Eq. 3. This value is obtained by summing the average of the $S_{PTAL}$ values that are assigned at stops, and the number of different transportation modes (DMT) within a 1200-meter walking distance to the M7 metro station.

$$M_{PTAL} = \frac{\Sigma(S_{PTAL})}{TNS} + DMT \tag{3}$$

$M_{PTAL}$ value can range from a minimum of 4 to a maximum of 12. The closer the $M_{PTAL}$ value is to 12, the higher the accessibility and integration of the stop.

**Results and Discussion (Findings)**

In this research, the M7 metro stations of Yıldız, Fulya, Mecidiyeköy, and Çağlayan were examined. Using ArcGIS Pro software, a service analysis was conducted assuming a walking distance of 400, 800, and 1200 meters from the four M7 metro stations which are considered destination points. The public transportation stop data retrieved from OpenStreetMap (OSM) and mentioned service analysis overlapped. The resulting map is shown in Fig. 1.

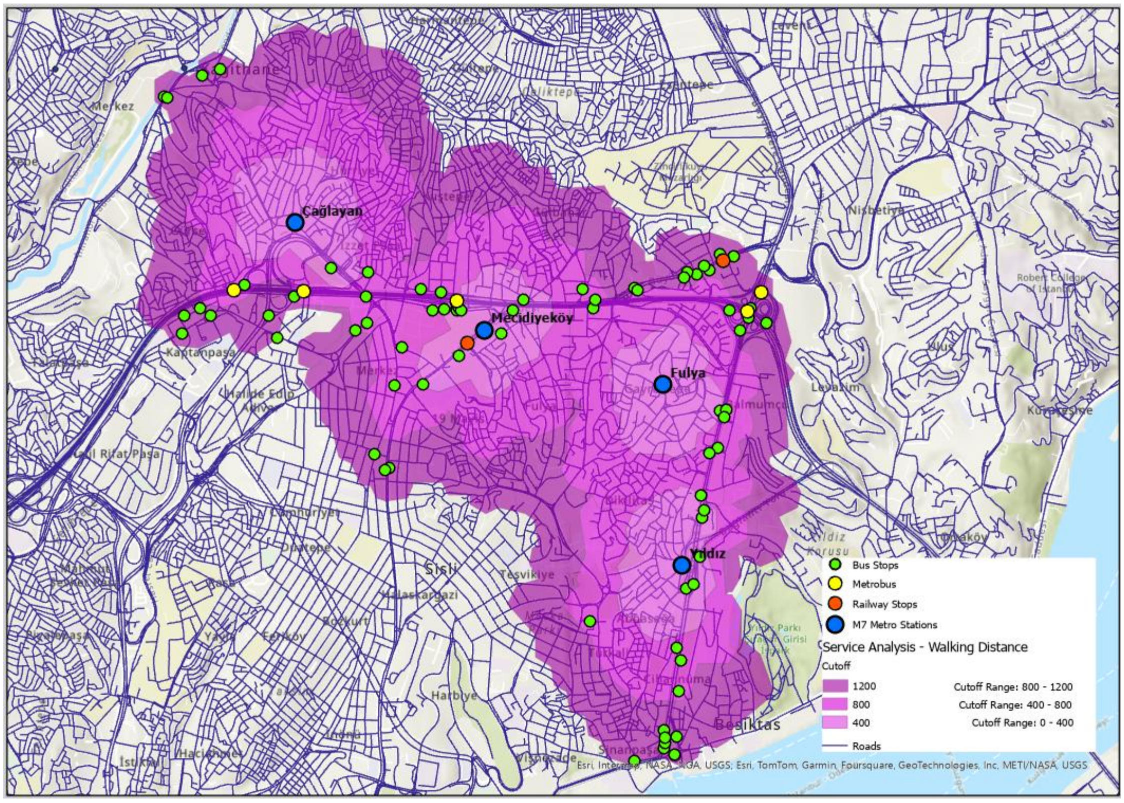

**Figure 1.** Service analysis for M7 metro stations and overlapped data in GIS.

The calculated $M_{PTAL}$ values for the four M7 metro stations are presented in Table 2.

**Table 2.** $M_{PTAL}$ values of M7 stations.

| M7 Stations | DMT | TNS | $\boldsymbol{\Sigma(S_{PTAL})}$ | $\boldsymbol{M_{PTAL}}$ |
|---|---|---|---|---|
| Yıldız | 1 | 18 | 106 | 6.9 |
| Fulya | 3 | 25 | 154 | 9.2 |
| Mecidiyeköy | 3 | 28 | 189 | 9.8 |
| Çağlayan | 2 | 28 | 171 | 8.1 |

It was determined that the M7-Mecidiyeköy metro station had the highest $M_{PTAL}$ value with 9.8 points, while the M7-Yıldız metro station had the lowest $M_{PTAL}$ value with 6.9 points. The M7-Fulya metro station received 9.2 points, and the M7-Çağlayan metro station received 8.1 points.

In other studies, when calculating the PTAL value, the study area is divided into grids, and PTAL values are assigned to the centroids of these grids (Saghapour, Moridpour, Thompson, 2016; NIUA, 2021). This method allows for the calculation of spatial accessibility and obtaining polygonal data. With the research method, $M_{PTAL}$ values were assigned to stations, measuring their integration and accessibility with other stops, and generating point data.

**Conclusions**

When a scale is created with equal intervals since the M_PTAL value can range from a maximum of 12 to a minimum of

4, $M_{PTAL}$ values equal to or lower than 6.6 can be classified as poor, those between 6.7 and 9.3 as moderate, and those between 9.4 and 12 as good. According to this classification, the Yıldız, Çağlayan, and Fulya metro stations fall into the moderate category, while the Mecidiyeköy metro station is in the good category.

By adapting the PTAL index, a method has been developed that provides general information about the integration and accessibility of the relevant station with other public transportation stops, utilizing open data sources and eliminating the need for fieldwork.

Upon examination of the 4 stops, which are the subject of this paper, it was calculated that stops with a higher number of transportation modes in their vicinity also had higher $M_{PTAL}$ values. When the correlation coefficient between the number of transportation modes (DMT) and $M_{PTAL}$ values was calculated, it was found to be 0.72, indicating a high correlation between these two values. This demonstrates that the developed method effectively measures the integration of different modes of public transportation.

The locations of public transportation stop and the departure times of buses, which are components of the calculation, were obtained from open data sources and assumed to be accurate. The quality of the data affects the accuracy of the calculations since open data sources were utilized in this method. The accuracy of the calculations could be influenced as the average waiting time at the stop was calculated for any half-hour period between 09:00 and 17:00. Additionally, the spatial distribution of roads and stops, as well as the distance from the M7 metro stations (DFS), directly affects the $M_{PTAL}$ value.

This study could play a significant role in the future planning of public transportation stops and may contribute to improving the accessibility and integration of existing public transportation stops. Furthermore, it has not been found that the PTAL index has not been used to measure the accessibility and integration between public transportation stops in the literature. Thus, the research method, which combines transportation planning with GIS, is distinctive.

## Acknowledgements

The authors would like to thank to the Istanbul Earthquake Science Board Studies of Istanbul Metropolitan Municipality (İBB) for providing road data set used in this study. AI-assisted technologies utilized for enhance the readability and linguistic quality of the full paper.

## References

Mayor of London. (2015). Assessing transport connectivity in London. Transport for London. https://content.tfl.gov.uk/connectivity-assessment-guide.pdf.

NIUA. (2021). Study on Public Transport Accessibility Levels (PTAL) in Delhi. https://online.dda.org.in/mpd2041dda/_layouts/MPD2041FINALSUGGESTION/Final_Project_Report.pdf

Yang, R. Liu, Y. Liu, Y. Liu, H. Gan, W. (2019). Comprehensive public transport service accessibility index - A new approach based on degree centrality and gravity model. Sustainability, 11 (5634).

Saghapour, T. Moridpour, S. Thompson, R.G. (2016). Public transport accessibility in metropolitan areas: A new approach incorporating population density, 54 (2016), pp. 273-284.

INTERNATIONAL SYMPOSIUM ON
APPLIED
GEOINFORMATICS
9-10 May 2024 · Wrocław/Poland

*International Symposium on Applied Geoinformatics (ISAG2024)*

# Comparative Accuracy Analysis of Algorithms Used in Automatic Detection of Power Lines from Lidar Data

Mertcan Nazar[1]*, Umut Gunes Sefercik[1]

**[1]** Gebze Technical University, Faculty of Engineering, Department of Geomatics Engineering, Kocaeli, Türkiye;
(mnazar/sefercik)@gtu.edu.tr; ORCID 0000-0002-3280-5685, ORCID 0000-0003-2403-5956
* Corresponding Author

## Abstract

Power lines are essential for distributing electricity to households, industries, healthcare facilities, and other areas. The rapid increase in population and resulting demand for urbanization, as well as forest overgrowth, can pose significant risks for power line areas. Accordingly, disruption of electric power transmission can result in significant economic losses and harm to people's well-being by depriving them of access to electricity. Moreover, in densely vegetated areas, power line disruptions and contact with forest fuel can result in forest fires, which can cause loss of life, environmental catastrophes, and infrastructural devastation. For these reasons, regular inspection and maintenance of power lines, especially in remote areas, is essential to prevent such disasters. However, instead of conventional methods for power line inspection, which can be time-inefficient, laborious, and costly, airborne light detection and ranging (LiDAR) systems can generate 3D point clouds with high geometric accuracy in a short amount of time, with less labor and at a lower cost. Airborne LiDAR systems can be used in difficult-to-access or hazardous areas, in contrast to terrestrial methods. In recent years, automatic detection algorithms have become increasingly popular for accurately and quickly detecting power lines on airborne LiDAR point clouds. Furthermore, LiDAR point clouds have become an indispensable tool in object detection studies. In this study, the Robust Railroad Infrastructure Detection Framework developed by Eötvös Loránd University (ELTE) Geoinformatics Laboratory was used to automatically detect power lines from an airborne LiDAR point cloud of an area with different land cover classes, including power lines, buildings, roads, and vegetation. To accomplish this task, five algorithms including Above, AngleAbove, AngleGroundAbove, VoronoiAbove and VoronoiGroundAbove were applied separately and their accuracies were compared by adopting accuracy metrics such as precision, recall, and $F_1$ score. In the investigation of results, VoronoiAbove outperformed others with an $F_1$ score of 0.94, closely followed by VoronoiGroundAbove with 0.93.

**Keywords:** *Automatic power line detection, LiDAR point cloud, Above, AngleAbove, AngleGroundAbove, VoronoiAbove, VoronoiGroundAbove, Accuracy*

## Introduction

Electricity is essential for modern activities and the well-being of society, and to ensure its safe distribution, it is vital that precautions are taken, regular monitoring is carried out and regular maintenance is carried out (Matikainen et al., 2016). Power lines can extend for long distances above ground, and vegetation encroachment can damage power line corridors, while contact between power lines and vegetation can lead to bushfires (Sun et al., 2006). In addition, one of the main causes of power line failures is storms, which bring strong winds and wet weather (Mills et al., 2010). Consequently, monitoring power lines, especially in densely vegetated areas, has become an important disaster management issue. Traditional monitoring methods, which rely on human labor, are time-consuming, expensive, and dangerous, and the current management of power line corridors in forested areas primarily involves the identification and pruning of high-risk trees that could fall and damage the structure (Jwa et al., 2009). However, compared to traditional power line inspection methods, airborne Light Detection and Ranging (LiDAR) technology offers the advantage of generating three-dimensional (3D) point clouds, making it a cost-effective and less labor-intensive alternative. In addition, high-quality and accurate

Digital Surface Models (DSM) can be generated from LiDAR point clouds (Sefercik et al., 2015; Sefercik et al., 2017). Airborne LiDAR technology is used in disaster-related studies, such as land cover classification of fuel types for forest fire management (Koetz et al., 2008), investigation of landforms near landslide areas, and periodic monitoring of their changes (Lato et al., 2019), analysis of earthquake-induced surface rupture and displacement (Oskin et al., 2012), and automatic detection and identification of forest fire risk regions near high-voltage power lines (Hernández-López et al., 2023). Furthermore, LiDAR point clouds can be used to automatically detect power lines in urban areas (Nazar et al., 2023). In this study, the Robust Railroad Infrastructure Detection Framework developed by Eötvös Loránd University (ELTE) Geoinformatics Laboratory was used to automatically detect power lines from an airborne LiDAR point cloud. The area under investigation contained various land cover classes, such as power lines, buildings, roads, and vegetation. To complete this task, five algorithms, namely Above, AngleAbove, AngleGroundAbove, VoronoiAbove, and VoronoiGroundAbove, were applied separately and their accuracies were compared using metrics such as precision, recall, and $F_1$ score. In addition, their performance was analyzed in terms of total processing time.

## Materials and Methods

The automatic detection of power lines was carried out using a point cloud of approximately 6.3 million points acquired from a traditional LiDAR survey. The power line corridor is situated in an urban area with various land cover classes, including power lines, buildings, roads, and vegetation. The power line corridor section being studied is approximately 800 m long and consists of two pylons spaced approximately 380 m apart, as shown in Figure 1.

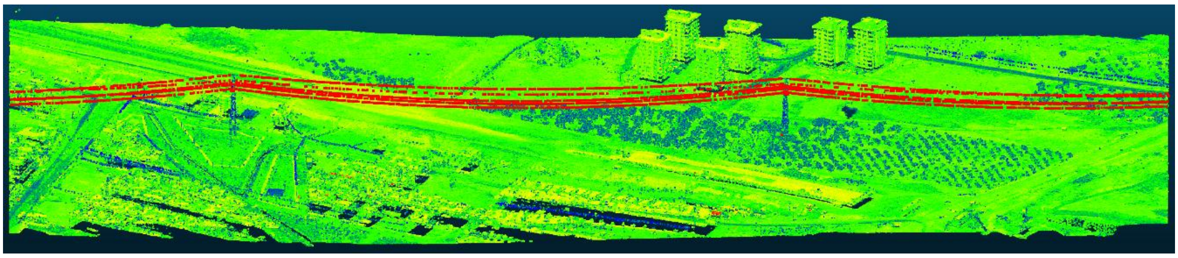

**Figure 1.** The provided LiDAR point cloud displays a section of the power line corridor highlighted in red.

The Robust Railroad Infrastructure Detection Framework, a software library that enables automatic detection of rail tracks and cables from LiDAR point clouds, was used for power line detection. The computational load of the automatic detection process was reduced by using filtering algorithms and projection filters included in the Robust Railroad Infrastructure Detection Framework to reduce the point size and generate a two-dimensional projection of the 3D point cloud (Cserép et al., 2018). Five different built-in algorithms including Above, AngleAbove, AngleGroundAbove, VoronoiAbove, and VoronoiGroundAbove were employed for power line detection. The power line detection process involves the application of a probabilistic Hough transform (Stephens, 1991) after the projection phase. The probabilistic Hough transform is shown in Eq. (1).

$$H(\vec{y}) = \sum_{i=1}^{n} \ln[f(\vec{x}_i|\vec{y})] + \ln[f_0] + C \tag{1}$$

Where input feature count is represented by $n$, $\vec{x}_i$ is a particular image measurement, $\vec{y}$ is an individual point in Hough space, given the value of $\vec{y}$, the probability density function of $\vec{x}_i$ is defined by $f(\vec{x}_i|\vec{y})$, a priori probability density function is given as $f_0$ and arbitrary constant is displayed as $C$. After the algorithms were applied their accuracies in terms of precision, recall, and $F_1$ were compared according to Eq. (2) (Goutte and Gaussier, 2005).

$$Precision = \frac{TP}{TP + FP}$$

$$Recall = \frac{TP}{TP + FN} \tag{2}$$

$$F_1 = \frac{2(Recall \times Precision)}{(Recall + Precision)}$$

In this context, true positives (TP) refer to correctly labeled instances of points as power lines, false positives (FP) refer to incorrectly labeled instances of points as power lines, and false negatives (FN) refer to incorrectly labeled instances of points as not power lines. Precision refers to the proportion of obtained instances that are relevant, while recall refers to the proportion of relevant instances that are obtained (Zhang et al., 2016). Furthermore, the $F_1$ is defined as the overall accuracy, considering both commission (or false positive) and omission (or false negative) errors (Li et al., 2012).

## Results

The results of the algorithms, namely Above, AngleAbove, AngleGroundAbove, VoronoiAbove, and VoronoiGroundAbove, are displayed in Figure 2.

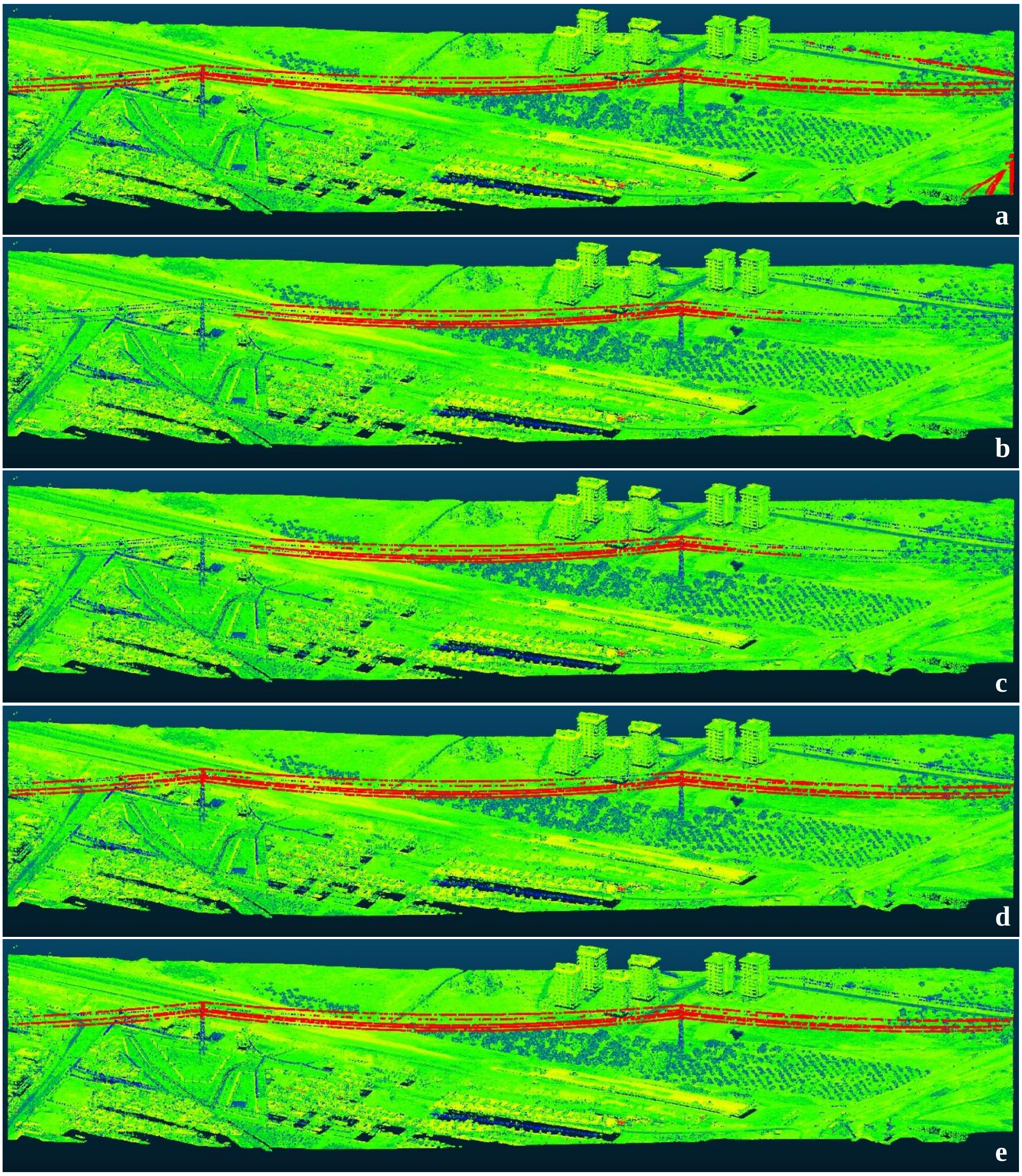

**Figure 2.** Results of the power line detection algorithms: Above (a), AngleAbove (b), AngleGroundAbove (c), VoronoiAbove (d), and VoronoiGroundAbove (e). Points identified as power lines are highlighted in red.

Visual analysis indicates that the AngleAbove and AngleGroundAbove algorithms mainly classified points between two pylons as power lines, while the Above, VoronoiAbove, and VoronoiGroundAbove algorithms detected points across the power line corridor. Furthermore, the visual interpretation reveals that there are points outside the power line corridor that have been classified as power lines. These points are clearly distinguishable in the Above algorithm results. To compare the accuracies of the applied algorithms, accuracy metrics such as precision, recall, and $F_1$ score were calculated, as shown in Table 1.

**Table 1.** Precision, recall, and $F_1$ score results of the applied algorithms.

| Algorithm | Number of total points | TP | FP | FN | Precision | Recall | $F_1$ Score |
|---|---|---|---|---|---|---|---|
| Above | 10507 | 5218 | 5289 | 491 | 0.50 | 0.91 | 0.64 |
| AngleAbove | 2979 | 2937 | 42 | 2772 | 0.99 | 0.51 | 0.68 |
| AngleGroundAbove | 2995 | 2940 | 55 | 2769 | 0.98 | 0.51 | 0.68 |
| VoronoiAbove | 5283 | 5179 | 104 | 530 | 0.98 | 0.91 | 0.94 |
| VoronoiGroundAbove | 5223 | 5100 | 123 | 609 | 0.98 | 0.89 | 0.93 |

Table 1. shows that the Above algorithm has the lowest precision at 0.50, compared to the others which have values between 0.98 and 0.99. For recall values, AngleAbove and AngleGroundAbove have the lowest values at 0.51, compared to the others which range between 0.89-0.91. When investigating $F_1$ scores, the VoronoiAbove algorithm has the highest value at 0.94. The overall performance results show that the VoronoAbove algorithm is superior to the other algorithms, while the VoronoiGroundAbove algorithm performed similarly.

## Conclusion

In conclusion, the Robust Railroad Infrastructure Detection Framework developed by Eötvös Loránd University (ELTE) Geoinformatics Laboratory was used to automatically detect power lines from a LiDAR point cloud. Five different detection algorithms, namely Above, AngleAbove, AngleGroundAbove, VoronoiAbove, and VoronoiGroundAbove, were applied separately to the point cloud. Additionally, their accuracies were compared using metrics such as precision, recall, and $F_1$ score. When accuracies of the applied algorithms were compared in terms of $F_1$ scores, the VoronoiAbove algorithm has the highest value at 0.94, followed closely by VoronoiGroundAbove at 0.93, while the other algorithms scored between 0.64-0.68. Overall, VoronoiAbove performed better than the other algorithms in automatic power line detection.

## Acknowledgements

We would like to thank EMİ Group Information Technologies for aerial LiDAR point cloud data and ELTE Geoinformatics Laboratory, Máté Cserép and Péter Hudoba for Robust Railroad Infrastructure Detection Framework.

## References

Cserép, M. Hudoba, P. and Vincellér, Z. (2018). Robust Railroad Cable Detection in Rural Areas from MLS Point Clouds. In Free and Open Source Software for Geospatial (FOSS4G) Conference Proceedings, 18(1), pp. 1-8.

Goutte, C. and Gaussier, E. (2005). A probabilistic interpretation of precision, recall and F-score, with implication for evaluation. In European Conference on Information Retrieval, pp. 345-359.

Hernández-López, D. López-Rebollo, J. Moreno, M. A. and Gonzalez-Aguilera, D. (2023). Automatic processing for identification of forest fire risk areas along high-voltage power lines using coarse-to-fine LiDAR data. Forests, 14(4), 662.

Jwa, Y. Sohn, G. and Kim, H. B. (2009). Automatic 3d powerline reconstruction using airborne lidar data. Int. Arch. Photogramm. Remote Sens, 38(Part 3), pp. 105-110.

Koetz, B. Morsdorf, F. Van der Linden, S. Curt, T. and Allgöwer, B. (2008). Multi-source land cover classification for forest fire management based on imaging spectrometry and LiDAR data. Forest Ecology and Management, 256(3), pp. 263-271.

Lato, M. J. Anderson, S. and Porter, M. J. (2019). Reducing landslide risk using airborne Lidar scanning data. Journal of Geotechnical and Geoenvironmental Engineering, 145(9), 06019004.

Li, W. Guo, Q. Jakubowski, M. K. and Kelly, M. (2012). A new method for segmenting individual trees from the lidar point cloud. Photogrammetric Engineering & Remote Sensing, 78(1), pp. 75-84.

Matikainen, L. Lehtomäki, M. Ahokas, E. Hyyppä, J. Karjalainen, M. Jaakkola, A. Kukko, A. and Heinonen, T. (2016). Remote sensing methods for power line corridor surveys. ISPRS Journal of Photogrammetry and Remote Sensing, 119, pp. 10-31.

Mills, S. J. Castro, M. P. G. Li, Z. Cai, J. Hayward, R. Mejias, L. and Walker, R. A. (2010). Evaluation of aerial remote sensing techniques for vegetation management in power-line corridors. IEEE Transactions on Geoscience and Remote Sensing, 48(9), pp. 3379-3390.

Nazar, M., Sefercik, U. G. and Aydın, I. (2023). Potential analyses of LiDAR-based automatic powerline detection algorithms. In Advanced Engineering Days (AED), 7, pp. 47-49.

Oskin, M. E. Arrowsmith, J. R. Corona, A. H. Elliott, A. J. Fletcher, J. M. Fielding, E. J. Gold, P. O. Garcia, J. J. G. Hudnut, K. W. Liu-Zeng, J. and Teran, O. J. (2012). Near-field deformation from the El Mayor–Cucapah earthquake revealed by differential LIDAR. Science, 335(6069), pp. 702-705.

Sefercik, U. G. Buyuksalih, G. Jacobsen, K. and Alkan, M. (2017). Point-based and model-based geolocation analysis of airborne laser scanning data. Optical Engineering, 56(1), 013101, pp. 1-10.

Sefercik, U. G. Glennie, C. Singhania, A. and Hauser, D. (2015). Area-based quality control of airborne laser scanning 3D models for different land classes using terrestrial laser scanning: sample survey in Houston, USA. International Journal of Remote Sensing, 36(23), pp. 5916-5934.

Stephens, R. S. (1991). Probabilistic approach to the Hough transform. Image and Vision Computing, 9(1), pp. 66-71.

Sun, C. Jones, R. Talbot, H. Wu, X. Cheong, K. Beare, R. Buckley, M. and Berman, M. (2006). Measuring the distance of vegetation from powerlines using stereo vision. ISPRS Journal of Photogrammetry and Remote Sensing, 60(4), pp. 269-283.

Zhang, Z., Zhang, L., Tong, X., Mathiopoulos, P. T., Guo, B., Huang, X. Wang, Z. and Wang, Y. (2016). A multilevel point-cluster-based discriminative feature for ALS point cloud classification. IEEE Transactions on Geoscience and Remote Sensing, 54(6), pp. 3309-3321.

INTERNATIONAL SYMPOSIUM ON
APPLIED
GEOINFORMATICS
9-10 May 2024 · Wrocław/Poland

*International Symposium on Applied Geoinformatics (ISAG2024)*

# An Assessment of The Potential Use of Sentinel-2 Imagery and Water Indices in Monitoring Water Quality: A Case Study of Sakarya River

Ismail Colkesen[1]*, Umut Gunes Sefercik[1], Nizamettin Ozdogan[2], Taskin Kavzoglu[1], Muhammed Yusuf Ozturk[1], Osman Yavuz Altuntas[1], Mertcan Nazar[1], Ilyas Aydin[1], Hasan Tonbul[1]

[1] Gebze Technical University, Faculty of Engineering, Department of Geomatics Engineering, Kocaeli, Türkiye; (icolkesen/sefercik/kavzoglu/m.ozturk2020/oyavuzaltuntas/mnazar/ilyasaydin/htonbul)@gtu.edu.tr; ORCID 0000-0001-9670-3023, ORCID 0000-0003-2403-5956, ORCID 0000-0002-9779-3443, ORCID 0000-0001-6459-9356, ORCID 0000-0001-5940-4091, ORCID 0000-0002-3280-5685, ORCID 0000-0002-4071-8063, ORCID 0000-0003-4817-6542
[2] Zonguldak Bulent Ecevit University, Faculty of Engineering, Department of Environmental Engineering, Zonguldak, Türkiye; (nozdogan)@beun.edu.tr; ORCID 0000-0001-5520-5124
* Corresponding Author

## Abstract

Rivers are vital components of global aquatic systems, but they face significant threats mainly caused by agricultural and anthropogenic that negatively impact water quality. Remote sensing technologies have been widely used as an essential tool for monitoring and protecting aquatic ecosystems. In this study, the Sentinel-2 imagery and derived water indices, Normalized Difference Chlorophyll Index (NDCI), Normalized Difference Aquatic Vegetation Index (NDAVI), and Automated Mucilage Extraction Index (AMEI) were used to monitor water quality level of the Sakarya River during the growth periods of maize plant. For this purpose, water quality parameters were calculated based on water samples collected during field campaigns and correlated with satellite imagery. As a result of the study, the Pearson correlation between the nephelometric turbidity unit (NTU) parameter and the NDCI index was 91%, while the correlation between the NDAVI index and suspended solids (SS), chemical oxygen demand (COD), biochemical oxygen demand (BOD), and total Kjeldahl nitrogen (TKN) parameters was above 90%. Furthermore, time series analyses based on NDAVI and normalized difference vegetation (NDVI) indices for the time interval covering the maize plant growth period using Sentinel-2 imagery showed significant changes in water quality parameters with plant growth.

**Keywords:** *Water quality, Spectral water indices, Sentinel-2, Maize plant, NDAVI, NDCI*

## Introduction

Global water resources are essential for life and sustainable development, but the increasing demands and environmental pressures on these sources are a growing concern. According to the United Nations World Water Development Report (2023), global water consumption has increased by approximately 1% annually over the past four decades (UNESCO, 2023). It was also underlined that the main contributors to this tendency were population growth, socioeconomic developments, and changing consumption demands, and it was projected to continue until 2050. The 2021 report issued by the Food and Agriculture Organization of the United Nations (FAO) underlined that water pollution has become a global threat with significant impacts on health, economy, and food security (FAO, 2021). Rivers play a crucial role in the intricate web of global aquatic systems. They serve as vital conduits, transporting freshwater and nutrients across vast landscapes, sustaining ecosystems, and meeting the water needs of countless human communities. These freshwater arteries are not only biologically diverse but also integral to the health of the earth (Sendzimir and Schmutz, 2018). Agricultural and anthropogenic activities such as rapid urbanization and industry are among the leading causes of river pollution and global water sources (FAO, 2021). Monitoring the changes in rivers and analysis of the water quality parameters are paramount for protecting and managing riverine ecosystems (Hanna et al., 2018; Hafeez et al., 2022). Remote sensing technologies, which can acquire imagery over large areas at different spatial and spectral resolutions regularly, have been widely used as invaluable tools for monitoring water sources. In parallel with recent advances in remote sensing technologies, significant literature has emerged in recent years around the theme of using remotely sensed imagery in monitoring and mapping water quality (Huangfu et al., 2020; Lv and Tian, 2021; Özdoğan et al., 2021; Pahlevan et al., 2022; Virdis et al., 2022). The spectral bands provided by remotely sensed imagery and the mathematical combination of these bands, water indices, provide critical information on water quality parameters. For example, (Sagan et al., 2020) evaluated the potential use of several spectral bant ratios and water indices, such as normalized Difference Chlorophyll Index (NDCI) and Normalized Difference Turbidity Index (NDTI) for monitoring inland water quality. Similarly, (Das et al., 2021) used different water indices, such as the Normalized Difference Water Index (NDWI), NDCI and NDTI, calculated from Sentinel-2 images to monitor stream water quality. The main objective of this study was to investigate the potential use of Sentinel-2 imagery and spectral water indices in monitoring water quality changes in the Sakarya River during the phenological development of maize crops. For this purpose, water samples were taken at three periods (i.e., pre-planting, flowering, and post-harvest period), and water quality parameters were calculated through laboratory measurements. The obtained quality parameters were associated with satellite imagery, and water quality analyses were estimated for the entire river within the study area.

## Study Area and Data Sets

In this research, Sinanoğlu, a neighborhood within the Ferizli district of Sakarya, Turkey, was chosen as the study site. A prominent characteristic of this study area is its rich agricultural history. Situated north of Sakarya province and surrounded by the Sakarya River, the region is renowned for cultivating diverse agricultural products, notably maize and hazelnuts. Corn cultivation dominates the agricultural landscape in this area, benefiting from the fertile lands along the banks of the Sakarya River. The proximity of the river is crucial in supporting and sustaining the local agricultural industry, as its waters provide the necessary irrigation for the maize fields that dominate the area. In this study, Sentinel-2 (Level-2A) images captured on 29 May, 23 July, and 10 November 2022 were used as the primary data source and downloaded from the Copernicus Open Access Hub to analyze the changes in the water quality of the Sakarya River during the period between planting and harvesting of maize crops. The Sentinel-2 provides imagery in 13 spectral bands, ranging from visible and near-infrared to short-wave infrared, with spatial resolutions of 10, 20, or 60 meters. In this study, blue (B02), green (B03), red (B04), and near-infrared (B08) bands at 10m spatial resolution and red edge (B05), near-infrared NIR (B06, B07, and B8A), and short-wave infrared SWIR (B11 and B12) at 20 m spatial resolution were used for the water quality monitoring. To harmonize the spatial resolution, the nearest neighbor was applied for downscaling the 20 m bands to 10 m spatial resolution. In the literature, water indices calculated from the spectral bands of Sentinel-2 images have been widely used in water quality monitoring (Jaskula et al., 2019; Curtarelli et al., 2022; Pahlevan et al., 2022; Virdis et al., 2022). This study applied three water indices, including the NDCI, Normalized Difference Aquatic Vegetation Index (NDAVI) and Automated Mucilage Extraction Index (AMEI), and their efficiency in monitoring water quality was thoroughly assessed. The fundamental formulations of the indices are given in Table 1. with related references.

**Table 1.** Water indices used in this study.

| Index Formulation | |
|---|---|
| $NDCI = (B05 - B04)/(B05 + B04)$ | (Mishra et al., 2012) |
| $NDAVI = (B08 - B02)/(B08 + B02)$ | (Villa et al., 2014) |
| $AMEI = (2*B04 + B08 - 2*B12)/(B03 + 0.25*B12)$ | (Colkesen et al., 2023) |

In addition to satellite imagery, water samples were taken from two points, one at the beginning and one at the end of the sample parcel, where maize was planted adjacent to the river during pre-planting, flowering, and post-harvest periods. The water quality of the Sakarya River was analyzed by calculating physicochemical parameters, including electrical conductivity (EC), the potential of hydrogen (pH), nephelometric turbidity unit (NTU), suspended solids (SS), chemical oxygen demand (COD), biochemical oxygen demand (BOD), concentration and total Kjeldahl nitrogen (TKN) in the water samples taken.

## Results

The main objective of this study is to correlate water quality parameters calculated from water samples collected by field studies with Sentinel-2 satellite images and derived water indices and to analyze the water quality of the Sakarya River surrounding the study area during the maize growth stages. For this purpose, physicochemical analyses were carried out through laboratory measurements of the collected water samples to assess the water quality parameters of the Sakarya River. The results of physicochemical water quality analyses in two water sampling points at pre-planting, flowering, and post-harvest periods are given in Table 2. As seen in the table, the selected water quality parameters are not within the permitted limit values according to the Turkish Water Pollution Control Regulation (Gazette, 2004) and the World Health Organization (WHO, 2018), and the pollution level was high in all three periods evaluated.

**Table 2.** Results of water quality analysis.

| Period | S.No | EC (µS/cm) | pH | NTU | SS (mg/L) | COD (mg/L) | BOD (mg/L) | TKN (mg/L) |
|---|---|---|---|---|---|---|---|---|
| Pre-P. | 1 | 637 | 8.35 | 24.3 | 98 | 231 | 31.0 | 8.25 |
| | 2 | 634 | 8.44 | 31.4 | 109 | 320 | 41.0 | 8.96 |
| Flow. | 1 | 796 | 8.45 | 35.9 | 142 | 441 | 54.0 | 11.40 |

| | | | | | | | | |
|---|---|---|---|---|---|---|---|---|
| | 2 | 807 | 8.44 | 44.7 | 158 | 550 | 70.0 | 11.10 |
| Post-H. | 1 | 987.3 | 8.40 | 38.4 | 159 | 435 | 56.4 | 10.90 |
| | 2 | 1000.4 | 8.35 | 46.8 | 161 | 456 | 67.5 | 10.30 |

In order to achieve the objective of the study, the relationship between the water quality parameters and the spectral values estimated for the same sampling points from the Sentinel-2 image was analyzed. For this purpose, spectral values were extracted from Sentinel-2 images taken on the dates of field studies, taking into account the spatial locations of the water sampling points. Moreover, NDCI, NDAVI, NDSSI, and AMEI indices were produced as ancillary data sets using the derived spectral values. Then, linear regression analysis was performed to determine the relationship between water quality parameters and the data set, representing the spectral characteristics of water, consisting of ten spectral bands of Sentinel-2 and water indices. Estimated Pearson correlation values, indicating how much the spectral/index values can explain the water quality parameters, are given in Table 3.

**Table 3.** Pearson correlation values of the regression analysis.

| Bands | EC (µS/cm) | pH | NTU | SS (mg/L) | COD (mg/L) | BOD (mg/L) | TKN (mg/L) |
|---|---|---|---|---|---|---|---|
| B02 | -0.04 | 0.29 | 0.35 | 0.76 | 0.64 | 0.42 | 0.69 |
| B03 | -0.33 | 0.00 | 0.06 | 0.80 | 0.39 | 0.15 | 0.46 |
| B04 | -0.21 | 0.07 | 0.17 | 0.89 | 0.46 | 0.21 | 0.57 |
| B05 | -0.55 | -0.42 | -0.29 | 0.69 | -0.03 | -0.28 | 0.18 |
| B06 | -0.58 | -0.66 | -0.55 | 0.31 | -0.44 | -0.59 | -0.12 |
| B07 | -0.65 | -0.68 | -0.59 | 0.33 | -0.44 | -0.60 | -0.16 |
| B08 | -0.91 | -0.85 | -0.84 | 0.23 | -0.64 | -0.78 | -0.50 |
| B8A | -0.43 | -0.62 | -0.44 | 0.31 | -0.39 | -0.54 | -0.01 |
| B11 | -0.70 | -0.93 | -0.85 | 0.04 | -0.85 | -0.92 | -0.58 |
| B12 | -0.68 | -0.91 | -0.92 | -0.30 | -0.98 | -0.96 | -0.87 |
| NDCI | -0.74 | -0.96 | -0.88 | -0.20 | -0.87 | -0.93 | -0.69 |
| NDAVI | -0.76 | -0.91 | -0.96 | -0.33 | -0.99 | -0.97 | -0.92 |
| AMEI | -0.72 | -0.89 | -0.89 | -0.17 | -0.89 | -0.91 | -0.69 |

As can be seen from the table, the calculated correlation values for the EC and pH parameters are generally low for almost all spectral bands and indices. The highest correlation value for the EC parameter is -0.91, obtained for the near-infrared band (B08), while the highest value for the pH parameter is 0.89 for the red band (B04). It can be observed that the correlation values for NTU, SS, COD, BOD, and TKN parameters are relatively high for middle-infrared (SWIR) bands of Sentinel-2, namely B11 and B12. Furthermore, it was also observed that the considered water indices showed a higher correlation with these parameters. While the highest correlation value was calculated for the NDCI index as -0.96 for NTU, the highest values for SS, COD, BOD, and TKN parameters were calculated with the NDAVI index as -0.96, -0.99, -0.97, and -0.92, respectively. Based on the high correlation between the NDAVI and water quality parameters, a time series covering periods from pre-planting to post-harvest was applied to analyze the water quality changes of the river during the phenological development of the maize plant. For this purpose, 12 cloud-free Sentinel-2 images covering the study area were detected in May and November 2022, and the time series curves calculated from these images are given in Figure 1. As can be seen from the figure, there is a strong inverse correlation between maize plant development and water quality in the neighboring Sakarya River. Specifically, NDVI values, which encompass the flowering period of corn plants, are at their highest levels in July and August. In contrast, NDAVI values are at their lowest levels during the same period.

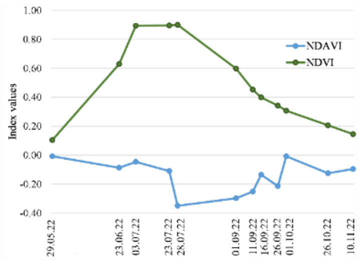

**Figure 1.** Time series graphs of NDAVI and NDVI.

To conduct a visual analysis of the water quality level of the Sakarya River, estimated regression coefficients and intercept values were applied to the whole Sentinel-2 imagery. As an example of the resulting water quality maps, the maps produced with the indices having the highest correlation representing NTU, SS (mg/L), COD (mg/L), and BOD (mg/L) values at three sampling periods are given in Figure 2. The first column of the figure shows water quality maps for the subsample area (shown in a red rectangle) for the pre-planting period, while the other two columns show water quality maps for the same area for the flowering period of the maize plant and the post-harvest period, respectively. It was observed that, in almost all periods, the water quality parameter values were lower in the narrower river segments with rapid flow, whereas it was higher in the broader areas where the water was stable. As can be seen from the figure, NTU, SS, BOD, and COD values in the part of Sakarya River within the study area during the pre-planting period were at the maximum of 65.42, 219.32 (mg/L), 97.16 (mg/L), and 744.05(mg/L), respectively. On the other hand, the increasing trend in water quality parameter values started during the flowering period, when vegetative vitality was the highest for maize plants, and reached peak levels in the post-harvest period. The highest NTU, SS, BOD, and COD values were 78.48, 242.65 (mg/L), 109.72 (mg/L), and 841.01 (mg/l) in the post-harvest period. In other words, with the start of agricultural activities in the lands adjacent to the river, the water quality level significantly changed and tended to decrease.

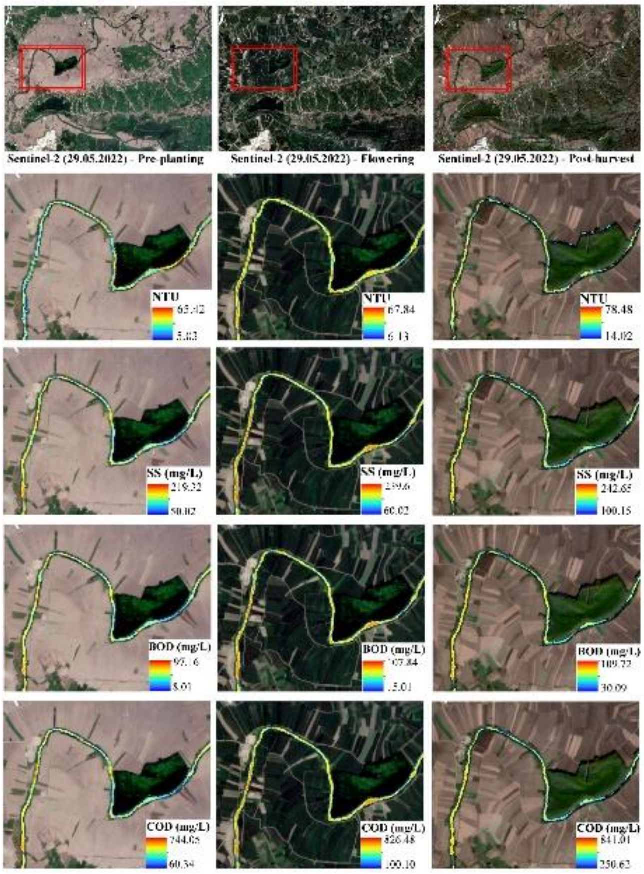

**Figure 2.** Thematic maps representing water quality parameters produced based on the Sentinel-2 imagery.

## Conclusion

Rivers have been under intense pressure recently due to agricultural and anthropogenic activities that significantly affect water quality. Remotely sensed imagery provides valuable spectral information for fast-detecting changes in these sensitive areas. This study discusses the relationship between Sentinel-2 images and different water indices derived from these images and water quality parameters. As a result of the study, a few critical points can be emphasized. First, the results showed that the red (B04), near-infrared (B08) and short-wave infrared (B11 and B12) bands of Sentinel-2 images were highly correlated with water quality parameters (i.e., EC, NTU, SS, COD and BOD). Second, the strong correlations were calculated between the three spectral water indices and water quality parameters (i.e., NTU, SS, BOD and COD). The NDCI index demonstrates the strongest correlation with the NTU parameter among the spectral indices examined, whereas NDAVI showed the highest correlation with the other water quality parameters, except for EC and pH parameters. Third, the time series analysis, based on the NDAVI and NDVI indices, showed that significant changes in water quality occurred during the period of highest plant vitality, namely, the flowering season, and this trend continued until after the harvest. Overall, the results showed the potential use of the Sentinel-2 imagery and derived water indices in monitoring water quality, whereas further studies are needed to assess their effectiveness for different data sets and study areas.

## Acknowledgements

This work was funded and supported by the Scientific and Technological Research Council of Turkey (TUBITAK) under project no: 121Y392.

## References

Colkesen, I. Kavzoglu, T. Sefercik, U. G. and Ozturk, M. Y. (2023). Automated mucilage extraction index (AMEI): A novel spectral water index for identifying marine mucilage formations from Sentinel-2 imagery. International Journal of Remote

Sensing, 44(1), pp. 105-141.

Curtarelli, M. Neto, E. de Siqueira, F. Yopan, F. Soares, G. Pauli, G. de Souza, J. Silva, L. Sagaz, M. Demay, M. and Bortolas, N. (2022). QDA-System: A cloud-based system for monitoring water quality in Brazilian hydroelectric reservoirs from space. Remote Sensing, 14(7), 1541.

Das, S. Kaur, S. and Jutla, A. (2021). Earth observations based assessment of impact of COVID-19 lockdown on surface water Quality of Buddha Nala, Punjab, India. Water, 13(10), 1363.

Food and Agriculture Organization (FAO), (2021). The state of the world's land and water resources for food and agriculture - managing systems at risk. Food and Agriculture Organization of the United Nations, Rome and Earthscan, London, ISBN 978–1–84971–327–6.

Gazette, O. (2004). Turkish Water Pollution Control Regulation (WPCR). Repub. Turkey, Off. Gaz. 26786.

Hafeez, S. Wong, M. S. Abbas, S. and Asim, M. (2022). Evaluating landsat-8 and sentinel-2 data consistency for high spatiotemporal inland and coastal water quality monitoring. Remote Sensing, 14(13), 3155.

Hanna, D. E. Tomscha, S. A. Ouellet Dallaire, C. and Bennett, E. M. (2018). A review of riverine ecosystem service quantification: Research gaps and recommendations. Journal of Applied Ecology, 55(3), pp. 1299-1311.

Huangfu, K. Li, J. Zhang, X. Zhang, J. Cui, H. and Sun, Q. (2020). Remote estimation of water quality parameters of medium- and small-sized inland rivers using Sentinel-2 imagery. Water, 12(11), 3124.

Jaskuła, J. and Sojka, M. (2019). Assessing spectral indices for detecting vegetative overgrowth of reservoirs. Polish Journal of Environmental Studies, 28(6), pp. 4199-4211.

Lv, Y. and Tian, Z. (2021). Study on water quality monitoring method of Jialing River based on Sentinel-2 MSI sensor data. Journal of Physics: Conference Series, 2006(1), 012003.

Mishra, S. and Mishra, D. R. (2012). Normalized difference chlorophyll index: A novel model for remote estimation of chlorophyll-a concentration in turbid productive waters. Remote Sensing of Environment, 117, pp. 394-406.

Özdoğan, N. Sefercik, U. G. Kılınç, Y. Çalışkan, E. and Atalay, C. (2021). Determination of water quality by analysing unmanned aerial vehicle data and physico-chemical parameters: The case of Aydınlar (Gülüç) Stream. European Journal of Science and Technology, (23), pp. 572-582.

Pahlevan, N. Smith, B. Alikas, K. Anstee, J. Barbosa, C. Binding, C. Bresciani, M. Cremella, B. Giardino, C. Gurlin, D. and Fernandez, V. (2022). Simultaneous retrieval of selected optical water quality indicators from Landsat-8, Sentinel-2, and Sentinel-3. Remote Sensing of Environment, 270, 112860.

Sagan, V. Peterson, K. T. Maimaitijiang, M. Sidike, P. Sloan, J. Greeling, B. A. Maalouf, S. and Adams, C. (2020). Monitoring inland water quality using remote sensing: Potential and limitations of spectral indices, bio-optical simulations, machine learning, and cloud computing. Earth-Science Reviews, 205, 103187.

Sendzimir, J. and Schmutz, S. (2018). Challenges in riverine ecosystem management. In: Schmutz, S. and Sendzimir, J. (eds) Riverine Ecosystem Management: Science for Governing Towards a Sustainable Future., pp. 1-16., ISBN: 978-3-319-73249-7, Springer Open, Cham.

UNESCO, (2023). The United Nations World Water Development Report: Partnerships and Cooperation for Water. Paris, ISBN 978-92-3-100576-3.

Villa, P. Mousivand, A. and Bresciani, M. (2014). Aquatic vegetation indices assessment through radiative transfer modeling and linear mixture simulation. International Journal of Applied Earth Observation and Geoinformation, 30, pp. 113-127.
Virdis, S. G. Xue, W. Winijkul, E. Nitivattananon, V. and Punpukdee, P. (2022). Remote sensing of tropical riverine water quality using sentinel-2 MSI and field observations. Ecological Indicators, 144, 109472.

World Health Organization (WHO), (2018). A global overview of national regulations and standards for drinking-water quality.

INTERNATIONAL SYMPOSIUM ON
APPLIED
GEOINFORMATICS
9-10 May 2024 · Wrocław/Poland

*International Symposium on Applied Geoinformatics (ISAG2024)*

# Comparison of Hyperspectral and Broad-Band Vegetation Indices for Estimation of Nitrogen Content in Grasslands

Ilina Kamenova[1]*

[1] Space Research and Technology Institute – Bulgarian Academy of Sciences, Bulgaria, ilina.kamenova@space.bas.bg
ORCID 0000-0003-4607-3064

* Corresponding Author

## Abstract

The role of nitrogen in ecological and agricultural systems is pivotal due to its influence on essential ecosystem processes and primary production rates. Nitrogen availability significantly impacts plant growth and crop yield, making it a crucial determinant among major plant nutrients. While artificial nitrogen supplementation is integral for optimizing crop productivity, mismanagement and over-application can lead to detrimental effects, profoundly altering the global nitrogen cycle. This study explores the utility of hyperspectral vegetation indices derived from APEX hyperspectral data and simulated spectra from Sentinel-2 and Landsat TM. Regression analysis was employed to assess the effectiveness of these indices in estimating nitrogen content, investigating linear and exponential relationships in the regression models. Our findings reveal comparable correlations between vegetation indices based on Sentinel-2 and those derived from APEX, highlighting the potential of Sentinel-2 for nitrogen estimation. Moreover, the study highlights the significance of red-edge bands, which are absent in Landsat TM, showing limitations in nitrogen estimation using Landsat TM-derived indices. This study underlines nitrogen's central role in ecological and agricultural systems and the challenges of its management. It explores remote sensing's potential, comparing hyperspectral data from APEX and Sentinel-2 with Landsat TM. Findings suggest Sentinel-2's effectiveness in nitrogen estimation, emphasizing the importance of red-edge bands absent in Landsat TM for accurate assessment of vegetation nitrogen content in grasslands.

**Keywords:** *Sentinel-2, Landsat TM, APEX sensor, Nitrogen content*

## Introduction

The productivity and dynamics of many unmanaged terrestrial and marine ecosystems, and most agricultural and managed-forestry ecosystems, are limited by the supply of biologically available nitrogen (Keeney and Hatfield 2008). Although an artificial supply of nitrogen to crops is fundamental to optimize crop yields, mismanagement of N and its excessive application, causes many negative effects, which has dramatically altered the global nitrogen cycle. Combined N in the atmosphere and precipitation fertilizes in natural ecosystems result in eutrophication, lowered biodiversity, N leakage, while acidity from nitric oxide and ammonia oxidation results in acid lakes and streams, and declining health of forests (Keeney and Hatfield 2008). The effect of anthropogenic activities on the N cycle has been addressed to some extent. Europe has had some success using rules and fines to modify the fertilizer and animal farm waste. Educational programs need to be further developed to modify human behaviour including the way farmers manage N fertilizers in their farms (European Commission 2021).

One of the largest challenges facing the agricultural sector is to produce enough food for the growing population while at the same time protecting the environment and human health from excess supply of fertilizers. This challenge requires knowledge about the crop status and good understanding for the responsible biological processes (Wolf et al. 2021). Among the fertilizers, nitrogen is essentially the most important one. Different methods have been developed and implemented for assessment of crop nitrogen status. Traditional methods require laborious field measurements and are costly in terms of time and money. Ideally a method is required that is accurate, non-destructive, simple to use, covering large areas . Hyperspectral remote sensing has large amount of spectral information measured by using narrow contiguous bands, which can provide a new means for non-destructive, fast, and real-time monitoring of plant biochemical parameters (Khan 2022). It should be noted that the use of hyperspectral data is much more complex and extensive than the multispectral data.

As mentioned before imaging spectrometers usually gather data in hundreds of near- contiguous narrow bands and the data volume is vast. The increase in data volume poses challenges in data storing and handling. This issue makes it essential to develop methods to handle the high-dimensional data or build specialized optimal sensors to gather data for specific applications in optimal band selection, excluding the redundant bands (Thenkabail et al. 2000). Sensors like Sentinel-2 address the issues posed by conventional broadband sensors and the limited spectral information they provide next to the vast and mostly redundant data offered by hyperspectral acquisition methods. These sensors have more than 10 and less than 50 bands, these bands are narrower than broadband, but they are not contiguous. In this sense they are in intermediate position between broad and hyperspectral remote sensing. The aim of this study was to investigate the possibilities to derive nitrogen content of grassland using data derived from APEX imaging spectrometer, to test the ability of hyperspectral data analysis to estimate nitrogen content and compare with the potential of Landsat TM and Sentinel-2. For this purpose a statistical approach using regressive models were adopted, relating in situ measurements and different hyperspectral vegetation indices and broadband vegetation indices.

## Materials and Methods

The study area is located in the South of the Netherlands in the province of Noord Braband, close to the village of Reusel. The APEX image is covering area of 11.4 km2. For the purpose of this study selective field sampling was performed over the study area in 3 pastures. In each field five different locations were examined. Every sample position was located using Differential Global Positioning System (DGPS) and projected in Rijks Driehoekstelsel (RD). The data analysis was divided in two main parts. The first step was to calculate nitrogen suitable hyperspectral VIs and broadband VIs (Table 1). In step two the results from the calculations were further analyzed in regression models aiming to determine the best predictors for nitrogen content.

**Table 1** Vegetation indices evaluated in this study.

| Index | Formulation | Reference |
|---|---|---|
| REP | $(((R_{670} + R_{780})/2 - R_{700})/(R_{740} - R_{700}))*40 + R_{700}$ | (Guyot and Baret 1988) |
| MTCI | $(R_{754} - R_{709})/(R_{709} - R_{681})$ | (Dash and Curran 2004) |
| MCARI/OSAVI RE | $(((R_{750} - R_{705})- 0.2*(R_{750} -R_{550}))*(R_{750}/R_{705}))/(1.16*(R_{750} - R_{705})/(R_{750} + R_{705} +0.16))$ | (Wu, Niu et al. 2008) |
| TCARI/OSAVI RE | $((R_{750} - R_{705}) - 0.2*(R_{750} - R_{550})*(R_{750}/R_{705}))*3/(1.16*(R_{750} - R_{705})/(R_{750} + R_{705} + 1.16))$ | (Wu, Niu et al. 2008) |
| CI red edge | $(R_{780}/R_{709}) - 1$ | (Gitelson, Keydan et al. 2006) |
| CI green | $(R_{780}/R_{550}) - 1$ | (Gitelson, Keydan et al. 2006) |
| SIPI | $(R_{800} - R_{445})/(R_{800} - R_{681})$ | (Penuelas, Filella et al. 1995) |
| NDRE | $(R_{790} - R_{720})/(R_{790} + R_{720})$ | (Tilling, O'Leary et al. 2007) |
| NDVI | $(R_{800} - R_{670})/(R_{800} + R_{670})$ | (Rouse, Haas et al. 1974) |
| CCCI | $((R_{790} - R_{720})/(R_{79}0 + R_{720}))/((R_{800} - R_{670})/(R_{800} + R_{670}))$ | (Barnes, Clarke et al. 2000) |
| WDRVI | $(0.2*R_{800} - R_{670})/(0.2*R_{800} + R_{670})$ | (Gitelson, et al. 2006) |

APEX hyperspectral data was geometrically corrected by VITO (Vlaamse Instelling voor Technologisch Onderzoek) own developed C++ module with pixel size of about 7 $m^2$. The available hyperspectral data derived from APEX consists of 288 bands in the range between 399 nm and 2461nm. One of the main research objectives of this study was to test the ability of hyperspectral data analysis in estimating nitrogen content and to compare with the potenential of multispectral sensors such as Sentinel-2 and the broadly used Landsat TM. Sentinel-2 bands were simulated calculating averaging the reflectance of APEX bands over the band width of the respective Sentinel- 2 bands. The 6 bands from Landsat TM, without the thermal one were used for the simulation, using the same principle as for Sentinel- 2 simulations. The resulting datasets were used for further calculations including vegetation broadband indices.

A number of VIs have been found in literature to measure chlorophyll and nitrogen content. They were considered as a good estimator of these properties. All the listed VIs in Table 1 were calculated, using the wavebands as reported in the literature. All the discussed indices were calculated based on data simulated from APEX spectral responses for the future Sentinel- 2 and Landsat TM. Often the VIs cannot be calculated with the exact wavelengths as mentioned in the literature, because they require very specific bands, most of the cases not available by the multispectral sensors. For the multispectral sensors approximately close wavebands were chosen to calculate each VI. Comparison of the results derived from previous steps namely VIs calculations were performed fitting linear and exponential regression models. Regression analysis was performed on the same way for broadband VIs and also hyperspectral VIs. The judgment of all results was performed by comparing coefficients of determination ($R^2$).

## Results and Discussion

The hyperspectral index providing the strongest linear relationship with nitrogen content was REP ($R^2 = 0.612$, significant at $p < 0.001$). The exponential model performed with a higher value of the coefficient of determination ($R2 = 0.713$, $p < 0.001$). The simulated Sentinel- 2 and Landsat TM band reflectance values don't suffice calculation of all the mentioned indices investigated (Table 1). Most of the vegetation indices can be calculated using Sentinel-2 simulations. Landsat did not provide a sufficient number of bands so only 4 indices were calculated (SIPI, CI green, NDVI, WDRVI). Results from the regression analysis of the available indices are also summarized in Table 2 in terms of R$^2$ values with the corresponding probability value derived from F test marked with an asterisk. They are compared with the values of the coefficients of determination derived from regressions based on APEX based hyperspectral VIs.

**Table 2 .** Overview of R2 values of the linear and exponential relationships between indices and nitrogen content for potato and grassland.

| Grass | APEX | | Sentinel_2 | | Landsat TM | |
|---|---|---|---|---|---|---|
| Index name | R$^2$ linear model | R$^2$ exponential | R$^2$ linear model | R$^2$ exponential | R$^2$ linear model | R$^2$ exponential |
| REP | 0,612*** | 0,713*** | 0,606*** | 0,717*** | | |
| MTCI | 0,599*** | 0,711*** | 0,525** | 0,642*** | | |
| MCARI/OSAVI$_{RE}$ | 0,607*** | 0,736*** | 0,597*** | 0,726*** | | |
| TCARI/OSAVI$_{RE}$ | 0,416** | 0,546** | 0,331* | 0,451** | | |
| CI red edge | 0,501** | 0,627*** | 0,487** | 0,612*** | | |
| CI green | 0,348* | 0,472** | 0,355* | 0,478** | 0,29* | 0,407* |
| SIPI | ns | 0,348* | ns | 0,291* | 0,276* | 0,386* |
| NDRE | 0,523** | 0,646*** | 0,65*** | 0,501** | | |
| NDVI | ns | 0,316* | ns | 0,316* | ns | 0,313* |
| CCCI | 0,604*** | 0,717*** | 0,712*** | 0,801*** | | |
| WDRVI | ns | 0,318* | ns | 0,319* | ns | 0,315* |

Notes: *p < 0.05; **p < 0.01; ***p < 0.001

The results for the vegetation indices, based on Sentinel-2, all had similar performance in terms of R$^2$ values to the indices based on APEX. Some of them (REP, MTCI, MCARI/OSAVI red edge, TCARI/OSAVI red edge, CI indices) had slightly less accurate predictions of the linear models. Surprisingly the NDRE VI performed with even higher accuracy judged on R$^2$ values, where the CCCI achieved R$^2$ for linear model of 0.712; for the exponential R2 = 0.801, both significant at $p < 0.001$. The results achieved from Landsat regressions performed with relatively lower accuracy than APEX and Sentinel-2 (Table 2). This could be expected taking into account the lower spectral resolution of the broad band sensor. Other studies have shown that red-edge bands are highly significant for nitrogen retrieval (Feng et al. 2015). This point was also confirmed by the current study, other sources of data were explored to further investigate the red-edge bands. Calculating the indices mentioned (Table 1) using the simulated Sentinel-2 data, resulted in similar performance to the indices calculated with APEX narrow bands. The absence of red-edge bands on board of Landsat TM makes the sensor with very limited value for nitrogen retrieval.

## Conclusion

Results from this study indicate that the hyperspectral vegetation indices are a promising tool to derive biochemical characteristics from arable crops, such as chlorophyll and nitrogen. Compared to multispectral sensors like Landsat TM the availability of narrow and contiguous bands is fundamental for retrieving nitrogen content. The Sentinel- 2 system has 12 bands, two of which are centered at the red-edge region (705 nm and 740 nm). They have good potential of retrieving canopy nitrogen and chlorophyll with high spatial resolution (20 m) and short revisit time. This study confirmed in accordance with previous studies the strength of the relation between vegetation indices based on Sentinel-2 band setting with chlorophyll and nitrogen.

## References

Barnes, E. M., Clarke, T. R., Richards, S. E., Colaizzi, P. D., Haberland, J., Kostrzewski, M., Waller, P., Choi C., R. E., Thompson, T., Lascano, R. J., Li, H., & Moran, M. S. (2000). Coincident detection of crop water stress, nitrogen status and canopy density using ground based multispectral data. Proc. 5th Int. Conf. Precis Agric.

Dash, J., & Curran, P. J. (2004). MTCI: The meris terrestrial chlorophyll index. European Space Agency, (Special Publication) ESA SP, 549, 151–161. https://doi.org/10.1080/0143116042000274015

Gitelson, A. A., Keydan, G. P., & Merzlyak, M. N. (2006). Three-band model for noninvasive estimation of chlorophyll, carotenoids, and anthocyanin contents in higher plant leaves. Geophysical Research Letters, 33(11). https://doi.org/10.1029/2006GL026457

Guyot, G. and F. Baret (1988). Utilisation de la haute resolution spectrale pour suivre l'etat des couverts vegetaux. Spectral Signatures of Objects in Remote Sensing.

European Comission. (2021). A Greener and Fairer Cap. https://agriculture.ec.europa.eu/system/files/2022-02/factsheet-newcap-environment-fairness_en_0.pdf

Feng, W., Guo, B.-B., Zhang, H.-Y., He, L., Zhang, Y.-S., Wang, Y.-H., Zhu, Y.-J., & Guo, T.-C. (2015). Remote estimation of above ground nitrogen uptake during vegetative growth in winter wheat using hyperspectral red-edge ratio data. Field Crops Research, 180, 197–206. https://doi.org/10.1016/j.fcr.2015.05.020

Keeney, D. R., & Hatfield, J. L. (2008). The Nitrogen Cycle, Historical Perspective, and Current and Potential Future Concerns (pp. 1–18). Elsevier Inc. https://doi.org/10.1016/B978-0-12-374347-3.00001-9

Khan, A., Vibhute, A. D., Mali, S., & Patil, C. H. (2022). A systematic review on hyperspectral imaging technology with a machine and deep learning methodology for agricultural applications. Ecological Informatics, 69. https://doi.org/10.1016/j.ecoinf.2022.101678

Penuelas, J., Filella, I., & Gamon, J. A. (1995). Assessment of photosynthetic radiation-use efficiency with spectral reflectance. New Phytologist, 131(3), 291–296. https://doi.org/10.1111/j.1469-8137.1995.tb03064.x

Thenkabail, P. S., Smith, R. B., & de Pauw, E. (2000). Hyperspectral Vegetation Indices and Their Relationships with Agricultural Crop Characteristics. Remote Sensing of Environment, 71(2), 158–182. https://doi.org/10.1016/S0034-4257(99)00067-X

Tilling, A. K., O'Leary, G. J., Ferwerda, J. G., Jones, S. D., Fitzgerald, G. J., Rodriguez, D., & Belford, R. (2007). Remote sensing of nitrogen and water stress in wheat. Field Crops Research, 104(1), 77–85. https://doi.org/10.1016/j.fcr.2007.03.023

Rouse, J. W., Hass, R. H., Schell, J. A., & Deering, D. W. (1973). Monitoring vegetation systems in the great plains with ERTS. Third Earth Resources Technology Satellite (ERTS) Symposium, 1, 309–317. https://doi.org/citeulike-article-id:12009708

Wolf, S., Teitge, J., Mielke, J., Schütze, F., & Jaeger, C. (2021). The European Green Deal — More Than Climate Neutrality. Intereconomics 2021 56:2, 56(2), 99–107. https://doi.org/10.1007/S10272-021-0963-Z

Wu, C., Niu, Z., Tang, Q., & Huang, W. (2008). Estimating chlorophyll content from hyperspectral vegetation indices: Modeling and validation. Agricultural and Forest Meteorology, 148(8), 1230–1241. https://doi.org/10.1016/j.agrformet.2008.03.005

INTERNATIONAL SYMPOSIUM ON
APPLIED
GEOINFORMATICS
9-10 May 2024 · Wrocław/Poland

*International Symposium on Applied Geoinformatics (ISAG2024)*

# Comparative Evaluation of The Consistency of Sentinel-2 Water Indices for Akyatan Lagoon

Balik Sanli Fusun[1*], Narin Omer Gokberk[2], Abdikan Saygin[3]

[1] Faculty of Civil Engineering, Department of Geomatics, Yildiz Technical University, Istanbul, Turkey, fbalik@yildiz.edu.tr; ORCID 0000-0003-1243-8299
[2] Faculty of Engineering, Department of Geomatics, Afyon Kocatepe University, Afyonkarahisar, Turkey, gokberknarin@aku.edu.tr; ORCID 0000-0002-9286-7749
[3] Faculty of Engineering, Department of Geomatics, Hacettepe University, Ankara, Turkey, sayginabdikan@hacettepe.edu.tr; ORCID 0000-0002-3310-352X
* Corresponding Author

## Abstract

Wetlands are dynamic ecosystems susceptible to changes driven by environmental factors and human activities, thereby impacting their natural habitat. The significance of spatial data becomes evident in determining these areas and enabling decision makers to act promptly. This study focuses on the Akyatan Lagoon, a wild habitat affected by pollution and other anthropogenic factors. The study area serves as a living and breeding ground for various birds and turtles. The water area was identified using remote sensing data with different spectral indices employed. In this context, one image from the two-year Sentinel-2 satellite was evaluated for each season. The Normalized Difference Water Index (NDWI), the Modified NDWI (MNDWI) and a newer index, the Sentinel-2 Water Index (SWI), were produced using the Google Earth Engine cloud environment. Correlation values were computed to analyze consistency among the indices. Additionally, an area-based comparison was conducted, revealing the highest degree of consistency between the SWI and MNDWI indices for both study years.

**Keywords:** *Sentinel-2, Water indices, Google Earth Engine, Consistency analysis*

## Introduction

Wetlands play an essential role in performing environmental functions, contributing significantly to biodiversity, and serving as crucial natural resources for agricultural and various human-related needs such as transportation, energy production and fishery (Dörnhöfer and Oppelt 2016). Coastal lagoons, in particular, interact with the seas and changes in water levels can be observed along with seasonal variations. Lagoons, which have a complex ecosystem, have a fragile balance structure (Yetis et al. 2014). It would be beneficial to manage them sustainably for reasons such as biodiversity and the protection of ecological balance. Remote sensing is a very important tool for monitoring lagoons, lakes, reservoirs and wetlands. With developing technology, both the temporal resolutions and band numbers of imaging satellites have increased over time. This has enabled us to identify water areas better and monitor seasonal changes. Spectral indices have been developed to identify water bodies such as the Normalized Difference Water Index (NDWI), which eliminates soil and vegetation and identifies water areas accurately (McFeeters, 1996). The NDWI index was modified, leading to the development of a new index named as the Modified NDWI (MNDWI) (Xu, 2006), which uses the middle-infrared (MIR) band instead of the near-infrared (NIR) band used by the NDWI index. This modification has increased the contrast between built-up areas and water bodies, offering advantages, particularly in regions with urban areas. A new index, Sentinel-2 water index (SWI), was developed for the Sentinel-2 satellite using vegetation red edge (Band 5) and SWIR (Band 11). This index provides enhanced contrast in water features such as turbid, salty, and pure water compared to NDWI, and it prevents the shadow effects in urban areas from interfering with water areas delineation (Jiang et al., 2021). Apart from these indices, numerous water indices have been proposed and used in the literature (Ma et al., 2019). Consequently, various indices have been examined for their applicability to different environmental features, with researchers assessing their accuracy and exploring their interrelationships. For example, Arekhi et al. (2019) studied indices relevant to forests, while

Nie et al. (2019) studied indices relevant to urban areas, and Tan et al. (2022) explored indices pertinent to lakes. Jiang et al., (2019) compared the NDWI and SWI indices in their study. They found that SWI gave better results in terms of overall accuracy (NDWI = 91.50%, SWI = 92.75% for Taihu Lake and NDWI = 86.6% and SWI = 93% for Yangtze River). Fisher et al. (2016) compared seven different water indices in their study and $WI_{2015}$ gave the best result in classified water (RMSE = 7.28, $r^2$ = 0.97). For the long-term analysis Google Earth Engine (GEE) cloud-computing platform have been utilized for waterbody extractions. Generally, NDWI has been used for different inland water extraction in Turkey (Albarqouni et al., 2022; Dervisoglu 2022; Firatli et al, 2022; Yilmaz 2023).

In this study, it was aimed to determine the dimensions of Akyatan Lake, a protected wilderness area in Turkey. This region is included in RAMSAR list of wetlands due to the global significance (RAMSAR 1016). Akyatan Lake is characterized as a coastal lagoon that covers large dunes and providing habitat for a diverse array of bird species, as well as serving as a crucial breeding, migrating, and wintering site for threatened and endangered marine turtles (FAO 2015). However, the lake is affected by coastal pollution, which is damaging the natural habitats (Gundogdu and Cevik 2019). Consequently, we are conducting on going monitoring of the lake to assess its condition. Our study aims to investigate the relationship between the NDWI, MNDWI and SWI indices in two different years (2021 and 2022) and in different seasons. In addition, we are calculating the difference between the two years by determining the water areas.

## Materials and Methods

The study area is a protected lagoon in the Mediterranean coastline district of Adana province in Turkey. Over time, the Akyatan Lagoon was disconnected from the sea, forming Turkey's largest lagoon lake, Akyatan Lake (Figure 1). It was declared a RAMSAR area on 15/04/1998 and is home to diverse range of flora and fauna.

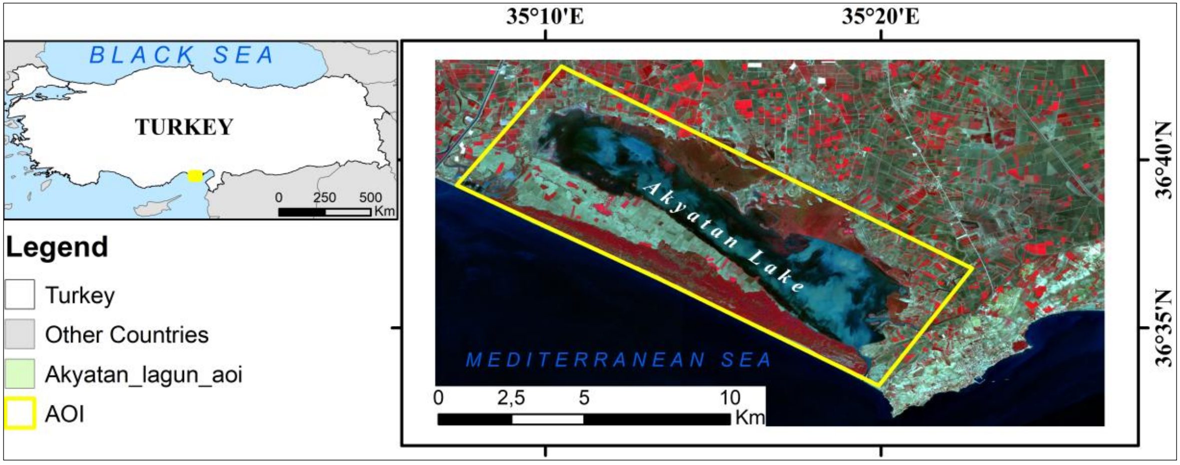

**Figure 1.** The study area shown in yellow boundary. Sentinel-2 RGB:8–4–3 image acquired on 22.10.2022

We have used Sentinel-2 satellite images in 3-month periods between 2021 and 2022. They were processed using the Google Earth Engine (GEE) platform (Gorelick 2017). We selected atmospherically corrected S2 L2A (corresponding to "COPERNICUS/S2_SR_HARMONIZED" in GEE) from the GEE catalog. Furthermore, we created a cloud mask for the study area and selected images without clouds. Once the images were selected, we produced indices on the GEE platform and exported the results to Google Drive (Table 1). We then explored the relationships among the indices using the R programming language (R Core Team, 2013) (Figure 2).

**Table 1.** WIs for Sentinel-2 satellite

| **WIs name** | **NDWI** (McFeeters 1996) | **MDNWI** (Xu 2005) | **SWI** (Jiang et al 2021) |
|---|---|---|---|
| **Equation** | (B3-B8)/(B3+B8) | (B3-B11)/(B3+B11) | (B5-B11)/(B5+B11) |

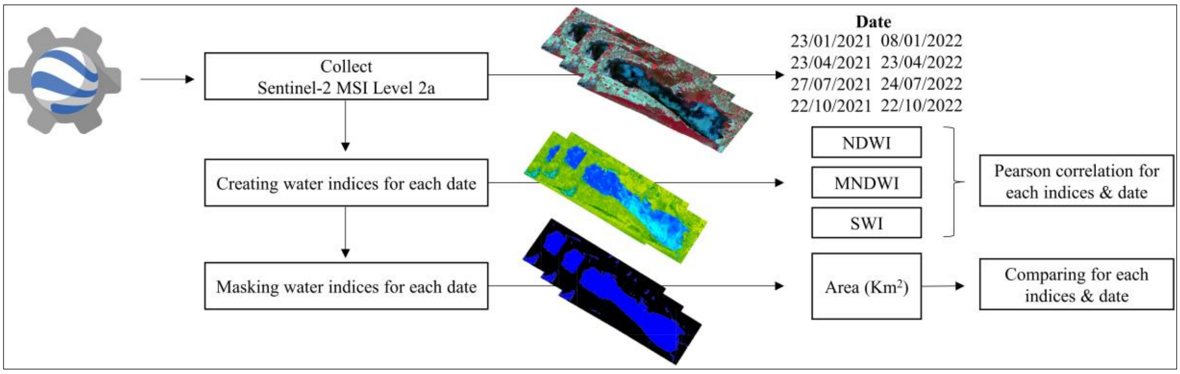

**Figure 2.** Flowchart of the study

## Results and Discussion

Generally, when examining the correlation values, it is determined that it is over 82%. In 2021, the highest correlations (R = 0.98-0.99) were found between SWI and MNDWI for all seasons (Table 2). Subsequently, the second order high values (R=0.9-0.99) were obtained between NDWI and MNDWI. Similarly, in 2022, the indices yielded comparable results with the highest values (R = 0.99) observed between SWI and MNDWI for all seasons. This was followed by the correlation values between NDWI and MNDWI (R = 0.86-0.95). When evaluated from a spatial perspective, there was minimal difference between MNDWI and SWI for both years (Table 2). Generally, higher areal values were obtained with SWI. A consistent pattern across all indices was observed, with January exhibiting the highest areal value, while October displayed the lowest value.

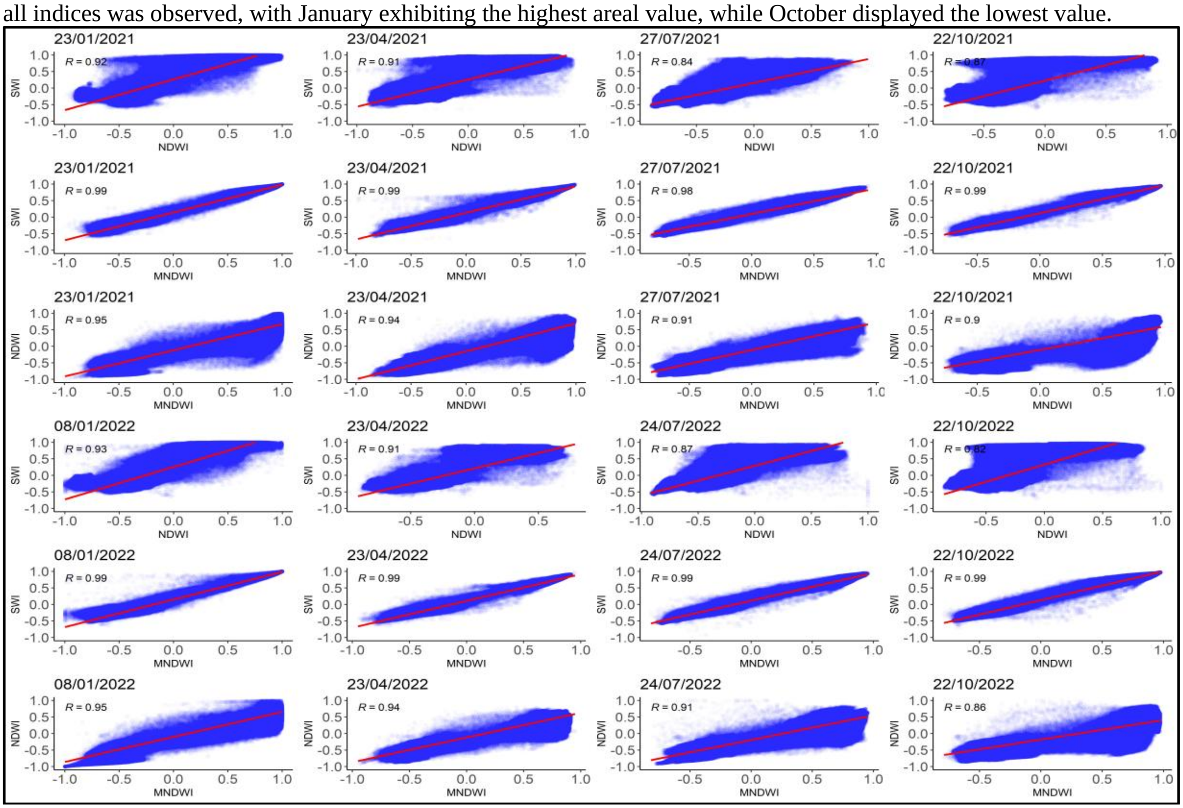

**Table 2.** Lake areas (Km$^2$) of each index in different dates

| Date | NDWI | MNDWI | SWI | Date | NDWI | MNDWI | SWI |
|---|---|---|---|---|---|---|---|
| 1/23/2021 | 60.808 | 63.735 | 65.859 | 1/8/2022 | 62.482 | 64.472 | 66.896 |
| 4/23/2021 | 57.402 | 61.437 | 64.789 | 4/23/2022 | 55.081 | 59.94 | 61.567 |
| 7/27/2021 | 59.178 | 62.618 | 64.113 | 7/24/2022 | 56.106 | 63.409 | 65.703 |
| 10/22/2021 | 53.199 | 61.279 | 63.421 | 10/22/2022 | 48.724 | 61.927 | 65.654 |

Khalid et al. (2021) conducted a spatial comparison of areas using seven water indices and identified the index incorporating the thermal band as yielding the best result. Additionally, they found that the classification success of NDWI exceeded that of MNDWI. Senel et al. (2020) compared the correlations of water indices produced from Landsat-8 and Sentinel-2 and found that the AWEInsh index performed the best, with MNDWI exhibiting the higher results compared to NDWI. Zhai et al. (2015) compared five water indices derived from Landsat data and concluded that the results obtained from MNDWI and AWEI are superior to those of NDWI and NDVI. Laonamsai et al. (2023) conducted a two-year (2015 and 2022) of monitoring of erosion and deposition formations in the river using five different water indices. In 2015, NDWI, AWEI and MNDWI presented the highest precision in the top three orders, while AWEI, MNDWI and NDWI demonstrated the best accuracy. Conversely, in 2022, while AWEI provided the highest precision, MNDWI yielded lower values compared to NDWI. Jiang et al. (2021) compared NDWI and SWI data and found that SWI data extracted water areas with higher accuracy. Although our findings are consistent with the literature, it is worth nothing that different indices may yield better results in various studies. This variation could be attributed to factors such as the satellite data used and the presence land cover other than the water in the study area.

## Conclusion

The extraction of water bodies is crucial for the accurate and sustainable management of water resources, particularly in the context of clean water and sanitation, which constitutes the 6th Sustainable Development Goal (SDG) of the United Nations. Providing data at various scales, establishing of long-term time series, enabling comparability with diverse satellites, analyzing with different geophysical measurements and climate data, and sharing images under an open data policy contribute achieving this SDG. Sentinel-2 data, which provides open data, facilitates the monitoring of wetlands such as lagoons that contain biodiversity and endangered species, offering opportunities for seasonal analyses. In this study, Sentinel-2 data was utilized to compare the relatively new SWI and the commonly used NDWI and MNDWI data over two year period and across four seasons. Statistical analysis revealed a stronger correlation between SWI and MNDWI data. However, as indicated in the literature, different indices may excel in different contexts. Detailed analyses can be obtained incorporating atmospheric data and generating long time series in a cloud-based environment such as GEE. The study did not employ reference data and instead relied on cross correlation analysis. Accuracy assessment can be performed utilizing high-resolution specific to each field study. Additionally, a threshold optimization procedure could provide more reliable results. The aim is to further expand this research by testing various water indices for comprehensive investigation.

**References**

Albarqouni MMY, Yagmur N, Bektas Balcik F, Sekertekin A. 2022. Assessment of Spatio-Temporal Changes in Water Surface Extents and Lake Surface Temperatures Using Google Earth Engine for Lakes Region, Türkiye. *ISPRS International Journal of Geo-Information*.; 11(7):407

Arekhi, M., Goksel, C., Balik Sanli, F., & Senel, G. (2019). Comparative evaluation of the spectral and spatial consistency of Sentinel-2 and Landsat-8 OLI data for Igneada longos forest. ISPRS International Journal of Geo-Information, 8(2), 56.

Dervisoglu A. Investigation of Long and Short-Term Water Surface Area Changes in Coastal Ramsar Sites in Turkey with Google Earth Engine. *ISPRS International Journal of Geo-Information*. 2022; 11(1):46

Demir Yetis, A., Selek, Z., Seckin, G. et al. Water quality of Mediterranean coastal plains: conservation implications from the Akyatan Lagoon, Turkey. Environ Monit Assess 186, 7631–7642 (2014). https://doi.org/10.1007/s10661-014-3954-8

Dörnhöfer K., Oppelt N., 2016. Remote sensing for lake research and monitoring – Recent advances, Ecological Indicators, 64, 105-122.

FAO 2015, Cataudella S., Crosetti D., Massa F. (eds). Mediterranean coastal lagoons: sustainable management and interactions among aquaculture, capture fisheries and the environment Studies and Reviews. General Fisheries Commission for the Mediterranean. No 95. Rome.

Gündoğdu S, Çevik C. 2019. Mediterranean dirty edge: High level of meso and macroplastics pollution on the Turkish coast, Environmental Pollution, 255, 3, 113351

Firatli, E., Dervisoglu, A., Yagmur, N. et al. (2022) Spatio-temporal assessment of natural lakes in Turkey. Earth Sci Inform 15, 951–964

Fisher, A., Flood, N., & Danaher, T. (2016). Comparing Landsat water index methods for automated water classification in eastern Australia. Remote Sensing of Environment, 175, 167-182.

Gorelick, N., Hancher, M., Dixon, M., Ilyushchenko, S., Thau, D., & Moore, R. (2017). Google Earth Engine: Planetary-scale geospatial analysis for everyone. Remote sensing of Environment, 202, 18-27.

Jiang, W., Ni, Y., Pang, Z., Li, X., Ju, H., He, G., ... & Qin, X. (2021). An effective water body extraction method with new water index for sentinel-2 imagery. Water, 13(12), 1647.

Khalid HW, Hhalil RMZ, Qureshi A., 2021. Evaluating spectral indices for water bodies extraction in western Tibetan Plateau, The Egyptian J. of Remote Sensing and Space Sciences 24, 619–634

Laonamsai J, Julphunthong P, Saprathet T, Kimmany B, Ganchanasuragit T, Chomcheawchan P, Tomun N. Utilizing NDWI, MNDWI, SAVI, WRI, and AWEI for Estimating Erosion and Deposition in Ping River in Thailand. *Hydrology*. 2023; 10(3):70.

Ma, S., Zhou, Y., Gowda, P. H., Dong, J., Zhang, G., Kakani, V. G., ... & Jiang, W. (2019). Application of the water-related spectral reflectance indices: A review. Ecological indicators, 98, 68-79.

McFeeters, S. K. (1996). The use of the Normalized Difference Water Index (NDWI) in the delineation of open water features. International journal of remote sensing, 17(7), 1425-1432.

Nie, Z., Chan, K. K. Y., & Xu, B. (2019). Preliminary Evaluation of the Consistency of Landsat 8 and Sentinel-2 Time Series Products in An Urban Area—An Example in Beijing, China. Remote Sensing, 11(24), 2957.

R Core Team, R. (2013). R: A language and environment for statistical computing.

RAMSAR (2016) An Introduction to the Ramsar Convention on Wetlands, 7th edn. Ramsar Convention Secretariat, Gland, Switzerland. https://www.ramsar.org/sites/default/files/documents/library/handbook1_5ed_introductiontoconvention_final_e.pdf. Accessed 15 Apr 2024

Senel G., Dogru AO., Goksel C., 2020. Exploring the potential of Landsat-8 OLI and Sentinel-2 MSI data for mapping and monitoring Enez Dalyan Lagoon, Desalination and Water Treatment, 177, 330-337.

Tan, J., Chen, M., Ao, C., Zhao, G., Lei, G., Tang, Y., ... & Li, A. (2022). Inducing flooding index for vegetation mapping in water-land ecotone with Sentinel-1 & Sentinel-2 images: A case study in Dongting Lake, China. Ecological Indicators, 144, 109448.

Xu, H. (2006). Modification of normalised difference water index (NDWI) to enhance open water features in remotely sensed imagery. International journal of remote sensing, 27(14), 3025-3033.

Yilmaz, O.S. Spatiotemporal statistical analysis of water area changes with climatic variables using Google Earth Engine for Lakes Region in Türkiye. Environ Monit Assess 195, 735 (2023).

Zhai K., Wu X, Qin Y., Du P., 2015. Comparison of surface water extraction performances of different classic water indices using OLI and TM imageries in different situations, Geo-spatial Information Science, 18, 1, 32-42.

INTERNATIONAL SYMPOSIUM ON
APPLIED
GEOINFORMATICS
9-10 May 2024 · Wrocław/Poland

*International Symposium on Applied Geoinformatics (ISAG2024)*

# FOREST FIRE ANALYSIS WITH LANDSAT SATELLITE IMAGES: 2023 GÖKÇEADA ISLAND FOREST FIRE (TÜRKİYE)

Deniz Bitek[1]*, Füsun Balık Şanlı[2], R. Cüneyt Erenoğlu[3]

[1] Planning and Risk Reduction Department, Provincial Disaster and Emergency Directorate, Edirne, Türkiye; deniz.bitek@afad.gov.tr; **ORCID 0000-0002-9830-6897**,
**[2]** Geomatic Engineering Department, Yildiz Technical University, Istanbul, Türkiye; fbalik@yildiz.edu.tr; **ORCID 0000-0003-1243-8299**,
[3] Faculty of Engineering, Department of Geomatics Engineering, Çanakkale 18 Mart University, Çanakkale, Türkiye; ceren@comu.edu.tr; **ORCID 0000-0002-8212-8379**
* Corresponding Author

## Abstract

Forest fires represent a significant environmental concern, ranking among the most destructive disasters worldwide. The increase in temperature resulting from climate change has contributed to the rise in the frequency of heat waves, which in turn hasled to an increase in forest fires. In Turkiye, the incidence of forest fires has been increasing in recent years due to the natural causes. Geographic Information Systems (GIS) and Remote Sensing (RS) techniques are frequently employed in monitoring, imaging, and analyzing these fires. This paper presents an analysis of a forest fire that occurred on the island of Gökçeada in the province of Çanakkale on 16 July 2023. The burned areas were identified and burn maps were created using Landsat satellite images before and after the fire. The Differenced Normalized Burn Ratio (dNBR) and the Normalized Difference Vegetation Index (dNDVI) indices were used in this analysis. The impact area of the forest fire was calculated as 336.51 ha (hectares). The accuracy of the areas calculated using the indices was evaluated. Four different statistical values were used in the evaluation. The result demonstrated that the dNBR index reached higher statistical values in determining the areas affected by fire.

**Keywords:** *Forest fire, Gökçeada, satellite imagery, remote sensing, spectral indices*

## Introduction/Background

Forest fires reperesents a significant form of natural disaster worldwide. They can occur naturally or can be caused by humans (Kavlak et al., 2020). These fires have adverse effects on natural ecosystems and can also cause issues in economic and social life (Sabuncu and Özener, 2019). In forest fires, the detection of burned forest areas is carried out using RS and GIS techniques rather than ground measurements. These techniques offer significant advantages, especially in detecting, analysing and interpreting the areas damaged after a fire (Pacheco et al., 2021). The Landsat satellite series is the first and longest active imaging system with medium spatial resolution, and its images are frequently used for monitoring and analysis. Landsat-8 satellite imagery has a temporal resolution of 16 days and a spatial resolution of 30m (Url-2). Many studies have been conducted on the detection, monitoring and analysis of forest fires utilising images from these satellite systems (Teodoro and Amaral, 2019; Barbazo Castillo et al., 2020; Kurnaz et al., 2020; Ngadze et al., 2020; Pacheco et al., 2021).

The objective of this study was to identify the areas affected by the fire that began at 16.15 on 15.07.2023 in the vicinity of Marmaros in Dereköy village, Gökçeada district, Çanakkale province. The extent of the burned areas was determined by utilizing Landsat-8 OLI satellite images, in conjuction with Normalized Burn Ratio (NBR) and NDVI remote sensing indices. The results were analysed and evaluated using ArcMap.

## Materials and Methods

### Study Area

Gökçeada is a district of Çanakkale province located at the western tip of Turkey. It is the largest island in Turkiye with an area of 285 km². It is situated on the Anatolian continental shelf and lies in the northern Aegean Sea. The island has a strategic importance due to its location, and has a district center and nine villages. (Kahraman, 2005; Özdemir, 2012). The Marmaros region of Dereköy village, located at the western end of the island, was selected as the study area (Figure 1).

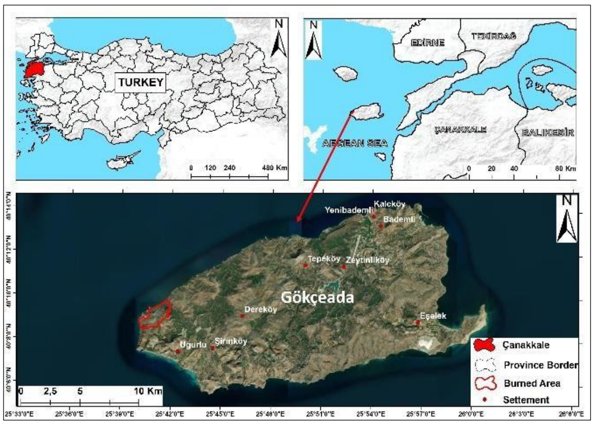

**Figure 1**. General view of the study area

### Data Set

Landsat 8 OLI satellite imagery data sourced from the US Geological Survey (USGS), formed the basis of analysis in this study. The Landsat-8 satellite is instrumental in monitoring and analyzing natural resources, including water bodies and vegetative areas. Furthermore, it offers data to users at no cost. With an orbital cycle spanning 16 days and an orbital inclination of 98.2 degrees, the Landsat-8 satellite supplies imagery captured by its Operational Land Imager (OLI) and Thermal Infrared Sensor (TIRS) (Turoğlu, 2020).The Landsat-8 images utilized in this study encompasses four bands in the visible region, one band in the near infrared (NIR), two bands in the shortwave infrared (SWIR), two thermal bands (TIRS), one Cirrus band and one panchromatic image as deteailed in Table 1 (Konkathi and Shetyt, 2021). The data set obtained free of charge from the US Geological Survey (USGS). For the analysis, image pairs from Landsat-8 dated June 30, 2023, and July 24,2023, were employed. The former reperesents data piriror to a forest fire event, while the letter corresponds imagery captured immediately after the fire.

**Table 1**. Propertiesof Landsat-8 satellite.

| Spectral Bands | Central Waveleng (nm) | Spatial Resolution (m) |
|---|---|---|
| 1 (Coastral Aerosol) | 0.43-0.45 | 30 |
| 2 (Blue) | 0.45-0.51 | 30 |
| 3 (Green) | 0.53-0.59 | 30 |
| 4 (Red) | 0.64-0.67 | 30 |
| 5 (NIR) | 0.85-0.88 | 30 |
| 6 (SWIR1) | 1.57-1.65 | 30 |
| 7 (SWIR2) | 2.11-2.29 | 30 |
| 8 (Panchromatic) | 0.50-0.68 | 30 |
| 9 (Sirrus) | 1.36-1.38 | 15 |
| 10 (TIRS) 1 | 10.6-11.19 | 100 |
| 11 (TIRS) 2 | 11.5-12.51 | 100 |

### Methodology

The methodology employed in this study aimed to assess changes in vegetation indices before and after the forest fire and followed by mapping the burned areas post-fire. To achieve this, atmospheric and geometric correction processes were applied to satellite images to ensure acurate surface detection of the forest fire affected areas. Pre-fire and post-fire NBR and NDVI indices were calculated from the satellite images. Susequently, dNBR and dNDVI were computed to quantify the changes in vegetation cover due to the fire.

Normalized Burning Ratio (NBR) shows that an unburned and healthy plant exhibits high reflectance in the near-infrared (NIR) wave range and low reflectance in the shortwave infrared (SWIR) wave range. Burned areas, on the otherhand, tipically display relatively low reflectance in the near-infrared and high reflectance in the shortwave infrared band. A high NBR value usually indicates healthy vegetation, while a low value indicates bare ground and recently burned areas. The NBR index ranges between -1 and 1 with values approaching 1 indicate increased severity of burning (Roy et al., 2006). The difference between pre-fire and post-fire NBR is expressed as Difference Normalized Burn Rate (dNBR) to identify recently burned areas and distinguish them from bare soil and other non-vegetated areas (Bitek and Erenoğlu, 2022). The Normalized Difference Vegetation Index (NDVI) developed by Rouse (Rouse et al., 1974) is used to measure the change in vegetation cover (Bar et al., 2020). Healthy vegetation reflects more near-infrared (NIR) and green light than other wavelengths, due to its chlorophyll content. However, it absorbs more red and blue waves. NDVI measures the density of vegetation by comparing the difference between these bands. The NDVI index typically

**Table 2.** Formulas of spectral burned indices.

| Index | Formula |
|---|---|
| NBR | (NIR-SWIR) / (NIR+SWIR) = (B5−B7) / (B5+B7) |
| dNBR | NBRpre-fire – NBRpost-fire |
| NDVI | (NIR-RED) / (NIR+RED) = (B5−B4) / (B5+B4) |
| dNDVI | NDVIpre-fire – NDVIpost-fire |

**Table 3.** Burn severity classification of dNBR and dNDVI.

| Severity Level | dNBR Values | Severity Level | dNDVI Values |
|---|---|---|---|
| Unburned | < 0.1 | Unburned | < 0.07 |
| Low | 0.1 - 0.26 | Low | 0.1 - 0.20 |
| Moderate | 0.27 - 0.43 | Moderate | 0.20 - 0.33 |
| High | 0.44 - 0.65 | High | 0.33- 0.44 |
| Very High | > 0.66 | Very High | > 0.45 |

ranges between -1and 1. Values approaching 1 indicate that the healthy vegetation value increases (Yılmaz et al., 2022). Formulas of spectral burned indices are provided in Table 2. The classifications in Table 3 were used for the interpretation and assessment of burned areas (Key and Benson, 2006), as well as for the interpretation of dNDVI values (Morante-Carballo et al., 2022; Yılmaz et al., 2023).

## Results and Discussion

In this study, Landsat-8 satellite images were used to delineate the areas affected by the forest fire in the Gökçeada district of Çanakkale in July 2023. Analysis of the NBR and NDVI index values in the pre-and and postfire images revealed a range between -1 and +1. Prior to the fire, the NBR index values ranged from -0.15 to0.71 while post-fire values shifted towards -0.36 to 0.64. Conversely, NDVI values were observed to be approximately +1 before the fire, but declined post-fire. Specifically, NDVI index values ranged from 0.01-0.81 before the fire and decreased to 0.01-0.74 after the fire.

The impact of the forest fire and its extent within the region are depicted in Figure 2. The illustrated maps are containing two different indices obtained with Landsat satellite images. These maps are categorized into the five different classes based on the severity of burning.

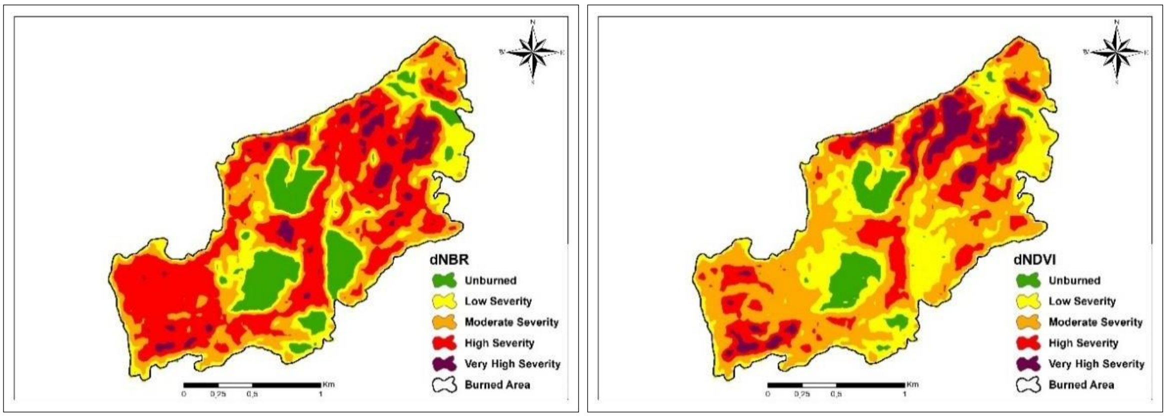

**Figure 2.** Burning severity maps prepared according to dNBR and dNDVI indices.

The forest fire that occurred in Gökçeada affected a total area of 336.51 ha. According to the Landsat-8 dNBR index, the total burned area was 296.28 ha, accounting for 88.04% of the affected area. Within the fire-affected area, 40.23 ha (11.96%) remained unaffected by the fire, while areas with low burning intensity covered 61.74 ha (18.35%), areas with medium burning intensity covered 70.11 ha (20.83%), areas with high burning intensity covered 124.11 ha (36.88%), and areas with very high burning intensity covered 40.32 ha (11.98%). According to the dNDVI index, the burned areas amounted to 305.82 ha, with an impact rate of 90.88%. Unburned areas accounted for 30.69 ha corresponding to 9.12% of the total area. A comparison of the classification values of these two indices reveals that areas classified as high and very high burning intensity cover more area according to the dNBR index, while the areas with low and medium-burning intensity cover more area according to the dNDVI values. In this study, the total area of burnt areas calculated by the dNDVI index exceeds that calculated by the dNBR index. The results obtained based on the classification values are presented in Table 4.

**Table 4.** Calculations of burned area and ratio.

| | | dNBR | | dNDVI | |
|---|---|---|---|---|---|
| **Region** | **Severity Level** | **Area (ha)** | **Ratio (%)** | **Area (ha)** | **Ratio (%)** |
| Çanakkale Gökçeada | Unburned | 40.23 | 11.96 | 30.69 | 9.12 |
| | Low Severity | 61.74 | 18.35 | 102.69 | 30.52 |
| | Moderate Severity | 70.11 | 20.83 | 147.15 | 43.73 |
| | High Severity | 124.11 | 36.88 | 39.69 | 11.79 |
| | Very High Severity | 40.32 | 11.98 | 16.29 | 4.84 |
| Total Burned Area | | **296.28** | **88.04** | **305.82** | **90.88** |
| Total | | **336.51** | **100** | **336.51** | **100** |

When vegetation health is analyzed with dNDVI values, almost all of the vegetation that was healthy before the fire in the area affected by the fire was impacted and classified as being poor health. While the area covered by healthy and very healthy vegetation was 305.73 ha (90.86%) before the fire, it decreased to 59.49 ha (17.67%) after the fire. Vegetation classified as in poor health was 30.78 ha before the fire and increased to 277.02 ha after the fire. Very healthy vegetation was 49.05 ha before the fire and almost all of it was affected by the fire, resulting in a post-fire coverage of 1.53 ha. The vegetation status determined by NDVI analysis is depicted in Figure 3.

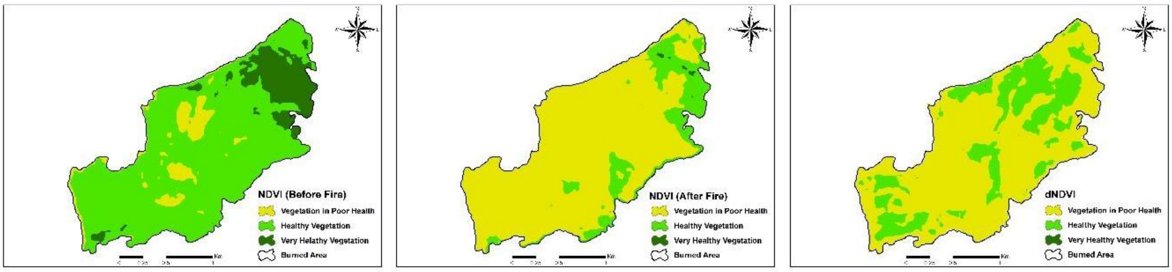

**Figure 3.** Vegetation Status with NDVI and dNDVI Index (Pre-Fire and Post-Fire NDVI values and dNDVI)

The accuracy assessment of the burn severity maps created using dNBR and dNDVI indices was obtained by calculating error matrices. The accuracy assessment and statistical values of the study are presented in Table 5. For the accuracy assessment, random points and 100 control points were used. The accuracy assessment was carried out using the high-resolution Sentinel-2 satellite image dated 24.07.2023. Stataistical values including overall accuracy, kappa, Recall, and F-1 Score were calculated. According to the results obtained, it was observed that the statistical values of the dNBR index were higher than those of the dNDVI index values. The kappa values were calculated as 82.65% for the dNBR index and 71.77% for the dNDVI index. Although the overall accuracy, Recall, and F-1 score values were close to each other, they were higher for the dNBR index. In the context of this study, it can be concluded that the dNBR index gives more successful results in identifying burned areas. This observation is supported by several studies in the literature (Mallinis et al., 2018; Dindaroğlu et al., 2021; Morresi et al., 2022; Qarallah et al., 2022; Gürbüz, 2023).

**Table 5.** Accuracy assessment of burn intensity maps.

| Gökçeada July Landsat-8 | Overall Accuracy (OA) | Kappa | Recall | F-1 Score (FS) |
|---|---|---|---|---|
| dNBR | 0.9485 | 0.8265 | 0.9390 | 0.9685 |
| dNDVI | 0.9278 | 0.7177 | 0.9294 | 0.9575 |

## Conclusion

This study used dNBR and dNDVI indices of Landsat-8 satellite imagery provided free of charge by the USGS, to identify areas affacted by forest fires. The performance of the indices was assessed using error matrices. Burn severity classification for the indices within the fire-area was catagorized into five classes. The burned areas determined by the dNBR index covered 296.28 ha, whereas those identified by the dNDVI covered 305.82 ha. A comparison of the classification values of these two indices revealed areas classified as having high and very high burning severity according to the dNBR index covered more area, while areas with low and medium-burning severity covered more area according to the dNDVI values. Despite the dNDVI index indicating larger burned areas, all statistical values obtained from the accuracy analysis using error matrices demonstrated that the dNBR index yielded higher values. Specifically, kappa statistical values were calculated as 82.65% for the dNBR index and 71.77% for the dNDVI index.

The dNDVI index, being a reflection of vegetation change, tends to produce various results depending on the factors such as vegetation condition, location, and density as evidence by various studies. It can serve as a valuable tool for detecting vegetation changes, particularly in natural rehabilitation processes following events like forest fires, and for monitoring recovery efforts. The European Forest Fire Information System (EFFIS) continuously provides data on forest fires, reporting the burned area in the forest fire in Gökçeada district of Çanakkale province is 287 ha. Comparing this data with our study's result, it is evident that both indices exhibited areal consistency rates exceeding 90%.

GIS-based methods and satellite-based remote sensing methods play crucial roles in detecting forest fires, particularly in emergency situsations where on-site measurements are impractical or spatial control is challenging. Numerious analyses indicate these methods can yield successful results without the necessity for extensive fieldwork. Morover they are often more effective in terms of time and cost compared to traditional analysis methods reliant on field studies.

## References

Bar, S., Parida, B. R., & Pandey, A. C. (2020). Landsat-8 and Sentinel-2 based Forest fire burn area mapping using machine learning algorithms on GEE cloud platform over Uttarakhand, Western Himalaya. *Remote Sensing Applications: Society and Environment*, *18*, 100324.

Barboza Castillo, E., Turpo Cayo, E. Y., de Almeida, C. M., Salas López, R., Rojas Briceño, N. B., Silva López, J. O., ... & Espinoza-Villar, R. (2020). Monitoring wildfires in the northeastern Peruvian amazon using landsat-8 and sentinel-2 imagery in the GEE platform. *ISPRS International Journal of Geo-Information*, *9*(10), 564.

Bitek, D., & Erenoğlu, R. C. (2022). Forest Fire Analysis with Sentinel-2 Satellite Imagery: The Case of Mati (Greece) in 2018. *Academic Platform Journal of Natural Hazards and Disaster Management*, *3*(2), 85-98.

Dindaroglu, T., Babur, E., Yakupoglu, T., Rodrigo-Comino, J., & Cerda, A. (2021). Evaluation of geomorphometric characteristics and soil properties after a wildfire using Sentinel-2 MSI imagery for future fire-safe forest. *Fire safety journal*, *122*, 103318.

Gürbüz, E. (2023). Uzaktan Algılama ile Yangın Şiddeti Belirlenmesinde Farklı İndekslerin Karşılaştırılması. *Harita Dergisi*, *170*, 8-22.
Kahraman, S. Ö. (2005). Gökçeada'da göçlerin nüfus gelişimi ve değişimi üzerine etkileri. *Coğrafi Bilimler Dergisi*, *3*(2), 39-54.
Kavlak, M. Ö., Kurtipek, A. and Çabuk, S. N. (2020). Coğrafi Bilgi Sistemleri ile orman yangını risk haritası oluşturulması: Ören örneği. *Resilience*, *4*(1), 33-54.

Key, C. H., & Benson, N. C. (2006). Landscape assessment (LA). *FIREMON: Fire effects monitoring and inventory system*, *164*, LA-1.

Konkathi, P., & Shetty, A. (2021). Inter comparison of post-fire burn severity indices of Landsat-8 and Sentinel-2 imagery using Google Earth Engine. *Earth Science Informatics*, *14*, 645-653.

Kurnaz, B., Bayik, C., & Abdikan, S. (2020). Forest fire area detection by using Landsat-8 and Sentinel-2 satellite images: A case study in Mugla, Turkey.

Mallinis, G., Mitsopoulos, I., & Chrysafi, I. (2018). Evaluating and comparing Sentinel 2A and Landsat-8 Operational Land Imager (OLI) spectral indices for estimating fire severity in a Mediterranean pine ecosystem of Greece. *GIScience & Remote Sensing*, *55*(1), 1-18.

Morante-Carballo, F., Bravo-Montero, L., Carrión-Mero, P., Velastegui-Montoya, A., & Berrezueta, E. (2022). Forest fire assessment using remote sensing to support the development of an action plan proposal in Ecuador. *Remote Sensing*, *14*(8), 1783.

Morresi, D., Marzano, R., Lingua, E., Motta, R., & Garbarino, M. (2022). Mapping burn severity in the western Italian Alps through phenologically coherent reflectance composites derived from Sentinel-2 imagery. *Remote Sensing of Environment*, *269*, 112800.

Ngadze, F., Mpakairi, K. S., Kavhu, B., Ndaimani, H., & Maremba, M. S. (2020). Exploring the utility of Sentinel-2 MSI and Landsat 8 OLI in burned area mapping for a heterogenous savannah landscape. *PLoS One*, *15*(5), e0232962.

Özdemir, S. (2012). Kırsal kalkınmada kırsal turizmden yararlanma olanakları: Gökçeada örneği. *Karamanoğlu Mehmetbey Üniversitesi Sosyal ve Ekonomik Araştırmalar Dergisi*, *2012*(2), 19-21.

Pacheco, A. D. P., Junior, J. A. D. S., Ruiz-Armenteros, A. M., & Henriques, R. F. F. (2021). Assessment of k-nearest neighbor and random forest classifiers for mapping forest fire areas in central Portugal using landsat-8, sentinel-2, and terra imagery. *Remote Sensing*, *13*(7), 1345.

Qarallah, B., Othman, Y. A., Al-Ajlouni, M., Alheyari, H. A., & Qoqazeh, B. A. A. (2022). Assessment of Small-Extent Forest Fires in Semi-Arid Environment in Jordan Using Sentinel-2 and Landsat Sensors Data. *Forests*, *14*(1), 41.

Rouse, J.W., Jr.; Haas, R.H.; Schell, J.A.; Deering, D.W. (1974). Monitoring Vegetation Systems in the Great Plains with Erts. NASA Spec. Publ. 351, 309.

Roy, D. P., Boschetti, L., & Trigg, S. N. (2006). Remote sensing of fire severity: assessing the performance of the normalized burn ratio. *IEEE Geoscience and remote sensing letters*, *3*(1), 112-116.

Sabuncu, A., & Özener, H. (2019). Uzaktan algılama teknikleri ile yanmış alanların tespiti: İzmir Seferihisar orman yangını örneği. *Doğal Afetler ve Çevre Dergisi*, *5*(2), 317-326.

Teodoro, A., & Amaral, A. (2019). A statistical and spatial analysis of Portuguese forest fires in summer 2016 considering Landsat 8 and Sentinel 2A data. *Environments*, *6*(3), 36.

Turoğlu, H. (2020). Coğrafi Bilgi Sistemlerinin Temel Esasları. *İstanbul: Çantay Yayınları*.

Yilmaz, O. S., Acar, U., Sanli, F. B., Gulgen, F., & Ates, A. M. (2023). Mapping burn severity and monitoring CO content in Türkiye's 2021 wildfires, using Sentinel-2 and Sentinel-5P satellite data on the GEE platform. *Earth science informatics*, *16*(1), 221-240.

INTERNATIONAL SYMPOSIUM ON
APPLIED
GEOINFORMATICS
9-10 May 2024 · Wrocław/Poland

*International Symposium on Applied Geoinformatics (ISAG2024)*

# Calculating The Carbon Footprint of Industrial Induction Motors Via Life Cycle Analysis

Erdem Coşkun[1], Ahmet Yiğit Arabul[2]*

[1] WAT Motor Company, R&D Department, Tekirdag, Türkiye
erdem.coskun@wat.com.tr
[2] Yildiz Technical University, Department of Electrical Engineering, Istanbul, Türkiye;
arabul@yildiz.edu.com.tr

* Corresponding Author

## Abstract

This paper presents an environmental analysis and life cycle costs of induction motors. Focusing exceptionally on consumption is no longer sufficient, energy savings initiatives must now account for all life cycle assessment (LCA), including from raw material production, usage, transportation to end-of-life. The analysis was carried out according to the Energy-Using Product Directive (EuP 2005/32/EC) and following the Methodology for the Eco-Design of Energy-Using Products (MEEUP methodology). Although electric motors are widely used, there is limited research on their life cycle carbon footprint. This study aims to provide valuable information to help people make the right decisions about the use of electric motors in different sectors by examining the carbon footprints, motor components and features of electric motors. It is possible to design the motor design with different combinations to meet the same power requirements. At this stage, there are many components that affect the design, from the lamination diameter to the thickness of the electrical sheet, from the quality of the enamel you use to the diameter of the wire. These components directly affect the consumption of active materials and can therefore be directly attributed to the carbon footprint. This study examines the impact of creating products that are more compact and have a lower carbon footprint through optimal design and LCA-oriented studies. This study also aims to identify ways to reduce material usage without compromising performance by focusing on different design factors. This approach not only helps to reduce the carbon footprint of all motors, not just induction motors, but also increases their sustainability; these findings can lead manufacturers to make more environmentally friendly design choices.

**Keywords:** *Electrical motors, Industrial induction motors, Life Cycle Analysis, Carbon footprint, Climate change*

## Introduction

The increase in $CO_2$ emissions in global warming is directly related to the increase in energy consumption. Use of energy efficient motors or strategies that reduce overall energy consumption (such as motors with increased power density, targeting higher energy efficiency, compact motors, PM motor or SynRM motors). Studies are carrying out to increase the efficiency of the process. For this reason, efforts to reduce energy consumption are critical elements for sustainability discourses and carbon footprint reduction today (Singh et al, 2019)

Footprint concept was first used in 1979 and carbon footprint products were added to the activity in 1999. Greenhouse gases can be classified according to their amounts as water vapor, carbohydrates ($CO_2$), methane ($CH_4$), nitrogen protoxin ($N_2O$) and ozone ($O_3$). Since carbon dioxide is the second most important gas released into the market, all other gases are measured in kilograms of carbohydrates (kg-eq-$CO_2$) and normalized by the separation of $CO_2$. This means that increasing the amount of gas will increase the value of the earth's surface. Programming that compares all raw materials, sub-representations, production, transportation, installation, use and recycling energies of a product or service and the $CO_2$ equivalent of their emission values is called carbon footprint programming. A programming approach should be created to program the value of $CO_2$ emissions caused by the product or service throughout its life cycle.

The EIB Group has witnessed carbon emissions increasing in many areas since 2021. The COVID-19 pandemic led to a significant drop in emissions in 2020 and 2021. This impact no longer exists as the restrictions expire in 2022, so the assessment of the carbon footprint becomes increasingly important day-by-day (Carbon Footprint Report, 2022).

The European Commission has published a package of recommendations to reduce greenhouse gas emissions by 55 percent by 2030. Among the products regulated under 17 headings to achieve this goal, the most important product in terms of the electrical energy consumed is industrial electric motors within the scope of IEC 60034-1 (Directive of the European Parliament and of the Council on Energy Efficiency, 2021).

According to statistical data published by the Ministry of Science, Industry and Technology, General Directorate of Efficiency, 36% of the total electrical energy consumed in our country and 67% in industry and infrastructures are used by industrial electric motors. In addition to sustainability targets, due to rising energy costs at unprecedented levels in history, it has become very important to replace the existing motor with more efficient motors in the same segment.

With growing concerns about environmental sustainability and climate change, understanding the environmental impact of electric motors is critical. Electric motors are widely used in many applications, from household appliances to industrial machinery and contribute significantly to global energy consumption. This study examines the carbon footprint of electric motors through a life cycle analysis.

## Methodology

The LCA environmental operation of the electric motor is shaped by the selection of energy efficiency, power polarity combination and its relationship with emission values. Starting with electrical modeling in the first step, the motor is assembled from a series of materials (steel, copper, aluminum, plastic and insulation materials, in the case of induction motors). At this stage, various material design processes such as pressing work, metal casting, enameled wire, winding process, assembly process and painting should take place. Another stage of the LCA study requires geometric modeling of the electric motor to determine all the parameters of each of the motor parts. All geometric dimensions of the motor are derived from two main parameters, the air gap diameter and the active length of the magnetic core, using real data from the manufacturer and the magnetic properties of the stator sheets (Rassolkin et al, 2016).

**Table 1.** Bill of materials, selected critical components

| Selected parts | Raw Material |
|---|---|
| Motor Body | Aluminium |
| ND Endshield | Aluminium |
| NDE Endshield | Aluminium |
| Rotor Lamination | Electrical Steel |
| Stator Lamination | Electrical Steel |
| Rotor Al | Aluminium |
| Enamelled Wire | Copper |
| Foots | Aluminium |
| Terminal Box | Aluminium |
| Terminal Box Cover | Aluminium |
| Fan | Plastic |
| Fan Cover | Steel |
| Fan Cover | Steel |

The second stage of LCA is to assess the impacts of the motor use phase, which are related to the operating energy losses. These losses are tightly connected with the cumulative operating time, the actual working conditions and total lifetime of motors (Boughanmi et al, 2012).

**Table 2.** Usage Phase Data

| Variable | Value |
|---|---|
| Lifetime years | 10 |
| Operating hours | 4350 |

The MEEUP methodology provides an MS Excel spreadsheet to estimate environmental impact (European Commission, 2005). In the first stage, data is collected (including materials, energy use and economic data). The model then transforms these inputs into measurable environmental impacts presented in Table I and Table II. With the references taken from the material matching table on the DEFRA side, the values determined in the relevant electrical motor parameters are matched and the equivalent carbon emission value is reached for each motors.

**Results and Discussion**

Due to the platforms used in high quantities, 90 frame platforms and 2.2 kW and 1.5 kW features were chosen. Since the regulation definition is IE3, this efficiency value was chosen in the first stage, since there has been a significant use of motors with lower efficiencies in the market, motor references of the IE1 efficiency class were compared. The increase in the motor efficiency level is directly positive effective in improving the energy consumption, thus reducing the operating costs of the manufacturer, increasing its system efficiency and reducing the carbon footprint. Calculated assuming that the motor life is 10 years and operated for an average of 4350 hours per year.

**Table 3.** Efficiency, power, total kWh carbon emission values

| Power | Efficiency | Pole | Total kWh -Causing Carbon Emission- |
|---|---|---|---|
| 2.2 kW | IE3 | 2P | 111408.61 |
| 1.5 kW | IE3 | 4P | 76494.72 |
| 2.2 kW | IE1 | 2P | 120075.28 |
| 1.5 kW | IE1 | 4P | 84520.72 |

**Table 4.** $CO_2$ eq. - Efficiency, power, total kWh

| Efficiency | Total kWh -Causing Carbon Emission- | Emission Factor 6 (ton/TJ) | Emission $CO_2$ (ton) |
|---|---|---|---|
| IE3-2.2 kW | 111408.61 | 0.25 | 28.098.84 |
| IE3-1.5 kW | 76494.72 | 0.25 | 19.293.06 |
| IE1-2.2 kW | 120075.28 | 0.25 | 30.284.70 |
| IE1-1.5 kW | 84520.72 | 0.25 | 21.317.33 |

IEA emission factors are detailed for methane and nitrogen, while DEFRA emission factors are given in carbon dioxide equivalent. DEFRA has closed free access to greenhouse gas emissions from world electricity consumption as of 2022. Calculation using the average of Europe's emission factors. EF is available for free. It says on the page that TR's emissions are higher, but there isn’t share additional information.

Material use conversion factors are used to report the consumption of supplied materials by origin (i.e. primary material or recycled materials). For primary materials, these factors include materials for extraction, primary processing, manufacturing, and transportation to the point of sale, not materials in use. For secondary materials, factors include sorting, processing, production and transportation to the point of sale, not the materials used. These factors are useful for reporting efficiencies gained through reducing material sourcing or the benefit of sourcing items that are the product of a previous recycling process. In this process, the main components that make up electric motors are focused on; copper wires, electrical sheets are evaluated as steel raw materials, aluminum materials used in covers, bodies and rotors, plastic materials and chemicals added for electrical-mechanical insulation are the basic components kept in this context. The raw material weights and carbon footprint effects of selected motors regarding DEFRA -Materials Use references were analyzed.

**Table 5.** IE3 efficiency, 90 frame, 2 Pole, 2.2 kW, old platform

| Material Types | Total Raw Material | Emission Factor (kg $CO_2$ e/ton) | Equivalent $CO_2$ |
|---|---|---|---|
| Copper | 2.47 | 4018.002952 | 9.93 |
| Steel | 12.30 | 4018.002952 | 49.42 |
| Plastic | 0.04 | 3116.291564 | 0.12 |
| Aluminum | 3.72 | 5583.938203 | 20.79 |
| Total | | | 80.27 |

**Table 6.** IE3 efficiency, 90 frame, 2 Pole, 2.2 kW, new platform

| Material Types | Total Raw Material | Emission Factor (kg $CO_2$ e/ton) | Equivalent $CO_2$ |
|---|---|---|---|
| Copper | 2.25 | 4018.002952 | 9.04 |
| Steel | 9.41 | 4018.002952 | 37.81 |
| Plastic | 0.07 | 3116.291564 | 0.20 |
| Aluminum | 2.57 | 5583.938203 | 14.37 |
| Total | | | 61.43 |

When we compared old and new two platforms are examined in the table, which emphasizes the importance of design in motors with equivalent energy efficiency. In this table, it can be seen that the motors designed with improvement in active material consumption meet the same requirements in high power density, while a significant improvement can be achieved in their carbon footprint.

**Table 7.** IE3 efficiency, 90 frame, 4 Pole, 1.5 kW, old platform

| Material Types | Total Raw Material | Emission Factor (kg $CO_2$ e/ton) | Equivalent $CO_2$ |
|---|---|---|---|
| Copper | 1.99 | 4018.002952 | 8.00 |
| Steel | 10.01 | 4018.002952 | 40.24 |
| Plastic | 0.03 | 3116.291564 | 0.10 |
| Aluminum | 3.51 | 5583.938203 | 19.60 |
| Total | | | 67.94 |

**Table 8.** IE3 efficiency, 90 frame, 4 Pole, 1.5 kW, new platform

| Material Types | Total Raw Material | Emission Factor (kg $CO_2$ e/ton) | Equivalent $CO_2$ |
|---|---|---|---|
| Copper | 2.20 | 4018.002952 | 8.84 |
| Steel | 8.60 | 4018.002952 | 34.55 |
| Plastic | 0.07 | 3116.291564 | 0.20 |
| Aluminum | 2.19 | 5583.938203 | 12.25 |
| Total | | | 55.85 |

Similarly, when a model with a different power-pole combination is examined, it appears the carbon footprint improves with better results that reduce active material consumption and provide the same efficiency and performance requirements. When you add components such as acceptance of routine production material transportation processes, production processes and usage numbers, it emerges as a very critical element that these companies should pay attention to for their sustainability discourse and carbon footprint targets.

## Conclusion

Applying the LCA approach to electric motors and using it to evaluate environmental impacts throughout the entire life cycle provides benefits and awareness. Each stage of the electric motor's life cycle has a different impact on the environmental impact. Just as it is important to stay within the limits set by standards and regulations during the design phase of the electric motor, it is also very critical important to carry out the designs by considering the carbon footprint during the design phase.

In electrical modeling, basic criteria such as determination of sheet grade, lamination diameters, conductor properties to be used, insulation class, lamination diameter, stator package size are directly related to the active material consumption used and therefore the carbon footprint values in the production of these raw materials. In the mechanical construction principles after electrical modeling stage such as motor body wall thicknesses, body lengths, wall thicknesses for end shields ND-NDE side, the number and positioning of fins in motor cooling directly affect the carbon footprint of mechanical parts.

Improvements in energy efficiency have been observed to not only increase operational efficiency and reduce operating costs for manufacturers, but also have a critical impact on achieving carbon neutrality and sustainability goals. Considering the carbon footprint, it has been determined that two different motors designed with equivalent power, equivalent energy efficiency class and equivalent pole combinations can provide nearly 25% improvement.

## Acknowledgements

The authors would like to thank Yasemin Zaim from WAT Motor Company's Sustainability OHS & Environment CoE and Abdullah Polat from the R&D department for their support of this study.

## References

Boughanmi W., Manata J.P. and Roger D. (2012), Contribution of LCA approach to the choice of rotating electrical machines for environmental impact minimization, 20th International Conference on Electrical Machines, pp. 122–128.

Carbon Footprint Report (2022), Greenhouse gas emissions resulting from EIB Group internal operations

Directive of the European Parliament and of the Council on Energy Efficiency (2021), Brussels.

European Commission (2005), Methodology Study Eco design for Energy using Products (MEEUP), Brussels.

Rassolkin A., Orlova S., Vaimann T., Belahcen A. and Kallaste A. (2016), Environmental and Life Cycle Cost Analysis of a Synchronous Reluctance Machine, 57th International Scientific Conference on Power and Electrical Engineering of Riga Technical University.

Singh, G., Kumar T.C.A and Naikan V.N.A. (2019). Efficiency monitoring as a strategy for cost effective maintenance of induction motors for minimizing carbon emission and energy consumption Reliability Engineering & System Safety, 184, pp. 193-201.

INTERNATIONAL SYMPOSIUM ON
APPLIED
GEOINFORMATICS
9-10 May 2024 · Wrocław/Poland

*International Symposium on Applied Geoinformatics (ISAG2024)*

# Investigation of The Impact of Slot Geometry on Brushless DC Motors

Zafer Zerafil Güldal[1], Emin Tarık Kartal[2]*, Fatma Keskin Arabul[3]

[1] Yildiz Technical University, Faculty of Electric & Electronic Engineering, Department of Electrical Engineering, Istanbul, Türkiye; zafer.guldal@std.yildiz.edu.tr
[2] Yildiz Technical University, Faculty of Electric & Electronic Engineering, Department of Electrical Engineering, Istanbul, Türkiye; etkartal@yildiz.edu.tr; ORCID 0000-0002-4966-7258
[3] Yildiz Technical University, Faculty of Electric & Electronic Engineering, Department of Electrical Engineering, Istanbul, Türkiye; fkeskin@yildiz.edu.tr; ORCID 0000-0002-9573-8440
* Corresponding Author

## Abstract

Brushless Direct Current (BLDC) motors are widely used in various industries such as electrical household appliances, defense, automotive, robotics, and especially in the electric vehicle industry due to their quiet operation, longer lifetime, and less maintenance. These motors are recognized for their high efficiency, compact size, and suitability for high-power operations, making them environmentally friendly and advantageous. In the study focusing on a BLDC motor with an inner rotor, 10 poles, and 12 slots, where it's noted that slot areas are kept constant, four different stator slot geometries are investigated. Through two-dimensional analyses using ANSYS software, parameters including power, efficiency, torque, torque ripple, losses, current density, and magnetic flux distribution are evaluated. Comparative analysis reveals significant differences among the slot geometries (SGs), notably in terms of torque ripple and harmonic components. Type-4 has the highest output power, torque and efficiency, although it has the lowest performance in terms of torque ripple. Conversely, Type-1 has the lowest torque ripple but the efficiency and output power of this type are low. Harmonic analysis shows that with variations in SG there are significant differences in specific harmonic components that affect motor performance. The maximum current value which is the highest in Type-4 varies with slot structures. Moreover, electromagnetic torque profiles illustrate an increase in average torque with successive SGs, while torque ripple ranges from 22.7% to 28.4%. Further analysis using Fast Fourier Transform (FFT) reveals harmonic components in torque spectra, emphasizing the effect of slot geometry on motor performance. Overall, these findings underline the importance of slot design in optimizing BLDC motor efficiency and performance, reaffirm their environmental friendliness and competitive advantages in various industrial applications.

**Keywords:** Brushless Direct Current Motor, Machine Design, Finite Element Method, Fast Fourier Transform.

## Introduction

Today, Brushless Direct Current (BLDC) motors are widely used in many industries. Electrical household appliances, defense industry, automotive industry, robotic systems and electric vehicle industry are the leading ones. Among these, the electric vehicle industry is in a very important position in terms of BLDC motor usage (Uygun and Solmaz, 2015). One of the reasons why BLDC motors are frequently preferred is their quiet operation due to their low electrical and mechanical noise levels (Dam and Basak, 2023). BLDC motors are highly efficient, small in size and can be easily used in operations requiring high power and torque, making them a preferred choice (İmren and Birbir, 2021; Hanselman, 1994; Moghaddam, Mirzahosseini, and Farajzadeh, 2023). Other important advantages of BLDC motors are that they have a longer lifetime due to being brushless and less maintenance needs (Kim, Lee, and Um, 2008; Mujianto, Nizam, and Inayati, 2014). Although the purchase cost of BLDC motor is higher than other motors, maintenance cost is lower since they require less maintenance (Moghaddam, Mirzahosseini, and Farajzadeh, 2023). In addition to these advantages, other important reasons for use are the high torque density and torque-to-weight ratio. Although the fact that brushless DC motors are controlled with a driver seems to be a disadvantage, energy consumption is very low compared to other motors used with a driver (İmren and Birbir, 2021). The motors that meet the needs in the industry are generally mass-produced at certain power and speeds. For this reason, BLDC motor designs can be made using various software for special applications (Hanselman, 1994). The cooling conditions of the BLDC motor vary according to the stator slot structures (Kim and Um, 2009). The analysis outputs of BLDC motors designed according to different SGs can be analyzed after speed control with PI (Kumar, Gandhi, Wilson, and Roy, 2020a; Kumar, Gandhi, Wilson, and Roy, 2020b).

In our study, a BLDC motor with inner rotor, 10 poles and 12 slots is designed. In the design process, slot areas are kept constant as well as all parameters and 4 different slot geometries are created. Then, two dimensional (2D) analyses are performed in the Maxwell interface of ANSYS program and the power, efficiency, torque, torque ripple, copper and core losses, current density, magnetic flux density distribution, which are determined as motor performance, are comparatively examined. Subsequently, the torque spectrum of the electromagnetic torque is generated with the help of Fast Fourier Transform (FFT) analysis, the results are given and harmonics are analyzed. The remainder of the paper is organized as follows: Material and Methods Section provides the detailing of the models created in 2D and the parameters of the designed motor, Results and Discussion Section gives the comparative presentation of the analysis results. Finally, Conclusion Section concludes the study with final evaluations.

## Materials and Methods

In this section, the models created in 2D for four different stator SGs of BLDC motor designed for electric bicycles and light segment electric vehicles are analyzed with Finite Element Method (FEM) in ANSYS program. In these models with different geometric stator SGs, the net slot area is constant. In addition, the materials, properties and parameters determined in the designed models are as given in Table 1.

**Table 1**. Specifications of the BLDC Motors

| | |
|---|---|
| Stator outer/inner diameter | 200/130 mm |
| Rotor outer/inner diameter | 129/45 mm |
| Stack length | 50 mm |
| Air-gap length | 0.5 mm |
| Number of slots | 12 |
| Number of poles | 10 |
| Rated voltage/phase | 48 V/3/Y |
| Rated speed | 450 rpm |
| Magnet material | NdFeB/ Arnold Magnetic-N40-80°C |
| Magnet thickness | 3 mm |
| Stator/Rotor core material | JFE steel-50JN400 |

Where, the parameters given in Table 1 are kept constant for all models with four different SGs. The stator winding type specified in the designs is given in Fig. 1.

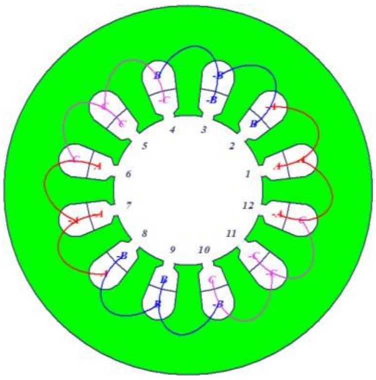

**Figure 1.** BLDC winding configuration of three phase

In the winding type created, the coil pitch is one slot pitch as given in Fig. 1 and a two-layer winding is used. There are a total of 45 turns of conductors in the stator slots. The conductors used in coils consist of 10 stranded round wires with a diameter of 0.607 mm and 0.04 mm individual insulation. There is also only one branch in each phase. The net slot fill is kept at 61% for four different SGs, including the slot insulation material, the insulation material between the winding layers and the insulation materials in the slot opening area. The 2D models of the designed BLDC motor in ANSYS program for the four different stator SGs are given in Fig. 2. The SGs of the models are presented as (a) Type-1, (b) Type-2, (c) Type-3 and (d) Type-4, respectively.

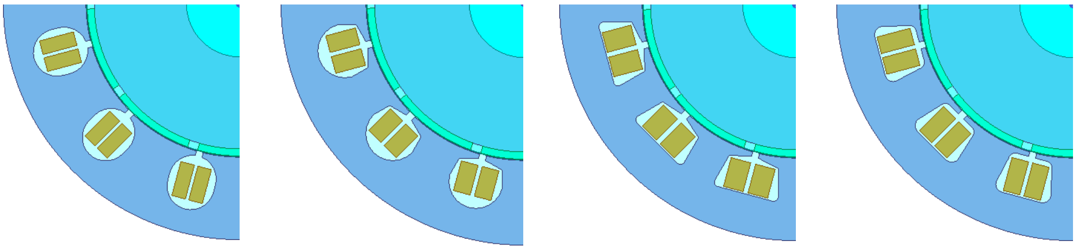

**(a)** **(b)** **(c)** **(d)**

**Figure 2.** 2D models of BLDC motors with different stator slots, **(a)** Type-1, **(b)** Type-2, **(c)** Type-3 and **(d)** Type-4

In all of the motor models given in Fig. 2, the net slot area is kept constant as 307 mm$^2$ and the material used in the stator windings is copper. Here, the amount of material used in the models; the amount of electrical steel material used in the rotor, the amount of magnet material, and the amount of stator winding copper are chosen equally for four different models. However, depending on the stator slot design, the amount of electrical steel used in the stator varies.

## Results and Discussion

In this section, the torque, torque ripple, iron losses, copper losses, efficiency, output power, current density and magnetic flux density distributions determined for the performance evaluation of the motors, whose 2D models are created and analyzed with FEM in ANSYS program, are given comparatively. The nominal speed of the motors are determined as 450 rpm. Fig. 3 shows the flux density distribution obtained as a result of analysis and modeling.

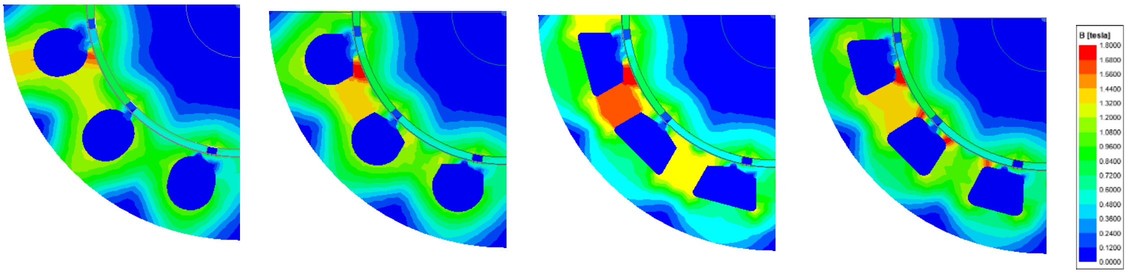

**(a)** **(b)** **(c)** **(d)**

**Figure 3.** Magnetic flux density distribution of BLDC motors with different stator slots, **(a)** Type-1, **(b)** Type-2, **(c)** Type-3 and **(d)** Type-4

As can be seen in Fig. 3 (a), the maximum flux density at the stator teeth in Type-1 is at 1.3 and 1.4 T values, while the maximum flux density at the stator tooth tip is forced to 1.6-1.7 T values. The Type-2 slot structure shown in Fig. 3 (b) has a denser flux density distribution compared to Type-1. In Type-2, while maximum values of 1.45-1.55 T are given at the stator teeth; it exceeds the limits of 1.8 T at the stator tooth tip. It can be said that the Type-3 slot structure shown in Fig. 3 (c) has a very dense flux density distribution compared to the others. While the stator tooth flux density value in Type-3 is 1.7-1.8 T, this density increases to 1.9-2 T at the stator tooth tip. The flux density distribution of the Type-4 slot structure presented in Fig. 3 (d) is similar to the flux density distribution of the Type-2 slot structure. In Type-4, the flux density of the stator teeth is around 1.5 T, while the stator tooth tip is between 1.8 and 1.85 T. As presented here, the slot structure that pushes the flux density limits the least is Type-1, while the highest flux density is analyzed as Type-3. Fig. 4 shows the single phase currents of the analyzed models.

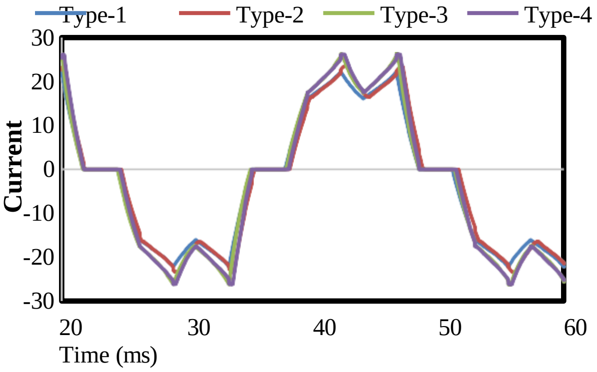

**Figure 4.** Phase current of BLDC motors with different stator slots

As seen in Fig. 4, the maximum current value in Type-1 stator SG is 22.17 A and the effective stator current is 14.9 A; the maximum current value in Type-2 stator SG is 23.4 A and the effective current is 15.5 A; the maximum current value in Type-3 and Type-4 stator SG is approximately 26.2 A and the effective current values are 16.8 and 17.1 A, respectively. The lowest current value is observed in Type-1 while the highest current value is observed in Type-4. Fig. 5 (a) and (b) shows the electromagnetic torques and torque spectra of motors with four different SGs.

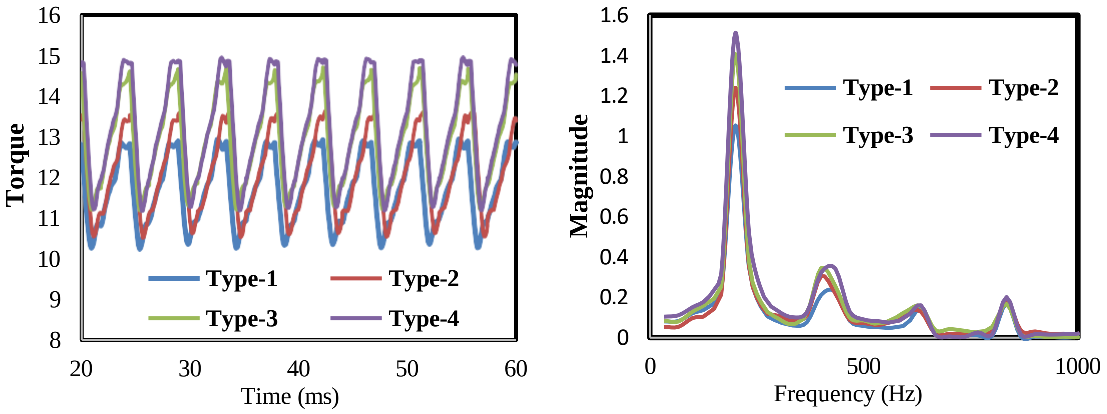

**(a)** **(b)**

**Figure 5.** Torque **(a),** and torque spectra **(b),** of BLDC motors with different stator slots

As shown in Fig. 5 (a), the steady state average torques of Type-1, Type-2, Type-3 and Type-4 are 11.72, 12.17, 12.95 and 13.24 Nm, respectively. As can be understood, an increase in the average torque is found in the SGs, respectively. The electromagnetic torque followed by the torque ripple is calculated and presented (Keskin Arabul, Şenol and Öner, 2020). In terms of torque ripple, the minimum torque ripple value is in Type-1 with 22.7% and the maximum torque ripple is calculated in Type-4 with 28.4%. Fig. 5 (b) shows the harmonic components of the torque resulted from the analysis and modeling of motors with different stator SGs with the help of FFT analysis. Since the steady-state average of the torque is equal to the fundamental component, Fig. 5 (b) shows the spectra including the first 1000 Hz excluding the fundamental component. For the analysis in 2D, the sampling time is chosen as 10000 Hz. As shown in the torque spectra shown in Fig. 5 (b), there are significant changes in some harmonic components with the change of SG. These are 166 Hz, 200 Hz, 400 Hz and 633 Hz components, respectively. The first of these components, 166 Hz, decreased by 6.3% in Type-2 compared to Type-1, but increased by 11% and 38.3% in Type-3 and Type-4, respectively. The most distinct component, 200 Hz, similar to the previous component, increased by 43.6% between Type-1 and Type-4. The same comments can be made for the following 400 Hz. For the 400 Hz component, the increase between Type-1 and Type-4 is 52.3%. For the last component, 633 Hz, there is a decrease of 11.2% in Type-2 compared to Type-1, but an increase of 7.6% and 10.9% in Type-3 and Type-4, respectively. At the end of this evaluation, Table 2 shows the performance parameters of the analyzed motors.

**Table 2.** Performance comparation of BLDC motors with different stator slots

| Parameters | Type-1 | Type-2 | Type-3 | Type-4 |
|---|---|---|---|---|
| Torque (Nm) | 11.72 | 12.17 | 12.95 | 13.24 |
| Torque ripple (%) | 22.7 | 25.4 | 26.9 | 28.4 |
| Power (W) | 552.3 | 573.5 | 610.2 | 624 |
| Efficiency (%) | 91.8 | 91.9 | 92.2 | 92.3 |
| Speed (rpm) | 450 | | | |
| Copper losses (W) | 26.5 | 28.14 | 27.6 | 29.4 |
| Core losses (W) | 12.66 | 12.46 | 13.6 | 12.2 |
| Frictional and Windage losses (W) | 10 | | | |
| Stator current (rms) | 14.9 | 15.5 | 16.8 | 17.1 |
| Current density (A/mm$^2$) | 5.15 | 5.36 | 5.81 | 5.92 |
| Stator slot fill (%) | 61 | | | |

As shown in Table 2, when efficiency and torque are considered, it is shown that Type-4 performs better than models with other SGs. It could not show this advantage in torque ripple and is found to be the SG with the highest torque ripple. In terms of torque ripple, Type-1 has the lowest torque ripple, but in terms of efficiency Type-1 has the lowest efficiency.

## Conclusion

In this study, BLDC motors designed in four different stator slot geometries are modeled in two dimensions in ANSYS program and analyzed with FEM. In the designs, the stator slot areas of the motors are kept constant and the power, efficiency, torque, torque ripple, copper and core losses, current density, magnetic flux density distribution determined for the motor performance of different slot structures are comparatively analyzed. Subsequently, the torque spectrum of the electromagnetic torque is obtained with the help of FFT analysis and the results are given. Significant differences are observed for Type-1 and Type-4. While Type-4 has the highest harmonic content in the torque spectrum; Type-1 has the lowest. In terms of motor performance, the highest output power of 624 W, the highest efficiency of 92.3% and the highest torque of 13.24 Nm are achieved in the Type-4 structure. However, in terms of torque ripple, Type-4 has the highest torque ripple with 28.4%. On the contrary, Type-1 has the lowest torque ripple with 22.7%, while the efficiency and output power are the lowest. Finally, torque, efficiency, power, current density and torque ripple increased from Type-1 to Type-4, respectively.

## References

Dam, D., & Basak, S. (2023). Design and Performance Analysis of an Outer Rotor Brushless DC Motor for Single-Phase Integrated Charger. In 2023 11th National Power Electronics Conference (NPEC).

Hanselman, D. C. (1994). Brushless Permanent-Magnet Motor Design. McGraw-Hill.

İmren, B., & Birbir, Y. (2021). Brushless Direct Current Motor Driver Design and Implementation. International Periodical of Recent Technologies in Applied Engineering, 1(1), 1-10.

Keskin Arabul, F., Şenol, İ., & Öner, Y. (2020). Performance Analysis of Axial-Flux Induction Motor with Skewed Rotor. Energies, 13(19).

Kim, M.-S., Lee, K.-S., & Um, S. (2008). Numerical investigation and optimization of the thermal performance of a brushless DC motor. International Journal of Heat and Mass Transfer, 52, 239-255.

Kim, M.-S., & Um, S. (2009). Numerical Investigation and Optimization of the Thermal performance of a brushless DC motor. International Journal of Heat and Mass Transfer, 52, 239-255.

Kumar, A., Gandhi, R., Wilson, R., & Roy, R. (2020a). Analysis of Permanent Magnet BLDC Motor Design with Different Slot Type. In 2020 IEEE International Conference on Power Electronics.

Kumar, A., Gandhi, R., Wilson, R., & Roy, R. (2020b). The Impact of Different Slot Design of BLDC Motor in A Complete Drive System. In IECON 2020 The 46th Annual Conference of the IEEE Industrial Electronics Society.

Moghaddam, H. A., Mirzahosseini, R., & Farajzadeh, A. (2023). Technical and Economic Feasibility Study of Using Fractional Slot Concentrated Winding BLDC Motor for Evaporative Cooler Application. In 2023 3rd International Conference on Electrical Machines and Drives (ICEMD).

Mujianto, A., Nizam, M., & Inayati. (2014). Comparation of the Slotless Brushless DC Motor (BLDC) and Slotted BLDC Using 2D Modeling. In 2014 IEEE International Conference on Electrical Engineering and Computer Science.

Uygun, D., & Solmaz, S. (2015). Design and Dynamic Study of a 6 kW External Rotor Permanent Magnet Brushless DC Motor for Electric Drivetrains. In 2015 IEEE 5th International Conference on Power Engineering, Energy and Electrical Drives (POWERENG).